THESE de DOCTORAT DE L'UNIVERSITE DE LYON
opérée au sein de
l'Institut National des Sciences Appliquées de Lyon

Ecole Doctorale MEGA ED162
Mécanique, Energétique, Génie Civil, Acoustique

Spécialité/discipline de doctorat :
Génie Mécanique

Soutenue publiquement le 19/01/2021, par :
JACQUET Nicolas

ELASTO-VISCO-PLASTIC BUCKLING OF THICK SHELLS

Devant le jury composé de :

THUILLIER, Sandrine	Professeur, Université Bretagne Sud	Rapporteuse
ZAHROUNI, Hamid	Professeur, Université de Lorraine	Rapporteur
KYRIAKIDES, Stelios	Professeur, Université du Texas	Examinateur
CORET, Michel	Professeur, École Centrale de Nantes	Président
BOUCLIER, Robin	Maître de conférences, INSA de Toulouse	Examinateur
ELGUEDJ, Thomas	Professeur, INSA de Lyon	Directeur de thèse
TARDIF, Nicolas	Maître de conférences, INSA de Lyon	Invité et co-encadrant de thèse
GARNIER, Christophe	Ingénieur, CEA Cadarache	Invité et co-encadrant de thèse

Remerciements

Ces travaux de thèse n'auraient pu avoir lieu sans l'aide de nombreuses personnes. Je souhaite tout d'abord remercier le CEA et le LaMCoS pour m'avoir permis de réaliser cette thèse et ceci malgré ma situation professionnelle particulière. Le soutien financier et humain apporté par ces deux entités a été précieux.

Je ne pourrais suffisamment remercier mon directeur Thomas ELGUEDJ et mes encadrants Nicolas TARDIF et Christophe GARNIER pour le temps et l'aide qu'ils m'ont accordés, et en particulier les nombreux coups de pouce de Nicolas lors des différentes taches expérimentales et en particulier pour les nombreuses coulées de fonderie.

L'étendue des travaux a aussi nécessité le soutient de nombreuses autres personnes et je souhaite remercier en particulier Alexandre ZELEZ pour les usinages des moules et des pièces d'essais. Son travail de qualité participe aussi aux résultats obtenus. De même, les résultats expérimentaux n'auraient pu être de si bonne qualité sans l'aide de Philippe CHAUDET.

De nombreux essais ont été réalisés dans les locaux du laboratoire GEOMAS de l'INSA. Je veux ainsi en remercier son directeur Stéphane GRANGE pour m'avoir permis de réaliser mes essais malgré les événements sanitaires de 2020. J'aimerais aussi remercier Romain TRUNFIO et Emeric BRUYERE pour leur support technique ainsi que Tina GUILLOT pour son aide dans la mise en œuvre du four lors de nos différentes opérations de fonderie.

Je remercie aussi tous mes camarades doctorants avec qui j'ai pu échanger et sans qui ces trois années n'auraient pas paru aussi courtes, je pense à Tristan, Thibault, Thomas, Alexis, Ethel, Florian, Marie, Karine, Efoe... j'espère ne pas en oublier.

Finalement j'aimerais remercier ma famille qui m'a soutenu tout au long de cette aventure, mes amis et en particulier ma compagne Zoé qui a su me soutenir dans les moments difficiles et m'écouter lorsque c'était nécessaire.

Une page se tourne mais de nouvelles restent à écrire.

Contents

List of Figures

16

List of Tables

17

Résumé étendu

0.1 Introduction et objectifs

0.1.1 Introduction

Ces travaux de thèse s'inscrivent dans un projet de recherche piloté par le CEA. Ce projet vise à développer un réacteur de génération IV. Il a aussi pour objectif de développer des démonstrateurs et des méthodes numériques permettant de comprendre et de modéliser certains phénomènes physiques. Du fait de la technologie du cœur du réacteur, le CEA a choisi le sodium liquide comme fluide réfrigérant. Au sein de ce projet, le Laboratoire de Conception et d'Innovation Technologique (LCIT) avait pour responsabilité la conception de l'échangeur de chaleur.
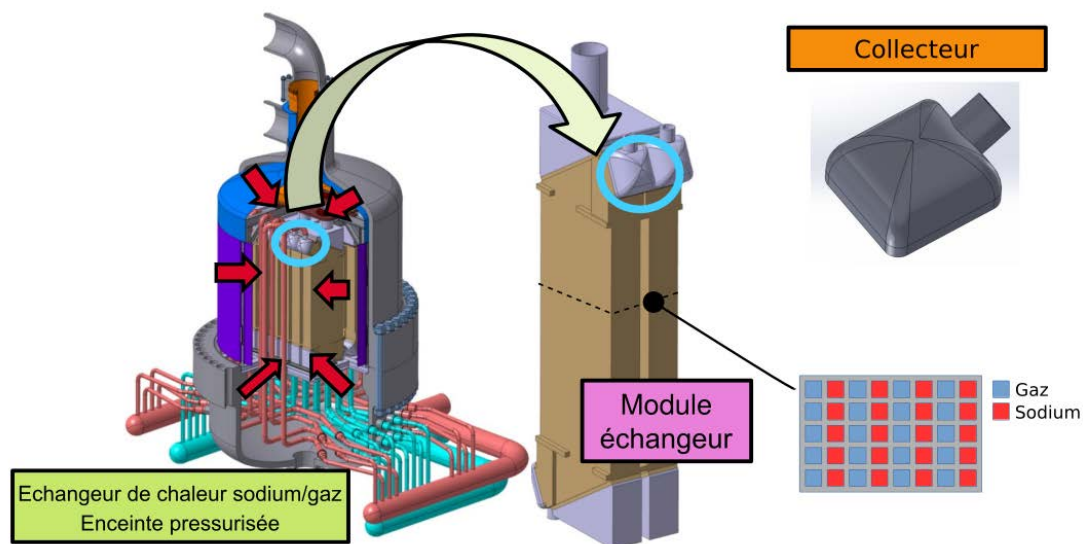
Figure 1: Option de conception de l'échangeur de chaleur sodium/gaz comprenant le concept d'échangeur compact à micro-canaux

Une fois la chaleur prélevée dans le cœur par le circuit de sodium primaire, celle-ci est transférée au circuit de sodium secondaire. Le circuit secondaire transfert

quant à lui sa chaleur au circuit de gaz tertiaire. Ce dernier transfert thermique est assuré par l'échangeur de chaleur sodium gaz. Le LCIT a choisi une technologie d'échangeur compacte à micro-canaux. Ce type d'échangeur permet d'augmenter le rendement thermique en augmentant la surface d'échange et en améliorant l'échange thermique avec la paroi. Pour cela les flux de sodium et de gaz sont répartis dans de nombreux canaux. Afin de distribuer et de collecter correctement le sodium dans l'échangeur, un collecteur est placé à l'entrée de chaque module de l'échangeur. L'ensemble de l'échangeur est placé dans une enceinte pressurisée où circule le gaz du circuit tertiaire. Cette enceinte joue le rôle de collecteur du circuit tertiaire et améliore la sécurité du système. La Figure 1 présente l'échangeur, un module et une section d'un module d'échangeur.

Le collecteur de sodium est défini comme une coque épaisse. Il travaille sous une pression externe de 180 bar et dans une ambiance chaude de 520°C. Le collecteur de sodium est fait d'acier inoxydable 316L(N). À cette température le 316L(N) a un comportement élasto-visco-plastique. Du fait du chargement, de la température et de la géométrie du collecteur, le CEA s'est interrogé sur la tenue et la stabilité structurale de ce collecteur.

Ainsi l'objectif de ces travaux de thèse est d'étudier numériquement et expérimentalement le flambage de coques épaisses dont le comportement est élasto-visco-plastique. Ces travaux de recherche ont été réalisés en vue de définir des règles de dimensionnement.

0.1.2 Le flambage

Le flambage est étudié dans de nombreux articles scientifiques. Il fut d'abord étudié sur des structures fines dont le comportement est élastique du fait d'une plus grande probabilité à flamber. Le lien entre flambage et perte d'unicité de la solution fut alors établi. Un critère développé par *Hill* permit de prédire le flambage de structure dont le comportement est élasto-plastique (cf. [HILL 1958]).

Lors d'essais sur des structures épaisses, il fut constaté que le point critique de flambage pouvait dépendre de la formulation du modèle constitutif. En effet des prédictions utilisant la théorie de la déformation plutôt qu'une théorie incrémentale présentaient une meilleure corrélation avec des résultats d'essais. Ceci fut en particulier discuté par HUTCHINSON dans [HUTCHINSON 1974]. Il fut ainsi admis que ce flambage précocement observé avec la théorie de la déformation était provoqué par l'apparition d'un coin sur la surface de charge. Celui-ci pourrait alors être prédit à l'aide d'une loi incrémentale complexe. HUTCHINSON conclut que toute loi incrémentale complexe correspond à une loi simple suivant la théorie de la déformation sur un certain intervalle de déformations.

Néanmoins, l'utilisation de lois de comportement basées sur la théorie de la déformation se limite aux chargements proportionnels. Afin de lever cette limitation, CHRISTOFFERSEN et HUTCHINSON développèrent une loi de comportement intégrant un coin sur la surface de charge et l'utilisation de la théorie de

la déformation pour les chargements quasi-proportionnels. Celle-ci est détaillée dans [CHRISTOFFERSEN et HUTCHINSON 1979]. Cette loi incrémentale permet de mettre un cadre théorique autour du paradoxe discuté par HUTCHINSON. Cette théorie fut appliquée avec succès à des structures épaisses au chargement non proportionnel (cf. [NEEDLEMAN et TVERGAARD 1982] ou [TVERGAARD 1983]).

Toutes ces observations et théories s'appliquent seulement à des structures dont le comportement n'est pas dépendant du taux de déformation. Il faut attendre l'hypothèse définie par BODNER, NAVEH et MERZER dans [BODNER, NAVEH et MERZER 1991] pour trouver une méthode de prédiction du flambage appliquée aux structures dont le comportement est dépendant du taux de déformation. BODNER, NAVEH et MERZER font l'hypothèse que le flambage est suffisamment soudain pour que le taux de déformation ne puisse varier pendant le flambage. Ainsi il définit un problème de plasticité instantané. Ce dernier permet d'appliquer, aux structures dont le comportement est dépendant du taux de déformation, toutes les méthodes déjà développées pour les structures dont le comportement est indépendant du taux de déformation.

0.1.3 Objectifs scientifiques

Les objectifs de ces travaux de thèse sont donc :

- de développer une méthode prédictive appliquée au flambage de coques épaisses soumises à un chargement non proportionnel et dont le comportement est dépendant du taux de déformation,

- observer le flambage de structures épaisses via des essais,

- comparer et évaluer la méthode prédictive vis-à-vis des résultats expérimentaux.

Pour atteindre ces objectifs une stratégie a été développée. Elle est détaillée dans la Figure 2.

Afin de réduire les contraintes expérimentales liées aux essais sur structures en 316L(N) à chaud, un matériau modèle dont le comportement à température ambiante est similaire a été choisi. Le matériau modèle retenu est un matériau à base étain, appelé SAC 305. Il a donc été nécessaire de développer un procédé de mise en forme de ce matériau. Une fois mis en forme, le comportement mécanique du SAC 305 a pu être identifié via une méthode inverse.

À la suite de ces deux tâches préliminaires deux campagnes d'essais de flambage ont été menées. La première porte sur le flambage de plaques épaisses en compression, la seconde sur le flambage de coques soumises à une pression externe.
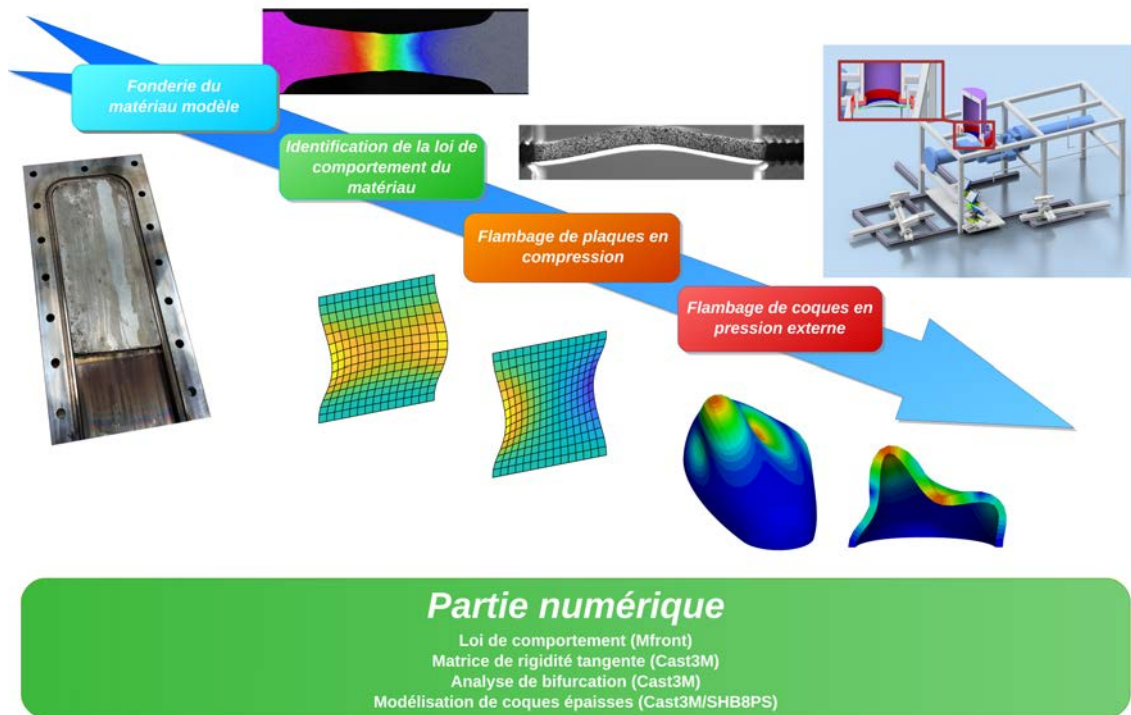
Figure 2: Stratégie de la thèse : étudier numériquement et expérimentalement le flambage de coques épaisses dont le comportement est élasto-visco-plastique

0.2 Un critère adapté aux coques épaisses et au comportement élasto-visco-plastique

Le critère développé s'appuie sur deux éléments : la théorie des coins de CHRISTOFFERSEN et HUTCHINSON, et l'hypothèse de *Bodner*.

Le premier élément permet de dériver un module tangent prenant en compte l'aspect épais des coques étudiées et l'aspect chargement non proportionnel. Le second élément permet quant à lui de dériver un module tangent en prenant en compte la dépendance du comportement au taux de déformation.

La théorie des coins en élasto-visco-plasticité

La théorie des coins s'appuie sur une surface de charge comprenant un coin. Ce coin est défini par un cône dont le sommet est orienté par le déviateur du tenseur de contraintes. Pour un incrément de contrainte donné, trois situations distinctes peuvent être définies en fonction de l'angle θ formé entre l'incrément de contraintes et le déviateur du tenseur de contraintes. Si l'incrément de contraintes est quasi-proportionnel, $\theta \leq \theta_0$, l'incrément de déformations plastiques est calculé en fonction de la théorie de la déformation. Si $\theta \geq \theta_c$, une décharge élastique est observée. Lorsque $\theta_0 < \theta < \theta_c$, l'incrément de déformation plastique est calculé grâce à une

22

loi de comportement non-linaire dérivée du potentiel suivant :

$$W(\dot{\boldsymbol{\sigma}}, \boldsymbol{\sigma}) = \dot{\boldsymbol{\sigma}}^t \left(\boldsymbol{\mathcal{L}}_e + h(\theta)\boldsymbol{\mathcal{L}}_p\right) \dot{\boldsymbol{\sigma}}, \tag{1}$$

avec $\boldsymbol{\mathcal{L}}_e$ la loi de comportement élastique inverse, et $\boldsymbol{\mathcal{L}}_p$ la loi de comportement plastique inverse dérivée de la théorie de la déformation. La fonction h est une fonction continue de θ définie comme suit :

$$h = \left\{ \begin{array}{ll} 1, & \theta \leq \theta_0 \\ 0, & \theta \geq \theta_c \\ h(\theta), & \text{autrement} \end{array} \right\} \tag{2}$$

Ainsi, de même que pour l'incrément de contraintes plastiques, le module tangent est calculé en fonction de θ. Si le chargement est quasi-proportionnel, le module tangent est égal à celui de la théorie de la déformation. Si une décharge élastique est observée, le module élastique est utilisé. Dans la zone de transition le module tangent est un tenseur non-linéaire de θ qui est égal au module élastique si $\theta = \theta_c$, ou qui est égal au module tangent de la théorie de la déformation si $\theta = \theta_0$.

La théorie des coins a été adaptée ici au comportement élasto-visco-plastique afin de prendre en compte de possibles décharges dans le domaine visco-plastique. Ceci permet en particulier de bien appréhender le flambage en régime de fluage. En cas de décharge dans le domaine visco-plastique, θ est remplacé par $\theta^\star$, avec :

$$\theta^\star = \left\{ \begin{array}{ll} \theta, & \text{si on est sur la surface de charge} \\ \theta, & \text{si le point considéré est en charge} : \theta \leq \pi/2 \\ \pi - \theta, & \text{si le point considéré décharge} : \theta > \pi/2 \end{array} \right. \tag{3}$$

La Figure 3(b) permet aussi d'illustrer le fonctionnement de ce critère de charge/décharge visco-plastique.

La condition de consistance instantanée de *Bodner*

L'Hypothèse de *Bodner* permet de définir une condition de consistance instantanée, celle-ci est définie comme suit :

$$d\dot{p} = d(g(f)) = g'(f)df = 0, \tag{4}$$

où g est la loi de fluage et f est le critère d'écoulement de la loi de comportement.

À partir de cette condition de consistance instantanée, le module tangent peut être dérivé pour n'importe quelles lois de comportement : incrémentales, basées sur la théorie de la déformation ou sur la théorie des coins.

En utilisant les outils classiques de recherche de bifurcation, le premier point de bifurcation peut être défini pour n'importe quelle structure. Dans notre cas nous avons choisi d'utiliser la théorie de la déformation pour le calcul des charges et modes de flambage des plaques en compression et la théorie des coins pour les coques en pression externe.
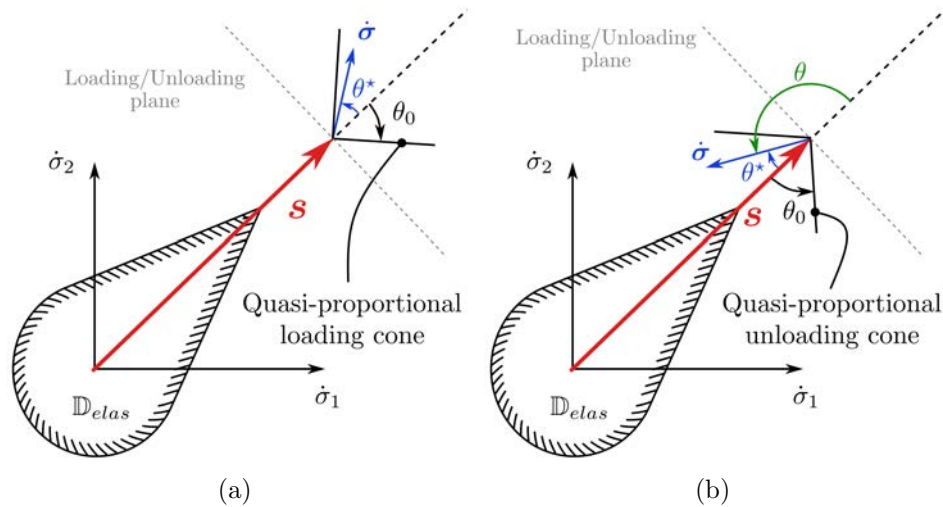
Figure 3: (a) Charge quasi-proportionnelle dans le domaine visco-plastique selon la théorie de coins ; (b) Décharge quasi-proportionnelle dans le domaine visco-plastique selon la théorie de coins

Dans tous nos calculs de bifurcation, nous avons utilisé les données de contrainte et de déformation issues d'un calcul incrémental utilisant une loi d'écoulement incrémentale comme données d'entrée au calcul des modules tangents.

0.3 Identification d'une loi de comportement

Comme indiqué précédemment, la loi de comportement du matériau modèle a dû être identifiée. Pour cela une méthode inverse appelée FEMU pour Finite Element Model Updating a été utilisée, celle-ci est décrite dans [Avril et al. 2008]. Cette méthode utilise des données expérimentales d'une part et un modèle élément fini des essais d'autre part. Un algorithme vient mettre à jour la loi de comportement jusqu'à ce que le modèle éléments finis converge sur les essais. Ainsi les paramètres de la loi de comportement sont identifiés de façon inverse.

0.3.1 La loi de comportement du SAC 305

Une loi de comportement permettant de modéliser finement le comportement du SAC 305 a été choisie. Elle est composée de trois variables d'écrouissage de type Voce. Ceci permet de bien modéliser le comportement tangent du SAC 305. Une loi d'écoulement visqueux de type Norton est utilisée pour modéliser la dépendance au taux de déformation. La propriété d'orthotropie du cristal d'étain dans sa phase bêta et des observations expérimentales ont mené à l'utilisation d'une surface de charge anisotrope de type *Hill*. Celle-ci est utilisée pour modéliser le comportement isotrope transverse du SAC 305 dans l'épaisseur des coques.

Le jeu d'équations 5 permet de définir la loi de comportement retenue.

$$
\begin{aligned}
\boldsymbol{\sigma} &= \boldsymbol{\mathcal{C}} \, \boldsymbol{\varepsilon}_e, \\
\boldsymbol{\varepsilon} &= \boldsymbol{\varepsilon}_e + \boldsymbol{\varepsilon}_p, \\
\dot{p} &= \left(\frac{F}{K} \right)^n, \\
F &= \sigma_{eq} - R(p), \\
R(p) &= R_0 + \sum_{i=1}^{3} R_i \left(1 - e^{-b_i p} \right), \\
\sigma_{eq} &= \sqrt{ \boldsymbol{\sigma} : \boldsymbol{H} : \boldsymbol{\sigma} },
\end{aligned}
\tag{5}
$$

avec, $\boldsymbol{\sigma}$ tenseur des contraintes de Cauchy, $\boldsymbol{\varepsilon}$ le tenseur des déformations de Biot, $\boldsymbol{\varepsilon}_e$ le tenseur des déformations élastiques et $\boldsymbol{\varepsilon}_p$ le tenseur des déformations inélastiques, $\boldsymbol{\mathcal{C}}$ le module d'élasticité isotrope, σ_{eq} la contrainte équivalente de *Hill*, $\boldsymbol{H}$ le tenseur de *Hill* (utilisé pour l'isotropie transverse), p la déformation plastique équivalente, R la variable d'écrouissage et $\dot{p}$ le taux de déformation plastique équivalent.

Les paramètres matériau à identifier sont : R_0, R_1, b_1, R_2, b_2, R_3, b_3, K, n, $\boldsymbol{H}$ complètement défini par le coefficient de Lankford R_{lank} et $\boldsymbol{\mathcal{C}}$ défini par le module d' Young et le coefficient de Poisson.

0.3.2   Essais et identification

Les paramètres de la loi précédemment présentée ont été identifiés par une méthode inverse (FEMU). Cette identification à été réalisée à partir d'essais de traction pilotés en taux de déplacement. Ces essais ont été conduits sur des éprouvettes à section utile évolutive. Ces dernières sont issues de quatre lots matière. La géométrie de l'éprouvette de traction ainsi que son installation dans la machine de traction est illustrée dans la Figure 4.

La forme de l'éprouvette a permi d'enrichir le jeu de données expérimentales. En effet, grâce à la géométrie de l'éprouvette, différents taux de déformation peuvent être observés à la surface de l'éprouvette. La simulation de ces essais et l'utilisation de la méthode FEMU ont permis d'identifier les paramètres de la loi de comportement pour chaque lot matière. Une étude de sensibilité des paramètres a aussi été menée afin d'évaluer le caractère unique de la solution identifiée.

À partir de ce jeu de lois de comportement, une loi de référence basée sur l'étude statistique des essais a été générée. Celle-ci est utilisée pour toutes les analyses numériques.
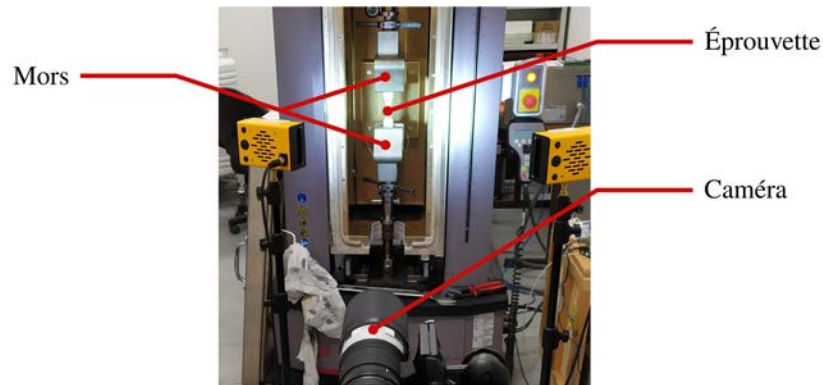
Figure 4: Présentation de l'éprouvette de traction montée dans la machine de traction

0.4   Essais de flambage sur plaques en compression

Cette campagne d'essais de flambage sur des plaques en compression a eu pour objectifs : d'étudier l'effet de la géométrie de la plaque sur le flambage ; mais aussi d'évaluer l'effet du taux de déformation sur le comportement en flambage des plaques.

Le Figure 5 montre un plaque montée dans le montage de mise en compression.
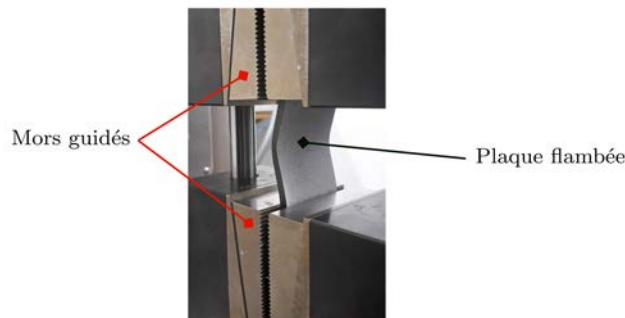
Figure 5: Présentation du montage de mise en compression et d'une plaque déformée dans le montage.

Des plaques épaisses avec différentes géométries ont été testées. L'effet de la géométrie sur les charges critiques, ainsi que sur les modes de flambage, a pu être observé. Le modèle prédictif a montré une bonne corrélation avec les essais. De plus, la proximité de deux modes a pu être observée. Cette observation a été possible grâce à l'utilisation de la stéréo-corrélation d'images pour mesurer le déplacement

26

en 3D à la surface des éprouvettes. Cette proximité de mode était aussi observable numériquement via le modèle prédictif développé.

D'autres plaques ont été testées avec des vitesses de sollicitation différentes. Ainsi l'effet du taux de déformation sur les charges et temps critiques a pu être observé. Il a pu être observée que le taux de déformation a peu d'effet sur le mode de flambage. Une fois encore le modèle prédictif a montré de bons résultats vis-à-vis des essais.

Ces essais à différentes vitesses, ainsi qu'une analyse élément fini en post flambage de plaques en compression sollicitées à différentes vitesses ont permis d'évaluer les limites de l'hypothèse de *Bodner*. En effet, il a pu être constaté que l'hypothèse de *Bodner* était inadaptée à la prédiction du flambage de structures sollicitées à trop hautes vitesses.

Ce premier jeu d'essais a permis d'évaluer le modèle prédictif par rapport à des résultats expérimentaux. Il a aussi permis de mettre en place un certain nombre de méthodes expérimentales. Compte tenu des bons résultats obtenus lors de cette campagne, tant d'un point de vue numérique qu'expérimental, la campagne d'essais sur des coques complexes soumises à un chargement non proportionnel a pu être envisagée avec confiance.

0.5 Essais de flambage sur coques épaisses en pression externe

Cette nouvelle campagne d'essais est similaire dans la méthode à celle appliquée aux plaques. L'instrumentation des essais y est similaire. Elle est principalement organisée autour de la stéréo-corrélation d'images. Les éprouvettes testées avaient la forme de demi-œufs. Cette forme peut être considérée comme la forme médiane entre la sphère et le cylindre. La Figure 6 présente le montage d'essai et une éprouvette flambée.

Compte tenu du temps de fabrication et du temps d'essai de chacune des éprouvettes, une seule géométrie d'œuf a été testée. Une loi de pression, inversement exponentiel dans le temps, a été appliqué. Deux vitesses de sollicitation ont pu être testées. En tout cinq œufs ont été fabriqués et testés.

Pour chaque œuf une plage de pressions et de temps encadrant l'instant le flambage a été défini. La borne inférieure de cette plage est définie par un point équilibre correspondant à une inversion du champ de déplacement au sommet de l'œuf. La borne supérieur est définie par le point d'équilibre correspondant à la pression maximale.

Le couplage des mesures de champs de déplacement par stéréo-corrélation d'images avec une transformation de Fourier rapide, a permis d'approximer les modes de flambage des oeufs testés. Comme pour les plaques, une proximité de deux modes a pu être observée expérimentalement.

Une analyse sur les conditions aux limites, a aussi montré la faible dépendance de cette structure aux imperfections.
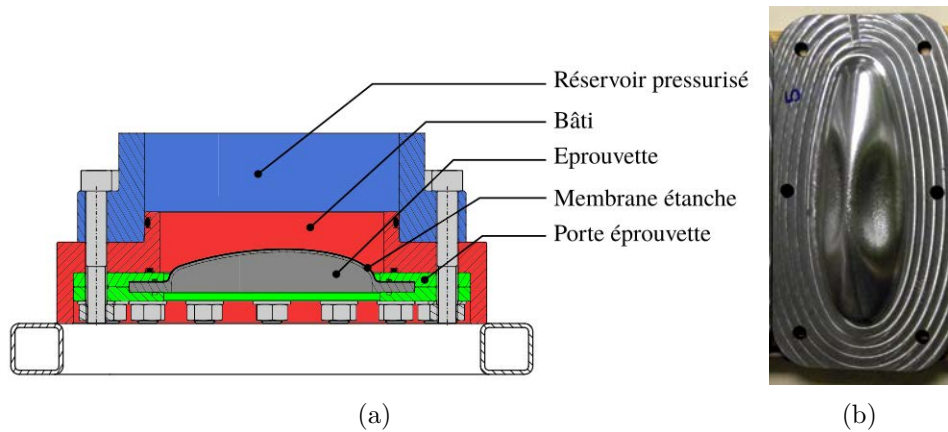
Figure 6: (a) Montage d'essais de flambage en pression externe ; (b) Éprouvette de flambage en pression externe déformée après flambage

Compte tenu du chargement et des conditions aux limites appliquées au demi-oeuf, le chargement subi par la structure est non proportionnel. Ce type d'essais permet d'évaluer la méthode prédictive vis-à-vis de la non-proportionnalité du chargement et de la dépendance du comportement matériau au taux de déformation. Le modèle prédictif, basé sur la théorie des coins a montré un bonne corrélation avec les résultats expérimentaux. Les prédictions du modèle corrèlent bien avec la plage de flambage définie expérimentalement. De plus, les modes prédits correspondent bien aux modes extraits du champ de déplacement.

Cette série d'essais plus complexes que ceux réalisés sur les plaques, montre la pertinence du modèle prédictif développé pour des structures complexes. De même que pour les plaques, les hypothèses sous-jacentes au développement du modèle doivent être respectées, et en particulier l'hypothèse de *Bodner*.

0.6 Conclusion

Les travaux présentés dans ce manuscrit donnent de nouveaux outils au CEA permettant de répondre à la problématique de ces travaux de thèse. La stabilité de structures industrielles épaisses et complexes dont le comportement est dépendant du taux de déformation peut ainsi être étudiée. Certains pré-requis restent nécessaires, comme une identification fine du comportement du matériau et en particulier sa loi d'écrouissage tangente. De plus, la définition des paramètres de la théorie des coins est nécessaire. En effet, ils peuvent faire varier de façon importante les valeurs critiques prédites.

La méthode détaillée dans ce manuscrit ne peut se soustraire à un essai structurel permettant de valider la conception et le dimensionnement d'une structure industrielle complexe.

Lors de cette étude, une autre méthode prédictive plus rigoureuse, mais aussi

plus difficile à implémenter dans un logiciel élément fini a été identifiée. Celle-ci s'appuie sur une condition suffisante de stabilité pour des structures dont le comportement est dépendant du taux de déformation. Cette méthode développée par TRIANTAFYLLIDIS, MASSIN et LEROY est détaillée dans [TRIANTAFYLLIDIS, MASSIN et LEROY 1997]. Afin de lever les limitations induites par l'hypothèse de *Bodner*, en particulier sur la vitesse de sollicitation, une telle méthode pourrait être utilisée. Cette nouvelle implémentation demanderait un travail de développement et de validation numérique conséquent.

Couplée à cette méthode rigoureuse, l'utilisation d'une surface de charge complexe comprenant des coins pourrait aussi être investiguée. L'utilisation conjointe de la condition suffisante de TRIANTAFYLLIDIS, MASSIN et LEROY et du surface de charge complexe, définirait un modèle prédictif rigoureux. Néanmoins, un gros travail de caractérisation de la surface de charge serait alors nécessaire. Les efforts de développement et de caractérisation semblent difficilement envisageables dans le cadre industriel. En ce sens, la méthode proposée dans ces travaux de thèse constitue une approximation suffisante à l'échelle industrielle. Elle permet de donner une bonne estimation des charges, des temps et des modes de flambages de structures complexes dont le comportement est dépendant du taux de déformation.

Introduction

Industrial context

The present work takes place in a research program driven by the CEA and focused on the development of the fourth generation of nuclear reactors. This new generation of reactors should increase the safety, reduce the amount of radioactive waste and be able to recycle plutonium. This program is also oriented on the building of technology demonstrators, the development of numerical tools and the characterization of specific phenomena. The choice of the reactor technology led the CEA to select the liquid sodium as coolant for the primary and secondary circuits.

Several concepts were studied to convert the heat energy from the core into electricity. One of the main innovative options under investigation for forth generation reactors is the use of a Brayton cycle gas-power conversion system. This system permits to avoid the energetic sodium-water interaction, which can occur in steam generators in case of tube failure if a traditional Rankine cycle is used. In this novel concept, steam generators would be replaced by a Sodium Gas Heat Exchanger (SGHE). The heat is extracted from the core of the reactor, it is transported through the primary and secondary circuits and transferred to a pressurized gas. It is then expanded within a turbine. This last one is linked to a generator. The thermal cycle is illustrated in Figure 7.
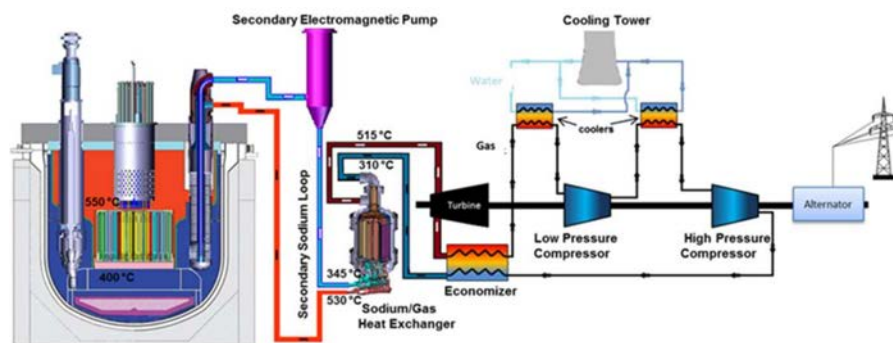
Figure 7: Sodium fast reactor diagram of general principle

It is therefore important to maximize the heat transfer between the sodium cir-

cuit and the gas, in order to increase the efficiency of the whole system. This heat transfer function is fulfilled by a sodium-gas heat exchanger. The design and technological innovation laboratory (LCIT) was in charge of the design of this component.

The LCIT based its design on the concept of compact microchannel heat exchanger. The main feature of this family of heat exchangers is to maximize the heat transfer by increasing the exchange surface. This is done by dividing both fluid fluxes into a large number of channels following a complex path. A section of the heat exchanger shows the different channels and their exchange surfaces in Figure 8.

In addition this technology presents interesting advantages such as mechanical strength (it can withdraw high pressures) and manufacturing technologies.
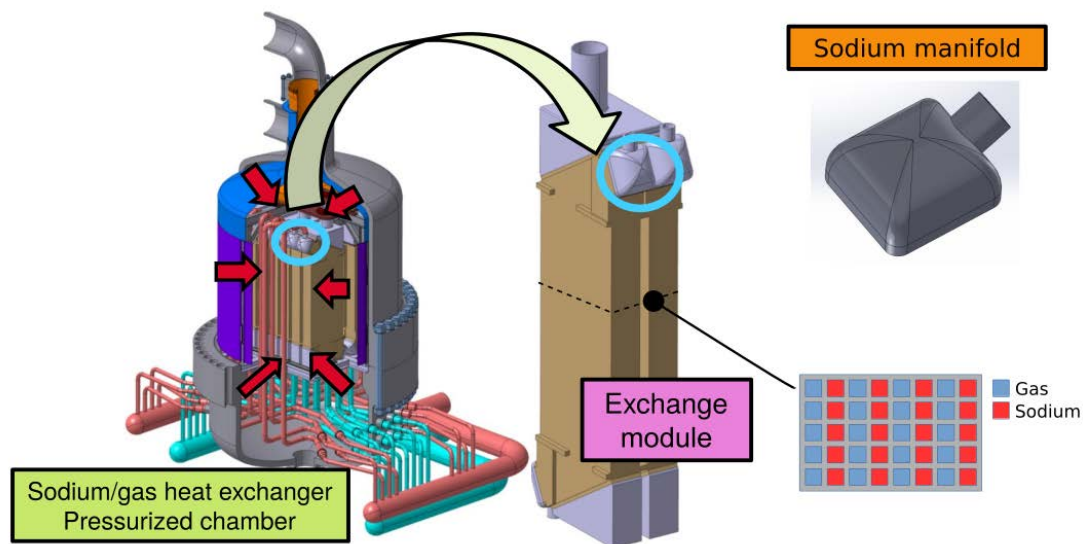
Figure 8: Design option of the sodium gas heat exchanger with the concept of compact microchannel heat exchanger

Therefore, the uniformity of the heat transfer in the heat exchanger is directly linked to the uniformity of the sodium distribution within the heat exchanger. The uniformity of the temperature also improves the mechanical strength of the heat exchanger by reducing the thermal stress. Sodium manifolds are mainly used for this purpose. Nevertheless this specific component of the heat exchanger needs to fulfil the following requirements:

- Insure the best distribution/collection of the sodium to/from the heat exchanger,

- Resist to mechanical loadings and in particular to an external pressure of 18 MPa,

- Resist to thermal loadings and in particular to a heating rate or cooling rate up to $2°\text{C.s}^{-1}$, and an environmental temperature of $530°\text{C}$.

As a consequence, the manifold insuring the sodium distribution is subjected to external pressure. From a mechanical point of view, this component can be considered as a thick shell. Buckling was identified as a potential failure case for ultimate loads. Because of the high temperature, as this component is made of 316L(N) stainless steel, its rate-dependency must be taken into account for the buckling analysis.

From a design point of view, as it is part of a safety component, it will be subjected to nuclear design requirements. Among them: the demonstration that buckling failure is avoided.

Scientific background

This work is therefore focused on the buckling of thick shells whose material presents a rate-dependency. The literature is very rich concerning the buckling of structures. Some are more oriented on the numerical predictions of this phenomenon, while others present experimental results. In some rare cases, experiments are compared to numerical predictions. In particular, it has been shown that it is a global failure mechanism, as it depends on the whole geometry of the structure, its loading and boundary conditions, and its material behaviour.

Many approaches were defined to predict the buckling of solids, the most famous and used one is *Hill*'s uniqueness criterion. This last one was successfully applied to predict buckling of elasto-plastic solids with the simplest incremental theory (the *Mises* flow theory). Unfortunately, for some structures, the predictions did not correlate with the experiments, especially for thick structures. Using any constitutive law based on the deformation theory, better agreements of the predictions with the experiments were observed. This buckling paradox was observed and discussed several times in the literature and especially by Hutchinson [Hutchinson 1974]. Finally the buckling prediction of thin or thick rate-independent solids is well documented for both numerical and experimental investigations.

For the buckling of rate-dependent structures the literature is not as rich as for rate-independent structures. The buckling of thin rate-dependent shells is almost exclusively studied in the literature. Nevertheless the literature gives clues on the numerical buckling prediction for rate-dependent shells.

To answer to the CEA interrogation on the structural stability of the sodium manifold, a strategy was developed. This strategy aims to complete the existing methods and data provided by the literature. It was developed to incrementally study the numerical and experimental buckling behaviour of thick rate-dependent shells subjected to non-proportional loadings. This strategy would finally provide an experimentally validated predictive method to the CEA. This predictive method

would allow the CEA to analyse the buckling behaviour of industrial components. The strategy is presented in the next section.

Objectives and strategy

The main objectives of this work are to evaluate experimentally the buckling of thick rate-dependent shells and to predict their buckling using a numerical model. To reach these final objectives, an incremental strategy has been developed, as shown in Figure 9.
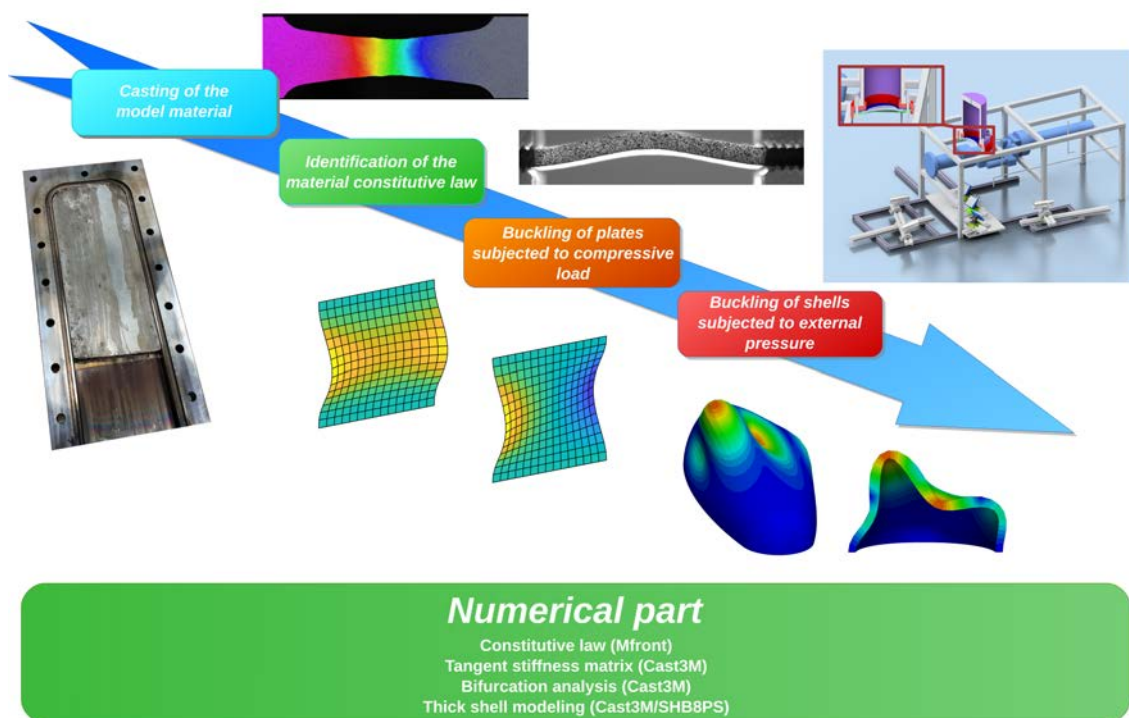
Figure 9: Strategy of the thesis to predict and experiment the buckling of thick elasto-visco-plastic shells

A global task is dedicated to the development of the numerical environment required to study the buckling of thick shells. More importantly, one of the objectives of this numerical task is to define a buckling criterion. This last one is used to predict the buckling of thick rate dependent shells subjected to complex loadings. In parallel, different experimental tasks are performed in order to generate the different sets of data to be compared to the numerical models.

As already said, the original component is made of stainless steel 316L(N) and it is used at high temperature (530°C). Using the same alloy under similar temperature conditions would generate important constraints on the experiments and their

instrumentations. Therefore a model material presenting a rate-dependency at room temperature was preferred. Nevertheless these types of materials are not common. Two preliminary tasks are focused on the manufacturing of the specimens and the mechanical characterization of the alloy (cf. Figure 9 first and second items). One preliminary task aims to develop a robust and repeatable manufacturing process. The other intends to finely characterize the mechanical behaviour of the alloy with its associated manufacturing process.

Then, two buckling test campaigns were performed. The first one was focused on the buckling of thick plates subjected to in-plane compression (cf. Figure 9 third item). This choice was motivated for two reasons. First, a plate subjected to in-plane loading is one of the simplest shapes to study experimentally and numerically. Moreover, the manufacturing of plates is also very simple. In addition, thick plates present an interesting buckling behaviour, as they are subjected to the so called "buckling paradox", as discussed in [Wang and Aung 2007]. This type of experiments was also chosen in order to evaluate both numerical and experimental methods on simple shell geometry. The objectives of this first type of experiment are:

- to define the adequate instrumentation in order to compare the numerical results to the experimental ones,

- to perform buckling experiments on thick rate-dependent plates,

- to evaluate the numerical buckling prediction model against the experimental buckling behaviour of thick plates.

The second buckling test campaign was focused on the extension of the preliminary results obtained with plates to more complex shells. Hemi-egg shells were tested under external pressure (cf. Figure 9, fourth item). The numerical model to predict buckling was generalized to complex shells subjected to complex loadings. The same instrumentation as for the plate buckling experiments was used. This second buckling test campaign would allow to reach the main objectives of this work.

In this work a great attention was given to the comparison of the experiments with the different numerical results. All experimental results were enriched by numerical analysis of the experiments. Therefore numerical and experimental results are presented together.

The results obtained with the model material can be generalized to any other elasto-visco-plastic material, in order to apply the present work to any thick rate-dependent shells.

Document organization

This thesis is organized in 5 chapters:

- In Chapter 1, we present a state of the art concerning the model material and associated constitutive models, and the buckling of shell structures.

- In Chapter 2, we introduce the manufacturing process and the material characterization method. We also presents the buckling criterion developed in this work and the experimental procedures.

- In Chapter 3, we show the results of the material characterization process.

- In Chapter 4, we present the experimental and numerical results obtained on thick plates subjected to in-plane loading.

- Finally, in Chapter 5, we discuss the numerical and experimental results obtained on thick hemi-egg shells subjected to external pressure.

Chapter 1

State of the art

This chapter presents the available data and existing methods to study the buckling of shells. Experimental and numerical aspects are considered.

Contents

In this chapter, a state of the art of the different items identified previously is presented. The model material is introduced first. Then, a brief description of the general method to define constitutive models and to identify their parameters is presented. The last section of this chapter is dedicated to a state of the art on buckling prediction and existing work on elasto-visco-plastic buckling.

1.1 A model material

In order to reduce the experimental constraints, a model material creeping at room temperature was chosen instead of the stainless steel alloy 316L(N). This representative material is one grade of the "SAC" alloy family. All grades of this family are mainly made of Tin (Sn) and two additional components, Silver (Ag) and Copper (Cu). They are also called Sn-Ag-Cu alloys. This family of material was selected as it is well documented in the literature (cf. [Dompierre 2011; Kim, Huh, and Suganuma 2002; Kim et al. 2009; Wei and Wang 2012]). The main properties of the SAC alloys are presented in the next section. Then, the properties of the selected alloy are presented, as well as its casting capabilities.

1.1.1 SAC alloys

This alloy family is mainly used in solder joints. As mentioned above, the SAC alloys are mainly made of Tin (Sn), for more than 95% of their mass. The two additional elements (Silver and Copper) are used in order to create inter-metallics, linking the Tin dendritic structures together. These inter-metallic elements improve the mechanical properties as well as the fluid properties when the alloy is in its liquid phase.

The Tin element presents three different crystal phases, as shown in Figure 1.1. In the temperature range corresponding to the room temperature, the Tin crystal takes its β phase. This phase shows natural orthotropic properties. This specific point is considered for the definition of the constitutive mode.

This alloy family presents an eutectic composition, which is Sn 95.5% - Ag 3.8% - Cu 0.7%. This particular eutectic composition induces a solidus temperature equal to the liquidus one. It also reduces the density of shrinkage defects during solidification of the alloy and increases the homogeneity of the inter-metallic (cf. [Dompierre 2011]).

Close to the eutectic composition, a uniform solidification should be observed. Nevertheless supercooling phenomenon can be observed during the solidification of the alloy (cf. [Bath 2007]), up to 34°C under the fusion temperature. This is mainly due to the dendritic microstructure of Tin. Indeed, when a SAC alloy is solidifying, inter-metallics are solidifying first. They generate initiation points for the formation of the Tin dendrites. In the inter-dendritic space, binary (Sn-Ag or Sn-Cu) or tertiary (Sn-Ag-Cu) eutectic phases are forming. A grain is composed of
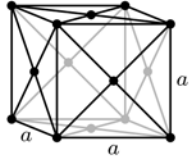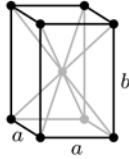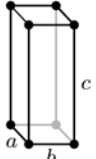
38

Figure 1.1: Crystal structures and allotropic forms of Tin [Dompierre 2011]

the Tin dendrite and its inter-dendritic phase.

These first properties of SAC alloys have an important impact on its mechanical and physical properties. It is especially important for the manufacturing process.

1.1.2 SAC 305 mechanical behaviour

Unfortunately the eutectic composition is rare in the commercial world and more expensive. A close eutectic composition is often used instead. This close eutectic composition is well documented in the literature. Its commercial name is SAC 305 or Sn 3.0 Ag 0.5 Cu, for 96.5% Sn, 3.0% Ag and 0.5% Cu. Its main physical properties are presented in Table 1.1.

Density [kg.m^{-3}]	7400
Liquidus Temperature [°C]	220
Solidus Temperature [°C]	217
Specific heat [J.g^{-1}.K^{-1}]	0,23
Thermal conductivity [W.m^{-1}.K^{-1}]	63
Coefficient of linear thermal expansion [10^{-6}.K^{-1}]	21,6

Table 1.1: Physical properties of SAC 305 alloy (cf. [Sawamura and Igarashi 2005])

In this section the main mechanical and physical properties of the alloy are presented. Moreover the main environmental parameters impacting either its microstructure or its mechanical properties are also presented.

1.1.2.1 Environmental parameters

Two parameters affect the mechanical properties of the SAC 305 alloy, either during its casting or during its storage; the cooling rate and the storage temperature.

Cooling rate

As presented in the previous section, the microstructural solidifying mechanism can generate supercooling phenomena. Depending on the cooling rate, the number of solidifying initiation points can be very different. A high cooling rate generates many small inter-metallics (cf. [Kim, Huh, and Suganuma 2002]). The number of initiation points is directly correlated to the number of dendritic structures formed and therefore to the grain sizes. The higher the cooling rate is, the finer the microstructure. As shown in Figure 1.2, the microstructure is very fine for a cooling rate equal to $100°C.s^{-1}$ and very coarse for a cooling rate equal to $0.14°C.s^{-1}$.
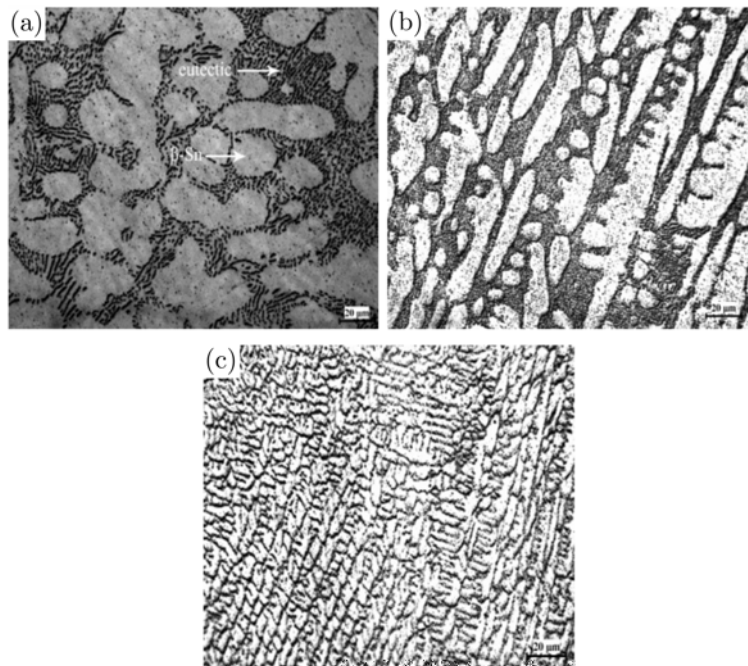
Figure 1.2: Effect of the cooling rate on the SAC 305 microstructure; cooling rate: (a) $0.14°C.s^{-1}$, (b) $1.7°C.s^{-1}$, (c) $100°C.s^{-1}$ [Wei and Wang 2012]

As the microstructure is affected, the mechanical properties are too, as shown in [Kim, Huh, and Suganuma 2002]. As an example, Kim, Huh, and Suganuma gives an average yield stress of 36.7 MPa for specimens which were rapidly cooled ($8.3°C.s^{-1}$), while specimens moderately cooled ($0.4°C.s^{-1}$) show an average yield stress of 32.8 MPa. This difference is quite important. The cooling rate at solidification is discussed in Section 2.1.

Thermal ageing

The other important parameter is the storage temperature. It was extensively studied by [Dompierre 2011]. Because of the rapid solidification, the solid alloy is found in a metastable state after solidification. At the end, it tends to recover a stable state. This is called ageing. During this time, the grains grow and the inter-metallics group together. The storage temperature can accelerate this process. As the grain size changes, the mechanical properties can be impacted.

Dompierre presented in his work (cf. [Dompierre 2011]) the impact of the storage temperature on the hardness with respect to the storage time. The results are presented in Figure 1.3.
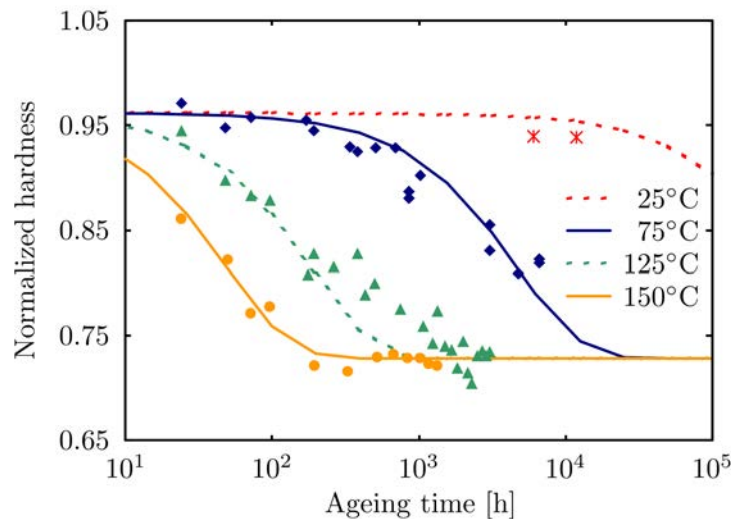
Figure 1.3: Ageing effect in time on Vickers hardness for different storage temperatures [Dompierre 2011]

One can see that at room temperature, the ageing time corresponding to a 5% decrease of the hardness is higher than 10000 hours. In other words, the ageing of the SAC 305 alloy is not an issue if the material is stored at room temperature.

Both environmental parameters (the cooling rate and the storage temperature) define constraints on the manufacturing and storage of the test specimens. The manufacturing process is discussed in Chapter 2, nevertheless the cooling rate will need to be high enough in order to obtain a clean and fine microstructure. On the ageing matter, the specimen will have to be tested in a reasonable time after manufacturing, as 10000 hours correspond to 14 months. Moreover the specimens were in a room where the temperature was controlled. The storage temperature did not exceed 25°C and did not get below 13°C (α / β Tin transition temperature).

1.1.2.2 Mechanical behaviour

The mechanical behaviour of the SAC 305 alloy was largely studied in the literature (cf. [Bai, Chen, and Gao 2009; Che et al. 2010; Cuddalorepatta and Dasgupta 2007; Dompierre 2011]). As this alloy has a low melting point, it presents an elasto-visco-plastic behaviour at room temperature, as demonstrated experimentally and shown in Figure 1.4 from [Bai, Chen, and Gao 2009]. Its strength increases with an increase of strain rate.
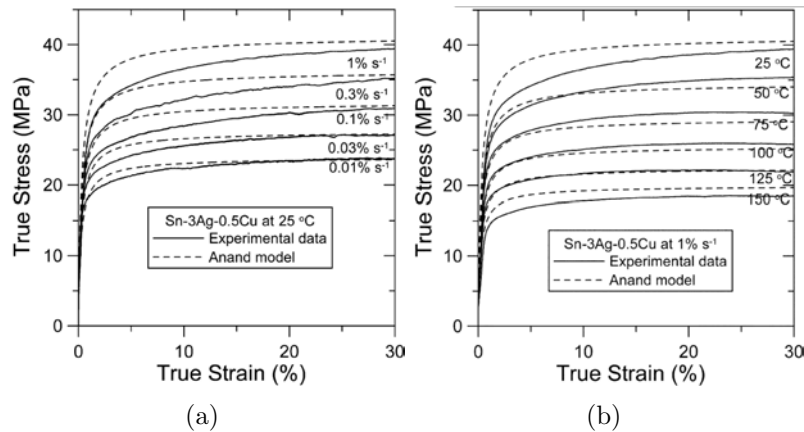
Figure 1.4: (a) Effect of the strain rate on the SAC 305 strength [Bai, Chen, and Gao 2009]; (b) Effect of the alloy temperature on the SAC 305 strength [Bai, Chen, and Gao 2009]

Two parameters have an important effect on the mechanical properties of the SAC 305 alloy, the strain rate (as the alloy has an elasto-visco-plastic behaviour), and its temperature, as shown in Figure 1.4(b) from [Bai, Chen, and Gao 2009]. Its strength is reduced by an increase of temperature. The alloy temperature also modifies the Young's modulus as demonstrated in [Dompierre 2011].

The effect of the temperature is often characterized by the activation energy Q. This quantity is introduced in the creep law in order to scale the strain rate according to the temperature of the alloy. For the SAC 305 alloy Bai, Chen, and Gao estimated the activation energy to 50460 J.mol^{-1}.

As mentioned previously, it is important to remember that the microstructre of the SAC 305 alloy is very dependent of the solidification process. Therefore the mechanical properties of the SAC 305 are also dependent on the solidification process. The mechanical properties of the SAC 305 found in the literature cannot be directly used, as either the solidification process is not well described or the volume of SAC 305 manufactured is too small (often the size of a solder joint).

Nevertheless the literature gives a long list of constitutive laws used to model the experimental behaviour of the SAC 305. [Dompierre 2011] summarized most of the experimental/numerical studies performed in order to characterize the SAC alloys. Some of these models are listed below:

- Anand model,

- Chaboche model,

- Power law.

These models will be presented in Section 1.2 of Chapter 2. Their benefits and issues according to the present work will also be discussed.

Nevertheless from the information collected in the literature, it is mandatory to characterize the mechanical behaviour of the SAC 305 with respect to the solidification process and the ingots dimensions.

1.1.3 SAC 305 casting process

As the solidification process is particularly important and especially its kinetics, the specimen manufacturing process needs to be investigated. In some studies the casting process is also documented, as [Che et al. 2010; Huh, Kim, and Suganuma 2001; Kim, Huh, and Suganuma 2002; Molnar et al. 2014]. In most cases, the mould is pre-heated to more than 300°C as well as the alloy. In some studies, like [Molnar et al. 2014], the mould and its content are kept for few minutes at a reduced temperature just above the SAC 305 melting solidus temperature.

The cooling phase is not often detailed, except in [Kim, Huh, and Suganuma 2002] and [Wei and Wang 2012] where the cooling rates are mentioned. Wei and Wang also mentioned the cooling means, furnace-cooling, air-cooling and water cooling.

After the cooling phase some authors mention a heat treatment in order to remove residual stresses.

The main manufacturing data are summarized in Table 1.2.

	Wei and Wang	Molnar et al.	Kim, Huh, and Suganuma
Mould material	no mould	n/d	Steel
Melting temperature [°C]	300	350	300
Mould pre-heating temperature [°C]	n/d	230	n/d
Cooling rates [°C.s^{-1}]	0.14;1.7;100	n/d	0.012;0.043;8.3
Heat treatment temperature [°C]	n/d	n/d	100
Heat treatment time [min]	n/d	n/d	30

Table 1.2: Summary of SAC 305 casting process characteristics, n/d: not defined

This different information will be really useful to define the manufacturing process of our specimens.

1.2   Definition of a constitutive model

In this section, the theoretical framework to define and identify a constitutive model will be presented.

Before going deeper in the mathematical definition of the different constitutive laws already used to model the SAC 305, a brief description of the creeping phenomenon is presented.

1.2.1   The creeping phenomenon

The creeping phenomenon is strongly linked to the alloy temperature and its melting temperature. The most convenient way to observe the creeping behaviour of an alloy is to perform a creep test. Post processing the deformation of the specimen with respect to the testing time allows to identify three phases, as shown in Figure 1.5.
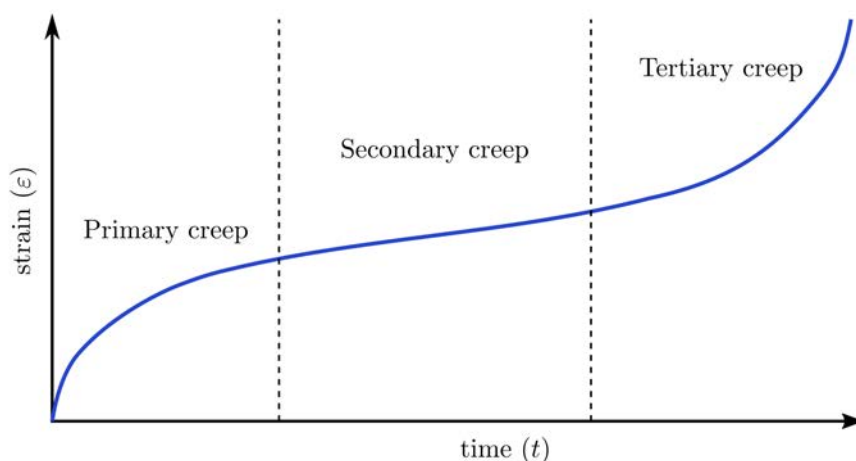
Figure 1.5: Identification of the three creep phases on a creep test

- **The primary creep**: corresponds to a phase where the strain increases quickly. The strain rate decreases rapidly with respect to the time. It corresponds to the initiation and the propagation of the dislocations within the material microstructure. This phase is highly dependent on the hardening law of the material.

- **The secondary creep**: corresponds to a phase where the strain grows regularly. The strain rate is constant or almost constant with respect to the time. The dislocations coalesce to form cellular structures. The dislocation density stays stable. This phase is dependent on the creep law (flow rule).

- **The tertiary phase**: leads to the failure of the specimen. The strain increases rapidly as well as the strain rate. Cavities appear within the material, grow and fuse together until failure of the specimen. The last phase is strongly linked to the damaging of the material (damage law).

This brief description allows to identify the effect of the different variables of the constitutive law during the different phases. As the buckling phenomenon often appears before any damage of the structure, the damaging of the material will be neglected in this work.

While a creep test is convenient to identify the three creep phases and to identify the secondary creep law, it may be very cumbersome to define accurately the hardening law. Several classical tensile tests at different strain rates are more efficient to identify both hardening law and creep law, as shown in Figure 1.6.
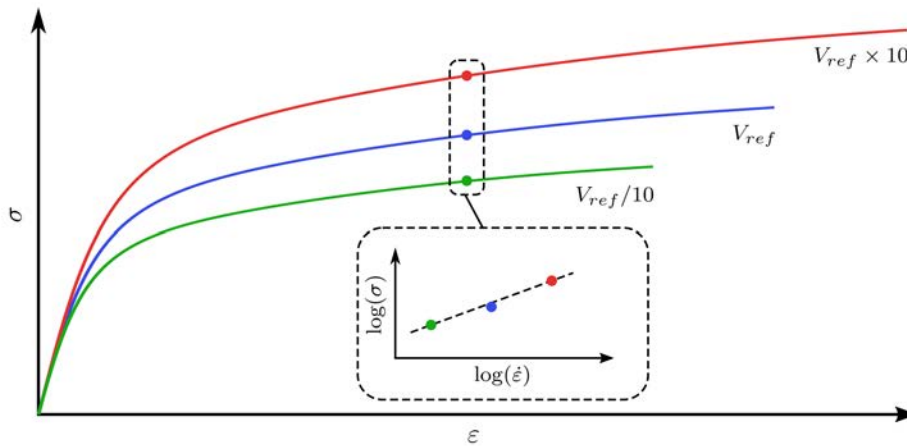
Figure 1.6: Illustration of the link between tensile tests performed at different strain rates and the creep law

This type of experiments is used latter to identify the parameters of the constitutive law. This last one only models the primary and secondary creep.

1.2.2 Theoretical framework of elasto-visco-plastic constitutive models

We constrain ourselves to the small strain assumption, which leads to the additive decomposition of the strain tensor:

$$\boldsymbol{\varepsilon} = \boldsymbol{\varepsilon}^e + \boldsymbol{\varepsilon}^{in}, \tag{1.1}$$

with $\boldsymbol{\varepsilon}$ the strain tensor, $\boldsymbol{\varepsilon}^e$ the elastic strain tensor and $\boldsymbol{\varepsilon}^{in}$ the inelastic strain tensor.

According to [Lemaitre et al. 2009], the following ingredients are needed to define a rate dependent constitutive law:

- a thermodynamic potential (Ψ),

- a set of state variables ($\boldsymbol{\varepsilon}$, T),

- a set of internal variables ($\boldsymbol{V_k}$, $\boldsymbol{\varepsilon}^{in}$),

- a dissipative potential (ϕ) and the associated flow rules,

- a yield criterion (f) associated to a stress norm (J).

The internal variables can group the kinematic and the isotropic hardening variables and in some cases the damage variables. The dissipative potential defines the flow rules and the viscous behaviour. The yield criterion defines the fully elastic domain as well as the flow direction for associative flows.

The thermodynamic foundation of the present theory can be found in [Lemaitre et al. 2009].

According to [Lemaitre et al. 2009], the dual dissipative potential ϕ^* of ϕ can be defined as an equipotential function in the stress space, as follows:

$$\phi^* = \Omega\left(\boldsymbol{\sigma}, T\right). \tag{1.2}$$

Ω can be subdivided into a function of equipotential in the stress space responsible of the plastic deformation Ω^p and a recovery potential Ω^r, as follows:

$$\Omega = \Omega^p + \Omega^r. \tag{1.3}$$

In this work, the recovery effects are neglected, therefore $\Omega = \Omega^p$. According to [Lemaitre et al. 2009], Ω can be written as a function of a stress norm, the internal variables, and the temperature:

$$\Omega = \Omega\left(J\left(\boldsymbol{\sigma} - \boldsymbol{X}\right) - R, \boldsymbol{X}, R, \boldsymbol{A}_k\right), \tag{1.4}$$

where R is the isotropic hardening variable, $\boldsymbol{X}$ is the kinematic hardening variable, and the $\boldsymbol{A}_k$ are additional thermodynamic forces associated to the other internal variables $\boldsymbol{V}_k$ (as damage variables).

The plastic flow rule can finally be written as:

$$\begin{aligned}
\dot{\boldsymbol{\varepsilon}}^p &= \frac{\partial \Omega}{\partial \boldsymbol{\sigma}}, \\
&= \frac{\partial \Omega}{\partial J} \cdot \frac{\partial J}{\partial \boldsymbol{\sigma}}, \\
&= \frac{\partial \Omega}{\partial J} \boldsymbol{n}.
\end{aligned} \tag{1.5}$$

where $\boldsymbol{n}$ is the flow direction and $\frac{\partial \Omega}{\partial J}$ corresponds to the creep law. $\frac{\partial \Omega}{\partial J}$ is also equal to the equivalent plastic strain rate $\dot{p}$.

In the case of the SAC 305 many models were used in order to characterize its behaviour. The next three paragraphs present the dissipative dual potential Ω of a basic creep constitutive model and two classical laws used to model the SAC 305 behaviour.

Norton creep law

The Norton model is the simplest one. It only considers isotropic hardening variable and a Norton creep law. Ω is defined as:

$$\Omega = \frac{K}{N+1} \left\langle \frac{J-R}{K} \right\rangle^{N+1},$$ (1.6)

where J is a stress norm, R is the isotropic hardening variable (law) and K and N are material parameters. N is the slope of the creep law in a log-log diagram (σ - $\dot{\varepsilon}$).

Therefore, the flow rule can be defined by:

$$\dot{p} = \left\langle \frac{J-R}{K} \right\rangle^{N},$$
$$\dot{R} = \frac{\partial R}{\partial p}\dot{p}.$$ (1.7)

This model is particularly efficient for monotonic loading, as any isotropic hardening law can be coupled to the classical Norton creep law. Its identification is also very convenient.

In order to take into account the effect of the temperature, an exponential function of the temperature is added to the previous expression:

$$\dot{p} = \left\langle \frac{J-R}{K^{\star}} \right\rangle^{N},$$
$$K^{\star} = K \left[\exp\left(\frac{Q}{R \cdot T} \right) \right]^{1/N}$$ (1.8)

with Q the activation energy already mentioned, R the universal gas constant and T the temperature in K (Kelvin).

In case of a non-linear creep law, an exponential function can be introduced to Equation 1.7 with same formalism:

$$\Omega = \frac{exp\left(\alpha_0 \langle J-R \rangle^{N+1} \right)}{\alpha_0 (N+1)K^{N}},$$
$$\dot{p} = \left\langle \frac{J-R}{K} \right\rangle^{N} exp\left(\alpha_0 \langle J-R \rangle^{N+1} \right),$$ (1.9)

with α_0, K and N material parameters.

This model is the most simple and flexible one for monotonic loads.

Anand model

The Anand model was largely used in the literature to model the SAC 305 behaviour.

The flow rule is defined as follows:

$$\dot{p} = K \left(\sinh \left(\xi \frac{J}{s} \right) \right)^{1/m},$$
$$\dot{s} = h_0 \left| 1 - \frac{s}{s^*} \right|^a \cdot \mathrm{sign} \left(1 - \frac{s}{s^*} \right) \dot{p}, \qquad (1.10)$$
$$s^* = \hat{s} \left(\frac{\dot{p}}{K} \right)^n,$$

where K, ξ, m, h_0, a, $\hat{s}$ and n are material parameters defining both hardening and creep laws.

The hardening is introduced through the s variable. As shown in [Bai, Chen, and Gao 2009], this model fits globally the SAC 305 behaviour, but the hardening law does not fit well all experimental data. In fact the tangential hardening law is not suitable for the SAC 305 behaviour. Moreover, there is not much freedom to fit the hardening tangential law, as it is more or less a power law.

Elasto-visco-plastic Chaboche model

Finally the elasto-visco-plastic Chaboche constitutive model includes kinematic and isotropic hardening variables. It is well adapted to model the cyclic behaviour of the SAC 305 alloy. Classically the isotropic hardening is modelled by a Voce type hardening variable, defined as follows:

$$\dot{R} = b(Q - R)\dot{p}, \qquad (1.11)$$

with b and Q material parameters.

As many kinematic variables as needed can be used. Their evolutions are defined as follows for isotropic material:

$$\dot{\boldsymbol{X}}_k = 2/3 C_k \dot{\boldsymbol{\varepsilon}}^p - \gamma_k \boldsymbol{X}_k \dot{p}, \qquad (1.12)$$

with C_k and γ_k material parameters.

The dual dissipative equipotential is defined by a Norton dissipative equipotential including the kinematic stress tensor $\boldsymbol{X}$:

$$\Omega = \frac{K}{N+1} \left\langle \frac{J(\boldsymbol{\sigma} - \boldsymbol{X}) - R}{K} \right\rangle^{N+1}. \qquad (1.13)$$

Equally, the flow rule is defined by:

$$
\begin{aligned}
\dot{p} &= \left\langle \frac{J(\boldsymbol{\sigma} - \boldsymbol{X}) - R}{K} \right\rangle^{N}, \\
\dot{\boldsymbol{\alpha}}_k &= \dot{\boldsymbol{\varepsilon}}^p - 3/2 \frac{\gamma_k}{C_k} \boldsymbol{X}_k \dot{p}, \\
\dot{R} &= b(Q - R)\dot{p},
\end{aligned}
\tag{1.14}
$$

where $\boldsymbol{\alpha}_k$ is the kinematic hardening variable tensors.

This model is one of the most complex models. Its complexity increases its accuracy and makes it a good candidate to model the SAC 305 behaviour. Moreover with its several hardening parameters it allows to fit well the tangential hardening law. This point is particularly important for buckling analysis.

In Chapter 2 the model used in the present work is detailed. This model corresponds to a modified Chaboche constitutive model with several Voce hardening variables and no kinematic hardening variables. Due to the several Voce hardening variables, this constitutive law can model efficiently a large number of material subjected to monotonic loading.

The next section of this chapter is focused on the buckling phenomenon and its prediction.

1.3   The buckling phenomenon

The buckling phenomenon is a challenging topic in mechanics. It leads to the failure of structures. It is often sudden, in opposition to other failure modes, as the damaging of materials or crack propagation. Moreover it is a global failure mode as the entire structure is involved. Therefore it depends on the structure geometry, its loading, its boundary conditions and more importantly the constitutive law of its material.

The buckling phenomenon can either lead to the global change of the structure (often called geometrical instability) or to a local change of the structure (localisation). In both cases the stiffness of the structure is affected and cannot fulfil its initial function. Same techniques are used to detect both buckling phenomena.

The geometrical instabilities are more often observed on thin walled structures, as tubes, plates or thin shells, while localisation issues is more often observed on thick ones. In some cases, thick or moderately thick structures can present geometrical instability issues. In the next subsections the buckling phenomenon is presented. First the general concepts are presented. Then the plastic buckling and the predicted methods associated are described. Finally a brief state of the art of existing works on elasto-visco-plastic buckling is presented.

1.3.1 Introduction to buckling

As mentioned above it exists two types of buckling. We distinguish the limit point buckling from the bifurcation buckling as depicted in Figure 1.7.
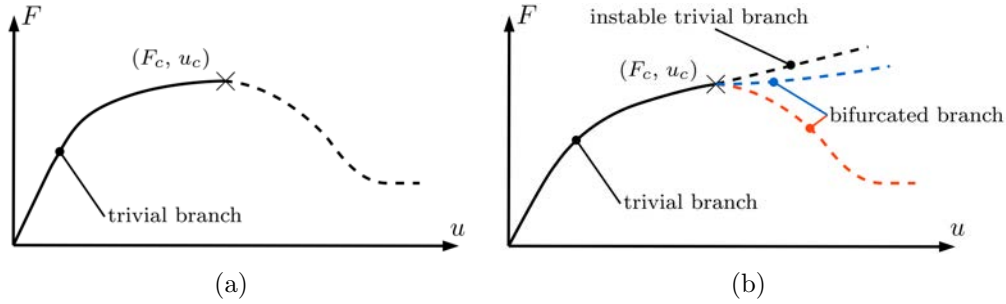
Figure 1.7: (a) limit point buckling; (b) bifurcation buckling

In the first case the solution stays unique, the structure follows its trivial branch defined by the load F and the displacement u until reaching a maximum point (F_c, u_c), called limit point. From this point, the stiffness is greatly affected and does not resist anymore to the load applied. The load starts decreasing without losing the uniqueness of the solution. This is often associated to imperfect structures or very thick ones. To detect the limit load a simple arc-length strategy can be used for all kind of elasto-plastic materials.

The bifurcation buckling is different in the uniqueness character of the solution. As in the previous case, the structure starts following its trivial branch until reaching a critical point where the uniqueness of the solution is lost. Several branches can emerge from this critical point (F_c, u_c), the trivial one and the bifurcated ones. We are interested in this type of buckling in the present work. The bifurcation buckling was first studied on elastic structures through the second derivative of the potential energy. The *Lejeune-Dirichlet* theorem defines an equilibrium, defined by the displacement $\boldsymbol{u}$ and the load λ, as stable if the potential energy reaches a strict minimum, i.e.:

$$\forall \partial u \text{ kinematically admissible } \partial^2 P(u, \lambda) > 0 \qquad (1.15)$$

with P, the potential energy.

In elasticity, the loss of stability also coincides with the bifurcation. This is not the case for inelastic behaviours (cf. [Benbagdad 1992]). Another criterion was developed by *Hill* for elasto-plastic materials. It is introduced later in this chapter.

In the following subsection some classical bifurcation buckling behaviours are presented, before introducing a classical bifurcation criterion.

1.3.1.1 Some classical buckling behaviours of shells

Some structures are more likely to buckle than others. It obviously depends on the load applied, the boundary conditions and the material properties. Nevertheless the geometry of a shell structure can affect the buckling load and more importantly its buckling mode.

As an example, cylinders subjected to external pressure present interesting buckling mode according to their geometrical properties. Montague performed several buckling experiments on cylinders subjected to external pressure. The results of the test campaign are presented in [Montague 1969]. Montague observed different buckling modes according to the cylinder geometry, as shown in Figure 1.8.
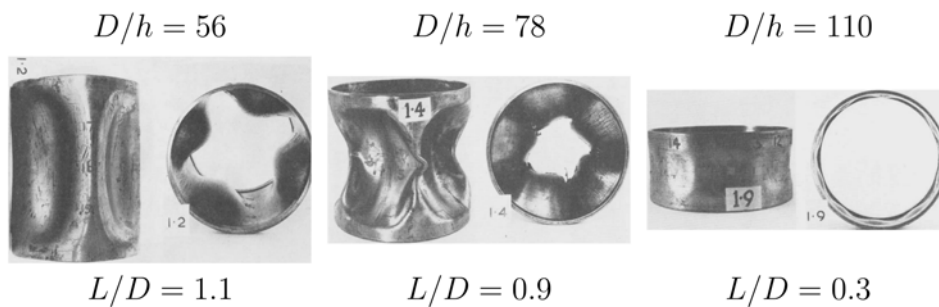
Figure 1.8: Typical lobar buckling mode shape for three cylinders with different geometries [Montague 1969]

More importantly, he shows that in some cases the buckling modes are so close that the structure buckles on several modes at the same time. A perturbed buckling mode can be observed, corresponding to the linear combination of the different buckling modes excited, as shown in Figure 1.9. In Figure 1.9, the buckling mode shape should be identical to the one presented in Figure 1.8 for the specimen with a L/D ratio equal to 1.1 and a D/t ratio equal to 56. Because of the mode proximity, each mode perturbs each others.

The effect of the geometry on the buckling behaviour is a well-known result. In addition the mode proximity is a key element in order to evaluate a buckling criterion. The point is discussed several times in this work.

The other element which has a major impact on the buckling behaviour is any kind of imperfection. This topic was extensively studied in the literature as in [Yeh and Kyriakides 1986] on the collapse of tubes subjected to external pressure, or in [Gusic, Combescure, and Jullien 2000] dealing with thickness imperfections. The geometrical imperfections are often preferred to loading ones as it is easier to implement in numerical models. Loading imperfections were also studied through loading interactions, as in [Kyriakides and Shaw 1982]. Imperfections can affect both the buckling load and the buckling mode. Moreover, when the modes are close, a geometrical imperfection can drive the structure to bifurcate on a mode
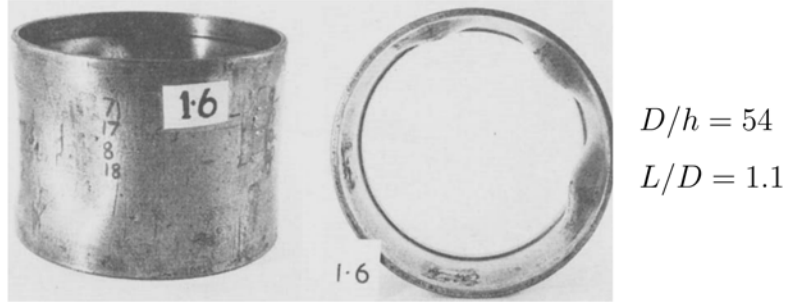
Figure 1.9: Buckling mode combination due to mode proximity [Montague 1969]

more compatible with the imperfection, as in Section 11.5 of [Kyriakides and Corona 2007].

These first observations show several points to look at in order to evaluate a buckling criterion and the buckling behaviour of any structure. In order to identify the critical point and the buckling mode, a bifurcation criterion is required. The most common bifurcation criterion used was developed by Hill in [Hill 1958], it is presented hereafter.

1.3.1.2   The Hill criterion

Hill proposed a theory to define the uniqueness of an equilibrium point for elasto-plastic material (cf. [Hill 1958]).

The equilibrium of a mechanical system $\mathcal{D}$ delimited by $\partial\mathcal{D}$ is defined by:

$$
\left.
\begin{aligned}
\mathrm{div}\,\boldsymbol{\sigma} &= 0 \\
\dot{\boldsymbol{\sigma}} &= \boldsymbol{C}_t\,\dot{\boldsymbol{\varepsilon}}
\end{aligned}
\right\}\forall P \text{ in } \mathcal{D},
$$
$$
\left.
\begin{aligned}
\dot{\boldsymbol{\sigma}} \cdot \boldsymbol{N} &= \dot{\boldsymbol{T}} \\
\dot{\boldsymbol{u}} &= \dot{\boldsymbol{U}}
\end{aligned}
\right\}\forall P \text{ in } \partial\mathcal{D},
\tag{1.16}
$$

where $\boldsymbol{\sigma}$ is the *Cauchy* stress tensor, $\dot{\boldsymbol{\sigma}}$ is the *Cauchy* stress rate, $\boldsymbol{C}_t$ is the tangential constitutive law, $\boldsymbol{N}$ is the normal to $\partial\mathcal{D}$ in P, $\dot{\boldsymbol{T}}$ is the load rate vector on $\partial\mathcal{D}$, $\dot{\boldsymbol{U}}$ is the velocity on $\partial\mathcal{D}$, $\dot{\boldsymbol{\varepsilon}}$ is the strain rate tensor and $\dot{\boldsymbol{u}}$ is the velocity within $\mathcal{D}$.

$$
\boldsymbol{C}_t = \begin{cases} \boldsymbol{C}_e \text{ the elastic modulus if elastic loading or unloading occurs,} \\ \boldsymbol{C}_p \text{ the elasto-plastic modulus if plastic loading occurs.} \end{cases}
\tag{1.17}
$$

Hill defined his theory under the small strain assumption, for associative materials following a normality rule. He assumes that if two velocity fields and their associated stress rate tensors $(\dot{\boldsymbol{u}}_1, \dot{\boldsymbol{\sigma}}_1)$ and $(\dot{\boldsymbol{u}}_2, \dot{\boldsymbol{\sigma}}_2)$ are solutions of the equilibrium, the solution to the equilibrium is unique if:

$$\int_V \Delta\dot{\boldsymbol{\sigma}} : \Delta\dot{\boldsymbol{\varepsilon}} + \boldsymbol{\sigma} : \dot{E}^Q(\Delta v)dV > 0, \text{ with } : \Delta. = (.)_1 - (.)_2, \tag{1.18}$$

and,

$$\dot{E}^Q_{ij}(v) = \frac{\partial v_k}{\partial x_i}\frac{\partial v_k}{\partial x_j}. \tag{1.19}$$

with v the velocity fields.

One of the displacement fields is therefore not kinematically admissible. This criterion is derived from the strict convexity of the potential energy with respect to any kinematically admissible displacement perturbation, as described in [Benbagdad 1992].

If both displacement fields are kinematically admissible,

$$\int_V \Delta\dot{\boldsymbol{\sigma}} : \Delta\dot{\boldsymbol{\varepsilon}} + \boldsymbol{\sigma} : \dot{E}^Q(\Delta v)dV = 0, \tag{1.20}$$

the solution is therefore not unique.

Hill shows in [Hill 1958] the following inequality:

$$\int_{\mathcal{D}} \Delta\dot{\boldsymbol{\sigma}} : \Delta\dot{\boldsymbol{\varepsilon}}dV \geq \int_{\mathcal{D}} \Delta\dot{\boldsymbol{\varepsilon}} : \boldsymbol{C}_t\Delta\dot{\boldsymbol{\varepsilon}}dV. \tag{1.21}$$

This leads to:

$$\Delta\dot{\boldsymbol{u}} : \left(\boldsymbol{K}_t + \boldsymbol{K}_\sigma\right)\Delta\dot{\boldsymbol{u}} = 0, \tag{1.22}$$

with $\boldsymbol{K}_t$ is the stiffness tensor of problem and $\boldsymbol{K}_\sigma$ the geometric stiffness tensor.

The uniqueness of the solution is therefore reduced to an eigenvalue problem on the stiffness tensors $\boldsymbol{K}_t$ and $\boldsymbol{K}_\sigma$:

$$\left[\left(\boldsymbol{K}_t + \boldsymbol{K}_\sigma\right) - \lambda\,\boldsymbol{I}\right] \cdot U = 0. \tag{1.23}$$

The critical point is reached when the smallest eigen-value λ_1 is equal to 0. As long as $min(\lambda_i) > 0$ the solution is unique. This is a sufficient condition of uniqueness as long as the bifurcation is not tangential, the solid does not experience elastic unloading at buckling and the loads do not change orientations between the initial and the current configuration. This condition is true as long as every point of $\mathcal{D}$ is loaded in a manner that any point of the plastic domain $\mathcal{D}_p$ does not unload elastically on the bifurcated branch.

For moving loads, such as pressure, an additional stiffness matrix ($\boldsymbol{K}_{nl}$) associated to the change of the loading orientation needs to be added in the eigen-values analysis:

$$\left[\left(\boldsymbol{K}_t + \boldsymbol{K}_\sigma + \boldsymbol{K}_{nl}\right) - \lambda\,\boldsymbol{I}\right] \cdot U = 0. \tag{1.24}$$

The next section discusses the application of the *Hill* bifurcation criterion to elasto-plastic solids and a paradox observed on some structures.

1.3.2 The buckling paradox in plasticity

The last method was successfully applied to many types of structure using the *Mises* flow theory to describe the plastic flow rule. Its efficiency is well known on thin structures (see [Yeh and Kyriakides 1986] or [Bardi and Kyriakides 2006]). Nevertheless, some thick structures, as plates, buckle before reaching *Hill*'s bifurcation load. A more accurate estimation of the bifurcation point was achieved using any deformation theory (as *Hencky*'s deformation theory) to define the tangent operator of the constitutive law as seen in Figure 1.10. This last method gives better correlation with experiments than the classical *Hill*'s method as demonstrated in [Hutchinson 1974] [Kyriakides and Corona 2007] or [Kyriakides, Bardi, and Paquette 2005].
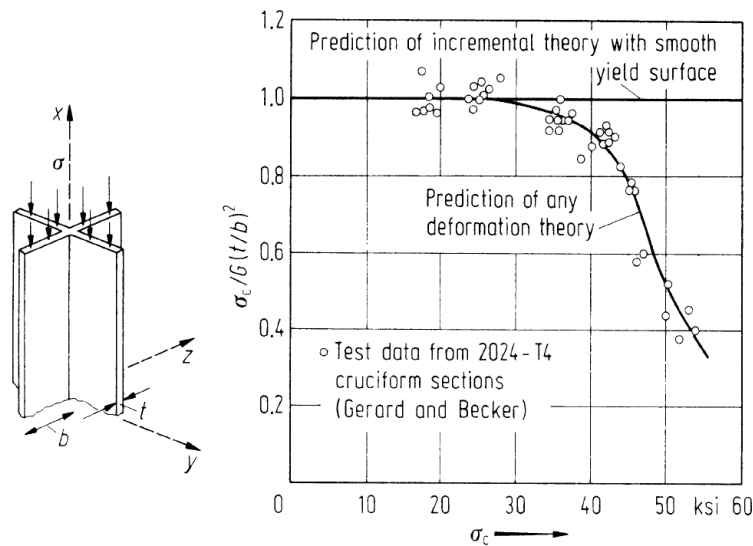
Figure 1.10: Comparison of tests and theories for torsional buckling of a cruciform column [Hutchinson and Budiansky 1976]

Hutchinson shows in [Hutchinson 1974] that the predictions using any deformation theory coincide with the predictions using complex flow theories such as the slip theory from [Batdorf and Budiansky 1949] for nearly proportional loadings. In addition Hutchinson states that as in the complex flow theories mentioned in [Hutchinson 1974], corners develop on the yield surface at bifurcation or prior bifurcation. It follows that any deformation theory coincides with a flow theory allowing the development of corners on the yield surface for nearly proportional loadings. Unfortunately, this equivalence is often only valid in a reduced strain range. Discussions about the real development of corners are still open. Moreover the experimental observation of a corner on the yield surface is very complicated.

Some authors explain that the delay of *Hill*'s method in predicting buckling is caused by a high imperfection sensitivity of the structure (cf. [Onat and Drucker 1953]). This is not always the case, as it depends on the geometry of the structure.

A difference between predictions using the simplest incremental theory (the *Mises* flow theory) and the simplest deformation theory (*Hencky*'s deformation theory) is especially observed on thick structures such as thick plates. Wang and Aung developed a model in [Wang and Aung 2007] in order to define the first critical equilibrium of thick plates subjected to compressive loading. As an example, Figure 1.11, extracted form [Wang and Aung 2007], presents three predictions using *Hencky*'s deformation theory (DT), the *Mises* flow theory (IT) and an elastic prediction with respect to the thickness ratio b/h (width over thickness). Figure 1.11 illustrates the buckling predictions on a square plate subjected to an in-plane equi-biaxial stress state. As shown, for thick plates the deformation theory gives a lower critical stress than the incremental one. Both theories converge when the thickness ratio increases or when the plate becomes thin.
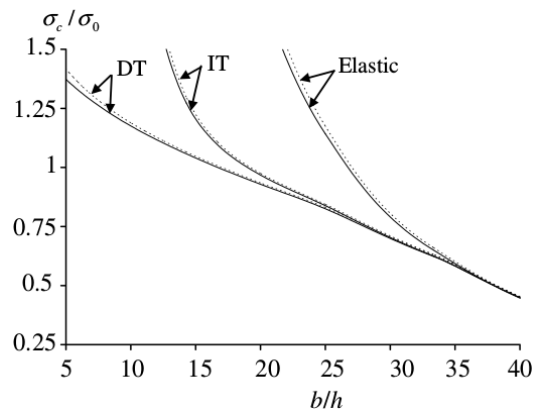
Figure 1.11: Normalized buckling stress versus b/h ratio for a fully clamped square plate subjected to an in-plane equi-biaxial loading (dashed curves thin plate theory, plain curves Reissner-Midlin plate theory). [Wang and Aung 2007]

Any deformation theory seems to be the best solution to predict efficiently the buckling of thick elasto-plastic structures, as illustrated with the cruciform beam in Figure 1.10. Nevertheless, any deformation theory is limited to structures subjected to proportional loading (cf. [Christoffersen and Hutchinson 1979]). This considerably restrains their domains of application to simple structures subjected to simple loadings. In this matter Christoffersen and Hutchinson, proposed an extension of the J2 deformation theory to non-proportional loading paths. This constitutive model called J2 corner theory is presented in [Christoffersen and Hutchinson 1979]. It coincides with the J2 deformation theory for quasi proportional loading.

This incremental theory based on the deformation theory was developed in order to define an accurate theoretical framework to the buckling paradox. Therefore the theory is appropriate to treat non-proportional loading. Moreover it gives buckling predictions close to the ones derived with the deformation theory, for nearly proportional loadings.

Its formulation is based on a potential depending of the stress rate orientation as follows:

$$W(\dot{\boldsymbol{\sigma}}, \boldsymbol{\sigma}) = \dot{\boldsymbol{\sigma}}^t \left(\boldsymbol{\mathcal{L}}_e + h(\theta) \boldsymbol{\mathcal{L}}_p \right) \dot{\boldsymbol{\sigma}}, \tag{1.25}$$

with θ the stress rate orientation with respect to the deviatoric stress direction, $\boldsymbol{\mathcal{L}}_e$ is the elastic moduli inverse and $\boldsymbol{\mathcal{L}}_p$ is the inverse of the J2 deformation theory plastic moduli, and:

$$h(\theta) = \begin{cases} 1 & \text{if: } \theta \leq \theta_0 \\ h(\theta) & \text{if: } \theta_0 < \theta < \theta_c \\ 0 & \text{if: } \theta \geq \theta_c \end{cases}, \tag{1.26}$$

with θ_0 the angle delimiting the quasi proportional range, and θ_c the angle defining the elastic unloading range as shown in Figure 1.12.
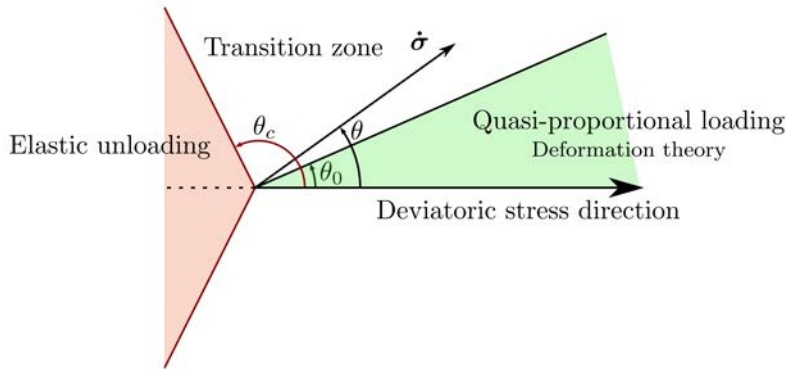
Figure 1.12: Description of the three loading zones around the corner of the yield surface (black curves are associated to the corner theory with two different sets of parameters θ_0 and θ_c).

It was first developed to perform both buckling and post buckling analysis using the same constitutive model, and especially a constitutive model close to the J2 deformation theory. It includes a non-smooth yield surface, with a corner positioned by the deviatoric stress tensor. The corner theory was successfully applied to the well-known cruciform column in [Needleman and Tvergaard 1982] and to elasto-plastic axially compressed cylinders in [Tvergaard 1983].

Furthermore, Tvergaard explains in [Tvergaard 1983] that the critical load predicted by the corner theory is rather an upper bound, as the stiffness in the transition zone ($\theta_0 < \theta < \theta_c$) is progressively equal to the elastic moduli. Nevertheless it showed good results in predicting buckling of structures subjected to non-proportional loading as shown in [Tvergaard 1983; Tvergaard and Needleman 2000], especially when compared to the simplest incremental theory. Indeed for non-proportional loading the deformation theory would give unrealistic buckling load, because of the disagreement of its formulation with the real stress state. The simplest incremental theory

would still give an overestimation of the buckling load. This two points are shown in Figure 1.13 from [Needleman and Tvergaard 1982].
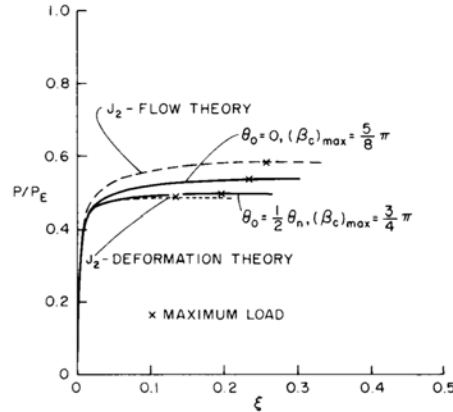
Figure 1.13: Comparison of theories for the torsional buckling of a cruciform column with imperfection [Needleman and Tvergaard 1982]

This paradox and its extension to non-proportional loading paths are also investigated in this work. Moreover the operator associated to these theories are detailed in Chapter 2 and extended to elasto-visco-plastic materials.

1.3.3 Elasto-visco-plastic buckling

In the previous sections, the existing methods to predict buckling and their domain of use, have been presented for elasto-plastic material or rate-independent material. In this study we are interested in materials presenting a rate dependency.

The rate dependency of the material can have several effects on the mechanical behaviour of the structure as well as its buckling. The possible initial imperfection can be magnified because of the rate dependency. Moreover the stiffness of the structure is also affected by the strain rate. It has also been shown that *Hill*'s criterion cannot be used directly in the inelastic range to predict buckling of rate dependent solids.

Many approaches were proposed in the literature to predict the bifurcation buckling of rate dependent structures. Many are imperfection dependent, the analysis of the bifurcated solutions are used to define the critical values. These methods are often time consuming and imply to well know the type and the amplitude of the imperfection experienced by the structure. Among all approaches, two were preferred as they are based on bifurcation criteria. One was defined by [Bodner, Naveh, and Merzer 1991], the other was defined by [Triantafyllidis, Massin, and Leroy 1997]. Both are briefly presented thereafter.

The *Triantafyllidis* sufficient condition

57

The method developed in [Triantafyllidis, Massin, and Leroy 1997] is a rigorous one. It gives a sufficient condition of bifurcation for rate-dependent solids. As its implementation in a FE software is complex, this method is not used in this work. Therefore its mathematical formulation is not presented here. Details of its formulation can be found in [Triantafyllidis, Massin, and Leroy 1997]. Two examples were treated numerically with this method, the Shanley's column by [Massin, Triantafyllidis, and Leroy 1999] and uniaxial plane strain test by [Nestorović, Leroy, and Triantafyllidis 2000].

As this thesis is more oriented on the experimental buckling and because of the complexity to implement in a FE software the Triantafyllidis, Massin, and Leroy sufficient condition, this approach was not selected in the work.

The *Bodner* hypothesis

Several attempts to define a simple creep buckling criterion are discussed by Bodner, Naveh, and Merzer in [Bodner, Naveh, and Merzer 1991]. *Bodner* proposed an approach based on an effective tangent modulus.

This method consists in defining an instantaneous plasticity problem. The instantaneous plasticity problem is defined through the assumption of a constant strain rate (in time) at buckling initiation. This method is inexact, but it allows to predict a lower bound bifurcation point for rate-dependent solids. The lower bound character is due to the neglected possible change of strain rate at buckling initiation. This method is particularly efficient when the strain rate is small enough (quasi static problems).

In particular, an effective or instantaneous consistency condition can be defined:

$$d\dot{p} = 0. \tag{1.27}$$

Using *Bodner*'s hypothesis, the existing methods to analyse the stability of rate-independent materials can be applied. The stability of the instantaneous plasticity problem is analysed. This method was applied numerically to different geometries by [Paley and Aboudi 1991], [Bodner and Naveh 1988], [Mikkelsen 1993] or [Mikkelsen 2001].

This approach is particularly simple to implement in a FE software. As mentioned above, this approach gives an estimation of the bifurcation point, therefore its results have to be analysed carefully.

It is also important to notice that both approaches have only been compared to numerical results. In [Mikkelsen 1993], *Bodner*'s critical values are compared to the numerical results from post-buckling analysis with different imperfection amplitudes. In some cases *Bodner*'s critical values are not anymore a lower bound of the buckling load of the imperfect structure. This could be explained by the buckling paradox in the visco-plastic domain.

58

This paradox was investigated once for rate dependent material in [Eslami and Shariyat 1997]. The prediction method used in [Eslami and Shariyat 1997] is close to the one proposed by Bodner, Naveh, and Merzer.

In Chapter 2, a model to predict the buckling of elasto-visco-plastic structures is proposed, including *Bodner*'s hypothesis and elements to consider thick shells, non-proportional loadings and the buckling paradox observed in plasticity.

1.3.4 Experimental elasto-visco-plastic buckling of shells

From an experimental point of view, the creep or visco-plastic buckling is not well documented. Many articles in the literature rather deal with numerical approaches and buckling prediction criteria than buckling experiments. Nevertheless some authors like [Hoff 1976], [Combescure and Jullien 2017] or [Gerard and Gilbert 1958] present experimental data on creep buckling.

The main interest of these articles is to describe how the mechanical behaviour and especially the rate dependency affects the buckling behaviour of the structure. Moreover it gives information on the experimental means as well as on the post processing methods used.

The experiments presented in [Gerard and Gilbert 1958] are the most relevant ones, as they consider thick tubes subjected to a compressive load or a torsional load. The experiments are performed as creep tests. The load applied is constant over time. Only the time to buckling defines the critical point. 3003-0 aluminium tubes at 343 °C are tested. First, the mechanisms of the creep buckling behaviour can be observed, as the strain rate dependency of critical stress presented in Figure 1.14 from [Gerard and Gilbert 1958]. Indeed the lower is the strain rate (associated to the critical time) the lower is the buckling stress. Unfortunately, little information is given about the buckling mode and the potential effect of the creep behaviour on the buckling mode. The same philosophy is followed by [Hoff 1976] on thin cylinders and plates.

The most complete set of experimental results on creep buckling can be found in [Combescure and Jullien 2017]. An important part of this article treats the shape and evolution of the buckling mode with respect to time as shown in Figure 1.15. More importantly a Fourier approach is followed to define the nature of the buckling mode, and their contribution to the final buckling mode. Moreover in [Combescure and Jullien 2017], a detection criterion based on the non-trivial velocity field is given. The non-trivial velocity increases faster before collapse of the shell.

The main conclusion from this test campaign is related to the initial imperfection. Indeed the component of the initial imperfection corresponding to the buckling mode seems to increase slowly during the test until the critical point. Its increase becomes exponential from the critical point.

More than the valuable results presented, the important information to notice from this test campaign is about the experimental means associated to the experimental buckling analysis. The post processing of the experimental data and espe-

(a)   (b)
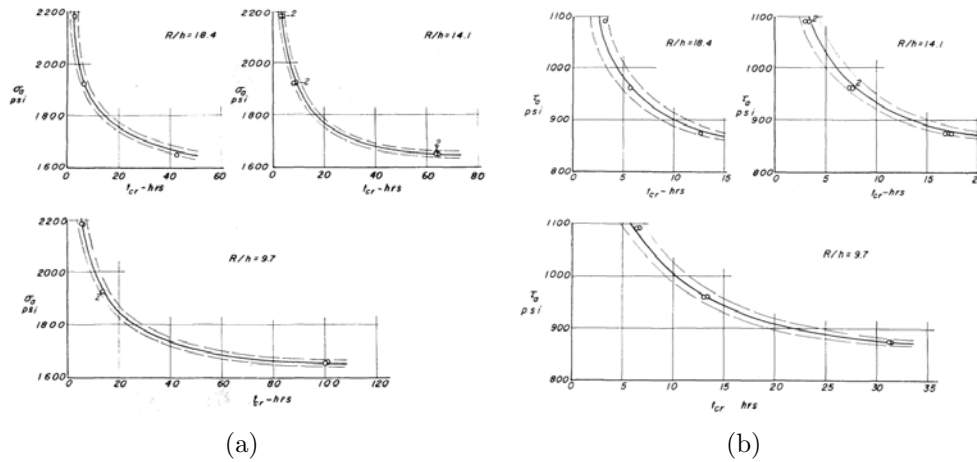
Figure 1.14: (a) Experimental critical compressive stress data with respect to the critical time (white bullet); (b) Experimental critical torsional shear stress data with respect to the critical time (white bullet) [Gerard and Gilbert 1958]

cially the displacement fields give valuable information on the buckling behaviour of the structure. The finite element simulation of each experiment also allows to better analyse the buckling behaviour of the tested structure.

A specific section in Chapter 2 is dedicated to the definition of the experiments and the instrumentation for the buckling experiments.

To conclude, only few authors treat the subject of the thesis (the elasto-visco-plastic buckling of thick shells). Among the published articles, one is of interest (cf. [Gerard and Gilbert 1958]), but it only gives reduced information on major critical variables (i.e. critical loads, times, strains, etc.). More importantly no information is given on the buckling modes, the buckling initiation and the buckling mode evolution with respect to the time. Other experiments found in the literature are further documented, but they are focused on thin shells. Moreover the selected specimen shapes are generally subjected to proportional loading paths. It facilitates the usage of simple bifurcation criteria and does not allow to generalize the methods and observations to complex structures, such as the sodium manifold considered in this work.
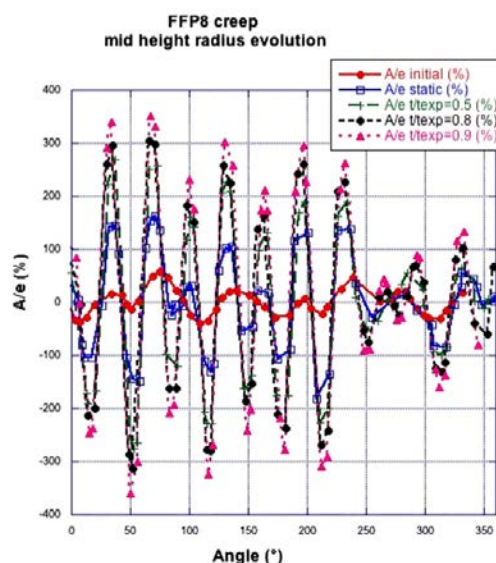
Figure 1.15: Evolution of creep radial displacement along the circumference of the shell (A/e radial displacement amplitude over cylinder thickness). [Combescure and Jullien 2017]

1.4 Conclusion

In this chapter the different available data as well as existing methods to study the buckling of shell structures has been presented. Some concern the experimental environment, others the numerical one.

From the data available on the representative material, we identified a need to characterize the material behaviour. Moreover existing publications show constraints on the manufacturing and the storage of the test specimens. These constraints will be taken into account to define the manufacturing process as well as the experimental procedures. In the next chapter the detailed strategy to manufacture the test specimens and to identify the material behaviour associated to the manufacturing process are presented.

On the same topic, several material constitutive models were tested in the past to characterize the SAC 305 mechanical behaviour. Their main properties have been presented in this chapter. An additional behaviour has been added in this work because of the natural orthotropic behaviour of the Tin crystal. An anisotropic yield criterion is used. The selected material constitutive model and the method of characterization are presented in the next chapter.

Two aspects of the buckling behaviour are treated in this work. First the numerical modelling of an elasto-visco-plastic thick shell bifurcation problem is a major issue. Then the experimental methods needed to observe and characterize the buckling behaviour of some specific shells have to be considered with attention in order

to obtain valuable results.

Concerning the numerical aspects, this chapter showed that some aspects of our problem are missing in the literature. Indeed, thick shell buckling was treated in the literature but the existing studies are limited to elasto-plastic materials. The elasto-visco-plastic bifurcation buckling of shells is often limited to thin shells. Moreover, the existing data generally concerns structures experiencing proportional loading. Concerning the numerical modelling of an elasto-visco-plastic thick shell buckling problem, the main idea of this work is to assemble all the elements discussed in this chapter into a single model. This model would consider the thick shell aspects, the elasto-visco-plastic behaviour of the material and the non-proportionality of the load path. These element are considered through an extension of the corner theory to elasto-visco-plastic materials and the application of *Bodner*'s hypothesis. This model is detailed in the next chapter. It will be evaluated against experimental results in Chapters 4 and 5.

Finally the experimental environment is also a major issue to get more valuable experimental results. As for the numerical modelling, experiments on thin shells were preferred in the literature. In the past, the authors were mainly interested in the values of the critical load, strain, stress or time. The analysis of the buckling mode was often omitted or studied approximately. The latest experimental means allow to study this particular property of shell buckling (as Digital Image Correlation). The analyses of the experimental buckling initiation and an accurate analysis of the buckling mode can allow to improve the confidence in the bifurcation criterion. For all experiments, a special attention was given to the instrumentation used to measure the deformation of the test specimens.

The next chapter addresses the points developed in this conclusion in order to create numerical and experimental frameworks for the analysis of the bifurcation buckling of elasto-visco-plastic thick shells.

<div align="right">

Chapter 2

Methods

</div>

This chapter presents the different developments performed to answer to the thesis subject. Some developments are experimental procedures, and others numerical methods. In addition, bridging tools were developed in order to connect experimental data with numerical results.

Contents

As presented in the introduction, this work covers several topics, from the specimens casting to the buckling experiments. In this chapter the different tools or methods developed in this thesis are presented. Two main tasks were driven in parallel, one was focused on experimenting the buckling, and the other was dedicated to its numerical prediction. The developments of both tasks are respectively presented in Section 2.4 for the buckling experiments and in Section 2.3 for the numerical buckling predictions. In order to compare experiments with numerical modelling, several satellite tasks were required.

These satellite tasks are focused on the manufacturing of the specimens, the identification of the material law with a FEMU approach, and the analysis of the experimental deformed shape and buckling modes using 3D Digital Image Correlation (DIC) and FE modelling methods. All satellite methods are described in Sections 2.1, 2.2 and 2.5. Figure 2.1 summarizes the different developments performed and their interactions with each others.

It was chosen to present the different tasks in a chronological manner. First the manufacturing process of the specimens is introduced, and then the method to identify the material behaviour is described. Following these two first satellite tasks, the methods to study the buckling of thick shells are presented. It is followed by the experimental approaches developed to experiment buckling of thick shells. Finally a specific interface linking DIC data to FE analysis is presented.
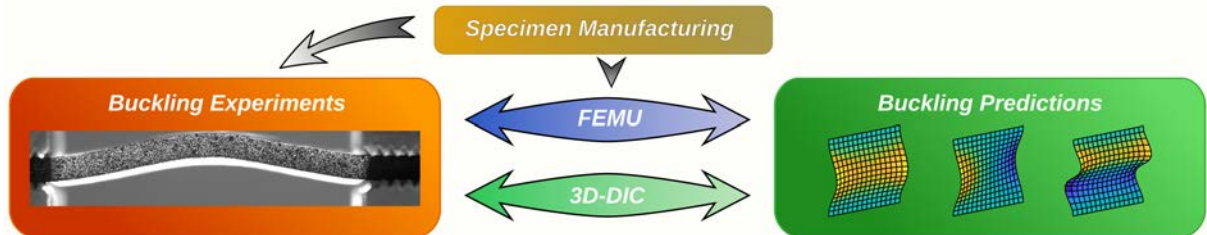
Figure 2.1: Development tasks and their interactions

2.1 Specimens manufacturing process

As mentioned in Chapter 1, a model material was selected in order to study the elasto-visco-plastic buckling of thick shells. This model material has an elasto-visco-plastic behaviour at room temperature. This specific property allows to remove any constraints for the thermal loading during the experiments.

This material is used to manufacture all specimens. The design of each type of specimen is detailed in the relevant sections (cf. Sections 2.2.1, 2.4.1 and 2.4.2). This section presents the manufacturing process, with a special attention to its casting phase.

The manufacturing process is identical for all specimens. The specimens are

machined from an ingot to their final shape by conventional milling methods. The ingots are obtained using a gravity casting process.

As already mentioned in Section 1.1.3 of Chapter 1, the casting process has a great impact on the material properties. Its characteristics are presented thereafter. The objective of the casting process is to obtain a close to shape ingot, with a sane microstructure. A repeatable process is also mandatory in order to minimize the material discrepancy due to the process. The casting process can be sub-divided into 5 phases:

- Heating of the alloy and the mould to 280°C for at least 3h,

- Gravity casting of the alloy in the mould at ambient temperature,

- Rest for 1h at 250°C (in order to obtain a homogeneous temperature field in the mould),

- Water quench of the mould and its content,

- Heat treatment for stress relieve, 1h at 100°C.

Figure 2.2 illustrates the whole casting process.
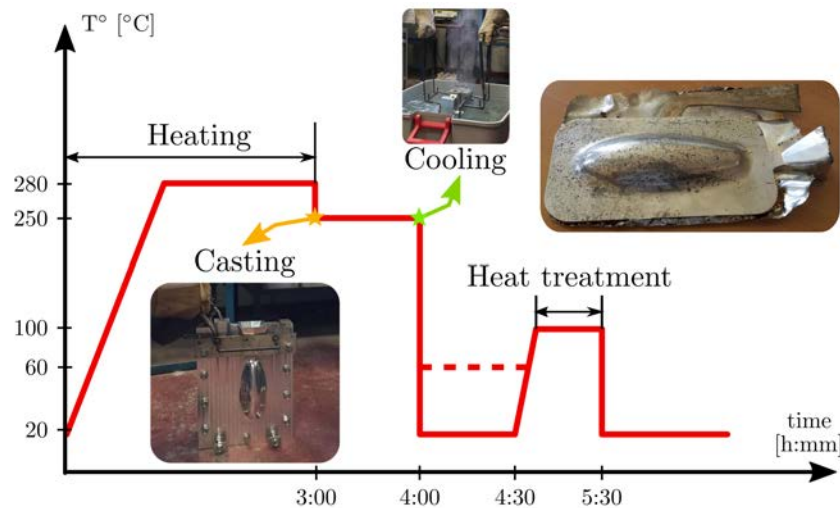
Figure 2.2: Illustration of the casting process

This controlled process guaranties a sane microstructure and a low material discrepancy. The most critical phase is the water quench, as its parameters can affect the cooling rate. As already mentioned in Chapter 1, this alloy is very dependent on the cooling rate during solidification. To reach our objectives, the water quench needs to be carefully defined and controlled.

The cooling rate has two major effects. A high cooling rate decreases the grain size and improves the mechanical properties. On the other hand, for massive components the efficiency of the riser is reduced with high cooling rates. High cooling rates increases the probability of porosity in the ingot bulk.

Moreover the cooling rate needs to be as much homogeneous as possible in the ingot during the solidification. Indeed, a homogeneous cooling rate guaranties the homogeneity of the material properties and reduces the porosity density and the size of the porosities.

Two moulds were designed and manufactured to produce the different ingots. The tensile specimens and the plate buckling specimens were extracted from ingots cast in a steel mould presented in Figure 2.3(a). Another mould was used to cast the ingots of the specimens used for the pressurized buckling tests (cf. Section 2.4.2). A specific aluminium mould was manufactured for this purpose (presented in Figure 2.3(b)). Both have the same wall thickness, 5 mm.

(a)   (b)
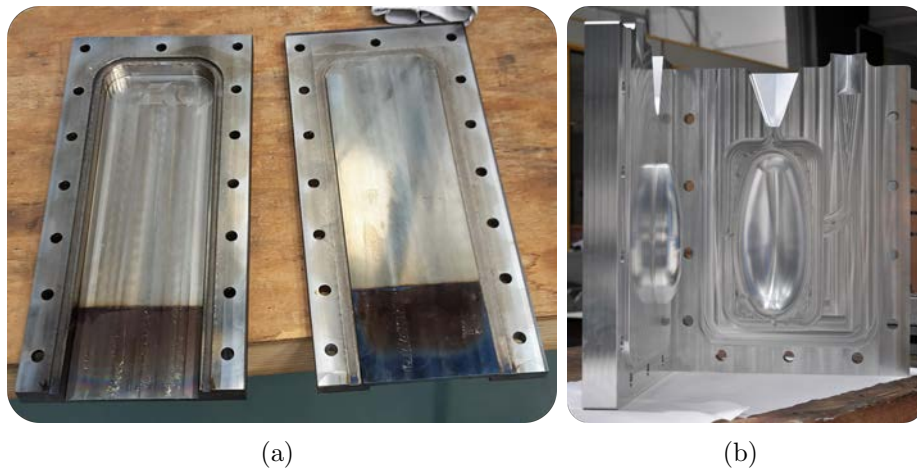
Figure 2.3: (a) Steel mould used to cast tensile and compressive specimens; (b) Aluminium mould used to cast externally pressured specimens

The water quench parameters associated to both moulds have been defined to achieve equivalent cooling rate, the detailed study is described in Appendix B. The water quench parameters are presented in Table 2.1.

Mould material n/a	Mould thickness [mm]	Quench temperature [°C]
Steel	5	20
Aluminium	5	40

Table 2.1: Quench temperatures and mould design parameters selected

The main difficulty is to maintain a constant quench temperature, as it can vary

by a few degrees. The material properties can be affected by this experimental variation. This issue is discussed later in Chapter 3.

The actual quench temperature were measured they are summarized in Table 2.2.

Following the casting process, two tensile or plate buckling specimens can be extracted from the ingot cast in the steel mould. Only one specimen is extracted from the aluminium mould.

Table 2.2 summarizes all the specimens produced, their ingot, their manufacturing group, and their dates of casting and testing.

Specimen	Ingot	Group ID	Quench $T°$ [°C]	Date of casting	Date of testing	Type of testing
TT/11	TTB 1		20	10/2018	11/2018	
TT/12			20	10/2018	11/2018	
TT/21	TTB 2		20	10/2018	11/2018	
TT/22		G1	20	10/2018	11/2018	Tensile testing
TT/31	TTB 3		20	10/2018	11/2018	
TT/32			20	10/2018	11/2018	
TT/41	TTB 4		20	10/2018	11/2018	
TT/42			20	10/2018	11/2018	
BTC1/01	PB 0		22	03/2019	04/2019	
BTC1/02			22	03/2019	04/2019	
BTC1/11	PB 1	G2	22	03/2019	04/2019	Plate buckling
BTC1/12			22	03/2019	04/2019	BTC 1
BTC1/21	PB 2		22	03/2019	04/2019	
BTC1/22			22	03/2019	04/2019	
BTC2/31	PB 3		28	07/2019	07/2019	
BTC2/32		G3	28	07/2019	07/2019	Plate buckling
BTC2/41	PB 4		28	07/2019	07/2019	BTC 2
BTC2/42			28	07/2019	07/2019	
O/001		G4	25	08/2019	03/2020	
O/002			20	11/2019	08/2020	
O/003			40	06/2020	08/2020	Pressurized egg
O/004		G5	40	06/2020	08/2020	buckling
O/005			40	07/2020	09/2020	
O/006			40	07/2020	09/2020	

Table 2.2: Produced specimens and their manufacturing history

2.2 Material constitutive law calibration: FEMU processing
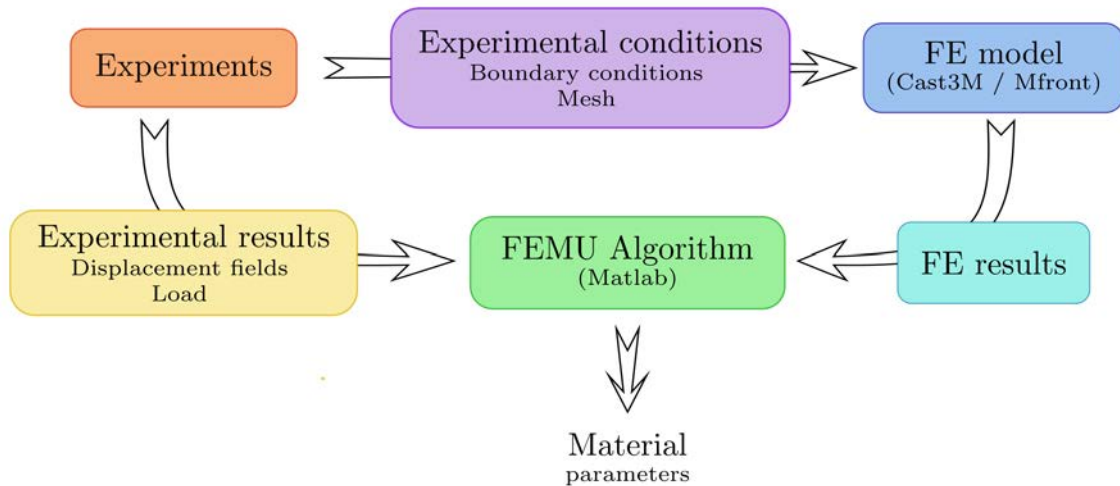
Figure 2.4: FEMU method data flow

The buckling behaviour of any structure is highly dependent on the constitutive law of its material. An inverse method was implemented to identify the mechanical behaviour of the SAC 305 alloy. This method is named FEMU for Finite Element Model Updating. This method is based on the update of the material parameters of a finite element model until convergence of the model with experimental data, as described in [Avril et al. 2008]. This identification is based on experimental data, a finite element model, the constitutive law chosen and an optimisation algorithm. The different elements and the flow of data are presented in Figure 2.4. The two main components of this approach are the tensile test procedure and the selected constitutive model. They are presented thereafter.

The details of the FEMU process used are presented in Appendix D.

2.2.1 Tensile tests

As mentioned in the previous chapter, the material chosen is rate-dependent at room temperature. It is intended to identify an elasto-visco-plastic constitutive law. In order to reduce the number of tests without reducing the robustness of our identification, a specific specimen was designed. As presented in Figure 2.5, the specimen shape presents a variable effective area along its principal direction. When a tensile load is applied to the specimen, a heterogeneous strain rate gradient can be observed on the specimen. A unique tensile test provides experimental data for a strain rate range.
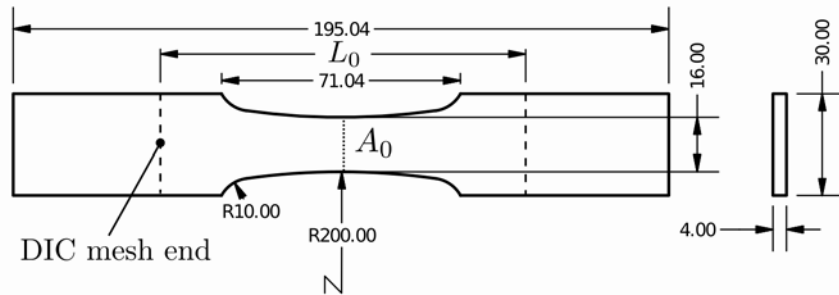
Figure 2.5: Tensile specimen drawing (in mm)

The tensile specimens were manufactured from four different batches according to the manufacturing process presented previously.

The tensile tests were performed on a 20 kN *Instron* electro-mechanical testing machine. Figure 2.6 presents a picture of the experimental set-up. The test specimen is clamped at each end in self-tightening grips. The specimen is aligned with the testing machine axial direction.

A 16 MPx camera with a 200 mm lens focusing on the center of the specimen is used for 2D-DIC means. The camera is positioned in order to use most of the camera sensor. The region of interest (ROI) on the specimen is included in a rectangle of 30x80mm^2. The camera frequency is set in order to obtain a mean strain increment of 2.0×10^{-5} mm.mm^{-1} between two pictures.
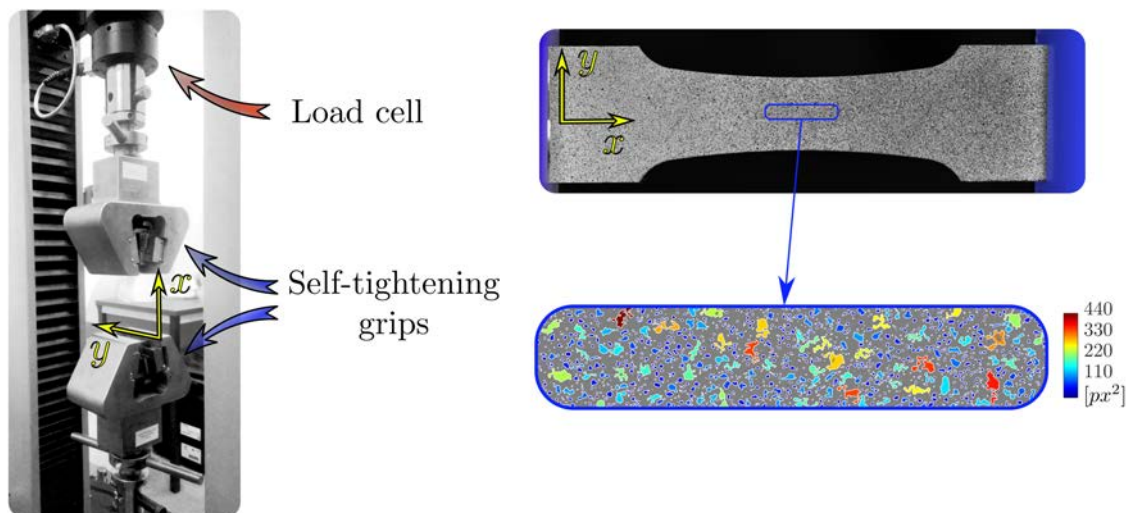
Figure 2.6: Tensile experimental set-up and speckle pattern

Tensile tests are driven in rate displacement mode. Two displacement rates were

tested, the lowest was 3.3×10^{-3} mm.s^{-1}, which covers a strain rate range from 1.0×10^{-5} s^{-1} to 1.0×10^{-4} s^{-1} and the highest was 10 times faster.

In-plane displacement fields were measured by 2D-DIC. For this reason, the specimen was painted with a random speckle pattern characterized by a Gaussian distribution of its gray level. The gray level is coded on 8 bits, each pixel takes a value between 0 and 255. The Gaussian distribution is defined by its mean value, 133 and its standard deviation 48. Each black pattern measures between 2 and 20 px.

2.2.2 Material constitutive law

The constitutive law of the SAC 305 alloy is modelled with a unified elasto-visco-plastic model. The creep behaviour is model with a Norton law and the hardening with three Voce hardening parameters. The SAC 305 isotropic transverse behaviour is modelled with *Hill*'s yield criterion. It was chosen to keep elasticity isotropic. The constitutive law is defined by the following set of equations:

$$
\begin{aligned}
\boldsymbol{\sigma} &= \boldsymbol{\mathcal{C}}\, \boldsymbol{\varepsilon}_e, \\
\boldsymbol{\varepsilon} &= \boldsymbol{\varepsilon}_e + \boldsymbol{\varepsilon}_p, \\
\dot{p} &= \left(\frac{F}{K}\right)^n, \\
F &= \sigma_{eq} - R(p), \\
R(p) &= R_0 + \sum_{i=1}^{3} R_i \left(1 - e^{-b_i p}\right), \\
\sigma_{eq} &= \sqrt{\boldsymbol{\sigma} : \boldsymbol{H} : \boldsymbol{\sigma}},
\end{aligned}
\tag{2.1}
$$

with, $\boldsymbol{\sigma}$ the Cauchy stress tensor, $\boldsymbol{\varepsilon}$ the Biot strain tensor, $\boldsymbol{\varepsilon}_e$ the elastic strain tensor and $\boldsymbol{\varepsilon}_p$ the plastic strain tensor, $\boldsymbol{\mathcal{C}}$ the isotropic elastic linear operator, σ_{eq} *Hill*'s equivalent stress defining the yield surface, $\boldsymbol{H}$ the Hill tensor (used here for transverse anisotropy), p the equivalent plastic strain, R the hardening variable and $\dot{p}$ the equivalent strain rate.

In the general case *Hill*'s tensor is defined by:

$$
\boldsymbol{H} = \begin{bmatrix}
F+H & -F & -H & 0 & 0 & 0 \\
-F & G+F & -G & 0 & 0 & 0 \\
-H & -G & H+G & 0 & 0 & 0 \\
0 & 0 & 0 & L & 0 & 0 \\
0 & 0 & 0 & 0 & M & 0 \\
0 & 0 & 0 & 0 & 0 & N
\end{bmatrix},
\tag{2.2}
$$

70

with:

$$F = 0.5 \left(\frac{1}{R_{11}^2} + \frac{1}{R_{22}^2} - \frac{1}{R_{33}^2} \right)$$

$$G = 0.5 \left(\frac{1}{R_{11}^2} + \frac{1}{R_{33}^2} - \frac{1}{R_{22}^2} \right)$$

$$H = 0.5 \left(\frac{1}{R_{22}^2} + \frac{1}{R_{33}^2} - \frac{1}{R_{11}^2} \right)$$

$$L = \frac{3}{2} \left(\frac{1}{R_{12}^2} \right)$$

$$M = \frac{3}{2} \left(\frac{1}{R_{23}^2} \right)$$

$$N = \frac{3}{2} \left(\frac{1}{R_{13}^2} \right)$$

(2.3)

In case of transverse isotropy *Hill*'s tensor is completely defined by the Lankford coefficient R_{lank}:

$$
\begin{array}{ll}
R_{11} = 1 & R_{12} = 1 \\
R_{22} = 1 & R_{13} = 1 \\
R_{33} = \sqrt{\frac{R_{lank}+1}{2}} & R_{23} = 1
\end{array}
$$

(2.4)

and:

$$R_{Lank} = \varepsilon_{yy} / \varepsilon_{zz},$$

(2.5)

with y the width direction of the specimen and z its thickness direction.

The material parameters to be identified are R_0, R_1, b_1, R_2, b_2, R_3, b_3, K, n, R_{lank} and $\boldsymbol{C}$ defined by Young's modulus and the Poisson ratio. Many parameters needs to be defined, the associated identification process is therefore complex. The complexity of the constitutive law allows to better model the SAC 305 behaviour and especially its tangential behaviour. This is particularly important for inelastic buckling analysis.

2.3 Buckling prediction of thick shell structures

This section presents the approach followed to predict buckling of thick shell structure. Based on state of the art methods for visco-plastic materials and thick plastic structures, a numerical method was developed. First the method was applied to plates subjected to in-plane compressive load through an analytical model. It was then generalized to any structure through its implementation in a finite element model. Whatever modelling approach chosen, the method is built on the definition of the tangential constitutive law, characterized by $\boldsymbol{C}_t$.

First the tangent constitutive law will be derived according to different theories, its implementation to an analytical model will be presented then. Finally the finite

element modelling approach and the implementation of the tangential constitutive law in Cast3M are presented.

2.3.1 Derivation of a tangent constitutive law

The tangent constitutive law is an important parameter for the stability analysis, as previously discussed. The tangent operator links the stress increment to the strain increment, with respect to the state and internal variables. The derivation of the tangent operator for the selected constitutive law is presented thereafter for three different approaches. The first one considers the flow rule developed by *Reuss* and *Von Mises*, while the second uses *Hencky*'s deformation theory. The third one is an extension of *Hencky*'s deformation theory to non-proportional loadings. *Reuss/Mises* theory can be applied to any load cases while *Hencky*'s deformation theory is limited to proportional loads, where principal strain directions cannot rotate in the material coordinate system during loading.

As discussed in Chapter 1, two methods can be followed to perform the stability analysis of elasto-visco-plastic structures. Either we choose to use the sufficient condition of stability developed by Triantafyllidis, Massin, and Leroy or the Bodner, Naveh, and Merzer hypothesis for rate dependent materials. In this work, we oriented our choice to the Bodner, Naveh, and Merzer hypothesis. This approach is relatively simple to implement in a FE software compared to Triantafyllidis, Massin, and Leroy sufficient condition. This choice will be discussed in Chapter 4.

The use of Bodner, Naveh, and Merzer hypothesis allows to write an instantaneous plastic problem by neglecting the strain rate variation at bifurcation. This is expressed by:

$$d\dot{p} = d(g(f)) = g'(f)df = 0, \tag{2.6}$$

where g is the creep law, f the yield criterion and $\dot{p}$ the equivalent inelastic strain rate.

This expression can be defined as an instantaneous consistency equation. With this instantaneous consistency equation, an instantaneous tangent operator can be derived for either plastic theory.

The tangent operator derived from *Reuss/Mises* flow theory is presented first, the tangent operator derived from *Hencky*'s deformation theory comes then. An extension proposed by Christoffersen and Hutchinson of *Hencky*'s deformation theory to non-proportional loadings is also presented. Finally their impacts on the stability analysis are presented and discussed.

2.3.1.1 *Reuss/Mises* flow theory

This theory was initiated by *Levy* and *Von Mises* for plastic material and extended to elaso-plastic material by *Prandlt* and *Reuss* (cf. [Hill 1998]). It is based on a proportional relation between the plastic strain increment and the stress increment. The so called flow rule defines this relation:

$$\dot{\boldsymbol{\varepsilon}}_p = \dot{p}\frac{\partial f}{\partial \boldsymbol{\sigma}}. \tag{2.7}$$

Using the constitutive law presented in Section 2.2.2, Equation 2.7 becomes:

$$\dot{\boldsymbol{\varepsilon}}_p = \dot{p}\frac{\boldsymbol{H} : \boldsymbol{\sigma}}{\sigma_{eq}}. \tag{2.8}$$

The consistency equation can be rearranged as follows:

$$\dot{p} = \frac{1}{R'(p)}\boldsymbol{n}, \text{ with: } \boldsymbol{n} = \frac{1}{\sigma_{eq}}\boldsymbol{H} : \boldsymbol{\sigma}. \tag{2.9}$$

The plastic increment can then be expressed with respect to $\dot{\boldsymbol{\varepsilon}}$ by introducing the elastic law and the flow rule in Equation 2.9, as follows:

$$\dot{p} = \frac{\boldsymbol{n}^t \boldsymbol{C}\,\dot{\boldsymbol{\varepsilon}}}{R'(p) + \boldsymbol{n}^t \boldsymbol{C}\,\boldsymbol{n}}. \tag{2.10}$$

Finally, using the strain decomposition, the elastic law and the flow rule, we obtain:

$$
\begin{aligned}
\dot{\boldsymbol{\sigma}} &= \boldsymbol{C}\left(\dot{\boldsymbol{\varepsilon}} - \dot{\boldsymbol{\varepsilon}}_p\right), \\
&= \boldsymbol{C}\left(\dot{\boldsymbol{\varepsilon}} - \dot{p}\boldsymbol{n}\right), \\
&= \left[\boldsymbol{C} - \frac{\boldsymbol{P} \otimes \boldsymbol{P}}{R'(p) + \boldsymbol{n}^t \boldsymbol{C}\,\boldsymbol{n}}\right]\dot{\boldsymbol{\varepsilon}}, \text{ with: } \boldsymbol{P} = \boldsymbol{C}\,\boldsymbol{n}.
\end{aligned}
\tag{2.11}
$$

The tangent operator $\boldsymbol{C}_t$ is defined by:

$$\boldsymbol{C}_t = \left[\boldsymbol{C} - \frac{\boldsymbol{P} \otimes \boldsymbol{P}}{R'(p) + \boldsymbol{n}^t \boldsymbol{C}\,\boldsymbol{n}}\right]. \tag{2.12}$$

Often, only its current value is considered in the stability analysis. Non-linear effects of the constitutive law are neglected around the equilibrium tested.

2.3.1.2 *Hencky*'s deformation theory

The deformation theory was largely used with success for stability analysis. In this case the plastic strain is proportional to the deviatoric stress tensor. The flow rule is defined as follow:

$$\boldsymbol{\varepsilon}^p = p\frac{\boldsymbol{H}\,\boldsymbol{\sigma}}{\sigma_{eq}}. \tag{2.13}$$

Its variational expression is then written as:

$$\dot{\boldsymbol{\varepsilon}}^p = \frac{\dot{\sigma}_{eq}}{\sigma_{eq}}\left(\frac{\dot{p}}{\dot{\sigma}_{eq}} - \frac{p}{\sigma_{eq}}\right)\boldsymbol{H}\,\boldsymbol{\sigma} + p\frac{\boldsymbol{H}\,\dot{\boldsymbol{\sigma}}}{\sigma_{eq}}. \tag{2.14}$$

Using the additive decomposition of the strain tensor, we can write:

$$\dot{\boldsymbol{\sigma}} = \boldsymbol{C} \cdot (\dot{\boldsymbol{\varepsilon}} - \dot{\boldsymbol{\varepsilon}}^p),$$
$$= \boldsymbol{C} \cdot \left(\dot{\boldsymbol{\varepsilon}} - \left[\frac{\dot{\sigma}_{eq}}{\sigma_{eq}} \left(\frac{\dot{p}}{\dot{\sigma}_{eq}} - \frac{p}{\sigma_{eq}} \right) \boldsymbol{H}\,\boldsymbol{\sigma} + p \frac{\boldsymbol{H}\,\dot{\boldsymbol{\sigma}}}{\sigma_{eq}} \right] \right). \tag{2.15}$$

Finally combining Equations 2.6 and 2.15, we obtain:

$$\dot{\boldsymbol{\varepsilon}} = \left[\boldsymbol{C}^{-1} + \frac{p}{\sigma_{eq}}\boldsymbol{H} + \left(\frac{\dot{p}}{\dot{\sigma}_{eq}} - \frac{p}{\sigma_{eq}} \right) \frac{\boldsymbol{H}\,\boldsymbol{\sigma} \otimes \boldsymbol{H}\,\boldsymbol{\sigma}}{\sigma_{eq}^2} \right] \dot{\boldsymbol{\sigma}}, \tag{2.16}$$

and therefore:

$$\boldsymbol{C_t} = \left[\boldsymbol{C}^{-1} + \frac{p}{\sigma_{eq}}\boldsymbol{H} + \left(\frac{\dot{p}}{\dot{\sigma}_{eq}} - \frac{p}{\sigma_{eq}} \right) \frac{\boldsymbol{H}\,\boldsymbol{\sigma} \otimes \boldsymbol{H}\,\boldsymbol{\sigma}}{\sigma_{eq}^2} \right]^{-1}. \tag{2.17}$$

In this work we apply *Hencky*'s deformation theory to plate buckling, as the plate subjected to in-plane loading experiences a proportional loading.

2.3.1.3 Corner theory

Hencky's deformation theory has shown excellent correlation with experiments for thick plastic solids as shown in [Hutchinson 1974]. Nevertheless it is only applicable to proportional loading because of its flow rule formulation. As mentioned in Chapter 1, an extension of this theory for structures with more complex load paths was proposed by Christoffersen and Hutchinson through the corner theory for elasto-plastic solids. Details can be found in [Christoffersen and Hutchinson 1979]. This theory is based on the definition of a potential, depending on the stress rate orientation, as follows:

$$W(\dot{\boldsymbol{\sigma}}, \boldsymbol{\sigma}) = \dot{\boldsymbol{\sigma}}^t \left(\boldsymbol{\mathcal{L}}_e + h(\theta)\boldsymbol{\mathcal{L}}_p \right) \dot{\boldsymbol{\sigma}}. \tag{2.18}$$

$\boldsymbol{\mathcal{L}}_e$ is the inverse elastic moduli, while Christoffersen and Hutchinson define $\boldsymbol{\mathcal{L}}_p$ as the plastic moduli of the deformation theory, defined by:

$$\boldsymbol{\mathcal{L}}_p = \frac{p}{\sigma_{eq}}\boldsymbol{H} + \left(\frac{\dot{p}}{\dot{\sigma}_{eq}} - \frac{p}{\sigma_{eq}} \right) \frac{\boldsymbol{H}\,\boldsymbol{\sigma} \otimes \boldsymbol{H}\,\boldsymbol{\sigma}}{\sigma_{eq}^2}. \tag{2.19}$$

$h(\theta)$ is a convex function of θ and θ is a smooth function of $\dot{\boldsymbol{\sigma}}$ and $\boldsymbol{\sigma}$.

In order to understand the role of θ and h, the definition of the non-smooth yield surface is needed. Christoffersen and Hutchinson define the yield surface as a cone oriented by the deviatoric stress tensor in the stress rate space as shown in Figure 2.7.

θ is the angle formed by the stress rate and the deviatoric stress tensor. If $\dot{\boldsymbol{\sigma}}$ is tangent to the cone, no plastic strain is generated by this stress rate, the material
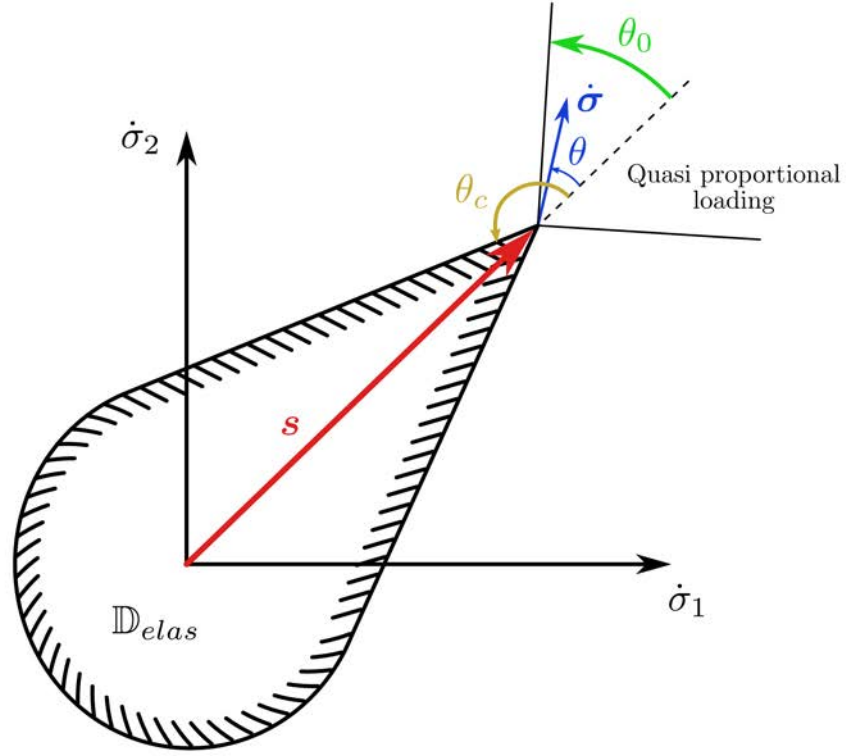
Figure 2.7: Shape of the yield surface for the corner theory, definition of the θ angle. In this configuration, the structure is in a quasi-proportional loading configuration.

follows the elastic law. If the stress rate, $\dot{\boldsymbol{\sigma}}$, is almost aligned with the deviatoric stress tensor, loading is quasi proportional, the deformation theory flow rule applies. Christoffersen and Hutchinson define two limit values of θ, θ_c and θ_0 respectively defining the beginning of the elastic unloading area and the quasi proportional loading area. Christoffersen and Hutchinson also demonstrate the following constraint on θ_0:

$$\theta_0 \leq \theta_c - \frac{\pi}{2}. \tag{2.20}$$

This geometric observation specifies $h(\theta)$ as follows:

$$h = \left\{ \begin{array}{ll} 1, & \theta \leq \theta_0 \\ 0, & \theta \geq \theta_c \end{array} \right\} \tag{2.21}$$

θ is defined by:

$$\cos \theta = \frac{(\boldsymbol{\mathcal{L}}_p \mathbb{U}_\sigma) : \dot{\boldsymbol{\sigma}}}{\left(\dot{\boldsymbol{\sigma}}^t \boldsymbol{\mathcal{L}}_p \dot{\boldsymbol{\sigma}} \right)^{1/2}} \tag{2.22}$$

with:

$$\mathbb{U}_\sigma = \frac{\boldsymbol{H}\,\boldsymbol{\sigma}}{(\boldsymbol{\sigma}^t \boldsymbol{H}\,\boldsymbol{\mathcal{L}}_p \boldsymbol{H}\,\boldsymbol{\sigma})^{1/2}} \tag{2.23}$$

Christoffersen and Hutchinson propose the following expression for h:

$$h(\theta) = \cos^2\left(\frac{\pi}{2}\,\frac{\theta - \theta_0}{\theta_c - \theta_0}\right), \text{ if: } \theta_0 < \theta < \theta_c. \tag{2.24}$$

θ_c and θ_0 can be considered as the parameters defining the yield surface shape. If $\theta_c = \frac{\pi}{2}$, a smooth yield surface is defined. If $\theta_0 = 0$, the yield surface vanishes and the tangent operator becomes non-linear.

Finally the tangent operator can be defined as follows:

$$\boldsymbol{C_t} = \left\{ \begin{array}{ll} [\boldsymbol{\mathcal{L}}_e + \boldsymbol{\mathcal{L}}_p]^{-1} & \theta \leq \theta_0, \\ \left[\boldsymbol{\mathcal{L}}_e + h(\theta)\left([1 - k(\theta)\cot\theta]\,\boldsymbol{\mathcal{L}}_p + \frac{k(\theta)}{\sin\theta\cos\theta}\mathbb{U}_\varepsilon \otimes \mathbb{U}_\varepsilon\right)\right]^{-1} & \theta_0 < \theta < \theta_c, \\ \boldsymbol{C} & \theta \geq \theta_c, \end{array} \right\} \tag{2.25}$$

with:

$$\begin{aligned} \boldsymbol{\mathcal{L}}_p &= \frac{p}{\sigma_{eq}}\boldsymbol{H} + \left(\frac{\dot{p}}{\dot{\sigma}_{eq}} - \frac{p}{\sigma_{eq}}\right)\frac{\boldsymbol{H}\,\boldsymbol{\sigma} \otimes \boldsymbol{H}\,\boldsymbol{\sigma}}{\sigma_{eq}^2}, \\ \mathbb{U}_\varepsilon &= \boldsymbol{\mathcal{L}}_p \mathbb{U}_\sigma, \\ k(\theta) &= -\frac{1}{2}\frac{h'(\theta)}{h(\theta)}. \end{aligned} \tag{2.26}$$

An unloading criterion for elasto-visco-plastic materials

The corner theory was formulated for elasto-plastic materials. An extension to elasto-visco-plastic materials is proposed here. Indeed, in order to consider visco-plastic unloading the variable $\theta^\star$ is defined as follows:

$$\theta^\star = \left\{ \begin{array}{l} \theta \text{ if: } \sigma_{eq} - R(p) = 0 \\ \theta \text{ if: } \sigma_{eq} - R(p) > 0 \text{ and } \theta \leq \pi/2 \\ \pi - \theta \text{ if: } \sigma_{eq} - R(p) > 0 \text{ and } \theta > \pi/2 \end{array} \right. \tag{2.27}$$

For elasto-visco-plastic materials, $\theta^\star$ is used instead of θ in all previously presented equations defining the corner theory model. $\theta^\star$ plays the role of a loading/unloading criterion.

Figure 2.8 depicts the loading and unloading mechanism defined through $\theta^\star$.

A symmetric loading/unloading strategy is adopted in the visco-plastic range, as shown in Figure 2.8. A quasi proportional unloading cone is defined. It is symmetrical to the quasi proportional loading cone with respect to the plane whose normal is the stress deviatoric.
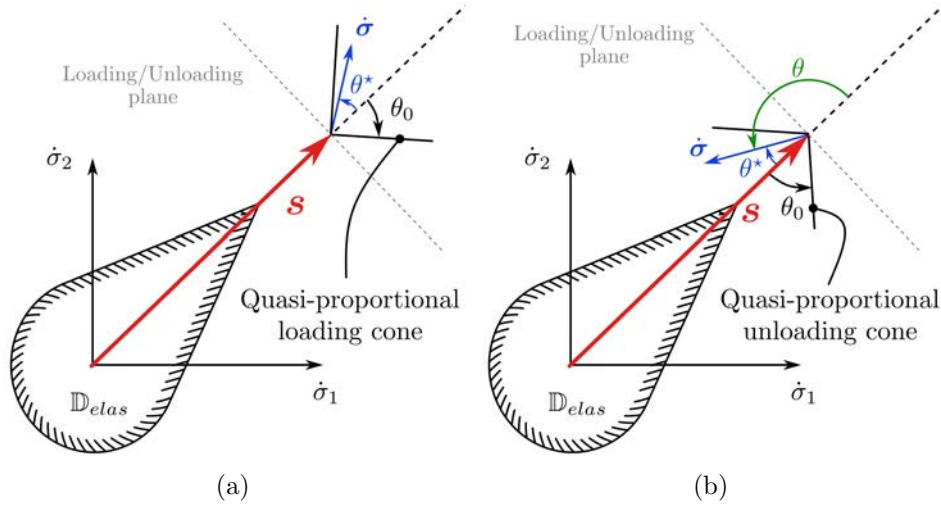
Figure 2.8: (a) Visco-plastic loading mechanism using the corner theory yield surface; (b) Visco-plastic unloading mechanism using the corner theory yield surface

If $\theta^\star < \theta_0$ at the considered point, this last one is loading or unloading quasi proportionally. The deformation theory is applied in both quasi-proportional loading and unloading cones.

If the point considered is on the yield surface, it follows the elasto-plastic corner theory.

This unloading criterion is mandatory so that the corner theory is compatible with the constitutive model selected, otherwise the unloading would be elastic. An elastic unloading would increase the stiffness of the structure and delay or even cancel the buckling of the structure in some loading conditions, as presented thereafter.

In Figure 2.9(a) the effect of the visco-plastic unloading criterion introduced to the corner theory is illustrated through the creep buckling of a clamped hemi-egg shell subjected to an external pressure evolution up to $P_{inf} = 4.1$ MPa. The evolution of the eigen pressures is depicted with respect to the time. Three eigen pressures are plotted, in blue the eigen pressure corresponding to the corner theory with the unloading criterion introduced here, in red the eigen pressure corresponding to the corner theory with an elastic unloading criterion and in magenta the eigen pressure defined with the deformation theory. In addition the applied pressure was plotted with respect to time in black. The bifurcation points are depicted with plain triangles.

As shown in Figure 2.9(a), the visco-plastic unloading criterion allows to detect a bifurcation while none is detected with the elastic unloading. An elastic unloading increases the stiffness of the shell structure and delays or cancels the bifurcation on the perfect structure. Moreover the bifurcation time predicted with the modified corner theory is close to the one predicted with the deformation theory as expected.

This new unloading criterion is especially important for creep buckling cases. The
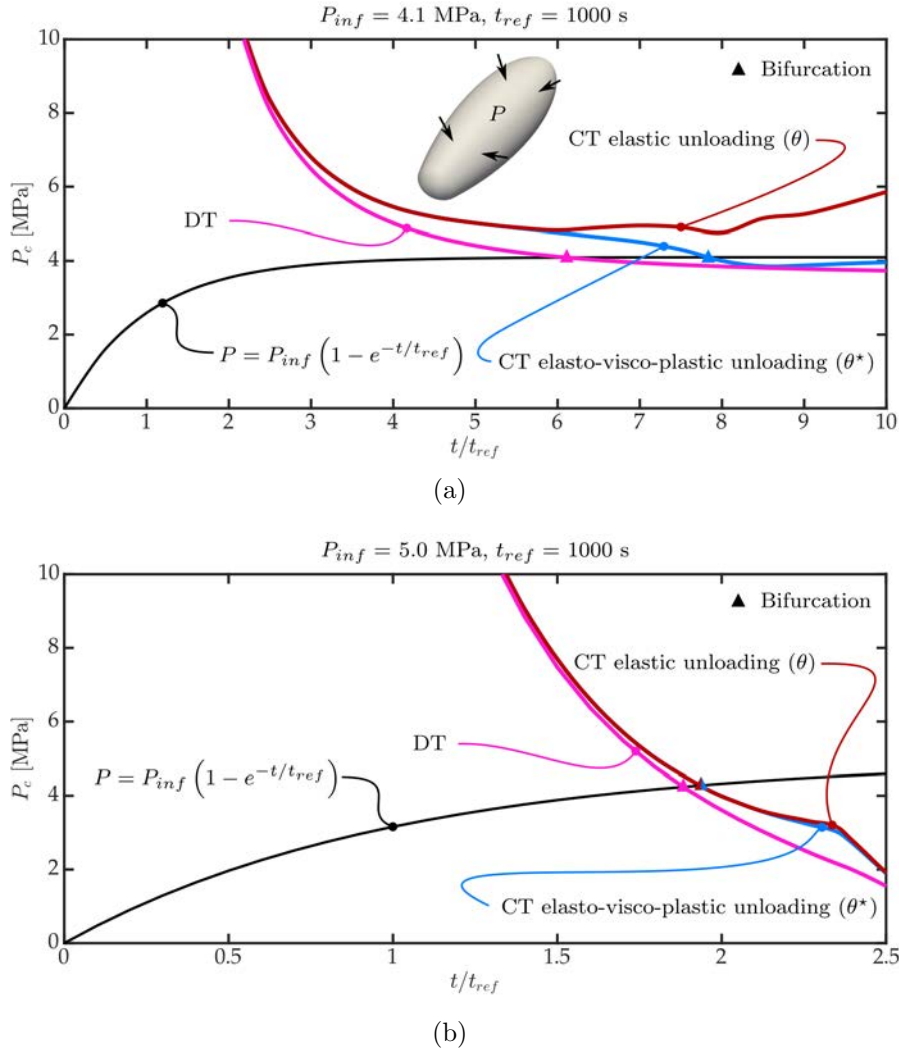
Figure 2.9: (a) Comparison of the eigen pressure from corner theory (CT) for both unloading criteria with the eigen pressure from the deformation theory (DT) in the creep regime, (b) Comparison of the eigen pressure from corner theory (CT) for both unloading criteria with the eigen pressure from the deformation theory (DT) in the elasto-visco-plastic regime. Results from a FE simulation with the material parameters from 3.5, and $\theta_0 = 10°$ and $\theta_c = 110°$.

results of the same analysis as presented in Figure 2.9(a) are depicted in Figure 2.9(b) with a pressure equal evolution up to $P_{inf} = 5.0$ MPa. In this case no difference is observed between the eigen pressure defined according to both unloading criterion. In this second load case, no unloading is experienced by the structure. Therefore the unloading criterion does not affect the results.

It is important to notice that for quasi-proportional loadings, *Hencky*'s defor-

78

mation theory and the corner theory are strictly equivalent. This is the key point of this theory. Moreover, using the deformation theory on load paths not strictly proportional is not theoretically right.

The advantage of the corner theory is to use *Hencky*'s deformation theory tangent operator for quasi-proportional loadings and a nonlinear tangent operator depending on θ for non-proportional loading. This allows to use a theory close to the deformation theory on structures subjected to non-proportional loadings, where the deformation theory cannot be used. The corner theory is used to predict the buckling of hemi-egg shells subjected to external pressure in this work, as a non-proportional loading is expected.

As already said, the corner theory yield stress depends of two parameters, θ_c and θ_0 defining respectively the inelastic loading range and the quasi-proportional loading range. Both parameters are identified in Chapter 5.

For all analysis in this work, the pre-buckling and post-buckling branches are computed using the *Mises* flow theory. The stress data from the pre-buckling branch is then used as an input to derive the tangent constitutive law with *Hencky*'s deformation theory or the corner theory and then to compute the bifurcation variables and modes. The corner theory could have been used for both the constitutive law integration and the tangent law derivation, with a lot more effort for small benefits as seen in [Tvergaard and Needleman 2000]. The main difference between the *Mises* flow theory and the corner theory is in the definition of the plastic increment.

The *Mises* flow theory tends to underestimate the plastic strain increment, while the corner theory overestimates the plastic strain increment. In order to reduce the difference between strain data used as input and the strain data associated to the corner theory, we restrict ourselves to a reasonable value of θ_c,i.e. $\theta_c < 130°$. This last value is recommended by Christoffersen and Hutchinson in [Christoffersen and Hutchinson 1979]. This is done in order to be close to the yield surface used for the constitutive law integration.

2.3.2 Analytical buckling prediction of thick plate subjected to in-plane compressive loads

The tangent operators derived previously could be directly used in a FE software with the conventional bifurcation tools. Nevertheless a FE model is time consuming for a parametric analysis especially for a simple geometry as a plate. In order to investigate in details the buckling of thick plates, an analytical model was developed.

The model is used to predict the critical values and the associated modes characterizing the buckling behaviour plates. The plate material behaviour was defined in Section 2.2. As an elasto-visco-plastic material is used, the strain and stress history needs to be defined before any stability analysis. The mechanical equilibrium is solved first, then its stability is tested using *Hencky*'s deformation theory.

Mechanical equilibrium and integration

The equilibrium is defined by the boundary conditions, the loading history and the material constitutive law. Plate edges can be constrained. Edges can be free, simply supported or clamped independently as long as the model is well constrained. Figure 2.10 illustrates the mechanical problem to solve.
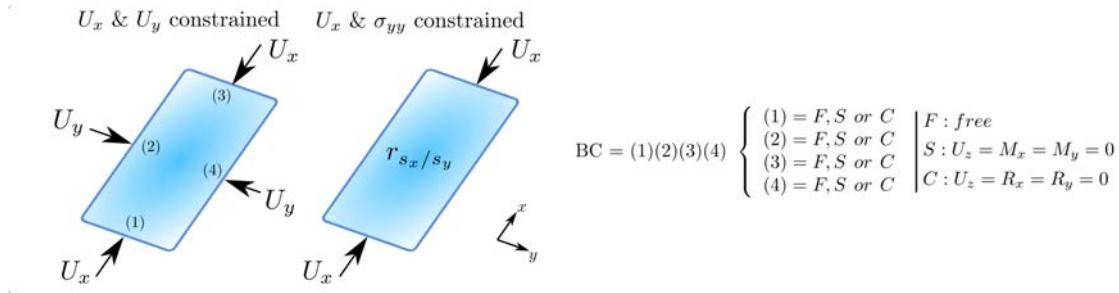
Figure 2.10: Definition of the plate buckling problem; F, S and C for free, simply supported and clamped; M_x and M_y the moments around x and y axis respectively; R_x and R_y the loads along x and y axis respectively

Two types of load case can be defined. Either one normal displacement (u_x or u_y) and the in-plane stress ratio σ_{xx}/σ_{yy} is known (the second in-plane displacement is unknown) (Figure 2.10 right) or both normal in-plane displacements are known (Figure 2.10 left). The spatial stress distribution is considered as homogenous ($\boldsymbol{\nabla}\,\boldsymbol{\sigma} = 0$).

The Reissner-Mindlin plate theory is used to define plate kinematics. The set of Equations 2.28 defines the relation between strain components and displacement fields:

$$
\begin{aligned}
\dot{\varepsilon}_{xx} &= \frac{\partial \dot{u}_x}{\partial x} + z\frac{\partial \dot{\phi}_x}{\partial x} \\
\dot{\varepsilon}_{yy} &= \frac{\partial \dot{u}_y}{\partial y} + z\frac{\partial \dot{\phi}_y}{\partial y} \\
\dot{\gamma}_{xy} &= z\left(\frac{\partial \dot{\phi}_x}{\partial y} + \frac{\partial \dot{\phi}_y}{\partial x}\right) \\
\dot{\gamma}_{xz} &= \dot{\phi}_x + \frac{\partial \dot{w}}{\partial x} \\
\dot{\gamma}_{yz} &= \dot{\phi}_y + \frac{\partial \dot{w}}{\partial y}
\end{aligned}
\tag{2.28}
$$

Bending of the plate is defined by one displacement field w (the out of plane displacement) and two rotation fields ϕ_x and ϕ_y around y and x respectively (as described in Appendix C).

Because of the rate dependency of the material, an integration algorithm is used to define the stress state according to loading history. The Mises flow theory is used for the constitutive law integration. A classical radial return mapping integration algorithm is implemented. This integration algorithm is based on an existing algorithms presented in [Simo and Hughes 1998]. The integration algorithm was generalized to anisotropic material and additive elasto-visco-plasticity. Plane stress formulation is used, as this hypothesis is verified during the pre-buckling phase. Other stress tensor components follow an elastic law.

The algorithm is defined with the assumption of small strain increment; additive decomposition of the strain tensor is still valid,

$$\boldsymbol{\varepsilon} = \boldsymbol{\varepsilon}^e + \boldsymbol{\varepsilon}^p. \tag{2.29}$$

The strain and stress tensors are defined by:

$$\boldsymbol{\varepsilon} = \begin{bmatrix} \varepsilon_{xx} \\ \varepsilon_{yy} \\ \gamma_{xy} \end{bmatrix}, \boldsymbol{\sigma} = \begin{bmatrix} \sigma_{xx} \\ \sigma_{yy} \\ \sigma_{xy} \end{bmatrix}, \tag{2.30}$$

with $\varepsilon_{zz} = -\frac{\nu}{1-\nu}(\varepsilon_{xx}^e + \varepsilon_{yy}^e) - (\varepsilon_{xx}^p + \varepsilon_{yy}^p)$ and $\sigma_{zz} = 0$.

Under plane stress conditions, the elastic modulus is defined by:

$$\boldsymbol{C} = \frac{E}{1-\nu^2} \begin{bmatrix} 1 & \nu & 0 \\ \nu & 1 & 0 \\ 0 & 0 & \frac{1-\nu}{2} \end{bmatrix} \text{ with } \boldsymbol{\sigma} = \boldsymbol{C} \cdot \boldsymbol{\varepsilon}^e. \tag{2.31}$$

Under plane stress assumption, *Hill*'s anisotropic yield criterion is defined by:

$$\sigma_{eq} = \sqrt{\boldsymbol{\sigma}^t \cdot \boldsymbol{H} \cdot \boldsymbol{\sigma}}, \tag{2.32}$$

where:

$$\boldsymbol{H} = \begin{bmatrix} F+H & -F & 0 \\ -F & G+F & 0 \\ 0 & 0 & L \end{bmatrix}. \tag{2.33}$$

The flow rule is defined by:

$$\dot{\boldsymbol{\varepsilon}}^p = \dot{p} \cdot \frac{\boldsymbol{H}\,\boldsymbol{\sigma}}{\sigma_{eq}}, \tag{2.34}$$

where p is the plastic parameter.

Hardening parameters R and creep law are defined by:

$$\begin{aligned} R &= R(p), \\ \dot{p} &= g(F) = \left(\frac{F}{K}\right)^n, \text{ with } F = \sigma_{eq} - R(p). \end{aligned} \tag{2.35}$$

Finally the radial return mapping integration algorithm is used to compute the stress increment according to previous stress/strain state and actual strain state.

For the elasto-visco-plastic integration algorithm the diagonalization of $\boldsymbol{C} \cdot \boldsymbol{H}$ is required, $\boldsymbol{Q}$ and $\boldsymbol{T}$ are then defined:

$$(\boldsymbol{C} \cdot \boldsymbol{H}) \cdot \boldsymbol{Q} = \boldsymbol{Q} \cdot \boldsymbol{T} \tag{2.36}$$

The radial return mapping integration algorithm is detailed in Algorithm 1.

Algorithm 1 Radial mapping algorithm

$\quad$ **Input**: $[\boldsymbol{\varepsilon}_{n+1}, \boldsymbol{\varepsilon}_n^p, \boldsymbol{\sigma}_n, p_n]$

$\quad \boldsymbol{\sigma}_{n+1}^{trial} = \boldsymbol{C} \cdot (\boldsymbol{\varepsilon}_{n+1} - \boldsymbol{\varepsilon}_n^p)$

$\quad \eta_{n+1}^{trial} = \boldsymbol{Q}^{-1} \cdot \boldsymbol{\sigma}_{n+1}^{trial}$

$\quad f_{n+1}^{trial} = \sigma_{eq}(\boldsymbol{\sigma}_{n+1}^{trial}) - R(p_n)$

$\quad$ **if** $f_{n+1}^{trial} \leq 0$ **then**

$\qquad (\cdot)_{n+1} = (\cdot)_{n+1}^{trial}$

$\quad$ **else**

$\qquad \hat{Q}_{i,j} = \delta_{i,j} \frac{1}{1+f_{n+1}}$

$\qquad \hat{f}_1(f_{n+1}) = \eta_{n+1}^{trial\,t} \hat{\boldsymbol{Q}}(f_{n+1}) \boldsymbol{Q}^{-1} \boldsymbol{H} \boldsymbol{Q} \hat{\boldsymbol{Q}}(f_{n+1}) \eta_{n+1}^{trial}$

$\qquad \hat{f}_2(f_{n+1}) = \left(R\left(p_n + f_{n+1}\sqrt{\hat{f}_1(f_{n+1})} \right) + g^{-1}\left(\frac{f_{n+1}\sqrt{\hat{f}_1(f_{n+1})}}{\Delta t} \right) \right)^2$

$\qquad \hat{f}(f_{n+1}) = \left(\hat{f}_1(f_{n+1}) - \hat{f}_2(f_{n+1}) \right)^2$

$\qquad$ **find**: $f_{n+1}, \hat{f}(f_{n+1}) = 0$

$\qquad \boldsymbol{\Theta} = \left(\boldsymbol{C}^{-1} + f_{n+1}\boldsymbol{H} \right)^{-1}$

$\qquad \boldsymbol{\sigma}_{n+1} = \boldsymbol{\Theta}\, \boldsymbol{C}^{-1} \boldsymbol{\sigma}_{n+1}^{trial}$

$\qquad p_{n+1} = p_n + f_{n+1}\hat{f}_1(f_{n+1})$

$\qquad \boldsymbol{\varepsilon}_{n+1}^p = \boldsymbol{\varepsilon}_{n+1}^p + f_{n+1}\boldsymbol{H}\boldsymbol{\sigma}_{n+1}$

$\quad$ **end if**

$\quad$ **Return**

As the stress is homogenous within the plate, the mechanical equilibrium is defined by the stress state.

Buckling prediction

For plates subjected to in-plane compressive loading, Chakrabarty defines the stability condition in [Chakrabarty 2000] as follows:

$$\int \Pi \, dV > 0, \tag{2.37}$$

with:

$$\begin{aligned}
\Pi &= \Pi_i + \Pi_e, \\
\Pi_i &= \dot{\boldsymbol{\sigma}}^t \cdot \dot{\boldsymbol{\varepsilon}}, \\
\Pi_e &= -\sigma_{xx}\left(\frac{\partial \dot{w}}{\partial x}\right)^2 - \sigma_{yy}\left(\frac{\partial \dot{w}}{\partial y}\right)^2 - 2\sigma_{xy}\left(\frac{\partial \dot{w}}{\partial x}\frac{\partial \dot{w}}{\partial y}\right).
\end{aligned} \tag{2.38}$$

The singular solutions of Equation 2.37 are identified using Ritz's method described by [Wang and Aung 2007]. Bending displacement and rotation fields are approximated by Ritz polynomial functions:

$$\begin{aligned}
w(x,y) &= \sum_{q=0}^{p}\sum_{i=0}^{q} c_m \phi_m^w, \\
\phi_x(x,y) &= \sum_{q=0}^{p}\sum_{i=0}^{q} d_m \phi_m^x, \\
\phi_y(x,y) &= \sum_{q=0}^{p}\sum_{i=0}^{q} e_m \phi_m^y,
\end{aligned} \tag{2.39}$$

with:

$$\begin{aligned}
\phi_m^w(x,y) &= \phi_b^w (x/a)^i (y/b)^{q-i}, \\
\phi_m^x(x,y) &= \phi_b^x (x/a)^i (y/b)^{q-i}, \\
\phi_m^y(x,y) &= \phi_b^y (x/a)^i (y/b)^{q-i}.
\end{aligned} \tag{2.40}$$

In Equation 2.39, p is the degree of the polynomial functions. c_m, d_m and e_m are the coefficients of the polynomial functions. ϕ_b^w, ϕ_b^x and ϕ_b^y are functions enforcing boundary conditions on the plate edges. m is defined by:

$$m = (q+1) \cdot (q+2)/2 - i \tag{2.41}$$

Singular solutions of Equation 2.37 are obtained by minimizing the total potential energy Π according to w, ϕ_x and ϕ_y. According to Ritz, they respect the following expression:

$$\left[\frac{\partial \Pi}{\partial c_m}, \frac{\partial \Pi}{\partial d_m}, \frac{\partial \Pi}{\partial e_m}\right] = [0, 0, 0]. \tag{2.42}$$

This last equation can be written as a linear problem:

$$[\boldsymbol{K}] \cdot \begin{bmatrix} c_m \\ d_m \\ e_m \end{bmatrix} = \boldsymbol{0}. \tag{2.43}$$

$\boldsymbol{K}$ contains the plate geometry, the material behaviour with the tangent operator, the boundary conditions as well as the loading conditions. For a given equilibrium, the modal analysis of $\boldsymbol{K}$ gives a set of eigenvalues and eigenvectors. Eigenvectors define the singular solutions of Equation 2.37 while the eigenvalues define their stability. An equilibrium is defined stable if the smallest eigenvalue is positive. On the opposite, if the smallest eigenvalue is negative the equilibrium is unstable. A critical or bifurcation point is defined by an eigenvalue equal to 0.

Testing the stability of every point on the equilibrium path allows to define every critical point and their associated buckling mode. The first critical point is reached when the smallest eigenvalue is 0, second critical point when the second smallest is 0 and so on. For this case of plate buckling, *Hencky*'s deformation theory is used to derive the tangent constitutive law. Indeed the plate experiences a proportional loading. This model is used in Chapter 4 to define the buckling predictions. The given predictions are compared to the FE post buckling analysis results and the experimental ones in Chapter 4.

Details of the present analytical prediction method can be found in [Wang and Aung 2007].

2.3.3 Buckling prediction of finite element shell structures

Analytical models are very efficient with simple structures, but very difficult to develop for complex ones. Finite element models are more flexible to model complex structures. In this section two topics are discussed. First the shell element chosen to model thick shell structures is presented briefly. Then the implementation of the bifurcation analysis tools in Cast3M is presented.

2.3.3.1 SHB8PS for anisotropic visco-plasticity

In this work, a great attention was given to the simulation/experiment link. In order to model closely the buckling experiments, a solid shell element was chosen. It is called SHB8PS, its formulation is detailed in [Abed-Meraim and Combescure 2009]. This shell element was selected for two reasons: it models closely the volume of the shell; it only considers displacement degrees of freedom compared to other shell elements.

These two properties make it a good candidate to model with fidelity the buckling experiments. With its 3D geometric representation, the measured displacement fields can be directly compared to the displacement fields measured on one face of the shell specimens.

84

Unfortunately this shell element was not completely implemented in Cast3M. Its implementation in Cast3M for elasto-visco-plastic buckling analysis was performed during this thesis with the following characteristics:

- It is formulated for large displacements and small strain increments using an updated Lagrangian formulation.

- Inelastic anisotropy can be considered.

- A large range of inelastic behaviour can be chosen thanks to the coupling of Cast3M with Mfront (cf. [Helfer et al. 2013]) for the constitutive law integration.

The details of its initial formulation and the developments performed can be found in Appendix C.

2.3.3.2 Buckling predictions

In this section the method applied to predict the buckling of complex shell structures from finite element analysis is presented.

Bifurcation analysis

As presented in Chapter 1, the bifurcation problem can be reduced to an eigenvalue problem involving the stiffness matrix of the structure studied. The difficulty is concentrated on the construction of the stiffness matrix. The stiffness matrix integrates the material constitutive law, the boundary conditions, and the linear and nonlinear loads. The stiffness matrix can be divided into four sub-matrixes as follows:

$$\boldsymbol{K}_T = \boldsymbol{K}_{MAT} + \boldsymbol{K}_{GEOM} + \boldsymbol{K}_{BC} + \boldsymbol{K}_{NL}, \tag{2.44}$$

with $\boldsymbol{K}_{BC}$ corresponding to the Lagrange multiplier matrix, $\boldsymbol{K}_{NL}$ the matrix associated to the non-linear load such as the following pressure, $\boldsymbol{K}_{GEOM}$ the geometric stiffness matrix is defined by:

$$\boldsymbol{K}_{GEOM} = \int_{\Omega_e} \boldsymbol{\sigma} : \boldsymbol{\varepsilon}_Q(\delta\boldsymbol{u}, \Delta\boldsymbol{u}) d\Omega, \tag{2.45}$$

and:

$$\boldsymbol{K}_{MAT} = \int_{\Omega_e} \boldsymbol{\varepsilon}^t \, \boldsymbol{C}_t \, \boldsymbol{\varepsilon} \, d\Omega, \tag{2.46}$$

The detailed expression of $\boldsymbol{K}_{GEOM}$ for the SHB8PS element can be found in [Abed-Meraim and Combescure 2009]. In plasticity $\boldsymbol{C}_t$ is ideally the consistent tangent constitutive law. Otherwise any of the tangent operator derived in Section 2.3.1 can be used, as long as the stress and strain state are compatible with the hypothesis used to derive the tangent constitutive law.

$\boldsymbol{K}_{NL}$ and $\boldsymbol{K}_{GEOM}$ are therefore linked to the applied load. The stability analysis of an equilibrium is performed trough the analysis of the eigenvalue of the stiffness matrix. The eigenvalue problem can be defined in two different ways:

$$
\begin{aligned}
&\text{CASE 1: } \det\left[\boldsymbol{K}_T - \lambda\boldsymbol{I}\right] = 0 \\
&\text{CASE 2: } \det\left[\boldsymbol{K}_{MAT} + \boldsymbol{K}_{BC} + \lambda\left(\boldsymbol{K}_{GEOM} + \boldsymbol{K}_{NL}\right)\right] = 0
\end{aligned}
\tag{2.47}
$$

In the first case the equilibrium is stable as long as the smallest eigenvalue is positive. This general expression from the generalized standard materials expression, was given through a variational approach of a minimisation problem as shown in [Benbagdad 1992]. In the second case the equilibrium is stable as long as the smallest eigenvalue is larger than 1. This case was defined through the *Rayleigh* ratio as mentioned in [Benbagdad 1992]. Both cases give equivalent results, as when the critical eigenvalue is reached, the global stiffness matrix is singular.

$$
\begin{aligned}
&\text{CASE 1, if: } \lambda = 0 \Rightarrow \boldsymbol{U}^t\boldsymbol{K}_T\boldsymbol{U} = 0 \text{ and } \boldsymbol{U} \neq \boldsymbol{0} \\
&\text{CASE 2, if: } \lambda = 1 \Rightarrow \boldsymbol{U}^t\left[\boldsymbol{K}_{MAT} + \boldsymbol{K}_{BC} + \boldsymbol{K}_{GEOM} + \boldsymbol{K}_{NL}\right]\boldsymbol{U} = 0 \\
&\qquad\qquad\qquad \Leftrightarrow \boldsymbol{U}^t\boldsymbol{K}_T\boldsymbol{U} = 0 \text{ and } \boldsymbol{U} \neq \boldsymbol{0}
\end{aligned}
\tag{2.48}
$$

For the bifurcation equilibrium, the mechanical variables, as the stress, the strain, the load or the displacement are defined as critical. They define the border between the stable domain and the unstable one.

To analyse the stability of a structure, the trivial branch is first computed using an updated Lagrangian formulation in small strain. The stability of the equilibriums is tested *a posteriori*. Either all equilibriums are tested or the bifurcation is found using a dichotomy approach. There is as many eigenvalues as degrees of freedom in the stiffness matrix. Only the first eigenvalues are required as they are more likely to appear. The eigenvalue analysis also generates the eigen-modes associated to the set of eigenvalues.

The eigen-modes give the shape of the buckling modes of the structure. They also allow to initiate the bifurcated branch. The bifurcated branch can be followed by perturbing the bifurcation equilibrium with respect to the buckling mode. An arc length method is then used to compute the bifurcated branch. This following path method allows to identify the nature of the bifurcation, and more importantly the possible successive bifurcation.

This method is particularly efficient for elasto-plastic material. For an elasto-visco-plastic material the bifurcation point is defined using *Bodner*'s hypothesis. The bifurcated branches can be approached keeping the same assumption of instantaneous elasto-plastic material.

Imperfection analysis

Another method can be used to approach the bifurcation equilibrium. When buckling experiments are performed, it is almost impossible to obtain perfect structures. This observation is applied to numerical models by introducing an imperfection to the perfect model. The imperfection can be geometric, modifying the initial shape of the structure; or it can be associated to the loading.

This method allows to approach the bifurcation equilibrium through several simulations with different imperfection amplitudes. The real benefit of this method is to estimate the imperfection sensitivity of the structure with respect to its buckling behaviour.

The different methods to predict the buckling of thick shells were presented, from the derivation of the tangential constitutive law to the bifurcation analysis, either with an analytical model or a FE one. These methods will be compared to the results of two buckling test campaigns. The testing procedure associated to these test campaigns are presented thereafter.

2.4   Buckling experiments

This section details the experimental set-ups as well as the specimens designed to experiment buckling on thick shell structures. One of the final objectives of this work is to assess the buckling of thick shell structures subjected to external pressure. Two different structures were selected. They both present an interest in the study of thick shell elasto-visco-plastic buckling.

Thick plates subjected to in-plane compressive load present an interest, as their buckling do not follow the classical flow theory. This particular point was mentioned by [Hutchinson 1974]. This first set of experiments allows to validate the numerical methods developed above, on a well-documented structure for elasto-plastic materials subjected to proportional loadings.

The second set of experiments concerns the buckling of thick shell structures subjected to external pressure. They can be presented as an extension to non-proportional loadings of the first set of experiments. The experimental set-up and the shape of the specimen were developed especially for this work.

2.4.1   Thick plate under in-plane compressive load

Numbers of authors studied the buckling of plate subjected to in-plane compressive load. The existing experimental studies are often limited to elasto-plastic materials when thick shells are studied [Hutchinson 1974; Yeh and Kyriakides 1986], while elasto-visco-plastic buckling of plate is limited to thin plates in the literature (cf. [Paley and Aboudi 1991]). The experiments performed in this work aim to validate the previously presented theory to elasto-visco-plastic thick plates.

The specimen geometry is characterized by its effective length a, its width b
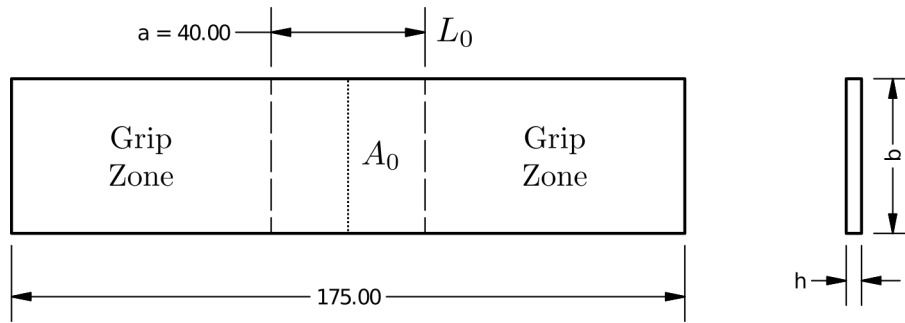
Figure 2.11: Plate buckling specimen drawings, dimension in mm

and its thickness h. The specimen geometry includes two grip zones. Figure 2.4.1 presents the geometry of the plate buckling specimen. The plate can also be characterized by its aspect ratio a/b and its thickness ratio b/h. Plates can be considered as thick when $b/h \leq 10$. Moreover if the plate is too thick, localization can be observed instead of buckling. It was chosen to limit the thickness ratio to 10 in order to observe buckling collapse of the plate.

2.4.1.1 Test rig and instrumentation
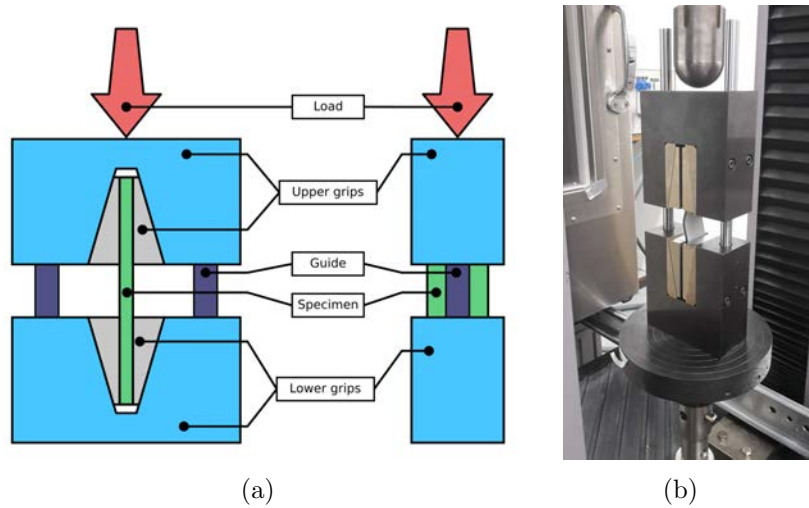
Figure 2.12: (a) Experimental set-up for plate buckling; (b) Experimental set-up in the testing machine, with a buckled specimen

The experimental set-up used for buckling tests is presented in Figure 2.12(a). Each ends of the specimen is clamped in self-tightening grips. Grips design allows transverse sliding of the specimen. The grips are guided by two columns. The lower grip is positioned on a rigid plate (part of the testing machine) and aligned with the vertical axis of the testing machine. The compressive load is applied through a

20 kN electro-mechanical testing machine which can be operated in displacement or load control. A point load is applied to the upper grip using a hemispherical punch. The testing machine displacement and the load applied are recorded during tests.
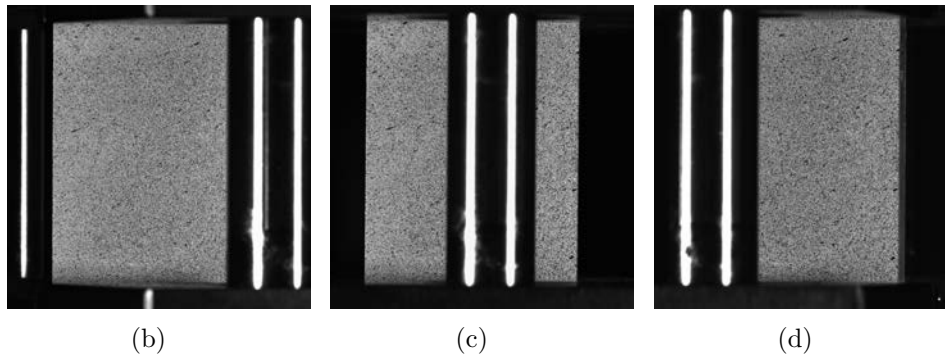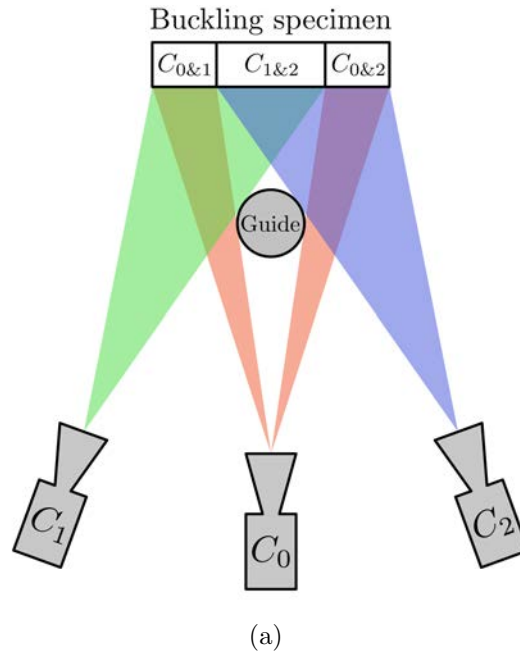
Figure 2.13: (a) Positions and coupling of the cameras for DIC (considering test rig environment); (b - d) Pictures of the three cameras from left to right, C_1, C_0 and C_2

Instrumentation of the testing machine is completed by three 12 Mpx cameras with 200 mm lenses. A random speckle pattern is applied to the surface of the specimen. The speckle pattern is characterized by the same properties as previously mentioned (cf. Section 2.2.1). 3D DIC is used to measure the displacement fields on the surface of the buckling specimen. Cameras are positioned in a manner to cover the entire surface of the plate as shown in Figure 2.13.

To cover the whole width of the specimen, three cameras are positioned at 20° of their nearest neighbour. Cameras are coupled with each other to identify the

displacement fields on the surface of the specimen with three 3D-DIC operations.

2.4.1.2 Test Conditions

Plates with aspect ratio of 1.00 and 1.33 are tested, while their thickness ratio varies from 15 to 10. All specimens have an effective length a of 40 mm.

During buckling experiments, the testing machine is turned on displacement rate control mode. Three displacement rates were tested, 2.0×10^{-2} mm.s^{-1}, 2.0×10^{-3} mm.s^{-1} and 4.0×10^{-4} mm.s^{-1}. The plate specimens were extracted from five ingots. The test as well as the ingots casting were performed in two campaigns.

Table 2.3 summarizes the geometry of the buckling specimens tested and their testing conditions.

Specimen ID	a/b	b/h	Speed [mm.s^{-1}]	Ingot #	BTC #
BT1/01	1.00	10	2.10^{-3}	0	1
BT1/02	1.33	10	2.10^{-3}	0	1
BT1/11	1.00	13	2.10^{-3}	1	1
BT1/12	1.33	10	2.10^{-3}	1	1
BT1/21	1.00	10	2.10^{-3}	2	1
BT1/22	1.33	15	2.10^{-3}	2	1
BT2/31	1.33	10	2.10^{-2}	3	2
BT2/32	1.33	10	4.10^{-4}	3	2
BT2/41	1.33	10	2.10^{-2}	4	2
BT2/42	1.33	10	4.10^{-4}	4	2

Table 2.3: Summary of plate geometries and testing conditions

The results of these tests are discussed and compared to the buckling predictions in Chapter 4.

2.4.2 Thick shell under external pressure

The second set of experiments intends to study the buckling of thick shells subjected to external pressure. Many experiments can be found in the literature on either cylindrical or spherical shells (cf. [Galletly et al. 1987; Kyriakides and Shaw 1982; Montague 1969; Yeh and Kyriakides 1986]). Most of them were performed on thin or moderately thick elasto-plastic shells. Only few works deals with elasto-visco-plastic materials, as [Combescure and Jullien 2017] or [Sammari and Jullien 1995]. In this work we intend to experiment buckling of moderately thick elasto-visco-plastic shells under external pressure.

2.4.2.1 Specimen design
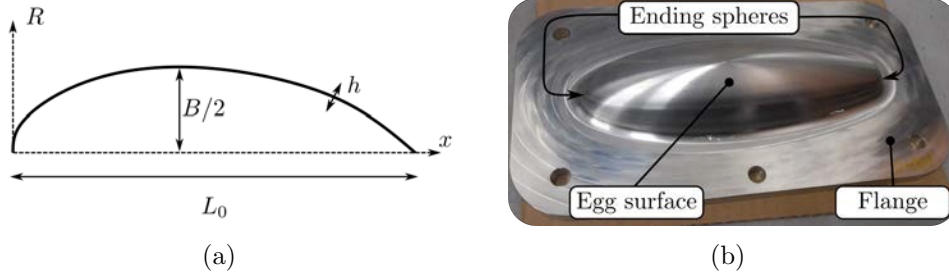
Figure 2.14: (a) Egg geometry; (b) Egg specimen after machining

The shape of the specimen was defined from [Zhang et al. 2017]. It is a hemi-egg defined by its major axis or length L, its minor axis or width B and its thickness h, as shown in Figure 2.14(a). The shape of the egg is defined by Zhang et al. as follows:

$$\text{for } x \in [0, L] : R(x) = \sqrt{L^{\frac{2}{n+1}} x^{\frac{2n}{n+1}} - x^2}, \tag{2.49}$$

with:

$$n = 1.057 \left(\frac{L}{B}\right)^{2.372}. \tag{2.50}$$

This shape is interesting as it is a mixed shape between a cylinder and a sphere. When $L/B = 1$ we have a spherical egg, when $L/B \to \infty$ the egg tends to be a long cylinder. B/L ratio is called the aspect ratio. As every axi-symmetrical geometry, its thickness ratio can be defined by the R/h ratio. Shells can be considered as thick when the R/h ratio is lower than 10. Figure 2.15 presents eggs geometry with different aspect ratio.
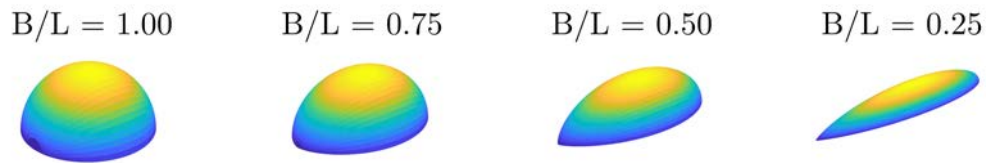
Figure 2.15: Examples of several egg shapes.

The basic egg shape was modified in order to be machinable. Each ends of the egg is closed by a spherical surface. Moreover a flange has been added to the egg in order to position the specimen in the test rig, as shown in Figure 2.14(b). Because of the manufacturing lead time and constraints, a single egg geometry was tested. The egg geometry selected is defined by a major axis length L of 220 mm, an aspect
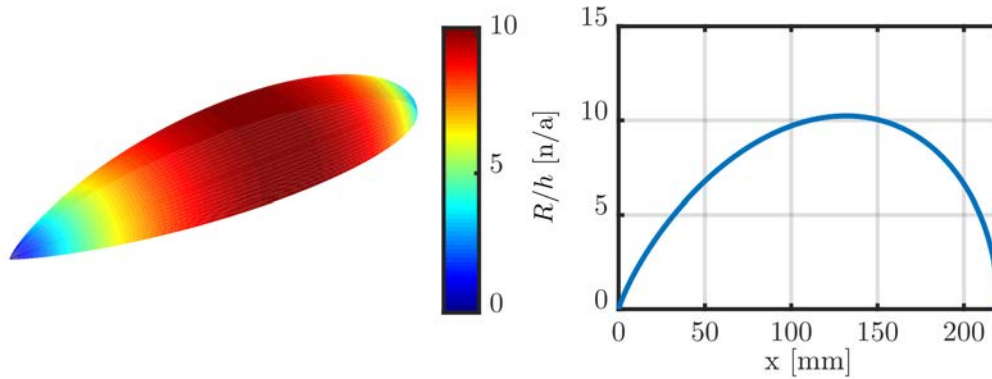
Figure 2.16: Thickness ratio R/h along major axis of the selected egg shape.

ratio B/L of 0.3 and a thickness h of 3 mm. Figure 2.16 presents the thickness ratio obtained with the selected egg shape.

This configuration gives a moderately thick shell in addition to a close cylinder shape. The property of moderately thick shell is defined for shell for a R/h ratio (radius over thickness ratio) between 10 and 20. This slender shape improves the strength of the structure. This favours the appearance of inelastic buckling instead of elastic buckling or localisation.

2.4.2.2 Test rig

The test rig used was specially developed to test the buckling strength of shells subjected to external pressure. It was already used in [Sammari and Jullien 1995]. The test rig is composed of a pressured tank (filled with oil) and closed by the specimen (in blue in Figure 2.17). The tank is pressurized by a syringe. The pressure is controlled through the displacement of the syringe piston. A 250 bars pressure sensor measures the pressure within the tank. Figure 2.17 presents the test rig pressurisation concept as well as a picture of the installation.

Sealing is an important issue for pressurized systems. As the specimen is part of the sealing system, special components were designed and manufactured to insure optimal sealing performances of the rig. The assembly used to close the pressurized tank is presented in Figure 2.18.

The specimen is positioned between two specimen holders (in green in Figure 2.18), an O-ring ensures sealing between the specimen and the upper specimen holder. This sub-assembly is then assembled to the tank thanks to 17 screws, tightened to 200 N.m as shown in Figure 2.18. In addition a film in elastomer covers the upper surface of the specimen to prevent any leakage due to material failure after buckling.
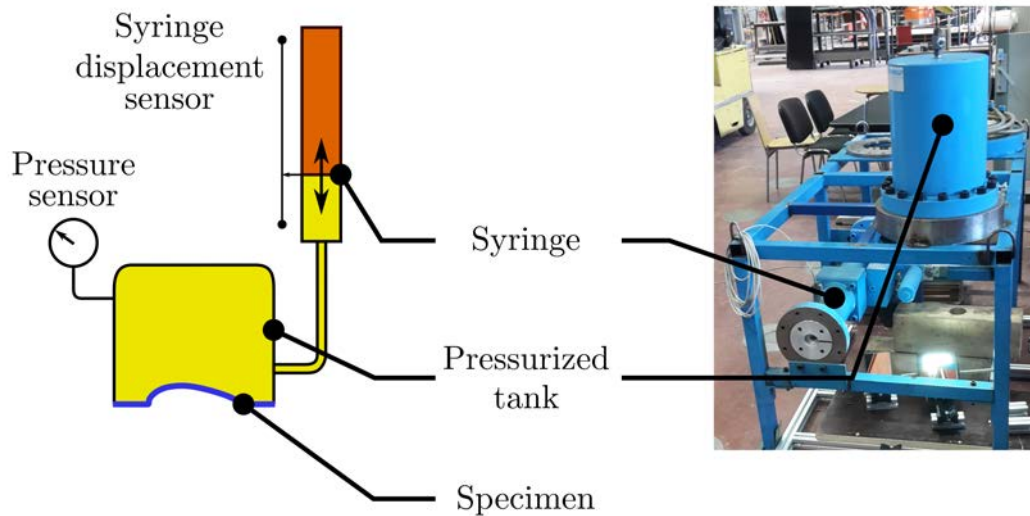
Figure 2.17: Test rig pressurisation concept
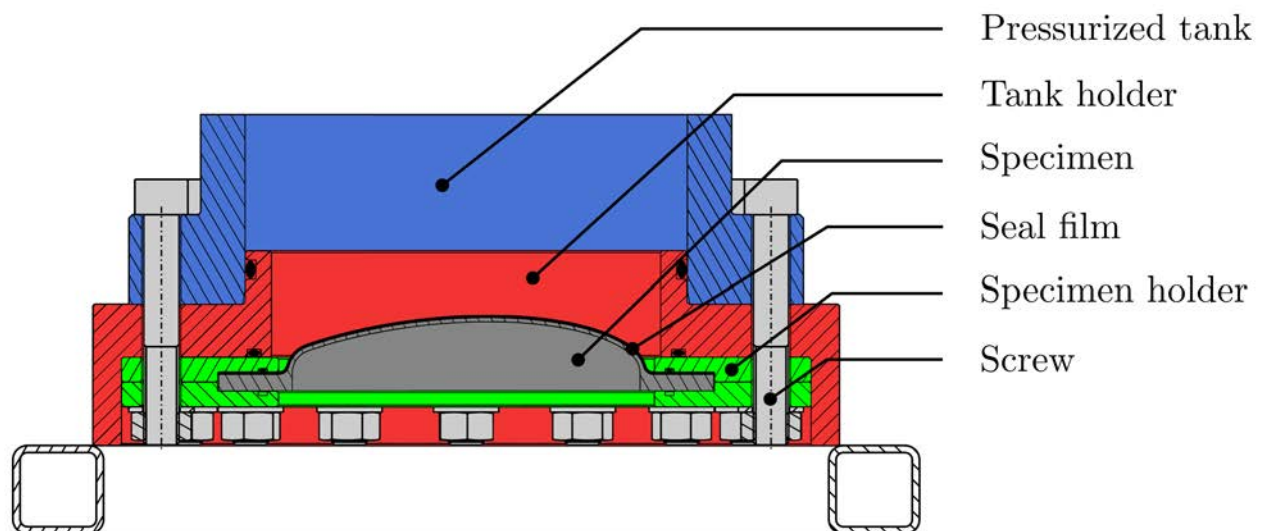
Figure 2.18: Test rig assembly with the specimen

2.4.2.3 DIC instrumentation

The displacement fields on the inner surface of the egg is measured by 3D-DIC means thanks to three cameras. The specimen inner surface is covered by a speckle pattern as already presented (cf. 2.2.1). To obtain a depth of field large enough the cameras needed to be positioned far from the specimen. Moreover, the likelihood of a leakage at buckling forbids the presence of cameras below the pressurized tank. It was chosen to use mirrors as shown in Figure 2.19(a).

The three cameras are positioned in order to fulfil the following constraints:

- Maximize the depth of field,

- Maximize the optical sensor coverage,

- Correlate a large area of the specimen,

- The mirrors and cameras must fit in the test rig environmental.

(a)   (b)
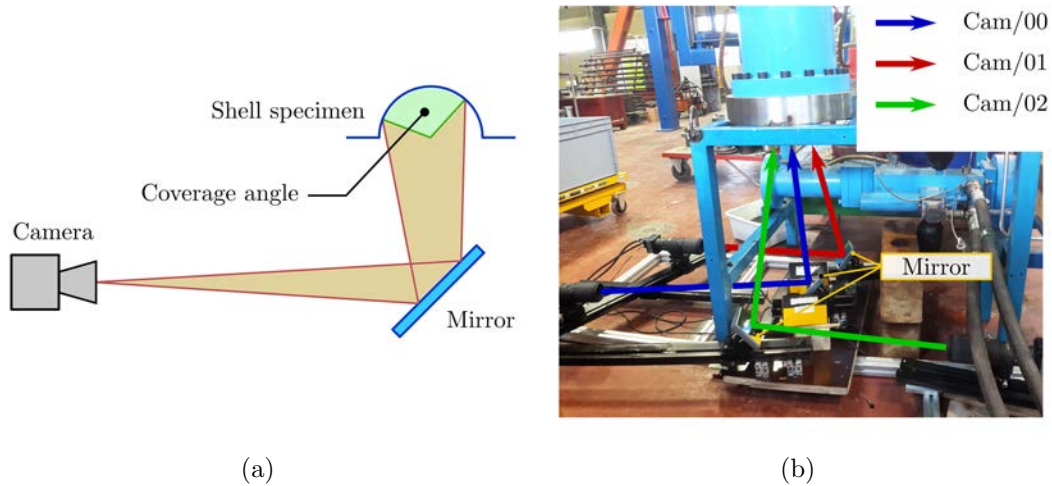
Figure 2.19: (a) Concept of indirect image acquisition; (b) Integration of the optical set-up in the test rig environment

Finally, three 12 Mpx cameras with 200 mm lenses were used with three 100 x 100 mm^2 mirrors. Table 2.4 summarises the optical characteristics of each camera.

Camera ID	focal [mm]	N	P [m]	ΔP [mm]	Resolution [MPx]
Cam/00	200	16	1.6	20.5	12
Cam/01	200	16	1.6	20.5	12
Cam/02	200	16	1.6	20.5	12

Table 2.4: Summary of camera properties; N corresponds to opening index, P is the distance between the object and the lens; and ΔP the depth of field.

With three cameras the total coverage angle (cf. Figure 2.19(a)) is equal to 140° against 110° with only two. These additional 30° insure a better observation of the buckling mode.

Figure 2.19(b) also presents the integration of the optical set-up in the test rig environment.

2.4.2.4 Testing conditions

In this section we present the approach followed to define the loading strategy. First the test rig was not designed to be controlled safely in pressure control mode. Only the syringe displacement rate can be controlled. To overcome this issue, a pressure versus syringe displacement law was defined experimentally. To define this law the egg specimen was replaced by an aluminium plate. Figure 2.20(a) presents the pressure / displacement law obtained.
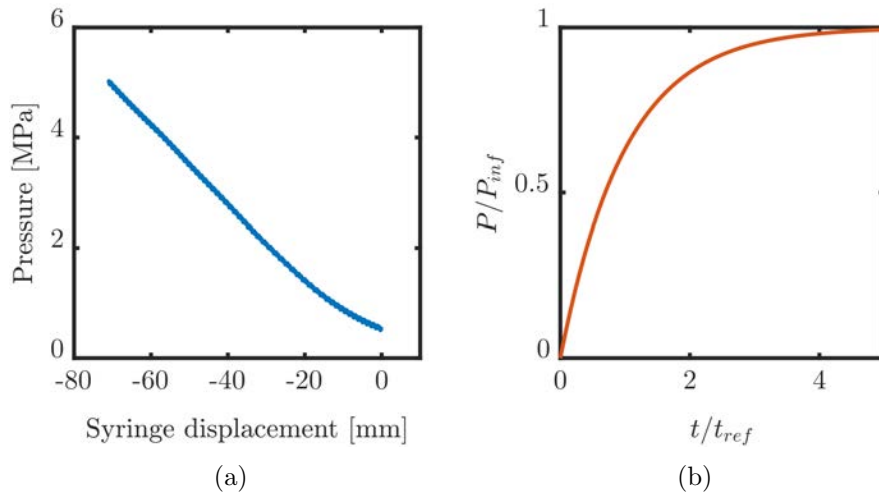
Figure 2.20: (a) Relation between the syringe displacement and the tank pressure; (b) Parametric pressure history applied to egg shell

We chose to apply an exponential pressure history saturating for a defined pressure. The pressure history is defined by the following equation:

$$P(t) = P_{inf} \left(1 - e^{-\frac{t}{t_{ref}}} \right). \tag{2.51}$$

The kinematic of the load is defined through the parameter t_{ref}, while the amplitude is defined by P_{inf}, the saturating pressure. The law is also plotted in Figure 2.20(b). The definition of t_{ref} and P_{inf} is discussed in Chapter 5. Six egg shells with the same geometries were tested according to the test conditions presented in Table 2.5. The first egg (O/001) tested was only used to evaluate the experimental procedure.

Specimen ID	L [mm]	B/L	h [mm]	P_{inf} [MPa]	t_{ref} [s]
O/001	220	0.3	3.0	5.0	100
O/002	220	0.3	3.0	5.0	100
O/003	220	0.3	3.0	5.0	100
O/004	220	0.3	3.0	5.0	100
O/005	220	0.3	3.0	5.0	1000
O/006	220	0.3	3.0	5.0	1000

Table 2.5: Summary of egg geometries and testing conditions (defined in Chapter 5)

2.5   From 3D-DIC to FE modelling

In this section the process to link 3D-DIC data to the FE modelling of each experiment is presented. For all buckling experiments 3D-DIC processing was used (cf. [Réthoré 2018]). The principle is to use at least two cameras in order to measure the 3D displacement fields on a surface of the specimen (called ROI for Region of Interest). For both types of buckling experiments, three cameras were used. This choice was driven by the need to observe the largest ROI on the specimen.

For both structures, the method to define the measured 3D displacement fields is globally the same. First the calibration is performed with all three cameras. This first point is important as a single optical coordinate system is defined. Then, the 3D-DIC processing of the images is done for a selection of camera couples. This is performed using the FE-DIC global approach software Ufreckles (cf. [Réthoré 2018]). From the 3D-DIC processing the following elements are obtained:

- The topology of the ROI corresponding to all camera couples,

- The measurement error on all three components of the displacement fields (U_x, U_y and U_z),

- The 3D displacement fields in the optical coordinate system for all camera couples.

These outputs are very useful, but not convenient to be compared to FE data. In order to make both types of data compatible with each other, the following process is defined:

(1) Projection of all DIC topologies on the theoretical shape,

(2) Evaluation of the topological error,

(3) Definition of a common mesh (DIC and FE) covering the largest ROI on the theoretical shape,

(4) Definition of a coordinate system attached to the tested specimen,

(5) Interpolation of all DIC displacement fields on the common mesh with poly-nomial functions of moderately high degree or splines.

Using this method, the DIC data are transported to a common coordinate system and a common mesh attached to tested specimen. The mesh is then used for the Finite Element Analysis (FEA) of the experiment.

As the DIC data are finally defined on a single mesh and in a common coordinate system, the FE model used to analyse the experiments can be built. It is important to notice that, at this step the mesh is a surface mesh. The mesh is therefore thickened according to the specimen thickness and using SHB8PS elements. The displacement fields are also propagated in the thickness direction using the Kirchhoff-Love plate kinematic.

In both cases, for plates subjected to compressive loading or thick shells subjected to external pressure, the same approaches are used with some small specificities presented thereafter.

FE modelling of plate buckling experiments

The boundary conditions are applied through the experimental displacement field to the constrained edges of the FE mesh. The FE model is therefore loaded through the enforcement of the boundary conditions. Figure 2.21 presents the global method used to build the FE model for this type of experiment.
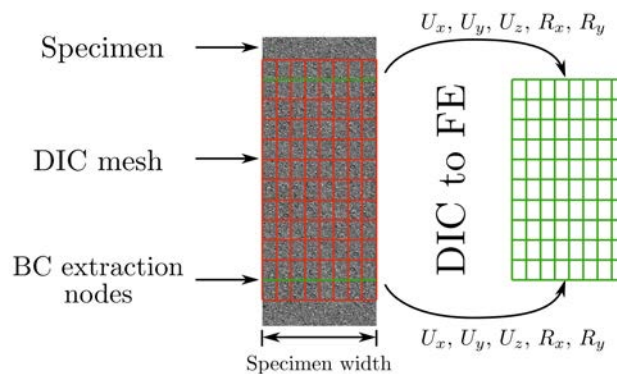
Figure 2.21: DIC to FE process for plate buckling experiments

FE modelling of the buckling experiments on thick shell subjected to external pressure

In this case, the experimental displacement fields are applied to the FE mesh boundaries as well. The FE mesh only considers a portion of the entire egg, as the cameras does not cover the whole egg. They are applied differently according to their positions:

- On the lower skin (observed experimentally), all membrane displacement fields (u_1, u_2) are applied to the edges of the lower skin,

- On the upper skin, only the normal in-plane component of the membrane displacement fields is applied to the edges of the upper skin,

- In order to consider the higher stiffness at both ends of the egg-shell, the out-of-plane displacement field is also applied to each ends of the lower skin.

Figure 2.22(a) illustrates the enforcement of the boundary conditions on the FE mesh of the ROI.

<div align="center">(a)   (b)</div>
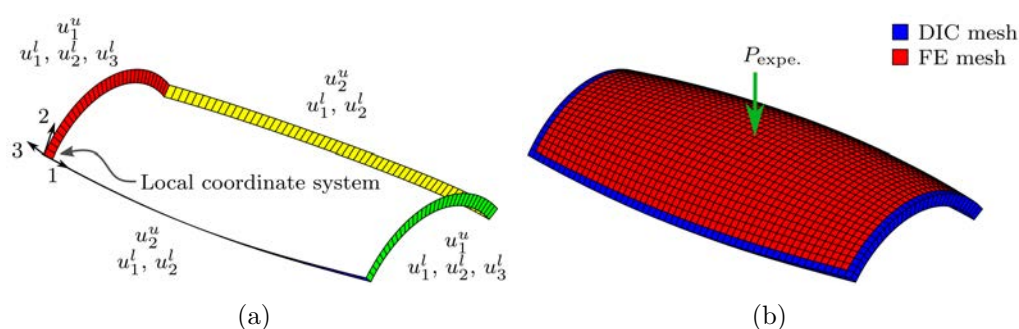
Figure 2.22: (a) Enforcement of experimental boundary conditions on the FE mesh, subscript ^{l} for lower skin and ^{u} for upper skin; (b) the FE mesh is equal to the DIC mesh with a mesh row removed on each edge, experimental pressure is applied on the FE mesh.

Only a reduced part of the specimen is covered by the cameras. In addition, the measured pressure is applied to the shell external skin as shown in Figure 2.22(b). Using this modelling method, the numerical out of plane displacement field can be extracted, analysed and compared to the experimental one with respect to the time and the measured pressure.

The FE-DIC method presented here is used to enrich the experimental data, as the evaluation of the loading imperfections or the evaluation of the experimental stress state. It is also used to create the FE model used to characterize the yield stress of each buckling experiment.

2.6 Conclusion

In this chapter the different methods to study experimentally or numerically the buckling of thick shells were presented. First the method to identify the material law was presented. This FEMU based method includes a strong link between experimental data and the parameters to be identified. Then buckling modelling methods

and a buckling prediction method were presented. In particular we can notice the buckling prediction model developed for thick elasto-visco-plastic structures, which uses the corner theory adapted to elasto-visco-plastic anisotropic materials. Finally the experimental procedures to experiment buckling on thick plates and thick shells were introduced. A special attention was also given to the experimental/numerical link in order to validate experimentally the buckling prediction method with respect to the critical values and buckling modes.

All methods were presented with respect to a set of assumptions. In the next chapters, discussions about these hypotheses and their validities are discussed. The buckling paradox and *Bodner*'s hypothesis will be especially discussed regarding the buckling predictions.

As already mentioned in the introduction, an incremental approach was chosen in order to study the buckling of thick shells. In the next chapters, the results concerning the identification of the constitutive law are presented first. Then the validity of the buckling prediction method against thick plate buckling experiments is discussed. Finally the buckling prediction method is compared to buckling experiments on thick egg shells subjected to external pressure. This last case of study groups all the issues identified in Chapter 1, an elasto-visco-plastic material behaviour, a thick shell geometry and a non-proportional loading.

Chapter 3

FEMU based identification of the SAC 305 elasto-visco-plastic behaviour

The chapter presents the identification of the elasto-visco-plastic behaviour of the SAC 305 alloy using a FEMU based approach.

Contents

This chapter presents the results of the finite element model updating (FEMU) approach used to identify the homogenized elasto-visco-plastic behaviour of the SAC 305 alloy. The chapter discusses first, the post-processing of the test data and more specifically the regularization of the measured strain fields due to the coarse microstructure. Then a special attention is given to the reliability of the identification in terms of parameters sensitivity, uniqueness of the solution and consideration of material discrepancies.

The reference law of the SAC 305 alloy used in this work was defined through a FEMU approach based on tensile tests on four different material batches. This chapter also presents the statistical approach followed to generate this reference law.

3.1 Experimental results
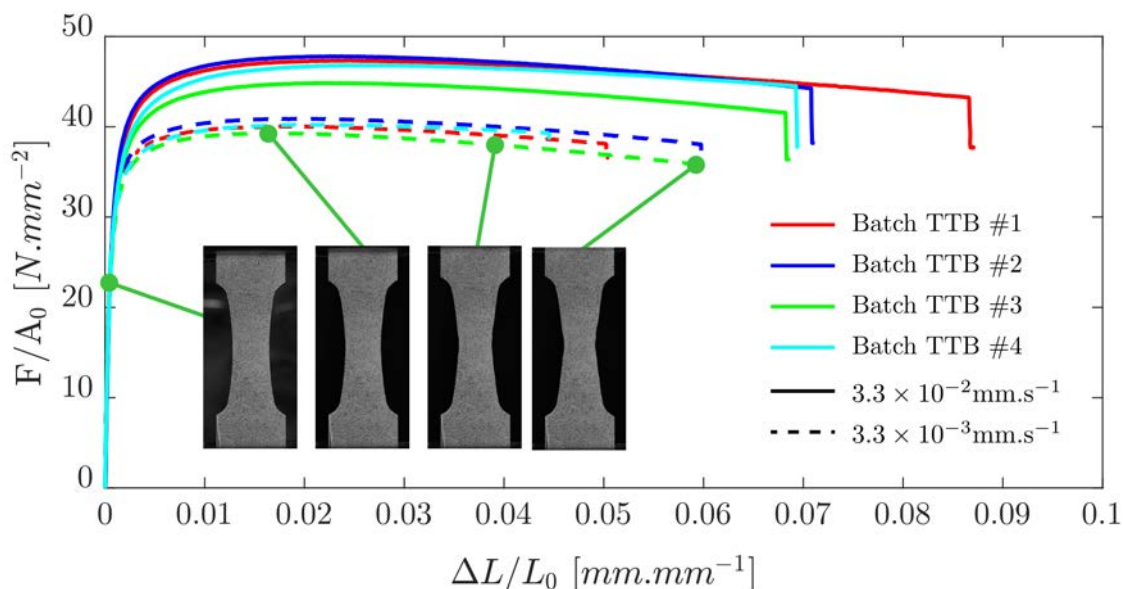
Figure 3.1: Tensile test data from the testing machine load cell and displacement sensor

The test campaign used to identify the reference law includes eight tensile tests. The tensile specimens were extracted from four material batches, as shown in Table 2.2. They were tested according to the testing conditions described in Chapter 2 Section 2.2.1. The tensile load and displacement were measured and synchronized with the camera. Raw results are drawn for each batch and each displacement rate tested in Figure 3.1.

In Figure 3.1, each colour designates a material batch. Each curve depicts the normalized load vs. normalized displacement history of a single specimen. First, the viscous effect is well visible as two groups of curves can be distinguished. They correspond to the two displacement rates tested (plain curve and dashed curve).

Material discrepancy is also observed within each group of curves. As a reminder, Table 3.1 presents the testing conditions of each tensile test.

Specimen ID	Batch TTB #	Displacement rate [mm.s^{-1}]	Testing temperature [°C]
TT/11	1	3.30 10^{-3}	20
TT/12	1	3.30 10^{-2}	20
TT/21	2	3.30 10^{-3}	20
TT/22	2	3.30 10^{-2}	20
TT/31	3	3.30 10^{-3}	20
TT/32	3	3.30 10^{-2}	20
TT/41	4	3.30 10^{-3}	20
TT/42	4	3.30 10^{-2}	20

Table 3.1: Summary of testing condition for all tensile test specimens

3.1.1 Effect of the microstructure on the strain fields

The in-plane displacement fields on the surface of the specimen were measured by 2D-DIC using the global FE DIC code Ufreckles (cf. [Réthoré 2018]) as detailed in Section D.1 of Appendix D.

The uncertainty analysis on the measured fields can be found in Appendix E. It shows that the displacement uncertainty is lower 1 μm, which is more than correct for this type of test.

The strain fields derived from the displacements present some localization issues. The scale of the strain heterogeneity coincides with the coarse microstructure of the material, as shown in Figure 3.2. An "orange skin" effect is observed on the surface of the specimen.

The macroscopic constitutive law chosen cannot take into account such micro-scale phenomena. A non-local approach was chosen to derive and to regularize the strain fields. The non-local approach is beneficial in the FEMU approach, as it regularizes the strain field singularities. It also improves the convergence of the FEMU algorithm. The regularization method used is detailed in Section D.3 of Appendix D. A comparison of the regularized strain with the non-regularized strain is presented in Figure 3.3. As shown, the non-regularized strain field presents strain hot spots localized on grain boundaries when the regularized field presents a smooth profile.

Moreover, the identified constitutive law is used in a strain range far from the ductile failure strain. The "orange skin" effect would therefore be negligible in all simulations and especially in pre-buckling phase.
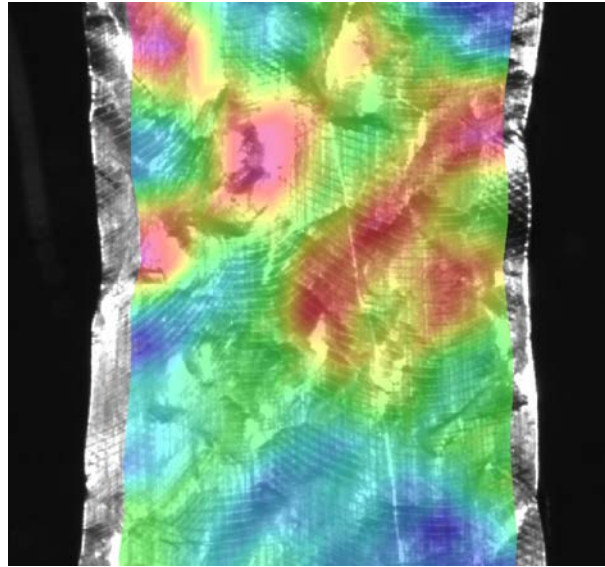
Figure 3.2: Comparison of the strain field with the material "orange skin" effect at the end of a tensile test
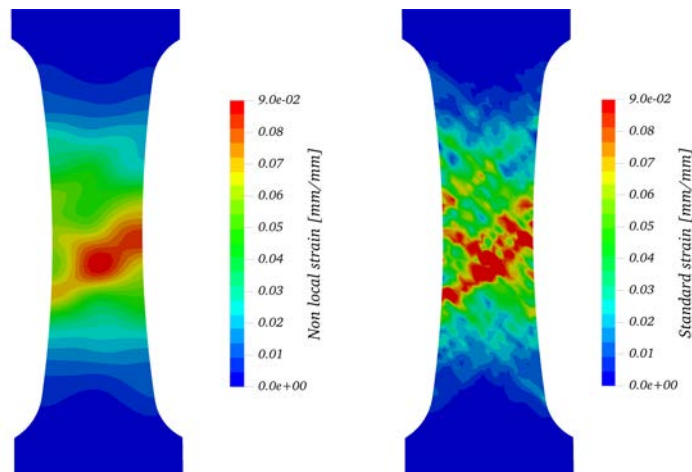
Figure 3.3: Equivalent strain field computed with a non-local approach (left) and a standard method (right). Specimen TT/32

3.1.2 Strain rate distribution on the specimen surface

Post processing the strain fields also allows to define the experimental strain rate experienced by the specimen as well as its spatial distribution. The experimental equivalent strain rate is defined as follows:

$$\dot{\varepsilon} = \frac{\sqrt{\frac{2}{3}\Delta\boldsymbol{\varepsilon} : \Delta\boldsymbol{\varepsilon}}}{\Delta t} \tag{3.1}$$

Figure 3.4 presents an example of the strain rate spatial distribution. It also

104

depicts the extraction areas used on all specimens to characterize the strain rate distribution along the axial direction of the specimen.
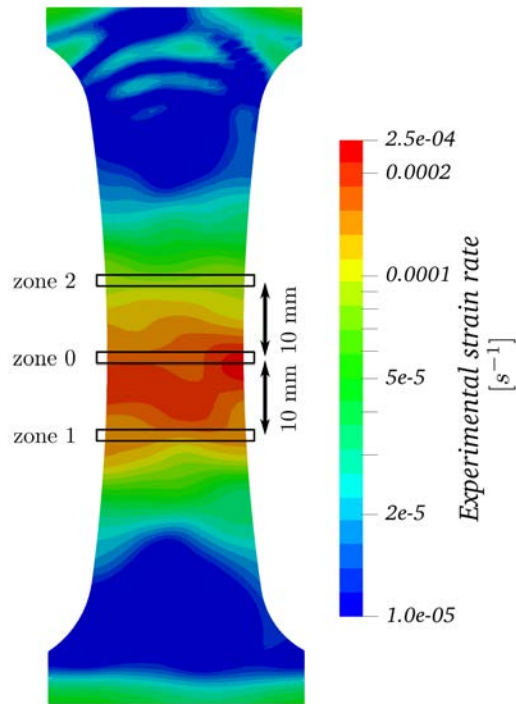
Figure 3.4: Spatial distribution of the experimental strain rate for specimen TT/21, at maximum load

Table 3.2 summarises the average strain rate in the areas mentioned in Figure 3.4. The strain rate is defined for all specimens at the maximum load.

A large strain rate range can be observed on all specimens, as shown in Figure 3.4 and Table 3.2. The strain rate value is divided by two for a point 10 mm away from the specimen center. This heterogeneous strain rate fields enriches each experiment in order to obtain a more robust identification process.

Specimen ID	Batch TTB #	Displacement rate [mm.s^{-1}]	$\dot{\varepsilon}$ zone 0 [s^{-1}]	$\dot{\varepsilon}$ zone 1 [s^{-1}]	$\dot{\varepsilon}$ zone 2 [s^{-1}]
TT/11	1	3.30 10^{-3}	1.17 10^{-4}	3.64 10^{-5}	3.21 10^{-5}
TT/12	1	3.30 10^{-2}	1.04 10^{-3}	8.24 10^{-4}	6.36 10^{-4}
TT/21	2	3.30 10^{-3}	9.83 10^{-5}	7.06 10^{-5}	1.00 10^{-4}
TT/22	2	3.30 10^{-2}	1.12 10^{-3}	6.97 10^{-4}	5.45 10^{-4}
TT/31	3	3.30 10^{-3}	1.53 10^{-4}	7.98 10^{-5}	7.50 10^{-5}
TT/32	3	3.30 10^{-2}	1.24 10^{-3}	8.19 10^{-4}	5.71 10^{-4}
TT/41	4	3.30 10^{-3}	1.06 10^{-4}	6.52 10^{-5}	5.51 10^{-5}
TT/42	4	3.30 10^{-2}	1.09 10^{-3}	1.10 10^{-3}	6.93 10^{-4}

Table 3.2: Summary of experimental strain rates at maximum load and at different locations for all tensile test specimens

3.2 FEMU Algorithm results

As a reminder the constitutive material law identified is defined as follows:

$$
\begin{aligned}
\boldsymbol{\sigma} &= \boldsymbol{\mathcal{C}}\, \boldsymbol{\varepsilon}_e, \\
\boldsymbol{\varepsilon} &= \boldsymbol{\varepsilon}_e + \boldsymbol{\varepsilon}_p, \\
\dot{p} &= \left(\frac{F}{K} \right)^n, \\
F &= \sigma_{eq} - R(p), \\
R(p) &= R_0 + \sum_{i=1}^{3} R_i \left(1 - e^{-b_i p} \right), \\
\sigma_{eq} &= \sqrt{\boldsymbol{\sigma} : \boldsymbol{H} : \boldsymbol{\sigma}},
\end{aligned}
\tag{3.2}
$$

with, $\boldsymbol{\sigma}$ the Cauchy stress tensor, $\boldsymbol{\varepsilon}$ the Biot strain tensor, $\boldsymbol{\varepsilon}_e$ the elastic strain tensor and $\boldsymbol{\varepsilon}_p$ the plastic strain tensor, $\boldsymbol{\mathcal{C}}$ the isotropic elastic linear operator, σ_{eq} the Hill equivalent stress defining the yield surface, $\boldsymbol{H}$ the Hill tensor (used here for transverse anisotropy), p the equivalent plastic strain, R the hardening variable and $\dot{p}$ the equivalent strain rate.

The material parameters to be identified are R_0, R_1, b_1, R_2, b_2, R_3, b_3, K, n, $\boldsymbol{H}$ defined by the Lankford ratio R_{lank} and $\boldsymbol{\mathcal{C}}$ defined by Young's modulus and Poisson's ratio.

As already mentioned the FEMU approach was selected because of the complexity of the constitutive law chosen and its large number of parameters. The experimental data generated through the tensile tests could not allow to define a unique set of material parameters. In particular, the number of parameters and the sensitivity of some parameters do not allow to define a unique solution. The sensitivity of each parameter and their relations with each others are detailed in

Appendix E.

From this sensitivity analysis, four groups of parameters can be defined, the hardening group containing the R_i coefficients, the b_i exponents and R_0, the creep group containing R_0, K and n, the geometrical group with R_{lank} and ν, and finally the elastic group with E and ν. The hardening group mainly affects the tangential hardening law. The creep law is defined through the creep group. The two other groups have a lower impact on the convergence of the algorithm.

The method was applied to the tensile tests identified as TT/__ in order to defined the reference law. A lighter process was applied to the buckling specimens BTC_/__ and O/00_ in order to only identify the yield stress. This point is discussed at the end of this chapter.

In this section the main results of the FEMU algorithm are presented, the quality of the results and the method to select the final material law are also discussed. The detailed results are presented in Appendix E.

3.2.1   From the Pareto front to the solution

A noticeable result from this analysis is the link between the creep law coefficients and the Pareto front obtained through the FEMU process.

As mentioned in Appendix D, a random multi-start strategy was followed. This strategy allows to build the Pareto front of the optimisation process. The Pareto front defines the set of optimal solutions minimizing the objective function. Usually the Pareto front is drawn with respect to the objective function components, i.e. $||\boldsymbol{R}_F||$, $||\boldsymbol{R}_{\varepsilon_{xx}}||$ and $||\boldsymbol{R}_{\varepsilon_{yy}}||$, respectively the residual load, the residual axial strain and the residual transverse strain. In this work, we observed that all the solutions converge to a pseudo Pareto front completely defined by the viscous parameters K and n, as shown in Figure 3.5.

As both viscous parameters are related, a 2D visualization of the Pareto front involving $||\boldsymbol{R}_F||$, $||\boldsymbol{R}_\varepsilon||$ and n can be plotted in Figure 3.6. The set of parameters selected on the Pareto front depends almost exclusively of the viscous parameters.

In Figures 3.5 and 3.6 each point depicts an increment of the algorithm.

In Figure 3.5, the colour of each point corresponds to its convergence state. If the point is blue the solution is not converged. If it is red, the algorithm has converged on this point. The different paths of convergence can be followed with the colour of each point (from blue to red). The Pareto front is visualized thanks to the concentration of red points in Figure 3.5.

In Figure 3.6, the colour of each point corresponds to the value of the creep exponent n.

Figures 3.5 and 3.6 show that the Pareto front is almost exclusively defined by the creep law parameters. The selection of the creep law parameters is equivalent to the selection of the solution. This is detailed in the next subsection.
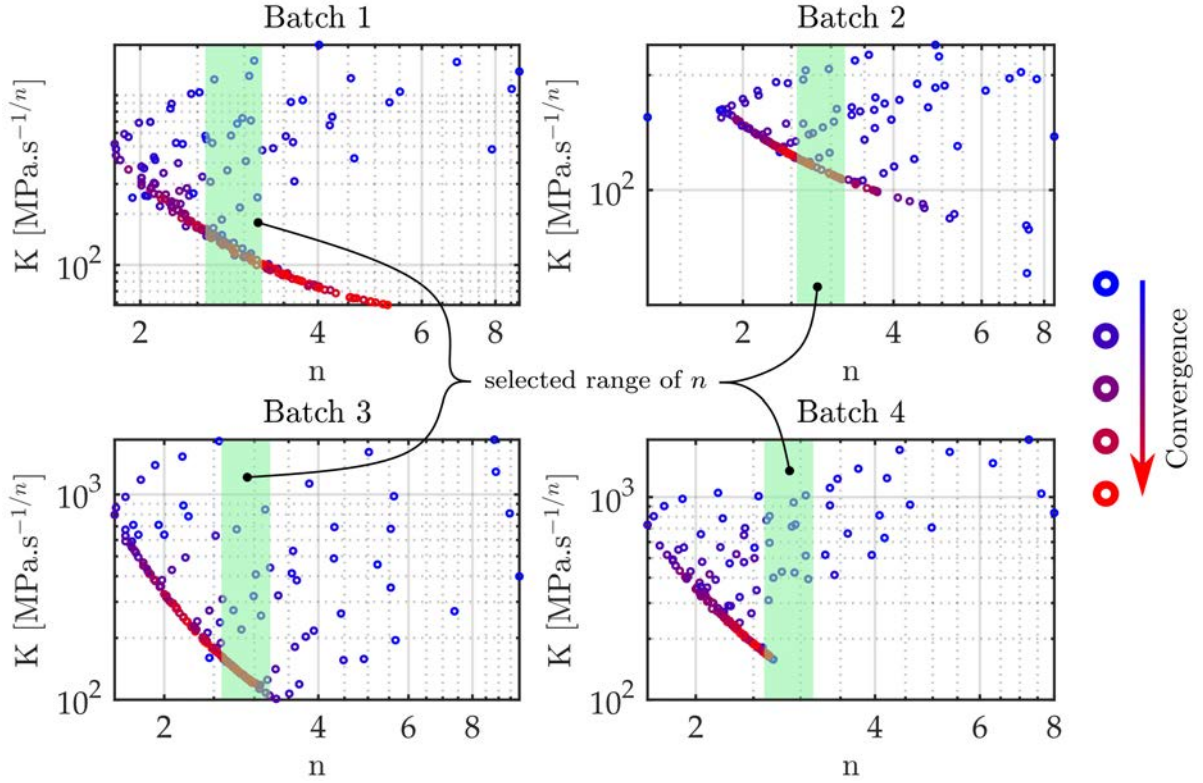
Figure 3.5: Pareto front in terms of viscous material parameters, all four batches

3.2.2 Selection of a solution

The strategy followed to select a set of material parameters on the Pareto front consists in selecting the set of parameters with the lowest residual and the smallest creep law discrepancy between all batches. Therefore the creep exponent n should respect the following constraint:

$$\forall i; n \in [n_{min}, n_{max}] = \left[\min_i \left(\max_j (n_{ij}^{conv}) \right), \max_i \left(\min_j (n_{ij}^{conv}) \right) \right], \qquad (3.3)$$

where i indicates the batch number, j the jth start of the algorithm for batch i. Finally subscript ^{conv} corresponds to all sets of parameters obtained after convergence of the algorithm.

This leads to:

$$\forall i, n \in [2.6, 3.2]. \qquad (3.4)$$

This range is depicted for each batch in Figure 3.5. Finally for each batch, the set with the smallest residual and $n \in [2.6, 3.2]$ is selected. All four sets of parameters are presented in Table 3.3.

First, all four batches have similar hardening, elastic and anisotropic parameters.
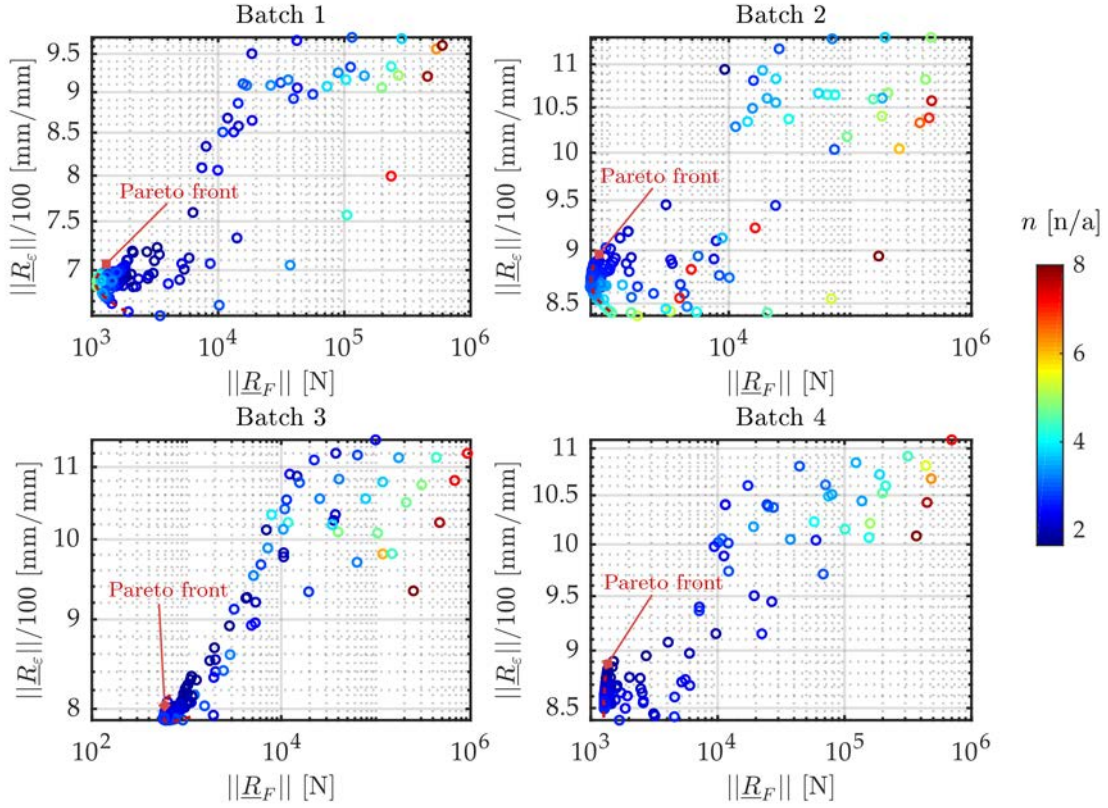
Figure 3.6: Pareto front, components of the residual vector with respect to the creep exponent

It shows that a unique convergence can be reached if the creep law is well defined. This also shows that the strain rate range is too small to define accurately the creep law, as there is a clear link between the parameters K and n in Table 3.3. Moreover, as the material behaviour includes a fully elastic domain, the following expression needs to be considered to compare the creep exponent n with literature data:

$$\frac{\partial \dot{p}}{\partial \sigma_{eq}} = \frac{n}{K} \left(\frac{\sigma_{eq} - R_0}{K} \right)^{n-1}. \tag{3.5}$$

Introducing the creep and yield parameters in Equation 3.5, we obtain a local creep exponent between 6.3 and 7.6. Those data can be compared advantageously with creep exponents presented in [Bai, Chen, and Gao 2009; Dompierre 2011], respectively 9 and 6.

The selected parameters are discussed in the next section through a detailed analysis of the simulation of each tensile experiment. Numerical load histories and strain fields are compared to the experimental data.

Parameters	TTB #1	TTB #2	TTB #3	TTB #4	Mean	Units
R_0	14.4	14.6	14.6	18	15.5	MPa
R_1	9.4	10.2	7.1	6.1	8.5	MPa
b_1	327.2	493.6	349.3	397.7	395.2	n/a
R_2	5.7	5.2	4.5	5.7	5.2	MPa
b_2	20.5	30.7	31.8	32.7	28.8	n/a
R_3	9.8	7.6	9.6	7.9	8.3	MPa
b_3	3064	2370	1916	1177	2134.2	n/a
K	100.6	167	122.2	167.1	133.8	$MPa.s^{1/n}$
n	3.2	2.7	3	2.6	2.9	n/a
R_{Lank}	1.82	2.05	1.59	1.68	1.18	n/a
E	41941	41318	41466	41326	41513	MPa
ν	0.36	0.35	0.36	0.33	0.35	n/a

Table 3.3: Summary of the constitutive law parameters identified from the tensile test campaign

3.3 FE results vs. Experimental results

The selected sets of parameters are then applied to their respective FE models with the adequate testing conditions. The strain fields from the FEA are compared to the experimental strain fields. The numerical tensile load is also compared to the experimental one. An example of this post processing is presented in Figure 3.7.
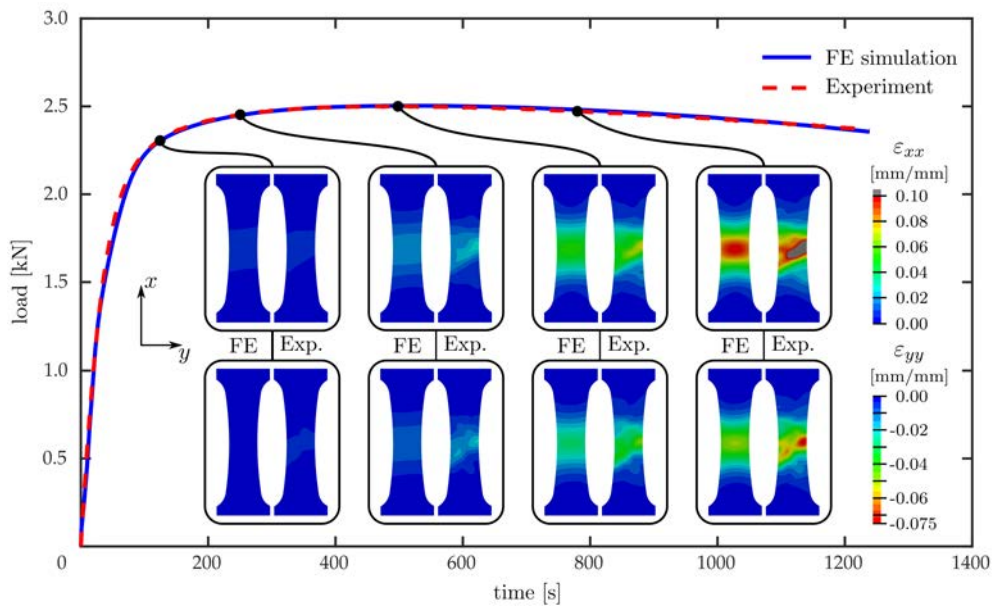
Figure 3.7: FE simulation vs. experiment TT/31

In Figure 3.7, the load history from the post identification FEA (in blue in Figure 3.7) fits well to the experimental load history (in red in Figure 3.7). A good agreement is observed between the numerical load curve and the experimental one, especially in the plastic region.

The strain fields obtained from the FE analysis are compared to the experimental strain fields for four time steps in Figure 3.7. For all four time steps, both numerical strain fields (ε_{xx} and ε_{yy}) are compared to the experimental ones. In Figure 3.7 the upper boxes depict the numerical and experimental ε_{xx} strain fields and lower ones the ε_{yy} strain fields.

The spatial distribution of the FE strain fields corresponds well to the experimental ones as shown in Figure 3.7. The plastic region as well as the strain amplitude extracted from the FEA on both components (ε_{xx} and ε_{yy}) are comparable to the experimental ones.

The difference observed is due to the localisation of the experimental strain on rare material defects due to cast induced porosities or grain boundaries. This can be observed in Figure 3.7 where strain hotspots can be observed on the edges of the specimen. This phenomenon does not correspond to a structural localization issue, even if it looks like it. Indeed, in Figure 3.7, the strain localization is visible even before reaching the maximum load.

The results of other specimens are similar to the ones presented for specimen TT/31. A good correlation of the strain fields and tensile load is observed between FEA and the whole set of experiments. It is detailed in Appendix E. Therefore the identified laws well model the mechanical behaviour of the SAC 305 alloy.

In the rest of this document, we refer to the material law identified as reference law. This reference law is defined according to a statistical analysis of all tensile tests as well as the manufacturing process parameters. The next section details how the reference material law is defined.

3.4   A constitutive law for the SAC 305

The buckling analysis is strongly dependant of the constitutive model used. In order to compare our buckling predictions to the different experiments performed, a reference constitutive model was defined. This reference law is defined with respect to the identified laws previously presented. As discrepancy was observed on the tensile test data as well as on the identified parameters, a statistical approach was followed in order to define a reference law. The reference law is defined through a mean reference law, and statistical descriptions of the hardening variable (excluding the yield stress) and the creep law.

3.4.1 Statistical analysis of the hardening law

As mentioned in Chapter 2, the cooling rate has a strong impact on the SAC 305 material properties. The cooling rate mainly impacts the yield stress as shown in [Kim, Huh, and Suganuma 2002], without modifying neither the hardening nor the viscous behaviour. As the cooling rate is difficult to control or measure, the yield stress $\overline{R}_0^{G_i}$ is identified for each group of batches. A group of batches contains several batches cast at the same time or under the same conditions (cf. Table 2.2). During this thesis, five groups of batches were cast. Every stress data mentioned thereafter are defined as follows:

$$\hat{\sigma} = \sigma - \overline{R}_0^{G_i}. \tag{3.6}$$

where $\overline{R}_0^{G_i}$ is the mean yield stress of a batches group i.
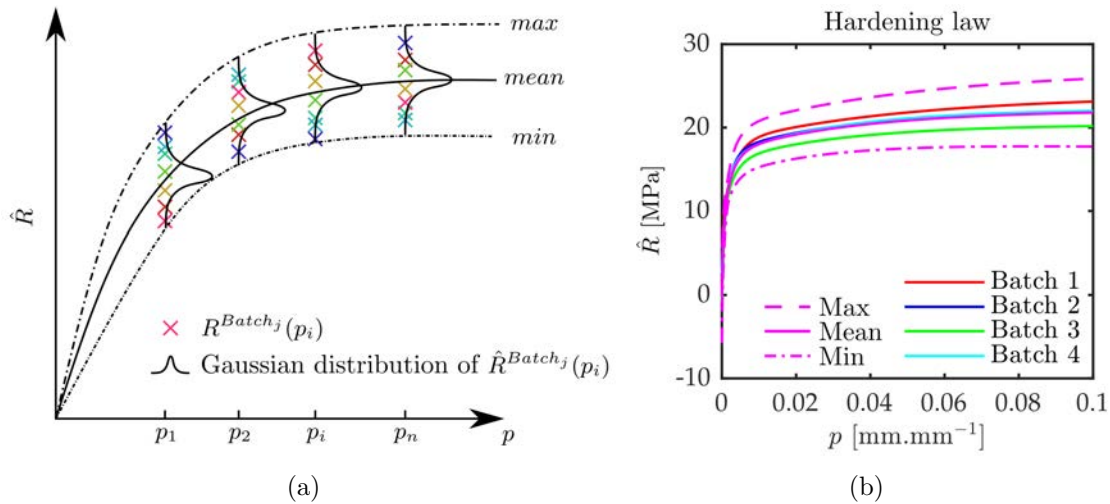
Figure 3.8: (a) Strategy to derive the reference hardening law (b) Envelope at 95% probability with 90% of confidence of the hardening variable and the different identified laws.

This statement excludes the mean yield stress parameters from the statistical analysis, but not its discrepancy. As shown in the sensitivity analysis (cf. Appendix E, the Young modulus E is not well identified, therefore its mean value is used. Equally, only the average values of ν and R_{lank} are considered as their identification is not accurate enough. These last parameters have a negligible impact on the buckling behaviour compared to the hardening variables in particular.

First the reference hardening law is defined. The hardening variable $\hat{R}$ is computed for a defined set of equivalent plastic strains p_i and for all material batches. The hardening variable $\hat{R}$ is defined by:

$$\hat{R}^{Batch_j}(p_i) = (R_0^{Batch} - R_0^G) + \sum_{k=1}^{3} R_k^{Batch_j}(1 - e^{-b_k^{Batch_j} p_i}). \tag{3.7}$$

Each batch includes two test specimens, therefore eight specimens are considered. A Gaussian distribution of the hardening variable $\hat{R}$ is defined for each equivalent plastic strain selected with respect to the batch number, as shown in Figure 3.8(a). The normality of the distribution is also tested. The parameters of the distribution are defined with 90% confidence. The upper and lower bounds of the stress distribution are defined at 95% probability. This method gives an envelope of the hardening variable as shown in Figures 3.8(a) and 3.8(b).

Figure 3.8(b) shows the identified laws, the average law and the maximum and minimum envelope boundaries with 95% probability and 90% confidence. It can be observed that the hardening laws are more or less parallel with each other's. One can see that the tangential law are extremely similar for all batches. The discrepancy on the tangential law is neglected here.

Both limits well envelope all batches. The 95/90 approach is conservative, but it well describes the discrepancy observed. A reduced domain of the Gaussian curve can be used for the buckling predictions.

3.4.2 Statistical analysis of the creep law

The same method as for the hardening law is used for the equivalent creep stress, as shown in Figures 3.9(a) and 3.9(b).

(a)   (b)
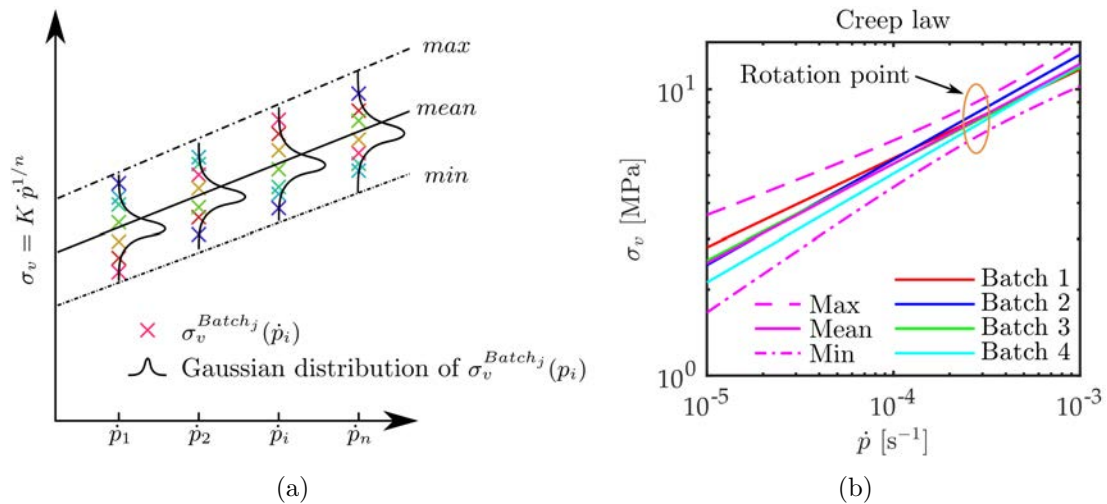
Figure 3.9: (a) Strategy to derive the reference creep law, (b) Envelope at 95% probability with 90% of confidence of the creep equivalent stress and the different identified laws

A different behaviour is observed on the creep laws. The envelope defined contains a rotation point as shown in Figure 3.9(b). The different creep laws rotate around this point. At this specific point the equivalent creep stress discrepancy can be observed and defined.

The rotation angle range is defined through the Norton exponent n discrepancy, while the equivalent creep stress discrepancy is defined through the discrepancy of $K\dot{p}_r^{1/n}$ for a fixed value of n at the rotation point. The rotation point is defined by the equivalent plastic strain rate $\dot{p}_r$. The rotation point is defined for $\dot{p}_r = 2.3\,10^{-4}\ \mathrm{s}^{-1}$ as shown in Figure 3.9(b).

The equivalent creep stress σ_v at $\dot{p}_r$ can be statistically analysed using the following relation:

$$\sigma_v = K_i \dot{p}_r^{1/n_i} = \hat{K}_i \dot{p}_r^{1/\overline{n}}, \tag{3.8}$$

with n_i and K_i respectively the Norton exponent and coefficient of batch i, $\overline{n}$ the average Norton exponent and $\hat{K}_i$ the Norton equivalent coefficient for $\overline{n}$.

This rotation issue is mostly due to numerical issues in the identification process. This was previously discussed and shown in Figure 3.5.

The creep coefficient K of the reference law is linked to n and $\hat{K}$ by the following expression:

$$K \cdot \dot{p}_r^{1/n} = \hat{K} \cdot \dot{p}_r^{1/\overline{n}}. \tag{3.9}$$

Figure 3.9(b) shows the identified creep laws, the average creep law and the maximum and minimum envelope boundaries with 95% probability and 90% confidence. Both limits well envelope all batches. As for the hardening variable, the 95/90 approach is conservative and a reduced domain of the Gaussian curve can be used for the buckling predictions.

3.4.3 A statistical reference law

Based on both statistical analyses, a set of constitutive laws can then be randomly defined and used for the numerical buckling analysis of shells. The buckling results obtained would then need to be analysed statistically as well.

Using a set of statistical parameters (α_i with i from 1 to 3), a set of material parameters can be defined with their associated probabilities. The statistical parameters α_1, α_2 and α_3 are respectively used to define the hardening law, the Norton n exponent and the Norton equivalent coefficient $\hat{K}$.

Table 3.4 presents the results of the statistical analysis of the hardening law and the creep parameters. As an example Figures 3.10(a) and 3.10(b) present a set of ten randomly defined material laws as well as the 95/90 envelope and the average law.

The Voce parameters can then be defined for each randomly generated law in order to fit $\hat{R}$ with respect to p. The statistical description and the mean reference curve are used for every numerical analysis.
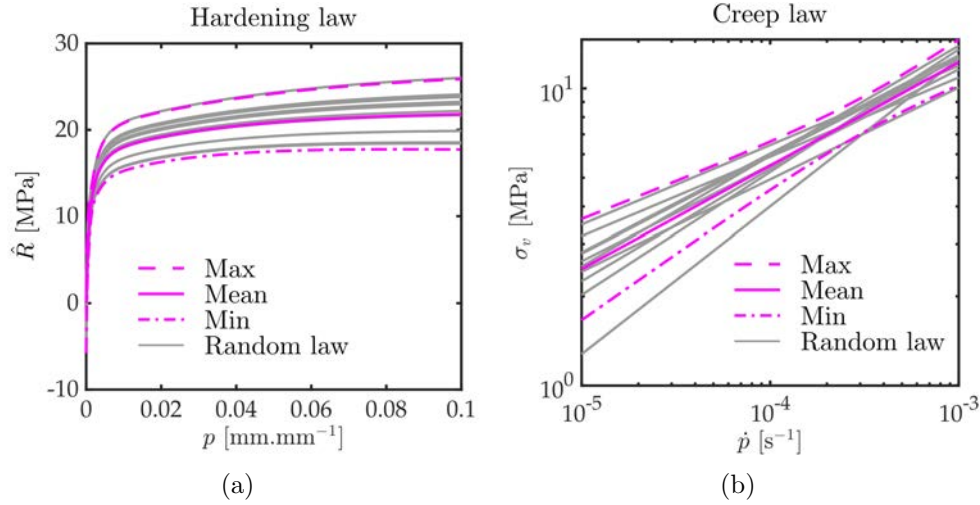
Figure 3.10: (a) Envelope at 95% probability with 90% of confidence of the hardening variable and random hardening laws, (b) Envelope at 95% probability with 90% of confidence of the creep equivalent stress and random creep laws

Parameters	Mean	StD	$\text{Max}_{95/90}$	$\text{Min}_{95/90}$	Units
$\hat{R}(0.005)$	16.4	0.7	18.9	13.9	MPa
$\hat{R}(0.010)$	18.0	0.7	20.8	15.3	MPa
$\hat{R}(0.020)$	19.2	0.8	22.1	16.3	MPa
$\hat{R}(0.050)$	20.9	0.9	24.2	17.5	MPa
$\hat{R}(0.100)$	21.8	1.1	25.9	17.7	MPa
n	2.9	0.2	3.9	2.1	n/a
$\hat{K}$	133.8	5.3	154.4	115.8	$\text{MPa.s}^{1/n}$
E	41513	n/a	n/a	n/a	MPa
R_{Lank}	1.8	n/a	n/a	n/a	n/a
ν	0.35	n/a	n/a	n/a	n/a

Table 3.4: Summary of the statistical study of the reference law from the tensile test campaign

The probability range used for the buckling predictions is mentioned when different from the 95/90 approach.

The parameters of the mean constitutive law are summarized in Table 3.5. The mean reference law is preferred in all numerical analysis.

Parameters	Mean	Units
R_0	15.5	MPa
R_1	8.5	MPa
b_1	395.2	n/a
R_2	5.2	MPa
b_2	28.8	n/a
R_3	8.3	MPa
b_3	2134.2	n/a
K	133.8	MPa.s$^{1/n}$
n	2.9	n/a
R_{Lank}	1.18	n/a
E	41513	MPa
ν	0.35	n/a

Table 3.5: Parameters of the mean reference law

3.4.4 Effect of the temperature

The model presented does not take into account the effect of the temperature on the mechanical properties. This choice is justified, as the yield stress is identified for each specimen. Moreover all experiments in this work are performed under isothermal conditions.

The identification of the yield stress for all specimens integrates the possible effect of the cooling rate on the strength of the material (discussed in the next paragraph), as well as the offset of the Norton creep law due to the difference of temperature between the tensile test and the other experiments.

As shown in Chapter 2, the effective viscous yield stress R_0^v can be defined as follows:

$$
\begin{aligned}
R_0^v &= R_0 + K\dot{p}^{1/n}, \\
K &= K^\star \left[\exp\left(\frac{Q}{R \cdot T} \right) \right]^{1/n},
\end{aligned}
\tag{3.10}
$$

with Q the activation energy of the SAC 305, R the universal gas constant and T the temperature of the alloy in Kelvin.

When the temperature is different between two tests, the effect of the temperature can be integrated to the yield stress offset, as shown in Figure 3.11.

Nevertheless the testing temperature was measured and is given for all experiments in the next chapters.

116
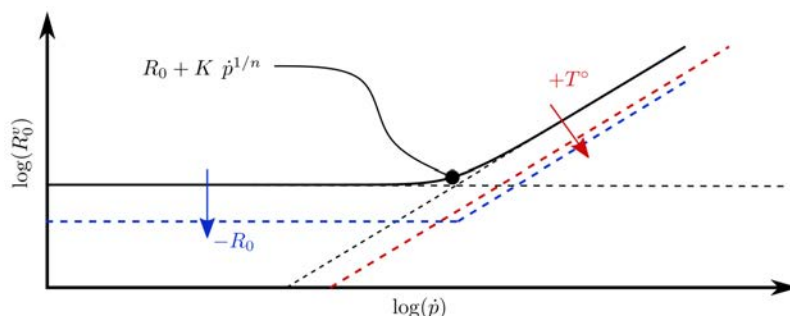
Figure 3.11: Effect of the temperature $T°$ and the yield stress R_0 on the effective viscous yield stress R_0^v

3.4.5 Effect of the cooling rate

The only element affecting the material law is the cooling rate during the water quench (cf. [Kim, Huh, and Suganuma 2002]). Neither the hardening nor the creep law are affected by the cooling rate. Only the yield stress is modified. For each group of batches the yield stress needs to be assessed numerically in the pre-buckling phase. Table 3.6 summarizes the yield stress for each group of batches.

Group ID	$\overline{R}_0$	$\Delta\overline{R}_0$	Unit	Quench Temp.	Specimens
G1	15.4	0.0	MPa	20°C	TT/.. (Tensile testing)
G2	14.0	-1.4	MPa	22°C	BTC1/.. (Plate buckling)
G3	9.9	-5.5	MPa	28°C	BTC2/.. (Plate buckling)
G4	n/a	n/a	MPa	20°C	O/001 (Thick shell buckling - pre-test)
G5	10.2	-5.2	MPa	40°C	O/002 to O/006 (Thick shell buckling)

Table 3.6: Summary of yield stress for the different groups of material batch

Some differences can be observed in the yield stress between all groups. This is explained by either the mould used (aluminium mould and hot quench water for G4 and G5) or the quench temperature for G3, G2 and G1.

3.5 Conclusion

This chapter presented the different elements allowing to define a constitutive law for the SAC 305 alloy. This law is strongly related to the manufacturing process detailed in Chapter 2. In this chapter, the tensile test results and the results from the FEMU algorithm were presented. The identified laws were compared to the experiments and a good correlation was observed. Despite the care taken in the manufacturing of the specimen, the discrepancy of the tensile test results cannot

117

be neglected. Finally a reference material law including a statistical description of the parameters as well as the effect of the manufacturing process was detailed. The constitutive model is then used as a baseline for every FE analysis or buckling analysis. The mean material is preferred for all numerical analysis unless mentioned otherwise.

Chapter 4

Validation of the buckling prediction method for thick plates subjected to in-plane compressive loadings

The experimental and numerical methods to study the buckling of thick shells are evaluated in this Chapter. Buckling experiments as well as numerical analysis are performed on simple shell structures defined by plates. In this chapter the buckling prediction method is evaluated for proportional loadings and thick shells.

Contents

In this chapter, the numerical method to predict buckling of thick plates is evaluated against the experimental results. In a first section the experimental results are analysed in order to identify the boundary conditions, the loading and the geometrical imperfections. An experimental buckling detection criterion is also defined. It is applied to the experiments to define the experimental critical values. Finally the experiments are analysed and the buckling prediction method is evaluated against the experiments with respect to two parameters, the plate geometry and the strain rate.

4.1   Experimental results

All buckling tests were performed in two test campaigns following the testing conditions listed in Tables 2.3 and 2.2. In a first test campaign (BTC #1), we were interested in the effect of plate geometry on its buckling behaviour, while in a second one (BTC #2), the effect of strain rate was investigated. To ease data comparison between all test campaigns, the load data is normalized according to the following expression in the rest of this chapter, as already mentioned in Chapter 3.

$$\overline{\sigma} = \frac{F}{A_0} - \overline{R}_0^{BTC\,\#i}, \tag{4.1}$$

with F the experimental load, A_0 the initial specimen area and $\overline{R}_0^{BTC\,\#i}$ the mean yield strength corresponding to the buckling test campaign #i.

All plate buckling experiments were performed according to the experimental procedure detailed in Section 2.4.1 of Chapter 2. For all plate buckling experiments the load history and the pictures from the three cameras are acquired. The pictures are post processed according to the procedure detailed in Section 2.5 of Chapter 2.

An example of testing results is presented in Figure 4.1. The plate deflection is plotted for various times and loads during testing. The coloured plots correspond to the out of plane displacement field. Despite the explicit 3D illustrations of the plate deformed shapes presented in Figure 4.1, a 2D cut of the plate deformed configuration is more convenient to describe the buckling modes. An example of 2D cuts of the plate at the center lines are presented in Figure 4.2.

The center lines are defined as the axial $(y = b/2)$ and the transverse $(x = 0)$ center lines respectively defined by c_1 and c_2 labels in Figure 4.2. The center lines deflection graphs (Figure 4.2b and Figure 4.2c) allow us to identify two geometric properties of the buckling modes. In the $\boldsymbol{x}$ direction, an Euler beam type mode can be observed, while in the $\boldsymbol{y}$ direction a "U shape" type mode is observed.

4.1.1   Boundary conditions and associated imperfections

As classically known, the buckling behaviour of a structure depends on its boundary conditions. Therefore, before any discussion or analysis, the boundary conditions
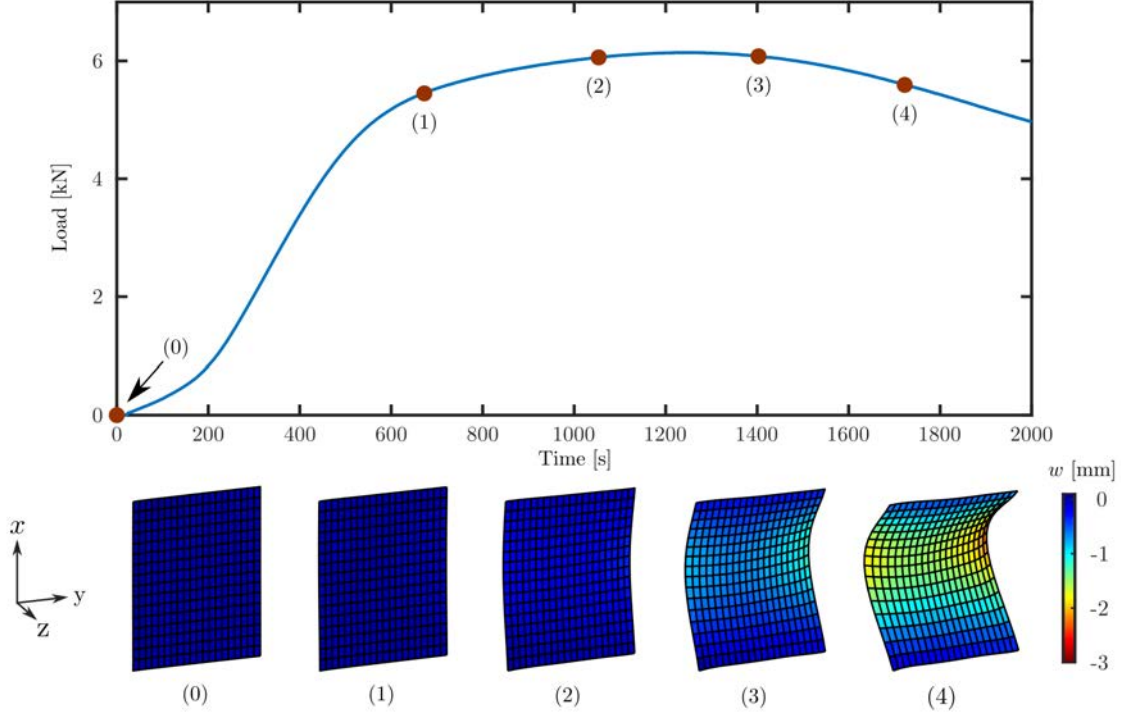
Figure 4.1: Experimental plate deflection evolution during buckling experiment (BT1/01)

need to be studied. Using the DIC post-processing procedure, the displacement fields close to the grips can be analysed. Figure 4.3 presents the positions of the two lines used to characterize the boundary conditions of the plate buckling specimen.

An example of post processed displacement fields on the DIC mesh boundaries is presented in Figures 4.4(a) and 4.4(b). The evolutions in time of the displacement and rotation fields presented in Figure 4.4(a) and Figure 4.4(b) are defined by:

$$
\begin{aligned}
\Delta U_x &= U_x^{up} - U_x^{low}, \\
\overline{U}_y &= \left(U_y^{up} + U_y^{low} \right)/2, \\
\Delta U_z &= U_z^{up} - U_z^{low}, \\
\hat{\phi}_y &= \left(\phi_y^{up} - \phi_y^{low} \right)/2, \\
\overline{\phi}_x &= \left(\phi_x^{up} + \phi_x^{low} \right)/2,
\end{aligned}
\tag{4.2}
$$

with the subscript ^{up} corresponding to the upper grip and ^{low} to the lower one. The rotation fields ϕ_x and ϕ_y are computed using the Kirchhoff-Love plate kinematic.

As shown in Figures 4.4(a) and 4.4(b), the boundary conditions present some imperfections. The spatial distribution of ΔU_x is not symmetric. The axial displacement (U_x) increases faster on one side of the plate than on the other side. The

122
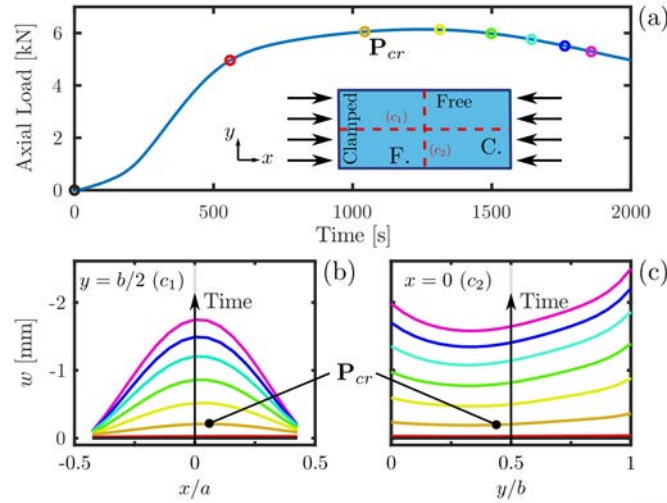
Figure 4.2: Evolution in time of the experimental out of plane displacement field on both center lines $x = 0$ and $y = b/2$ of the plate (Specimen BT1/01: plate dimensions $a = b = 40$mm and $h = 4$mm)
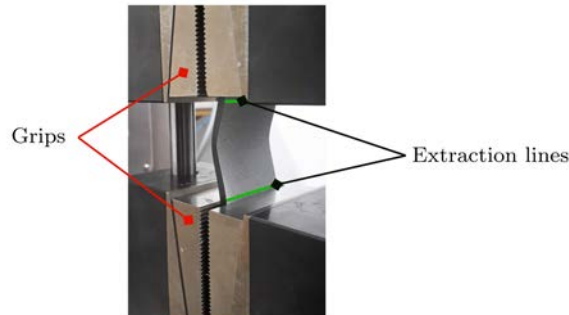
Figure 4.3: Positions of the extraction lines used to characterize the boundary conditions.

same behaviour is observed for ΔU_z. Moreover ΔU_z is not equal to 0. A plate misalignment appears from the beginning of the experiments despite the guiding system used.

The averaged rotation field, $\hat{\bar{\phi}}_y$, increases from the beginning of the experiment. Its value is constant with respect to the plate width, except at the end of the experiment (mostly due to the buckling mode). $\overline{\phi}_x$ is almost constant with respect to time, except at the end of the experiment (mostly due to the buckling mode)

These observations made on the boundary conditions of specimen BT1/01 were also observed on the other specimens.

Each source of imperfection has a different impact on the buckling behaviour

(a) (b)
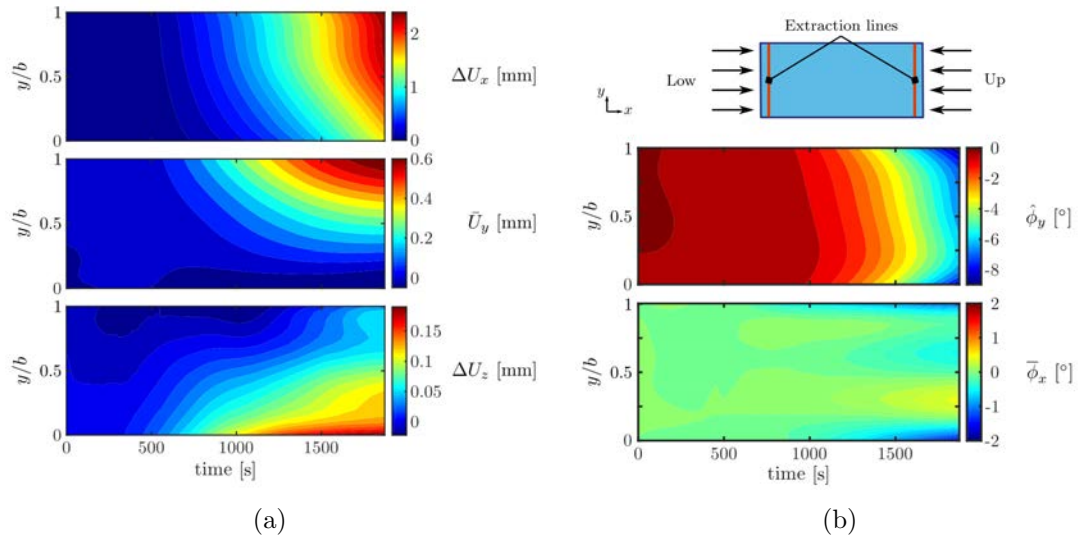
Figure 4.4: (a) Displacement fields characterizing the loading conditions of plate BT1/01. From top to bottom: ΔU_x, $\overline{U}_y$ and ΔU_z; (b) Rotation fields characterizing the loading conditions of plate BT1/01. From top to bottom: $\hat{\phi}_y$ and $\overline{\phi}_x$

and its initiation. Two types of imperfection can be identified from the previous observations: the plate misalignment (from ΔU_z) and the plate bending (from $\hat{\phi}_y$). Those two types of imperfection affect differently the buckling behaviour of the plate.

Using an analogy with the buckling of a clamped beam axially compressed, the misalignment imperfection may be rather related to the second mode and its bending to the first mode as shown in Figure 4.5.
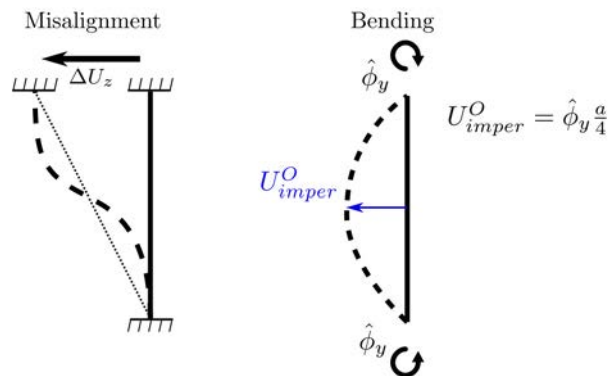
Figure 4.5: Effect of imperfection on buckling (clamped beam of length a)

The deformed shape due to the imperfection on $\hat{\phi}_y$ is closer to the experimental buckled shape than the deformed shape due to the misalignment ΔU_z. Therefore,

124

the buckling of the tested plates seems to be mostly due to the imperfection on $\hat{\phi}_y$.

The bending quantity $\hat{\phi}_y$ is used later to define a buckling initiation criterion.

4.1.2 Experimental buckling initiation criterion

For plates subjected to compressive load, the tangential singularity at the bifurcation point is not always satisfied. This property is often demonstrated in the literature (cf. [Hutchinson and Budiansky 1976] and [Wang, Xiang, and Chakrabarty 2001]) by comparing the *Mises* flow theory with *Hencky*'s deformation theory (DT) in the buckling prediction. The collapsing load is therefore not sufficient to estimate accurately the critical variables.

4.1.2.1 Post buckling analysis of thick plates

The tangential bifurcation is illustrated here with a FE post bifurcation analysis. This analysis is focused on the effect of the loading imperfection on the collapse of the plate. A rectangular plate with an aspect ratio of 1.33 and a thickness ratio of 10 is considered here. The plate is subjected to a uni-axial compressive load at constant strain rate. The bending degrees of freedom of the plate (w, ϕ_x, ϕ_y) are constrained at both ends.

A pure bending imperfection is introduced through the rotation ϕ_y at both ends of the plate. The rotation field ϕ_y at each end of the plate is linear with respect to the time. Its value is defined in order to obtain a plate deflection equal to a percentage of the plate thickness at t_f (end of the simulation). It is defined by:

$$\phi_y = \left(R_\% \cdot h \frac{4}{a} \right) \frac{t}{t_f}, \qquad (4.3)$$

where $R_\%$ is the imperfection amplitude, h the plate thickness, t the time, and t_f the total time.

Several imperfection amplitudes are tested numerically. The bifurcated solutions (coloured curves in Figure 4.6a) correspond to a different imperfection amplitude. They are compared to the perfect solution (black curve in Figure 4.6a).

First, we see that the collapsing load (i.e. the maximum load) is very dependent on the imperfection amplitude. It does not converge to a unique value when the imperfection amplitude tends to 0.

Moreover, the evolution of the plate out of plane displacement at the center (w^O) is analysed. w^O is normalized by the plate deflection due to the loading imperfection at collapse (U^O_{imper}). Its evolution, with respect to the axial strain, is plotted in Figure 4.6b for each imperfection amplitude. The equilibrium points corresponding to $w^O = U^O_{imper}$ are identified by crosses in Figure 4.6. U^O_{imper} is defined at plate collapse by:

$$U^O_{imper} = (R_\% \cdot h) \frac{t_{collapse}}{t_f}. \qquad (4.4)$$
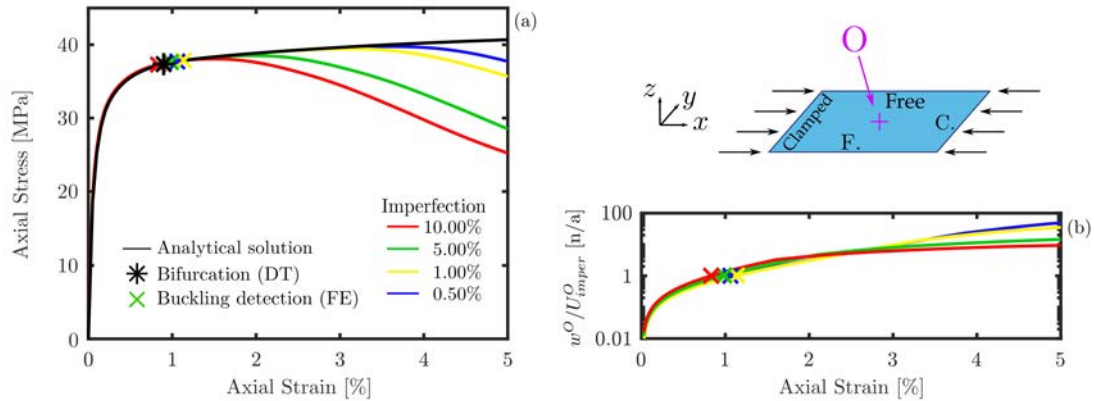
Figure 4.6: Buckling analysis of a square plate for various loading imperfection amplitudes, comparison of post buckling solutions (FE) and the perfect solution (analytical model); detection of buckling initiation depicted by crosses. (a) axial stress vs. axial strain, (b) imperfection ratio vs. axial strain.

The identified equilibriums are compared to the bifurcation point computed with the analytical model (black star in Figure 4.6a). The equilibrium points defined by $w^O = U^O_{imper}$ are close to the bifurcation point for all imperfection amplitudes tested. This condition allows to estimate accurately the equilibrium corresponding to the buckling initiation.

The doubling of the imperfection (i.e. $w^O = U^O_{imper}$) seems to be efficient to detect the buckling initiation of thick elasto-visco-plastic plates. It is also used to assess the experimental critical values.

4.1.2.2 Application to the experimental detection of buckling

The criterion corresponding to the doubling of the imperfection ($w^O = U^O_{imper}$) is used to detect the buckling initiation on experiments.

For the experiments, the imperfection at the center of the plate (U^O_{imper}) is linked to the imperfection on $\hat{\phi}_y$ by simple pure bending beam equations (as shown in Figure 4.5). The experimental bending imperfection is evaluated at collapse of the plate (i.e. at the maximum load).

The discrepancy of the buckling detection is evaluated through the statistical analysis of ϕ_y in $\boldsymbol{y}$ direction at both ends of the plate.

This method is used to assess the buckling initiation as well as its discrepancy. As observed numerically, buckling initiates before collapse of the plate, as shown in Figure 4.2 with the label P_{cr}.

4.1.2.3 Experimental critical stresses and strains

Table 4.1 presents the critical values for each specimen defined with the previously defined criterion.

$\overline{\sigma}_{crit}$ is the mean critical stress and ε_{crit} the mean critical strain. Std_{---} corresponds to the standard deviation of each value described previously. As a first observation, the discrepancy on stress data is limited while the discrepancy on the critical displacement and strain is in the same order of magnitude as the DIC process accuracy (0.02 mm). The experimental critical values are discussed in the next subsections.

Specimen	$\overline{U}_{imper}^{O}$	$\overline{\sigma}_{crit}$	$\overline{\varepsilon}_{crit}$	$StD_{U_{imper}^{O}}$	$StD_{\sigma_{crit}}$	$StD_{\varepsilon_{crit}}$	Temperature
	mm	MPa	%	μm	MPa	%	°C
BT1/01	0.24	22.3	1.67	0.04	0.2	0.17	20
BT1/02	0.12	22.1	0.83	0.02	0.1	0.04	20
BT1/11	0.08	20.5	0.95	0.02	0.1	0.07	20
BT1/12	0.10	20.5	1.05	0.01	0.1	0.03	20
BT1/21	0.21	21.6	1.58	0.05	0.2	0.15	20
BT1/22	0.07	16.4	0.53	0.01	0.1	0.02	20
BT2/31	0.15	26.6	1.12	0.03	0.1	0.04	20
BT2/32	0.08	19.7	0.69	0.02	0.2	0.06	20
BT2/41	0.17	24.6	0.80	0.01	0.1	0.03	20
BT2/42	0.10	19.5	1.10	0.01	0.1	0.02	20

Table 4.1: Summary of the experimental buckling initiation criterion and critical values

4.2 Effect of the plate geometry on its buckling behaviour

The effect of the plate geometry on the buckling behaviour is investigated in this subsection. Our discussion will be supported by experimental results from BTC #1 as well as numerical analysis. The plate geometry is defined by its aspect ratio a/b and its thickness ratio b/h. The strain rate is identical for all specimens tested in BTC #1.

4.2.1 FE simulations of the experiments

All experiments were simulated by FEA, with the experimental conditions as an input, as detailed in Section 2.5 of Chapter 2. The introduction of imperfect experimental conditions in the FE model leads to the collapse of the plate. The

load history and the deformed shape extracted from the FE model are compared to the experiments, as presented in Figure 4.7. In Figure 4.7, the red plain curve and black dashed curves correspond respectively to the FE and the experimental load histories. The box plots added to the FE load history curve illustrate the effect of the material discrepancy (cf. Table 3.4) on the numerical load history. The iso-value field plotted in background represents the evolution with respect to time of the out of plane displacement deviation between the FE model and the experiment. The out of plane displacement field is only extracted on the axial center line ($y = b/2$).
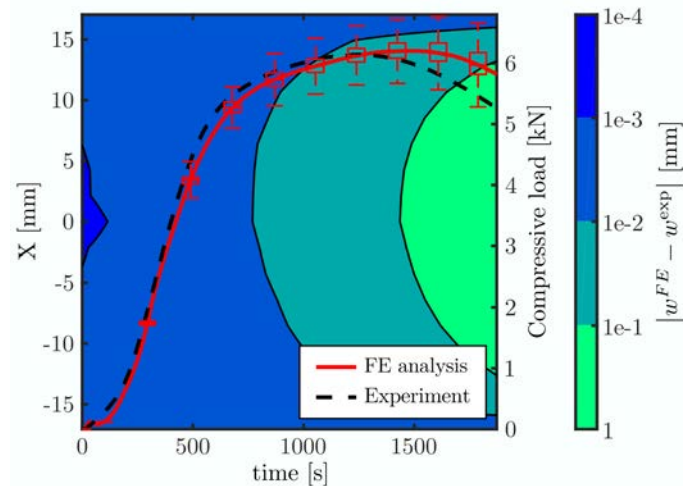
Figure 4.7: FEA vs. experiment for BT1/01 specimen, Evolution of compressive load and chronograph of the out of plane displacement deviation on the middle line ($y = b/2$) according to time and axial coordinate x

The FEA correlates well with the experiments on both load and out of plane displacement histories, as shown in Figure 4.7. Both quantities (load and out of plane displacement) start diverging close to the experimental plate collapse. Even if the post buckling evolution can be slightly different, the pre-buckling and the buckling initiation are identical between the FE model and the experiments.

The same behaviour is observed with other specimens from BTC #1. The FE and experimental load histories are presented in Figure 4.8.

The FE simulations of the experiments tend to validate the relevancy of the identified constitutive law. The reference law reproduces well the structural instability. The experimental buckling behaviour of thick plates and the buckling predictions are discussed in details in the next subsections.

4.2.2 Comparison of the predicted and experimentally observed critical values

As a reminder the predicted critical values were defined using *Bodner*'s hypothesis coupled with a tangent law derived with *Hencky*'s deformation theory.

Figure 4.8: FEA and experimental normalized load according to normalized displacement, for all specimens from BTC #1 (plain curves: FE simulations and dashed curves: experimental data)

Moreover, 30 randomly generated constitutive laws were used to model the material discrepancy. The random constitutive laws were generated with respect to the statistical description of the reference law (cf. Table 3.4).

The critical stress is normalized in order to better visualize the material discrepancy. This normalisation includes the section dimensions h and b as well as the plate bending rigidity $D = Eh^3/[12(1 - \nu^2)]$.

The experimental normalized critical stresses as well as the critical strains are compared to the analytical predictions in Figure 4.9. The buckling predictions and the critical test data are plotted with respect to the geometrical properties of the plates in Figure 4.9.

The experimental and predicted normalized critical stresses are presented on the left plots in Figure 4.9, while right plots present the experimental and predicted critical strains. The plain lines correspond to the analytical predictions of the effective normalized critical stress and strain with respect to the aspect ratio a/b. These predictions are defined with the mean reference law. The dashed curves correspond to the prediction of the minimum and maximum critical stress and strain at 95% probability with 90% confidence. The shaded surfaces correspond to the second and third quartiles of the predicted critical stress and strain. The experimental critical values are depicted by box plots, including discrepancy in the buckling detection (defined in Table 4.1).

First, while a limited discrepancy is observed on the experimental critical

129
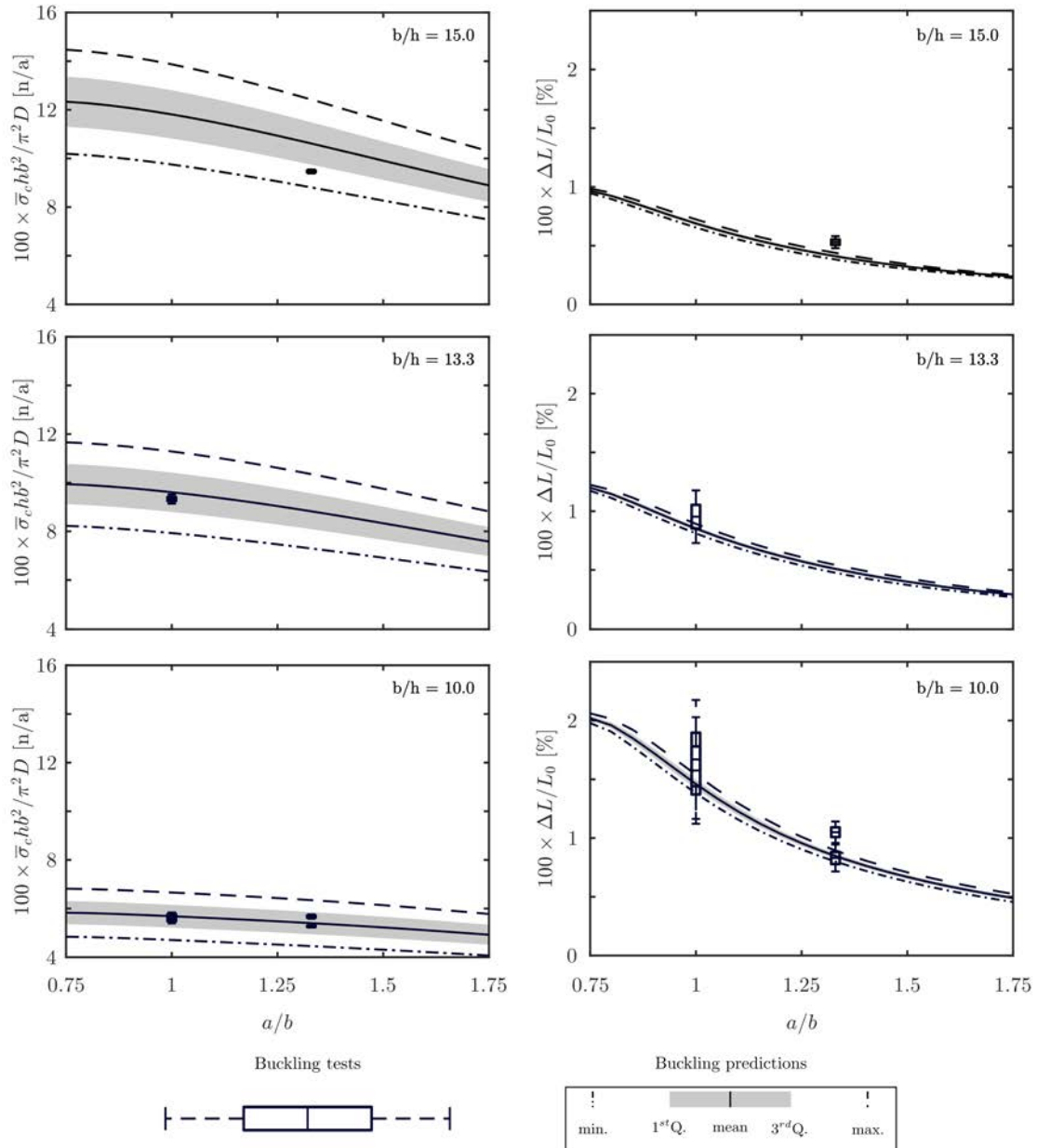
Figure 4.9: Analytical buckling predictions vs. experimental effective normalized critical stress (left) and critical strain (right), plotted according to the plate aspect ratio and for each plate thickness ratio

stresses, a large discrepancy is observed on the predicted critical stress. The exact contrary is observed for strain data.

For $b/h = 15$, the thinnest plate, the critical stress is out of the second and third quartile range, but within the min/max envelope. The critical strain data of the same plate ($b/h = 15$) is out of the min/max envelope. This poor correlation can be

explained because of the imperfections and the thickness ratio. Indeed, thin plates are often more sensitive to imperfections. Loading imperfections observed earlier could have initiated the buckling earlier, explaining the poor correlation.

For other thickness ratio, the critical strain predictions are enveloped by the experimental strain data. Errors between predictions and experiments can seem important for some b/h ratio. Nevertheless these errors are around 0.1% strain, which corresponds to a 0.04 mm displacement in the axial direction of the plate. These errors have to be considered with respect to the DIC process used. The DIC uncertainty was evaluated at 0.02 mm. Moreover the detection criterion is also based on the imperfection amplitude. Depending on when the imperfection is evaluated, it can affect the evaluation of the critical strain. Therefore the correlation is considered as good on the strain data according to the instrumentation means. The same correlation quality is observed on stress data. The box plots are within the range defined by the second and third quartiles of the buckling predictions.

To conclude on the critical values, except for $b/h = 15$, all experimental critical strains and stresses correlate well with the buckling predictions, as shown in Figure 4.9.

For the smallest plates ($b/h = 13$ and 15), only one experiment was performed. Despite the good results observed on those plates, the generalization of the results have to be considered carefully. Additional experiments would be required in order to generalize these observations..

The effective critical stress and critical strain seem to decrease when the aspect ratio increases. Moreover the effective critical stress increases with the thickness ratio, and the critical strain decreases with the thickness ratio.

4.2.3   Analysis of the buckling modes

For each specimen, the buckling mode can be extracted from the experimental and FE deformed shape. The buckling modes are extracted from a post buckling deformed shape. They are extracted on both center lines. They are plotted for each plate aspect ratio in Figure 4.10.
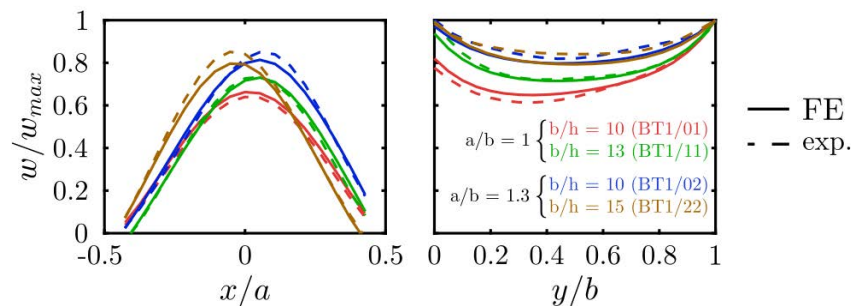
Figure 4.10: FEA vs. experimental buckling modes, plain curves: FE buckling mode and dashed curves: experimental buckling mode.

In Figure 4.10, the plain curves are associated to the FE buckling modes and the dashed curves to the experimental ones. Each colour corresponds to a different plate geometry (defined by its aspect ratio and its thickness ratio) in Figure 4.10.

As already observed, the FEA correlate well with experiments (cf.Figure 4.8). FE and experimental buckling modes also coincide as shown in Figure 4.10. The effect of the plate geometry on the buckling mode can also be observed in Figure 4.10. On the y center line ($x = 0$), all modes are very similar and look like Euler beam modes. On the x center line ($y = b/2$), symmetrical and asymmetrical modes can be observed.

Thick square plates ($a/b = 1$ and $b/h = 10$) present a slight rotation on their buckling modes (red curves in Figure 4.10) compared to other plate geometries. This particular point is analysed in the next paragraph.

4.2.4 Mode proximity for thick plates ($b/h = 10$)

Eigen analysis

For this particular thickness ratio ($b/h = 10$), the critical stress and strain were computed with the analytical model for the three first buckling modes with respect to the plate aspect ratio. The results of this analysis are presented in Figure 4.11. Red, green and blue curves correspond respectively to the evolution of the critical values for the first, the second and the third modes. The shape of each mode is presented on the right part of Figure 4.11. The third mode is only plotted from $a/b \geq 0.95$. Before this value the third eigenvalue corresponds to the fourth mode.
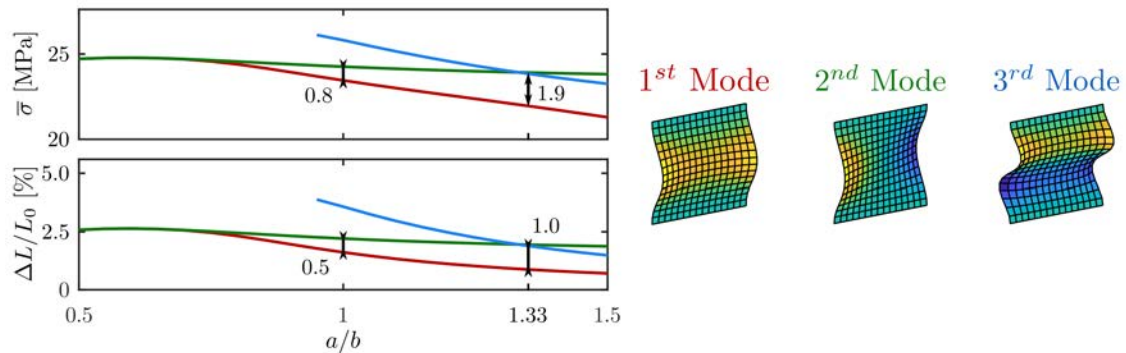
Figure 4.11: Evolution of critical stress and strain for the first three modes with respect to plate aspect ratio (derived from the analytical model).

The first and the second mode share the same critical values for plates with a low aspect ratio. A mode inversion can also be observed between the third and the second mode in Figure 4.11 when $a/b = 1.33$. The first mode corresponds to the one generally observed in the experiments. The second mode is its anti-symmetric shape. The third one is a more energetic mode with two bumps. The difference between the critical stresses of the first two modes is only 0.8 MPa for a square plate and

132

1.9 MPa for a 1.33 aspect ratio plate. Equally, the difference on the critical strain is 0.5% for a square plate and 1.0% for a 1.33 aspect ratio plate.

The first two modes are very close for a square plate. This proximity could generates a combination of the first two modes at bifurcation, either by simultaneous buckling or successive bifurcations. In both cases, a loading or a geometrical imperfection can ease the apparition of the second mode in the post buckling deformed shape. This point is investigated in the next paragraph.

Post buckling analysis and effect of imperfections

Using a FE model, two post buckling simulations were performed. Both simulations are identical except on the nature of the initial geometric imperfection.

Case 1: A geometric imperfection derived from the first mode only is applied to a perfect plate. Two plate aspect ratios are investigated, a square plate and a 1.33 aspect ratio plate.

Case 2: A geometric imperfection derived from the first two modes is applied to a perfect plate. Two plate aspect ratios are investigated, a square plate and a 1.33 aspect ratio plate.

In both cases the plates have a thickness ratio equal to 10.

For both cases, the buckling modes are extracted on both center lines and presented in Figure 4.12. The buckling modes of the 1.33 aspect ratio plate are drawn in Figure 4.12-2, while the buckling modes of the square plate are drawn in Figure 4.12-1.
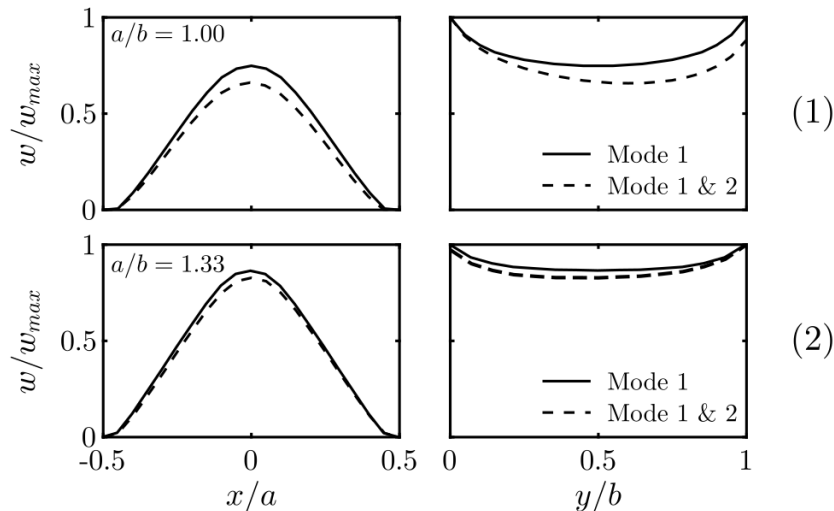
Figure 4.12: (1) Post buckling modes obtained for a square plate; (2) Post buckling modes obtained for a 1.33 aspect ratio plate (from FEA)

The buckling modes corresponding to Case 1 are drawn with plain lines. The buckling modes corresponding to Case 2 are drawn with dashed lines in Figure 4.12.

As observed experimentally, the buckling mode of the square plate highly depends on the nature of the imperfection. The second mode appears when the nature of the imperfection favours its expression, as shown with the dashed curve in Figure 4.12-1. The buckling mode shapes of the 1.33 aspect ratio plate are almost not affected by the second buckling mode as shown in Figure 4.12-2. The first and the second modes are already too far away for the 1.33 aspect ratio plate.

Modes proximity can lead to successive bifurcations as observed experimentally and numerically. This investigation shows the accuracy of the buckling predictions as well as the FE model with respect to the experiments.

From this first discussion several observations can be made. The effect of the plate geometry on the buckling behaviour has been observed. The aspect ratio as well as the plate thickness ratio affects the critical values. Moreover the plate aspect ratio has also an effect on the nature of the buckling mode. This phenomenon was observed experimentally for square plate, where successive bifurcations or a simultaneous buckling was observed. The nature of the imperfection can have an important effect on the buckling mode when the first bifurcation points are close to each others.

The strain rate was held constant for all specimens tested within BTC # 1 and discussed in this section. The next section discusses the effect of the strain rate on the buckling behaviour of thick plates.

4.3 Effect of the strain rate on the buckling of thick plates

The effect of the strain rate on the buckling behaviour is investigated in this section. Only the results of specimens with $a/b = 1.33$ and $b/h = 10$ from BTC #1 and #2 are used. The FE model and the analytical model are used to investigate the effect of strain rate on the buckling behaviour.

Table 4.2 summarizes the testing conditions of the specimens used in this section.

Specimen ID	a/b	b/h	V [mm.s^{-1}]	Ingot #	BTC #	V/V_{ref}	T° [°C]
BT1/02	1.33	10	2.10^{-3}	0	1	1	20
BT1/12	1.33	10	2.10^{-3}	1	1	1	20
BT2/31	1.33	10	2.10^{-2}	3	2	10	20
BT2/32	1.33	10	4.10^{-4}	3	2	1/5	20
BT2/41	1.33	10	2.10^{-2}	4	2	10	20
BT2/42	1.33	10	4.10^{-4}	4	2	1/5	20

Table 4.2: Summary of plate geometries and testing conditions

The variation of the strain rate is characterized by the speed ratio V/V_{ref}, where

V is the displacement rate applied and V_{ref} is the displacement rate applied to specimens BT1/02 and BT1/12.

4.3.1 FE simulations of the experiments

As in the previous section the experiments are also simulated with the post buckling FE model. The correlation with the FEA is still very good on load histories as shown in Figures 4.13 for $V/V_{ref} = 0.2$ and 10. The FE and the experimental curves are close, especially in the pre-buckling phase. The buckling initiates at similar times (or strains) in the FE simulations and the experiments. The correlation on the displacement fields is similar to the one presented in Figure 4.7
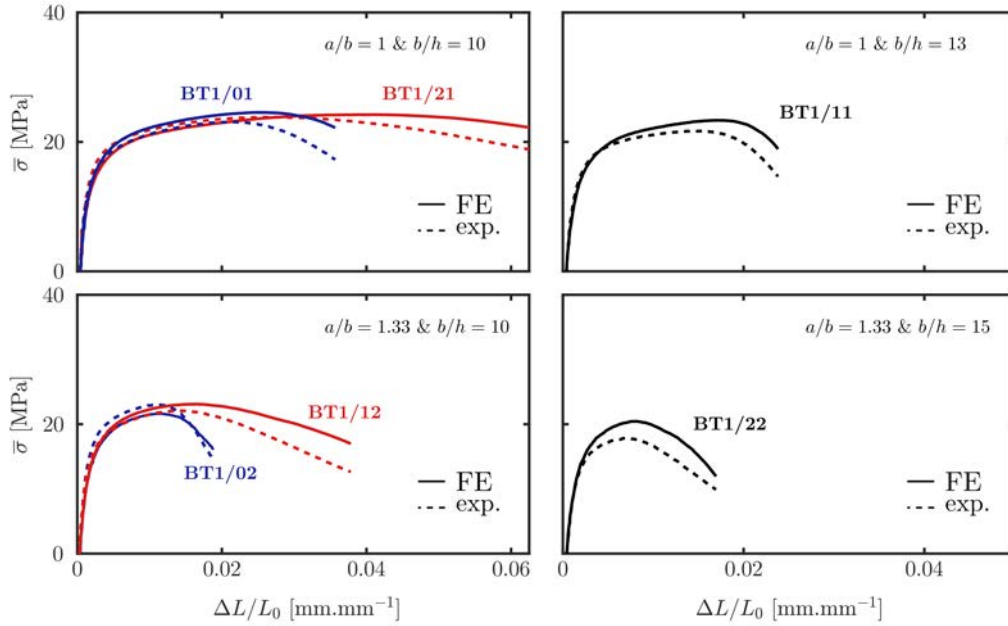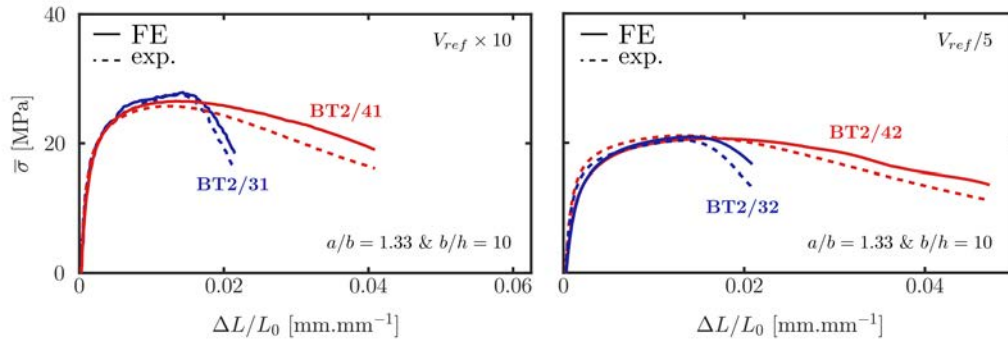

Figure 4.13: FEA and experimental normalized load according to normalized displacement, for all specimens from BTC #2 (plain curves: FE simulations and dashed curves: experimental data)

4.3.2 Comparison of the predicted and experimentally observed critical values

The experimental critical stresses and strains were also identified for each specimen of BTC #2. The critical values, including buckling detection discrepancy, are presented and compared to the buckling prediction in Figure 4.14. The buckling predictions were computed with the analytical model. The same normalization as in the previous section was used for the critical stress.

The box plots in Figure 4.14 correspond to test data. The mean buckling prediction is plotted with respect to speed ratio (plain curve). As in the previous section the minimum and maximum buckling predictions at 95% with 90% confidence are depicted by dashed curves. Finally the second and third quartiles are plotted with a shaded surface.

The critical stress increases with the strain rate while the critical strain seems to stay constant in the speed range covered.

The predicted critical stresses correlate well with the experimental ones.
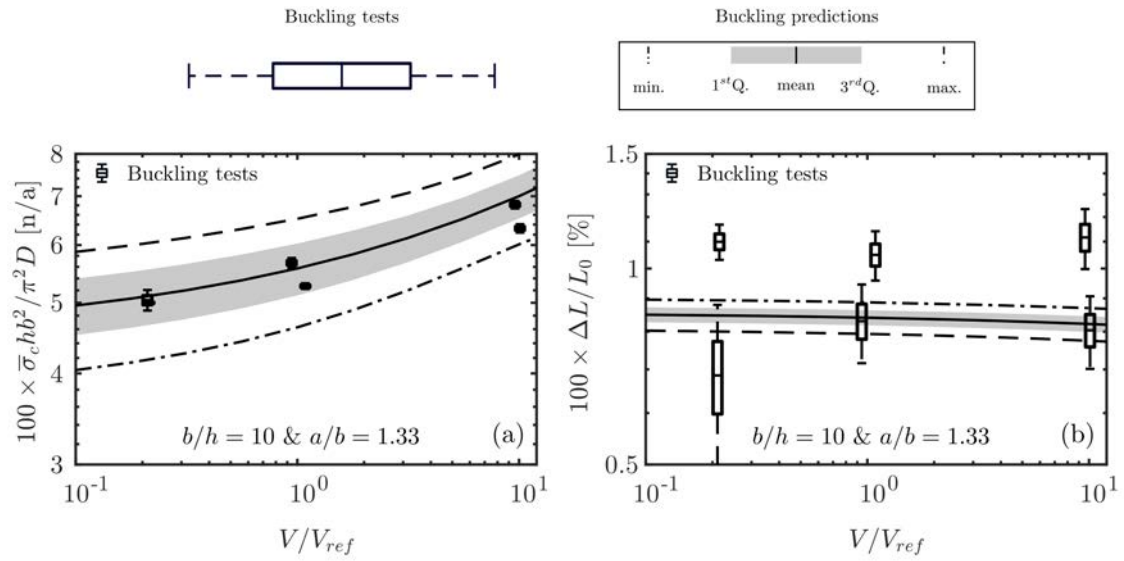
Figure 4.14: Experimental normalized critical stress and critical strain with respect to speed ratio

Regarding the critical strains, even if the box plots seem to not comply well with the predictions, the difference is around 0.1% of strain. As previously stated, this difference corresponds to a 0.04 mm displacement in the axial direction. This is of the same order of magnitude as the DIC error of measure.

To conclude the predicted critical values correlate well with the experimental ones.

4.3.3   Analysis of the buckling modes

As for specimens from BTC #1 the buckling modes are extracted on both center lines. They are plotted in Figure 4.15 for each speed ratio.
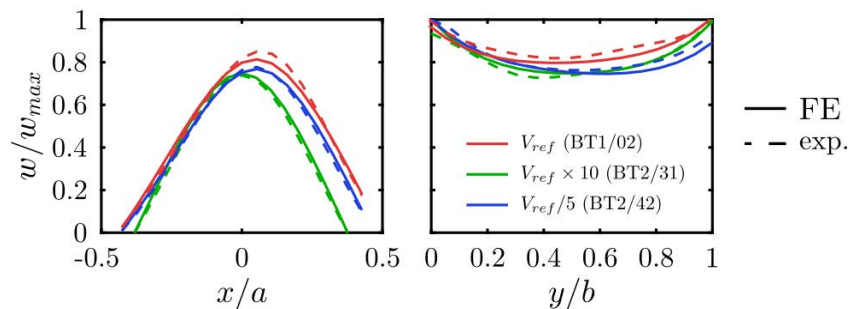
Figure 4.15: FEA vs. experimental buckling modes, plain curves: FE buckling mode and dashed curves: experimental buckling mode.

First, a good correlation on the buckling modes is also observed between the

FEA and the experiments. The buckling modes present identical shapes in Figure 4.15 for the three displacement rates tested. For the tested plate geometry and in the strain rate range covered, the buckling mode does not seem to be affected by the strain rate.

4.3.4 Validity of Bodner's hypothesis

It is important to notice that the buckling prediction is correct as long as the strain rate stays constant during buckling. This hypothesis is difficult to verify. In this subsection we intend to investigate the validity of *Bodner*'s hypothesis.

4.3.4.1 Critical values from a post buckling analysis for a large strain rate range

In order to complete the experimental observations, a parametric analysis was performed to investigate the strain rate effect in a larger strain rate range. The buckling predictions from the analytical model were compared to the buckling detection data obtained from a FE post buckling model.

The FE critical values were defined with respect to the buckling detection method presented in subsection 4.1.2. A plate with an aspect ratio of 1.33 and a thickness ratio of 10 was chosen. The speed ratio is the main parameter of this parametric analysis. It varies from 0.01 to 100, which corresponds to a strain rate between 5.0×10^{-7} s^{-1} and 5.0×10^{-3} s^{-1}. An initial imperfection is applied to the FE model, it is derived from the first buckling mode.

The buckling detection discrepancy is directly linked to the density of probability applied to the geometric imperfection amplitude. This density of probability is modelled by a lognormal distribution. This distribution is characterized by its mean value (5% of the plate thickness) and its standard deviation (5% of the plate thickness).

The results of the parametric analysis are presented in Figure 4.16. The plain blue curve corresponds to the buckling predictions from the analytical model. The red box plots depict the buckling initiation points detected from the FE post buckling model with respect to the strain rate. In this paragraph, the green box plot of Figure 4.16 are not discussed.

Even if the critical strain values from the analytical predictions and the FE post buckling model are close, the tendency is inverted. The critical strain detected with the FE model increases when the strain rate increases. The critical strain predicted with the analytical model decreases when the strain rate increases. This inverted tendency can be easily explained by the change of strain rate at buckling initiation.

4.3.4.2 Effect of a rapid strain rate change at buckling

For elasto-visco-plastic materials, when the buckling initiates, the strain rate increases, as for elasto-plastic materials. In elasto-plasticity, this strain rate increase
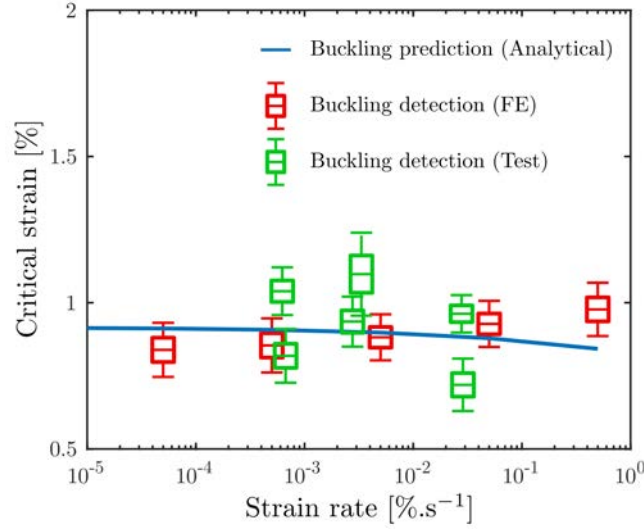
Figure 4.16: Buckling prediction vs. FE post buckling data, and test data, plate
geometry: $a/b = 1.33$ and $b/h = 10$.

is due to the loss of stiffness caused by the buckling mode shape.

For elasto-visco-plastic materials a rapid strain rate increase implies a rapid
increase of the tangent stiffness matrix. This tangent stiffness increase can delay
the buckling.

The time scale of the strain rate increase can be compared to the relaxation time
of the material. If the strain rate change occurs in a time scale greater than the
relaxation time, the effect on the tangential stiffness is negligible. On the contrary, if
the strain rate increase occurs in a very small time scale compared to the relaxation
time, the stiffness modification cannot be neglected.

A rapid change of strain rate can be introduced in the analytical model through
the instantaneous tangent modulus defined by the ratio $\dot{\sigma}_{eq}/\dot{p}$. A Taylor expansion
of $\dot{\sigma}_{eq}$ with respect to $\Delta\dot{p}$ can be written as:

$$
\begin{aligned}
\dot{\sigma}_{eq}\left(\dot{p} + \Delta\dot{p}\right) &= \dot{\sigma}_{eq}\left(\dot{p}\right) + \frac{\partial\dot{\sigma}_{eq}}{\partial\dot{p}}\Delta\dot{p} \\
&= \dot{\sigma}_{eq}\left(\dot{p}\right) + \frac{K}{n}\dot{p}^{1/n-1}\Delta\dot{p}
\end{aligned}
\tag{4.5}
$$

A new tangent modulus can be defined by:

$$
\frac{\dot{\sigma}_{eq}\left(\dot{p} + \Delta\dot{p}\right)}{\dot{p} + \Delta\dot{p}} = R'(p)\frac{\dot{p}}{\dot{p} + \Delta\dot{p}} + \frac{K}{n}\dot{p}^{1/n-1}\frac{\Delta\dot{p}}{\dot{p} + \Delta\dot{p}}
\tag{4.6}
$$

This tangent modulus can be considered as the one caused by a rapid change
of strain rate at buckling initiation. $\dot{p}$ defines the strain rate from the pre-buckling
loading, while $\Delta\dot{p}$ defines the change of strain rate at buckling. Figure 4.17 shows
how the critical strain is affected by the strain rate variation at buckling initiation.
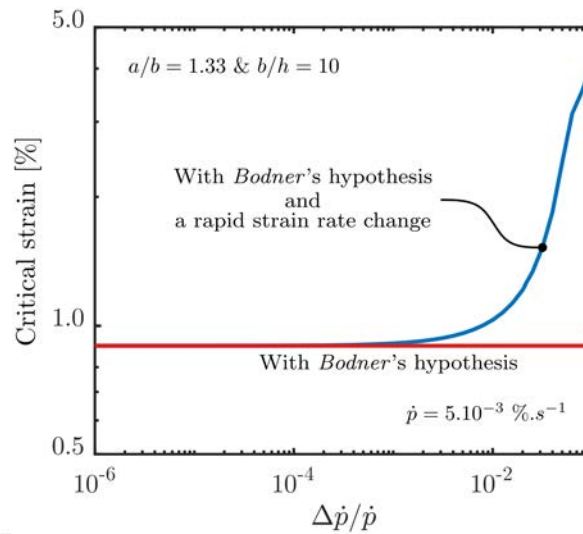
Figure 4.17: Effect of strain rate variation during buckling on critical strain.

As long as the strain rate change is small, the critical strain is the same as predicted with *Bodner*'s hypothesis. In this particular case, for a strain rate change higher than 1%, a significant variation on the critical strain can be observed, as shown in Figure 4.17.

Bodner's hypothesis seems suitable for small strain rate changes at buckling. For high strain rate changes at buckling, *Bodner*'s hypothesis is not accurate anymore. The predictions defined with *Bodner*'s hypothesis gives only a lower bound of the bifurcation point.

It seems reasonable to assess that the highest is the strain rate the highest is the strain rate change at buckling. This assumption can explain the inverted tendency observed in Figure 4.16. This assumption also limits the usage of *Bodner*'s hypothesis to structure subjected to reasonable strain rates.

In addition, the difference between both predictions (analytical and post buckling analysis) is of the same order of magnitude as the experimental discrepancy (between green box plots) in Figure 4.16. Therefore the predictions defined with *Bodner*'s hypothesis seem relevant in a reasonable strain rate range.

The method implemented here allows to define an estimation of the critical values. To predict more accurately the buckling of thick plates, the deformation theory should be coupled to the methods described by [Triantafyllidis, Massin, and Leroy 1997]. Nevertheless, according to the experiments and the FE modelling, for reasonable strain rates, the present method predicts well the buckling of thick plates. The buckling predictions comply with the experiments and the FEA on both critical values and buckling modes, as shown previously in Figures 4.8, 4.13, 4.10, 4.15, 4.9 and 4.14.

4.4 Conclusion

This chapter presented an efficient method to assess the buckling of thick shells with a rate-dependent behaviour. It also validates experimentally the approach inspired from [Eslami and Shariyat 1997] as well as the analytical model proposed by [Wang and Aung 2007] for the plastic buckling of thick plates.

The present work also shows the limitation of the *Bodner*'s hypothesis to reasonable strain rates. Higher strain rates should be investigated using the method proposed by [Triantafyllidis, Massin, and Leroy 1997]. High strain rates also induce potential dynamic effects and thermal effects out of the scope of the present work.

The prediction method gives a new experimentally validated tool to predict the buckling of rate dependent thick plates. The generalisation of the method to complex rate dependent thick shells is presented in the next chapter.

Chapter 5

Validation of the buckling prediction method for thick shells subjected to external pressure

In this chapter, the buckling prediction method based on the corner theory is evaluated against the experimental results obtained on hemi-egg shells subjected to external pressure. This chapter intends to validate the buckling prediction method to complex shells subjected to non-proportional loadings.

Contents

142

In the previous chapter the numerical and experimental methods to study the buckling of thick shells were evaluated against the buckling behaviour of simple structures, i.e. thick plates. The buckling predictions given by the deformation theory correlates well with experiments. The limits of *Bodner*'s hypothesis were investigated as well. In order to reach our final objective, i.e. to predict the buckling of complex thick shells subjected to non-proportional loadings, hemi-egg shells were tested under external pressure. The experiments were instrumented as described in Section 2.4.2 of Chapter 2. In this chapter the experimental results obtained on the hemi-egg shells are analysed and compared to the buckling predictions given by the corner theory.

First a numerical analysis intends to identify the corner theory parameters (θ_c and θ_0). Then the best experimental conditions to observe the buckling of hemi-egg shells are defined.

In a second part the experimental data are investigated, including measurement uncertainties and potential geometrical or loading imperfections. Two experimental buckling detection criteria are also defined. The simulation of each experiment through FEA is presented and discussed.

Finally, the validity of the prediction method is discussed and compared to other prediction methods.

In this chapter, unless otherwise specified, the mean reference material law is used for all numerical analysis (cf. 3.4).

The section of biggest radius is often mentioned in this Chapter, Figure 5.1(a) presents its location along the egg major axis. Because of the shape of the hemi-egg, a cylindrical coordinate system is often used in this chapter. This cylindrical coordinate system is described in Figure 5.1(b).

Section of biggest radius

(a)   (b)
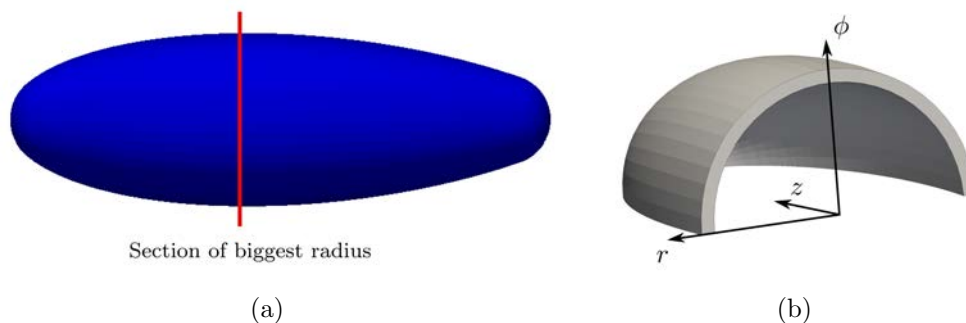
Figure 5.1: (a) Location of the section of biggest radius along the egg major axis; (b) Cylindrical frame attached to the egg for the FFT post processing of the displacement fields.

5.1 Calibration of the corner theory parameters

In this section we intend to calibrate the buckling prediction method through the identification of the corner theory parameters, θ_c and θ_0. θ_c and θ_0 define respectively the yield stress corner and the quasi-proportional cone as illustrated in Figure 2.7 of Chapter 2. The calibration of θ_0 and θ_c is done numerically through the minimization of the difference between the predicted critical times and the detected critical times from post buckling analysis. The detected critical times are defined through post bifurcation analysis of imperfect hemi-egg shells. The post bifurcation analysis is performed with a FE model, where the evolution of the bifurcated solution is analysed. In order to cover a large strain rate range, two pressure rates (defined by P_{inf} and t_{ref}) are considered.

The trivial solution is presented and discussed first. Then the results of post bifurcation analysis are presented and analysed. The detection criterion is then defined, and the detected critical times are identified from post bifurcation simulations. Finally the corner theory parameters are identified.

5.1.1 FE model of the hemi-egg shell

As already mentioned the analyses of the perfect or imperfect hemi-eggs are performed with a FE model. This latter only considers the egg shape of the specimen presented in Figure 2.14(b) (the flange is not modelled). The hemi-egg shell is clamped on its border. The geometry of the perfect hemi-egg shell is defined in Chapter 2.

As mentioned previously, two load histories are used, they are defined by $P_{inf} = 4.5$ MPa and $t_{ref} = 100$ or 10000 s, and:

$$P(t) = P_{inf} \left(1 - e^{-\frac{t}{t_{ref}}} \right). \tag{5.1}$$

The value of P_{inf} was selected in order to be close to the limit between elasto-visco-plastic buckling regime and creep buckling regime (constant load with respect to time). In this region, the differences between all predictions defined with respect to θ_c and θ_0 are magnified. The simulations are run until $P/P_{inf} = 0.999$, corresponding to $t = -t_{ref} \ln(0.001)$.

5.1.2 Analysis of the trivial solution

For each value of t_{ref}, the simulation is first run on the perfect hemi-egg shell. Figure 5.2 presents the evolution of the FE deformed shape with respect to the time.

First the top of the egg is deformed entirely due to the pressure. Then two lobes appear and develop on the deformed shape between $t/t_{ref} = 2$ and 4 as shown in Figure 5.2. The development of the two lobes corresponds to a limit point buckling mode. This limit point buckling is due to the specimen shape and the boundary
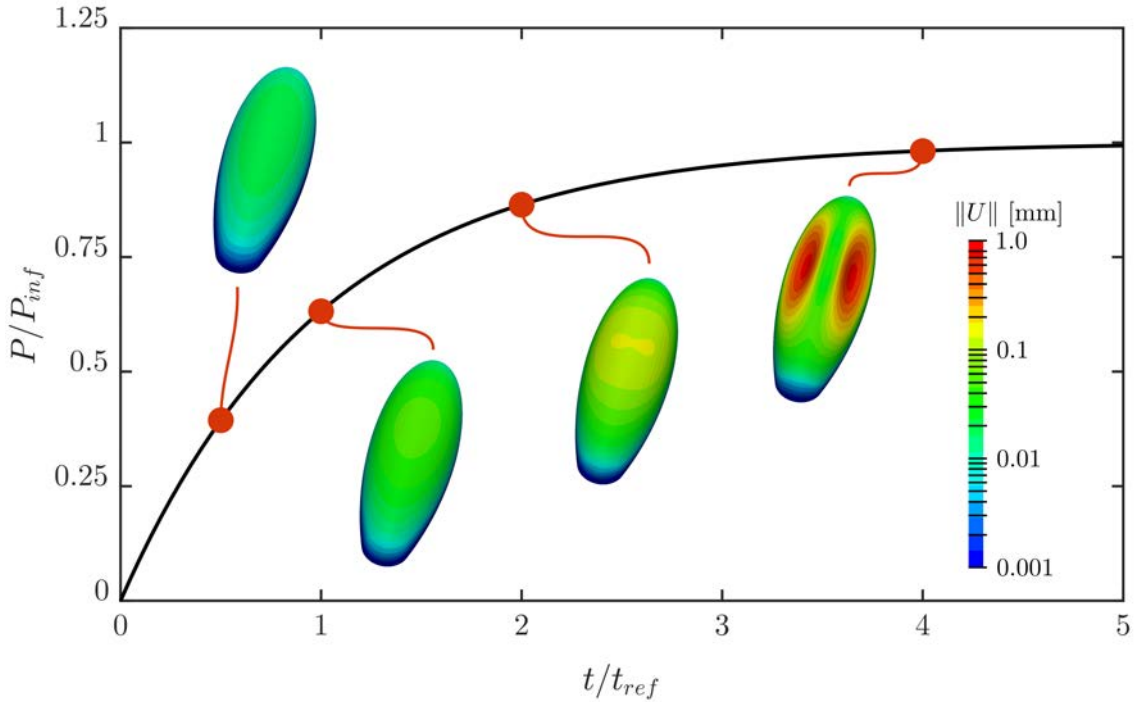
Figure 5.2: Evolution of the hemi-egg numerical deformed shape with respect to time for a pressure profile defined by $P_{inf} = 4.5$ MPa and $t_{ref} = 100$ s

conditions. Any additional buckling mode will have to be studied by considering this limit point buckling branch as the trivial one.

In order to estimate the non-proportionality of the loading path, the spatial distribution of θ can be analysed according to pressure and time, as illustrated in Figure 5.3. Each couple of iso-values corresponds to the upward and downward views of the egg. The left view presents the value of θ on the upper skin and the right one the value of θ on the lower skin.

One can see that the stress rate direction follows a quasi-proportional loading up to $t/t_{ref} = 2$ (θ is lower than 30° almost everywhere). Because of the deformation of the hemi-egg shell, the stress state becomes highly triaxial after $t/t_{ref} = 2$ and the loading highly non-proportional.

The deformed shape is then post processed through a Fast Fourier Transformation (FFT). This FFT is carried out in order to analyse the displacement field. This FFT is only performed on a circumferential line extracted from the inner surface of the egg. This line is positioned at the section of biggest radius as shown in Figure 5.1(a).

The displacement fields are then transported to a polar frame, where $\boldsymbol{z}$ is defined by the axial axis of the egg, $\boldsymbol{r}$ and $\boldsymbol{\phi}$ respectively the radial and tangential direction of the egg shell as shown in Figure 5.1(b).

From the simulation of the perfect hemi-egg shell, one can extract from the FFT
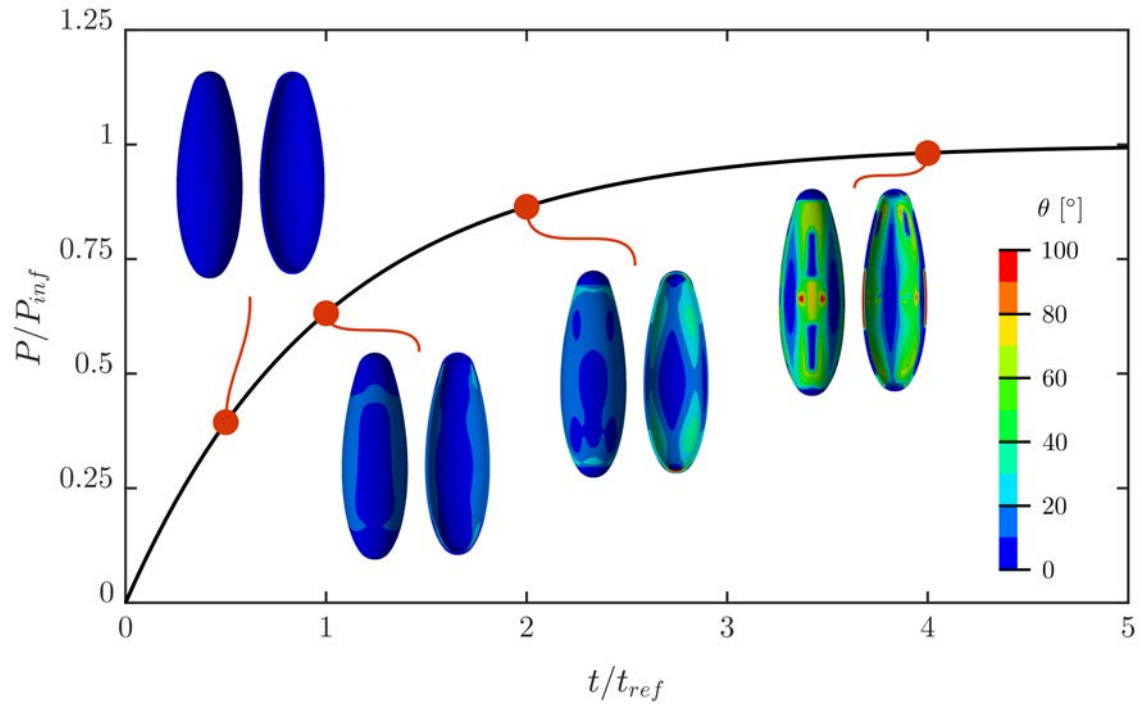
Figure 5.3: Numerical evolution in time of the stress rate direction θ on the upper and lower skin for a pressure profile defined by $P_{inf} = 4.5$ MPa and $t_{ref} = 100$ s

analysis the five first harmonics of the radial displacement field. The evolution of their modulus with respect to time is presented in Figure 5.4 (left). In Figure 5.4 (right) the shape of each harmonic is depicted. The first harmonic corresponds to the trivial elastic deformation and the second one to the trivial plastic one. This identification can be done by comparing the shape of the two first harmonics in Figure 5.4 (right) to the evolution of the egg deformed shape in Figure 5.2. One can assume that the other harmonics have a negligible effect on the trivial response of the egg shell in the pre-buckling phase, as shown in Figure 5.4.

This FFT post processing is also used later in order to filter the displacement field and to better visualize the singular solution. The first and the second harmonics can be removed from the total displacement field on the bifurcated solution in order to visualize the singular solution.

5.1.3 Analysis of bifurcated solutions

For the post buckling analysis, an initial geometric imperfection defined by a linear combination of the fifteen first elastic buckling modes is applied to the perfect hemi-egg shell. Its amplitude is defined as a percentage of the shell thickness. Figure 5.5 presents the shape of the imperfection generated. The imperfection amplitude ranges from 0.5% to 10%.

146
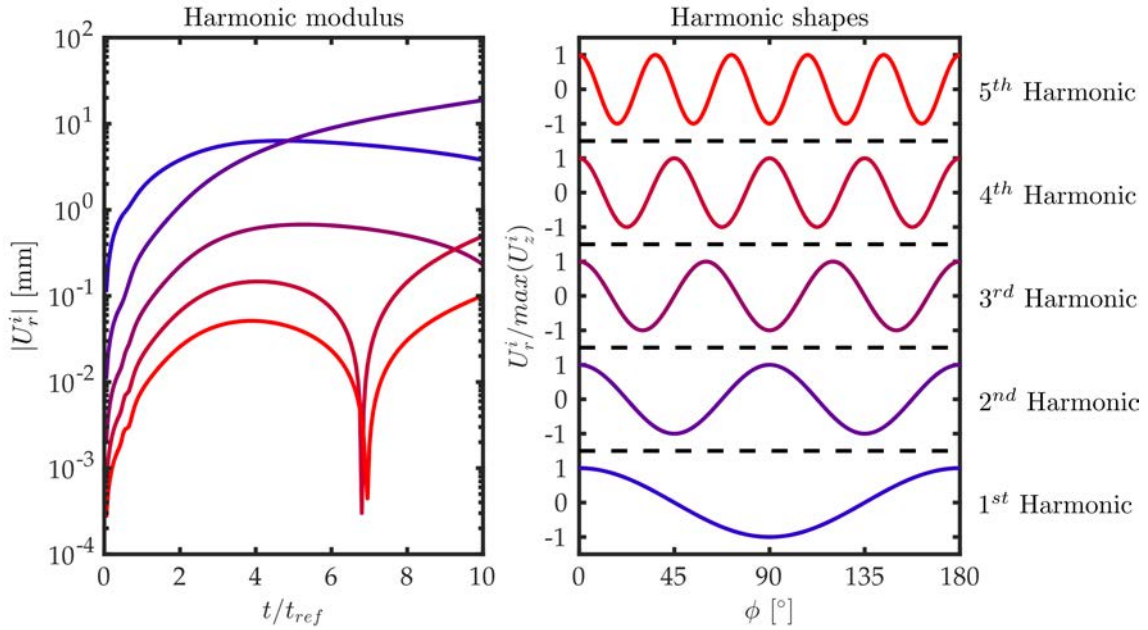
Figure 5.4: Harmonic modulus and shapes from the post processing of the perfect shell simulation with a pressure profile defined by $P_{inf} = 4.5$ MPa and $t_{ref} = 100$ s
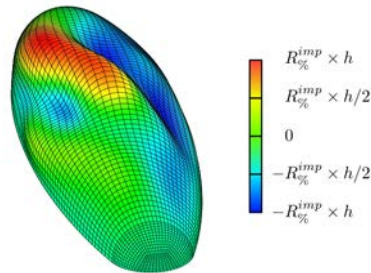
Figure 5.5: Normalized magnitude of the initial geometric imperfection applied to the hemi-egg initial geometry

As for the simulation of the perfect hemi-egg shell, the displacement field can be post processed by FFT. It is important to notice that the buckling mode is not clearly visible on the post buckling deformed shape. A filter based on a FFT analysis of the displacement field is applied in order to remove the main components of the trivial elastic and plastic deformation.

On the bifurcated branch, the buckling mode is combined with the trivial solution (i.e. mainly the 1st and 2nd harmonics). The symmetrical or asymmetrical properties of the buckling mode localizes the strain to one of the two lobes of the 2nd harmonic of the trivial displacement fields. The effective deformed shape often looks like a single lobe observed on one side of the hemi-egg shell, as shown in Figure 5.6.
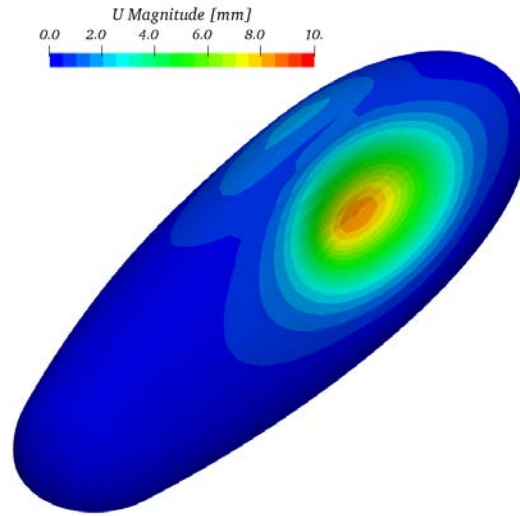
Figure 5.6: Post buckling deformed shape

This post buckling deformed shape does not correspond to the buckling mode. When the trivial solution (i.e. mainly the 1st and 2nd harmonics) is removed from the bifurcated one, the singular solution (i.e. the buckling mode) can be approximated.

5.1.4 Definition of a bifurcation detection criterion for post bifurcation analysis

To define our buckling detection criterion the displacement field is approximated by the five first harmonics from its FFT analysis. To detect the bifurcation on egg shells, the same strategy as for plates is adopted. The detection criterion is based on the analysis of the post buckling deformed shape. In this case the initial imperfection is also analysed by FFT. The buckling detection criterion is defined as follows:

$$
\begin{cases} |\alpha| \geq 1, \text{ buckling detected} \\ |\alpha| < 1, \text{ no buckling} \end{cases} \text{, with: } \alpha(r, \phi, \overline{z}) = \frac{\sum_{i=1}^{5} \left(U_r^i - \hat{U}_r^i \right)}{\sum_{i=1}^{5} U_r^i \big|_{imp}}, \tag{5.2}
$$

where $\overline{z}$ is the axial coordinate of the section of biggest radius, U_r^i is the radial component of the ith harmonic of the bifurcated solution, $\hat{U}_r^i$ is the radial component of the ith harmonic of the trivial solution and $U_r^i \big|_{imp}$ is the radial component of the ith harmonic of the imperfection.

This detection criterion is applied to both pressure rates and to all imperfection amplitudes. The evolution of a local maximum of $|\alpha|$ with respect to the time ratio is depicted in Figure 5.7. The point where $\alpha = 1$ is depicted for each imperfection

amplitude by a bullet in Figure 5.7. In addition, the singular solution (i.e. mainly the combination of the 3rd, 4th and 5th harmonics) is plotted at the detected buckling initiation for each imperfection amplitude. The followed peak of deformation is located in the angular sector $[60°, 80°]$. It is identified by the label P in Figure 5.7.

(a)

(b)
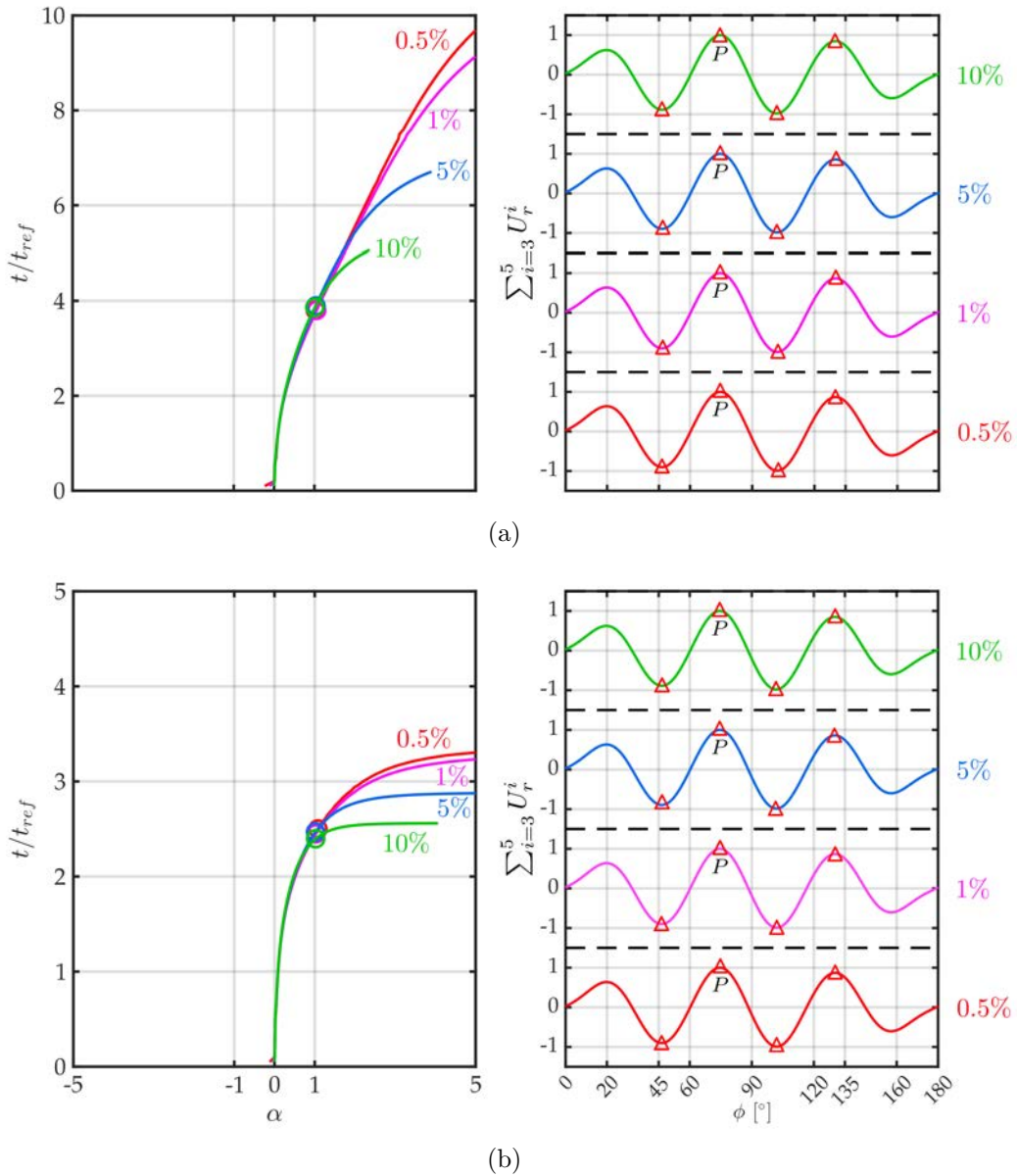
Figure 5.7: (a) Evolution of the singular solution α with respect to time and the imperfection amplitudes (left); approximation of the singular solution for each imperfection amplitude (right) for $t_{ref} = 100$ s; (b) Evolution of the singular solution α with respect to time and the imperfection amplitudes (left) approximation of the singular solution for each imperfection amplitude (right) for $t_{ref} = 10000$ s

One can see that the detected critical times are very close to each others for both pressure rates.

Asymmetric buckling modes can be extracted from the filtered displacement field. They present two peaks and two valleys as shown in Figures 5.7(a) and 5.7(b).

For a pressure profile defined by $t_{ref} = 100$ s, the first bifurcation is detected from a time ratio (t/t_{ref}) equal to 3.86 and 2.40 for a pressure profile defined by $t_{ref} = 10000$ s. The detected critical times are summarized in Table 5.1, and the retained critical time ratio are highlighted with bold typography.

| t_{ref} [s] | CT | t/t_{ref} - 1st bifurcation | | | |
| | | $R^{imp}_{\%}$ | | | |
		10%	5%	1%	0.5%
100	3.53	**3.86**	3.89	3.90	3.90
10000	2.55	**2.39**	2.47	2.50	2.60

Table 5.1: Predicted critical time ratio on a perfect geometry (with the (CT) corner theory, $\theta_c = 112.5°$ and $\theta_0 = 0.45(\theta_c - \pi/2)$) vs. detected buckling time ratio according to the imperfection amplitude $R^{imp}_{\%}$, bold values correspond to the targeted critical time ratio

The retained critical values are used in the next paragraph in order to identify θ_0 and θ_c. The retained values are then called detected critical time ratios, $\bar{t}_{c_1}^{100}$ and $\bar{t}_{c_1}^{10000}$. The buckling modes extracted from the post bifurcated solution are then compared to the ones predicted with the identified θ_c and θ_0. This is done in order to validate the identification process.

This mean surface imperfection based criterion will not be applied to the experiments. First this criterion is based on the knowledge of the initial imperfection. In our case the initial imperfection is too low to be well described by DIC measurements. In second, it is also based on the knowledge of the trivial solution. The trivial solution cannot be defined accurately for each experiment, because of the boundary condition imperfections, the loading imperfection and so on.

5.1.5   Identification of θ_c and θ_0

In order to identify the parameters of the corner theory, an optimisation process is followed. The identified couple of parameters shall predict the bifurcation points identified previously for both pressure profiles. A tolerance area for both parameters will also be defined.

To find such parameters, a parametric analysis on θ_c and θ_0 was performed. If a high value of θ_0 is chosen, the buckling predictions will correspond to the prediction from *Hencky*'s deformation theory. θ_c also affects the predictions, when θ_c tends to $\pi/2$, the yield surface becomes smooth and the linear tangent operator tends to the

Mises flow theory one. In order to avoid such effects, it was chosen to study both parameters in the following ranges, $\theta_c \in [100°, 130°]$ and $\theta_0 \in [0°, (\theta_c - \pi/2)/2]$.

As a reminder, the two pressure profiles defined by $P_{inf} = 4.5$ MPa and $t_{ref} = 100$ s or 10000 s are used. A bifurcation analysis using the corner theory is performed in order to define the properties of the first three bifurcation points.

As an example Figure 5.8 depicts the evolution of the eigen pressures for the first three modes with respect to the ratio t/t_{ref} (green, blue and red curves). The bifurcation point is reached when the eigen pressure is equal to the actual pressure. The shape of the first three buckling modes is also presented in Figure 5.8. The shape of each mode is not affected by θ_c and θ_0. Only the sorting can be modified. The first critical pressure defined with the *Mises* flow theory and *Hencky*'s deformation theory are also shown for information in Figure 5.8. They are respectively depicted with a black and a magenta curves. This two additional eigen pressures show how the corner theory is bounded by the *Mises* flow theory and *Hencky*'s deformation theory.
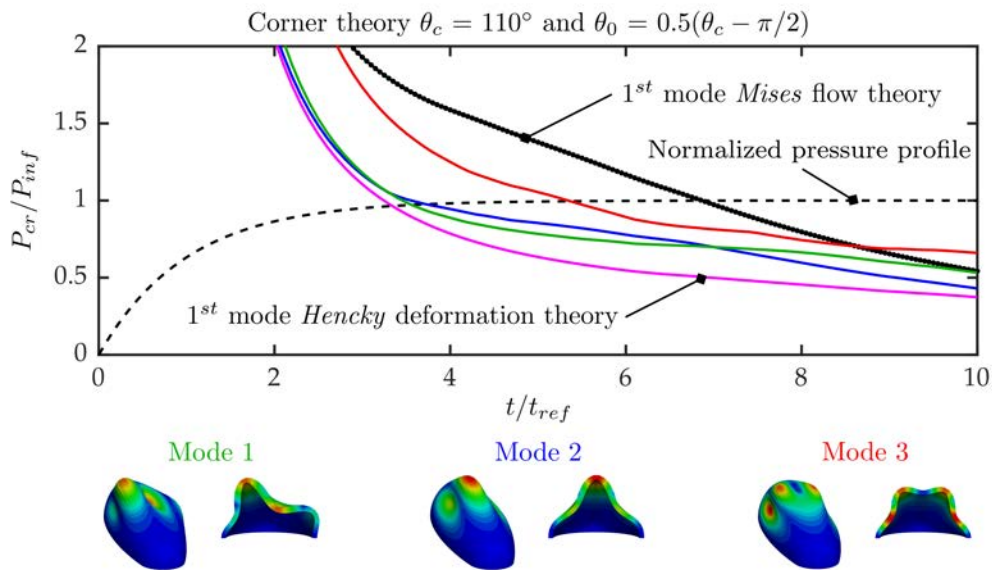
Figure 5.8: Evolution of the eigen pressure according to the normalized time and the three first buckling mode predicted with the corner theory for a pressure profile defined by $P_{inf} = 4.5$ MPa and $t_{ref} = 100$ s

Figure 5.8 shows that the first two modes almost share the same eigenvalue. The first two modes are quasi periodic modes. They share the same wave length (around 85° cf. Figure 5.8). They only differ on their phases. The first buckling mode is asymmetric, while the second one is symmetric. As a matter of fact, the third mode corresponds to the second bifurcation point. It is also a quasi periodic mode. Its wave length is approximately equal to 60° with a symmetric shape.

From the parametric analysis, the critical time ratio of the first bifurcation point $t_c^{1\&2}/t_{ref}$ (first and second eigenvalue) was extracted and plotted with respect to θ_c and θ_0 in Figure 5.9 for both pressure profiles.

(a)   (b)
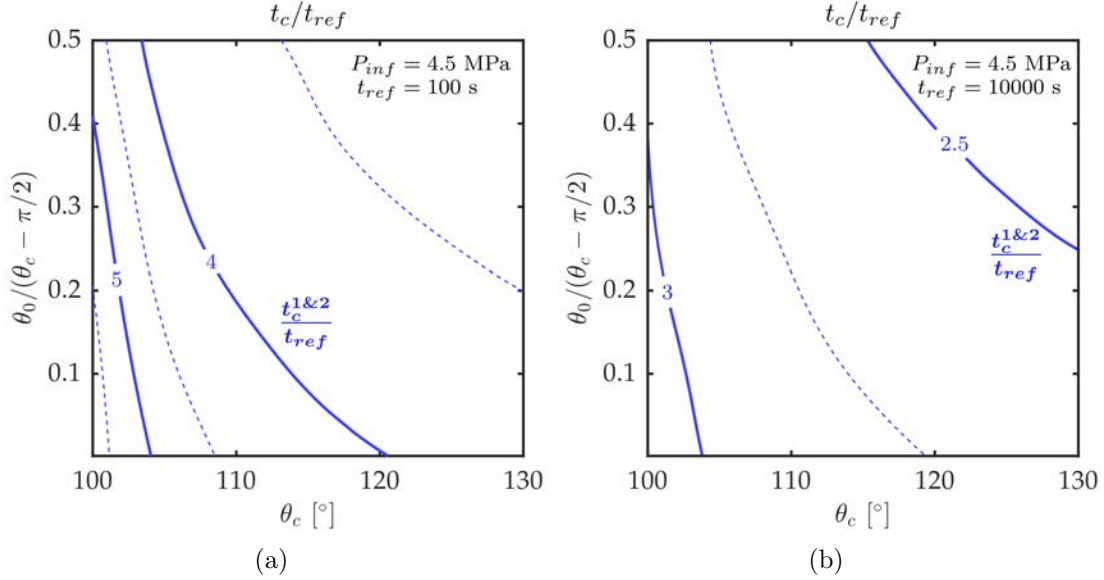
Figure 5.9: (a) Evolution of the first ($t_c^{1\&2}$ blue iso-values) critical time ratio with respect to θ_c and θ_0 for a pressure profile defined by $P_{inf} = 4.5$ MPa and $t_{ref} = 100$ s; (b) Evolution of the first ($t_c^{1\&2}$ blue iso-values) critical time ratio with respect to θ_c and θ_0 for a pressure profile defined by $P_{inf} = 4.5$ MPa and $t_{ref} = 10000$ s

In Figure 5.9(a) the predictions of the first $t_c^{1\&2}/t_{ref}$ critical time ratio for a pressure profile defined by $P_{inf} = 4.5$ MPa and $t_{ref} = 100$ s are depicted with respect to θ_c and θ_0. The blue iso-values (plain and dashed) correspond to $t_c^{1\&2}/t_{ref}$. The same strategy is followed in Figure 5.9(b) for a pressure profile defined by $P_{inf} = 4.5$ MPa and $t_{ref} = 10000$ s. One can see that the critical time is reduced by a combined increase of θ_c and θ_0. This is true for both load cases.

Using an optimisation process the best couple of parameters was determined. In this optimisation process we intend to find the couple of parameters predicting the detected critical points of Table 5.1. The function to minimize is defined as follows:

$$f(\theta_c, \theta_0) = \left(\frac{\boldsymbol{R}^t \boldsymbol{R}}{4}\right)^{0.5} \text{ with: } \boldsymbol{R} = \left[\begin{array}{c} \frac{t_c^{1\&2}(\theta_c, \theta_0, P_{inf}=4.5, t_{ref}=100)}{\bar{t}_{c_1}^{100}} - 1 \\ \frac{t_c^{1\&2}(\theta_c, \theta_0, P_{inf}=4.5, t_{ref}=10000)}{\bar{t}_{c_1}^{10000}} - 1 \end{array} \right], \quad (5.3)$$

with $\bar{t}_{c_1}$ the detected critical times.

This function is plotted in Figure 5.10 with respect to θ_c and θ_0 in the parametric domain previously defined.

152
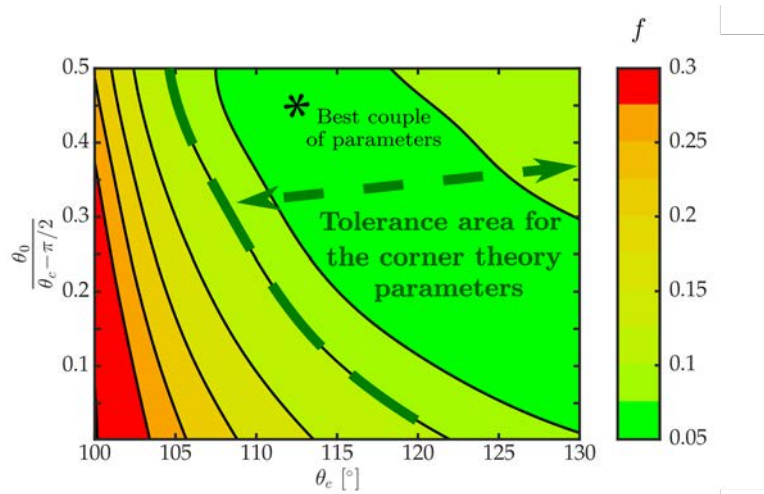
Figure 5.10: Iso-values of the minimized function used to define the best couple of parameters of the Corner theory (mentioned with a star)

The minimum of f is reached for $\theta_c = 112.5°$ and $\theta_0 = 0.45(\theta_c - \pi/2)$, as shown in Figure 5.10. In addition a tolerance area for the values of θ_c and θ_0 is also defined in Figure 5.10.

The mode shapes obtained with this couple of parameters correspond to the ones presented in Figure 5.8. They can be compared advantageously with the ones observed in the post buckling analysis (cf. Figure 5.7). They all present an asymmetrical shape and similar wave length, same number of peaks and valleys. A good agreement is observed between the first buckling mode predicted and the ones identified.

The critical values predicted for the first bifurcation points are also compared to the detected ones in Table 5.1. This couple of parameters underestimates the detected time for the load case defined by $t_{ref} = 100$ s and slightly overestimate the one for the load case defined by $t_{ref} = 10000$ s.

The couple of parameters identified in this section is used for all buckling predictions presented in this chapter unless otherwise specified.

5.2 Parametric analysis of the buckling of a hemi-egg shell

A second task was focused on the definition of the experimental loading conditions in order to observe the buckling of hemi-egg shells. Two parameters characterize the load history, the pressure P and the pressure rate $\dot{P}$. In Section 2.4.2 of

Chapter 2, the theoretical loading history is defined by:

$$P(t) = P_{inf} \left(1 - e^{-\frac{t}{t_{ref}}} \right).$$ (5.4)

The pressure amplitude is therefore defined by P_{inf} and the pressure rate amplitude by P_{inf}/t_{ref}. The effect of the pressure and the pressure rate will then be investigated in order to define the experimental conditions.

The main objective of this section is to define the best experimental conditions to validate the buckling prediction method developed. A parametric bifurcation analysis is used for this purpose. It takes P_{inf} (the saturation pressure), t_{ref} (the reference time), $R_\%^{imp}$ (the initial imperfection amplitude) and ΔR_0 (the yield stress discrepancy) as inputs. This last is important as the different specimens can have different yield stress because of the discrepancy in the cooling rate during their manufacturing.

This parametric analysis is also used to generate numerical data to compare the experiments with the numerical analysis. All bifurcation analyses are performed with the corner theory and the parameters defined previously $\theta_c = 112.5°$ and $\theta_0 = 0.45(\theta_c - \pi/2)$.

P_{inf}	t_{ref}	$R_\%^{imp}$	ΔR_0
[MPa]	[s]	[%]	[MPa]
4.00	10	0	-7.5
4.25	20	0.1	-5.5
4.50	50	0.2	-2.5
4.75	100	0.5	0
5.00	200	1.0	2.5
5.25	500	2.0	5.0
5.50	1000	5.0	
5.75	2000	10	
6.00	5000	20	
	10000		

Table 5.2: Summary of input parameter values

This parametric analysis follows a numerical experiment chart with four inputs. Table 5.2 summarizes the different values taken by each parameter. Every combination is simulated. The outputs of the analysis are the critical pressure P_c and the critical time t_c.

The results of the parametric analysis are presented in Appendix F. From this analysis, two important points are discussed here. First a projection method is presented. It is used to compare the experimental critical values with the predictions in a perfect space defined by (P_{inf}, t_{ref} and ΔR_0). The parametric analysis is also used to define the experimental conditions.

5.2.1 Projection of the experimental critical values in the perfect space

To define the projection, two normalisation ratios are defined as follows:

$$r_{P_c}\left(P_{inf}, t_{ref}, \Delta R_0\right) = P_c\left(P_{inf}, t_{ref}, \Delta R_0\right)/\overline{P}_c\left(\left(\overline{P}_{inf}, \overline{t}_{ref}, \Delta \overline{R}_0\right)\right),$$
$$r_{t_c}\left(P_{inf}, t_{ref}, \Delta R_0\right) = t_c\left(P_{inf}, t_{ref}, \Delta R_0\right)/\overline{t}_c\left(\left(\overline{P}_{inf}, \overline{t}_{ref}, \Delta \overline{R}_0\right)\right). \tag{5.5}$$

where $P_c\left(P_{inf}, t_{ref}, \Delta R_0\right)$ is the critical pressure for a set of loading and material parameters and $\overline{P}_c\left(\left(\overline{P}_{inf}, \overline{t}_{ref}, \Delta \overline{R}_0\right)\right)$ is the critical pressure for a set of reference parameters $(\overline{P}_{inf}, \overline{t}_{ref}, \Delta \overline{R}_0)$. The same convention is used for the critical time.

As an example, in Figure 5.11 (left), the normalisation ratio r_{P_c} is plotted with respect to ΔR_0 and t_{ref}, and with $\overline{P}_{inf} = P_{inf} = 4.5$ MPa, $\overline{t}_{ref} = t_{ref}$ and $\Delta \overline{R}_0 = 0$ MPa. In Figure 5.11 (right) the normalisation ratio r_{P_c} is plotted with respect to ΔR_0 and P_{inf}, and with $\overline{P}_{inf} = P_{inf}$, $\overline{t}_{ref} = t_{ref} = 100$ s and $\Delta \overline{R}_0 = 0$ MPa.
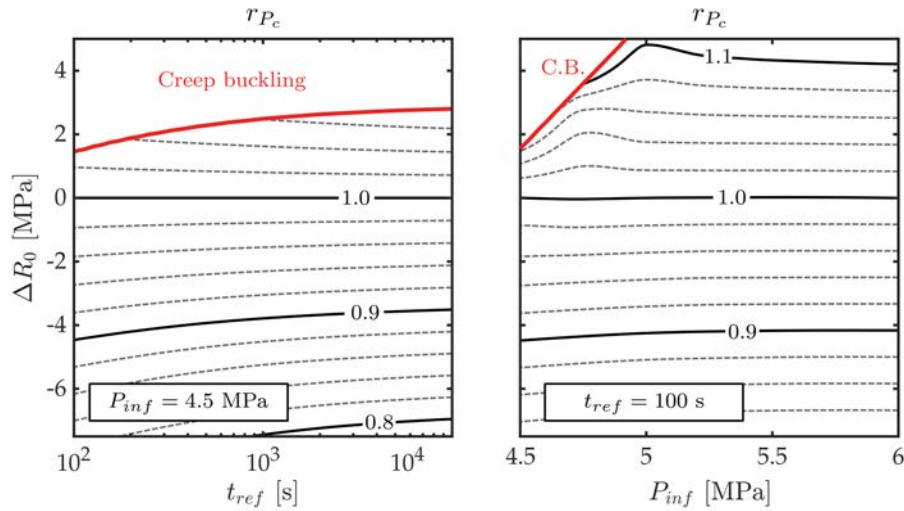
Figure 5.11: Iso-values of the predicted normalized critical pressure with respect to t_{ref} with $P_{inf} = 4.5$ MPa (left) and with respect to P_{inf} with $t_{ref} = 100$ s (right).

Only r_{P_c} is drawn in Figure 5.11 as r_{t_c} is linked to $\overline{P}_c$ through the pressure profile expression:

$$P_c = P_{inf}\left(1 - exp(-t_c/t_{ref})\right). \tag{5.6}$$

The abacuses in Figure 5.11 allow to define the equivalent perfect critical values from experiments thanks to r_{P_c} and r_{t_c}. They are defined as follows:

$$P_{c\ exp}^{eq} = P_c^{exp}\left(P_{inf}, t_{ref}, \Delta R_0\right)/r_{P_c},$$
$$t_{c\ exp}^{eq} = t_c^{exp}\left(P_{inf}, t_{ref}, \Delta R_0\right)/r_{t_c}. \tag{5.7}$$

This projection is used in Section 5.3 to define the experimental critical values for an equivalent perfect material.

5.2.2 Definition of the experimental conditions

It is important to experiment several pressure rates in order to observe different strain rates among the hemi-egg shells tested. Moreover due to the possible material imperfection it is better to apply a pressure profile with P_{inf} higher than 5.0 MPa, as discussed in Appendix F. This is done in order to be sure to buckle in the elasto-visco-plastic regime. We also want to be on the limit between of the two regimes (elasto-visco-plastic and creep regimes). Therefore P_{inf} needs to be as low as possible. From these observations two pressure profiles were defined. The fastest with $P_{inf} = 5$ MPa and $t_{ref} = 100$ s and the slowest with $P_{inf} = 5$ MPa and $t_{ref} = 1000$ s.

For both sets of testing conditions, their characteristics and the expected critical values are summarized in Table 5.3.
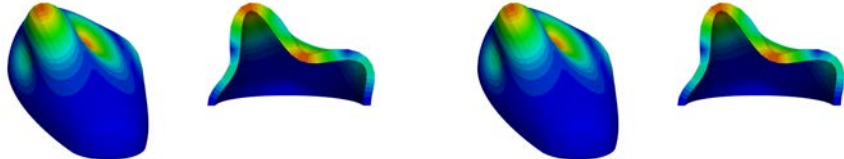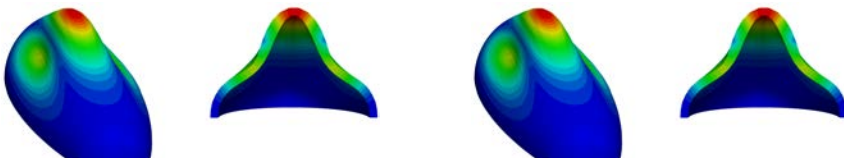
Case	1	2
t_{ref} [s]	100	1000
P_{inf} [MPa]	5	5
$\dot{p}_{mean}$ [s^{-1}]	1.22×10^{-5}	1.80×10^{-6}
$\dot{p}_{max}$ [s^{-1}]	4.77×10^{-5}	8.17×10^{-6}
θ_{max} [°]	49	61
1st Mode		
t_c/t_{ref} [n/a]	2.258	1.929
P_c [MPa]	4.476	4.273
2nd Mode		
t_c/t_{ref} [n/a]	2.261	1.952
P_c [MPa]	4.478	4.289

Table 5.3: Summary of experimental conditions for both testing cases

One can notice that the first two bifurcation points almost coincide. Therefore, both modes can be expected. Nevertheless, any asymmetrical imperfection will lead

the structure to buckle on the asymmetrical buckling mode. Moreover the strain rate difference between both cases is noticeable. Indeed for the fast load case the mean plastic strain rate is almost seven times higher than the one of the slow load case.

In the next sections of this chapter, the results of these two preliminary numerical tasks are used in order to analyse the experimental results and to evaluate the buckling prediction method.

5.3 Experimental results vs. FE modelling

This section is dedicated to the results obtained from the experiments performed on the thick hemi-egg shells. Five specimens were tested (cf. 2.5).

As already said, these experiments were instrumented with three cameras in order to measure the lower skin of the shell using DIC. The pressure histories and the images acquired are analysed in order to characterize experimentally the buckling of thick hemi-egg shells subjected to external pressure.

This section is organised in three subsections. The first one introduces the different sources of uncertainty on the experimental measurements. The second subsection presents the results for the analyses of the experiments, such as the experimental critical values and their associated criteria or the buckling modes identified. Finally the last subsection presents the results from the FE analysis of the experiments.

5.3.1 Experimental uncertainties

The experimental process was defined in Section 2.4.2 of Chapter 2. The measurements obtained from the experiments are the pressure history and the images from the three cameras.

5.3.1.1 Uncertainties on the applied pressure

As already mentioned, the rig was set in displacement control mode. A pressure/displacement law was defined experimentally for each test in order to approach the desired pressure profile (cf. Table 2.5). The actual pressure history was measured. Figure 5.12 illustrates a typical experimental pressure history and its four phases. The four phases correspond to different test phases:

I The pressure is maintained at 0.2 MPa. Images are acquired to evaluate the errors on the displacement fields (discussed later in this section).

II A manual pressure ramp from 0.2 MPa to 0.5 MPa is followed. The pressure is then maintained at 0.5 MPa until the launch of the automatic test procedure.

III The automatic test procedure is launched. The pressure increases according to the defined displacement/pressure law. This is the pre-buckling phase.
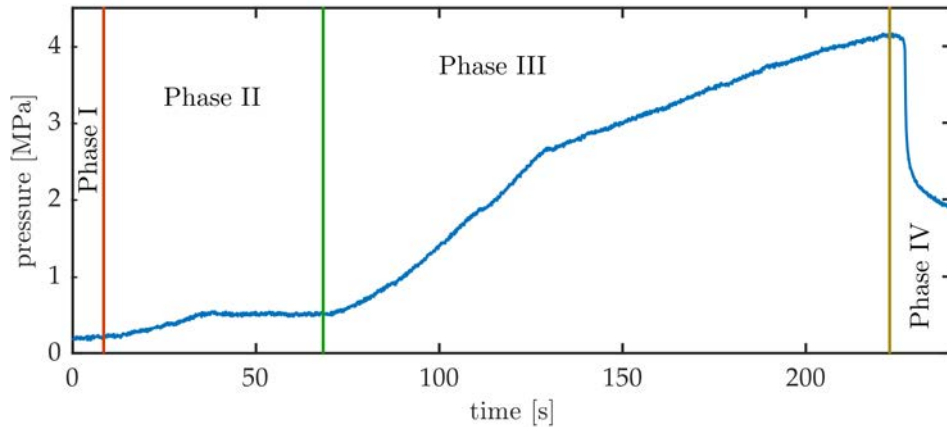
Figure 5.12: Typical pressure history measured and its four phases (Egg O/003)

IV The automatic test procedure is still running, a drop of pressure is observed. This is the collapsing phase.

The position of the buckling initiation point is discussed later.

For each specimen, theoretical pressure profiles can be defined using the following equation in phase III,

$$P(t) = P_{inf} \left(1 - e^{-(t_{exp}-t_0)/t_{ref}}\right), \tag{5.8}$$

where t_{exp} is the experimental time and t_0 the effective initial time of the pressure profile identified.

For each specimen, three profiles are defined:

- the average pressure profile corresponding to the best fit of the experimental pressure history by Equation 5.8,

- the minimum pressure profile defining the lower bound of the experimental pressure history with Equation 5.8,

- the maximum pressure profile defining the upper bound of the experimental pressure history with Equation 5.8.

Figure 5.13 depicts the measured pressure history and the three pressure profiles identified for each specimen.

The identified parameters P_{inf}, t_{ref} and t_0 are presented in Table 5.4 for each specimen and each scenario (min, max and average).

The identified parameters are close to the ones targeted. Moreover the two loading kinematics are well visible between specimens 2, 3 and 4 and specimens 5 and 6. These sets of parameters are used later for the validation of the buckling prediction method.

158
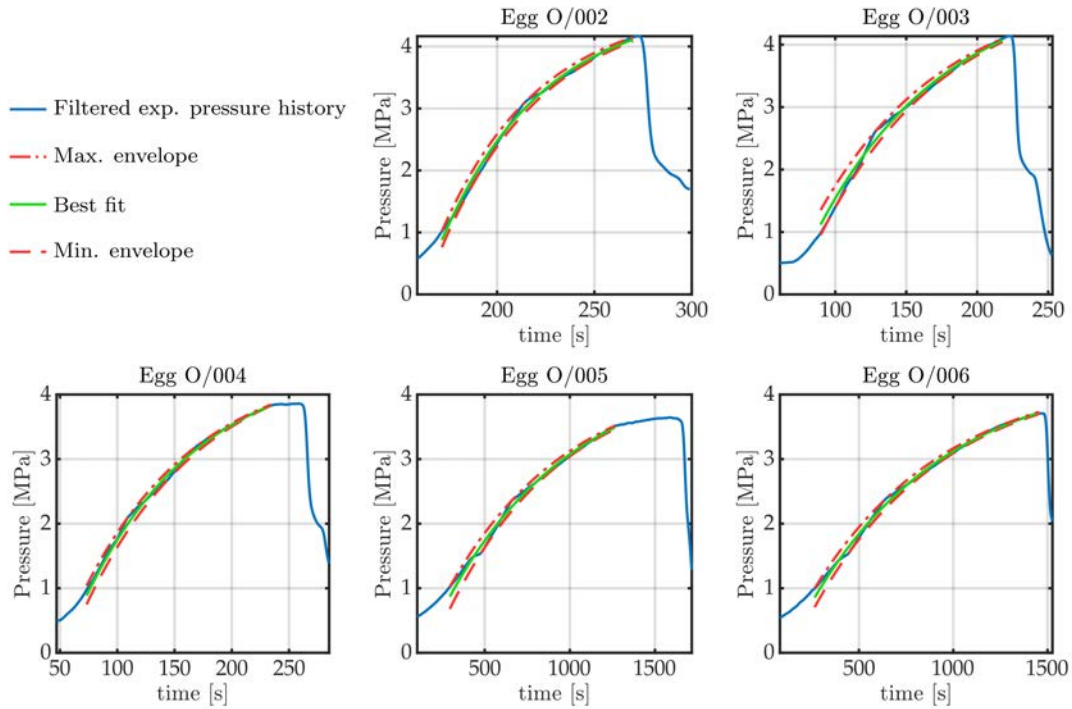
Figure 5.13: Pressure profiles identified for each specimen

O/00#	Target		Min.			Mean.			Max.		
	P_{inf}	t_{ref}	P_{inf}	t_{ref}	t_0	P_{inf}	t_{ref}	t_0	P_{inf}	t_{ref}	t_0
	MPa	s	MPa	s	s	MPa	s	s	MPa	s	s
2	5	100	4.71	53.4	162.3	4.70	52.4	160.9	4.67	50.7	159.2
3	5	100	5.02	89.7	70.8	5.01	90.4	66.9	4.96	89.5	61.2
4	5	100	4.67	104.4	54.9	4.58	100.6	51.6	4.55	100.4	47.2
5	5	1000	4.35	683.5	179.4	4.47	745.7	134.0	4.40	721.8	104.7
6	5	1000	4.35	691.9	142.4	4.40	722.6	108.7	4.35	707.8	81.1

Table 5.4: Identified pressure profile parameters

5.3.1.2 Uncertainties on the geometry and displacement fields measured

The images were post-processed using Ufreckles (cf. [Réthoré 2018]) to identify the geometry of the lower skin of the hemi-egg shell and the displacement fields. Three cameras are used for this purpose. The hemi-egg shell is divided in two regions. The first one is covered by cameras 0 and 1 the other by cameras 0 and 2.

First the uncertainties on the egg geometry are presented before discussing the uncertainties on the displacement fields.

Uncertainties on the specimen geometry

As for the plates, the topography of the specimen is obtained by DIC. Usually this technology allows to define the geometrical imperfection of the specimen. Because of the high curvature of the specimen, errors due to the DIC process itself and optical issues are also introduced. Thanks to the chosen manufacturing process followed and the experience acquired on the plate manufacturing, the shape imperfection are assumed to be negligible, lower than 0.05 mm. Therefore it is assumed that most of the errors on the egg topography are probably due to optical issues and to the DIC process itself.
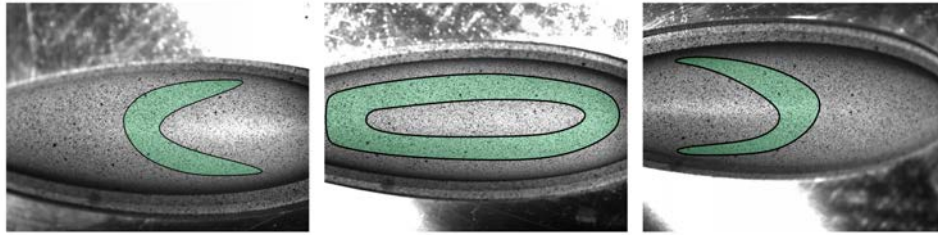
Figure 5.14: Optimal depth of field areas for the three cameras defined with the camera lens diaphragm completely open; from left to right, camera 1, camera 0 and camera 2

The main optical issue is due to the depth of field. Because of the high curvature of the specimen, the depth of field is just slightly greater than the specimen depth. The best areas for each camera are presented in Figure 5.14. Because of this phenomenon, errors in the DIC process can be introduced on the border of the measured area. This is also observable on the topology error maps in Figure 5.15. They depict the error between the theoretical radius and the measured one, ΔR, for each node of the DIC meshes. The same convention as defined in Figure 5.1(b) is used to define the egg radius. One can see, that the error maps are closely linked to the best depth of field areas presented in Figure 5.14. The errors are especially magnified on the borders of the ROIs.

Moreover, in some areas of high curvature, the mesh and the speckle pattern are deformed. This can also impact the quality of the DIC process. This phenomenon can be observed in Figure 5.16.

Nevertheless, the topological errors can be normalized by the theoretical radius as in Figure 5.17. The topological errors are then lower than 3% of the radius measured.

To conclude, even if errors are introduced in the DIC process and the optical means, the measured geometry well agrees with the theoretical one. Table 5.5 summarizes the statistical parameters of the measurement errors on the topology for both camera couples. The standard deviation (StD) of the error field is the most valuable information as it defines the range of the error field. With a standard deviation between 0.2% and 0.6% for all specimens, it corresponds to a relative error
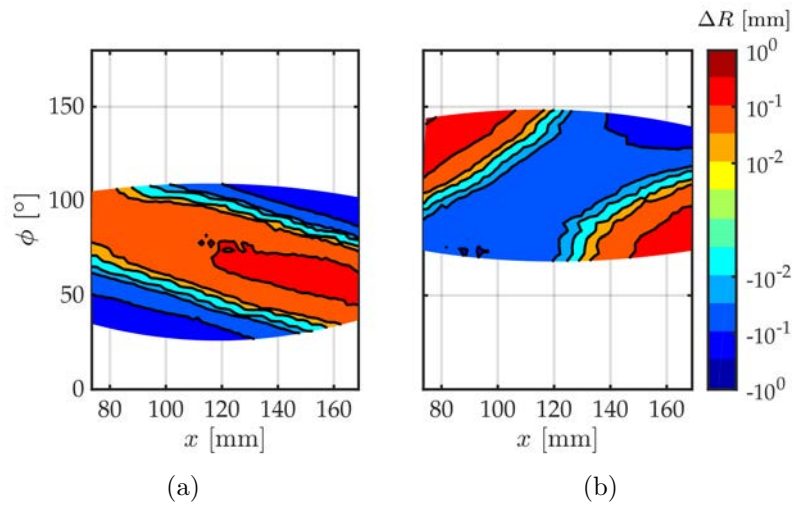
Figure 5.15: (a) Absolute error map on the area analysed with the images of camera 0 and 1; (b) Absolute error map on the area analysed with the images of camera 0 and 2 (Egg O/003)
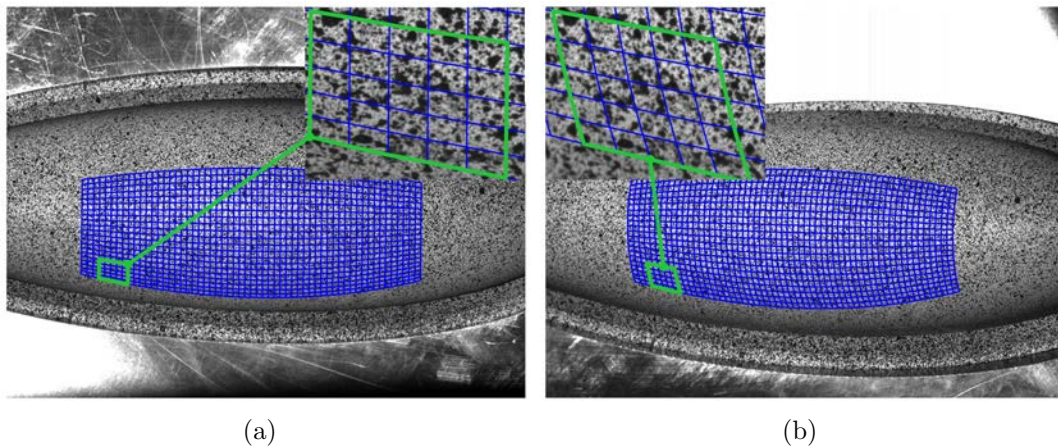
Figure 5.16: (a) Mesh on the area analysed with the images of camera 0 and 1 (Camera 0); (b) Mesh on the area analysed with the images of camera 0 and 1 (Camera 1) (Egg O/005)

range between +/- 1% and +/-3%. Moreover in the region where the buckling mode develops (i.e. between $x = 100$ mm and $x = 140$ mm), the errors observed are even lower. The amplitude of error is very good.

One can see that the measurement uncertainties are too big too identify the nature of any initial imperfection. As the manufacturing mean surface imperfections are expected to be lower than 0.05 mm.

(a)   (b)
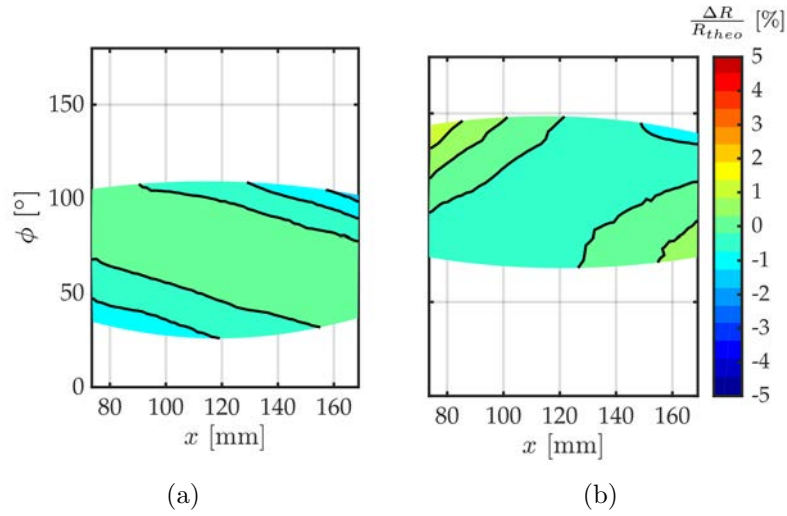
Figure 5.17: (a) Relative error map on the area analysed with the images of camera 0 and 1; (b) Relative error map on the area analysed with the images of camera 0 and 2 (Egg O/003)

O/00#	Cameras 0 and 1				Cameras 0 and 2			
	Mean	StD	Mean	StD	Mean	StD	Mean	StD
	mm	mm	%	%	mm	mm	%	%
2	0.014	0.079	0.06	0.30	-0.016	0.079	-0.05	0.29
3	0.003	0.094	0.01	0.34	-0.008	0.092	-0.02	0.34
4	0.073	0.140	0.27	0.52	-0.079	0.150	-0.29	0.56
5	0.038	0.057	0.14	0.21	-0.045	0.120	-0.17	0.47
6	0.050	0.075	0.19	0.27	-0.055	0.067	-0.20	0.25

Table 5.5: Statistical parameters of the topological error field

Uncertainties on the displacement fields measured

The next step intends to estimate the error introduced by the instrumentation chain into the displacement field identified by DIC. At the beginning of each experiments (phase I) at least 20 images of the undeformed egg are acquired by each camera in order to assess the accuracy of the measurement method. In theory, the displacement field identified should be zero. The accuracy of the method is defined by the amplitude of the displacement noise measured. Figure 5.18 presents for specimen O/003 the mean value and the standard deviation of the displacement amplitude on the first 20 images for each couple of cameras. One can see that the mean field is centred on zero without any noticeable spatial distribution. The standard deviation of the error field is also small around 5 μm for this specimen.

The statistical parameters describing the DIC accuracy on the displacement field
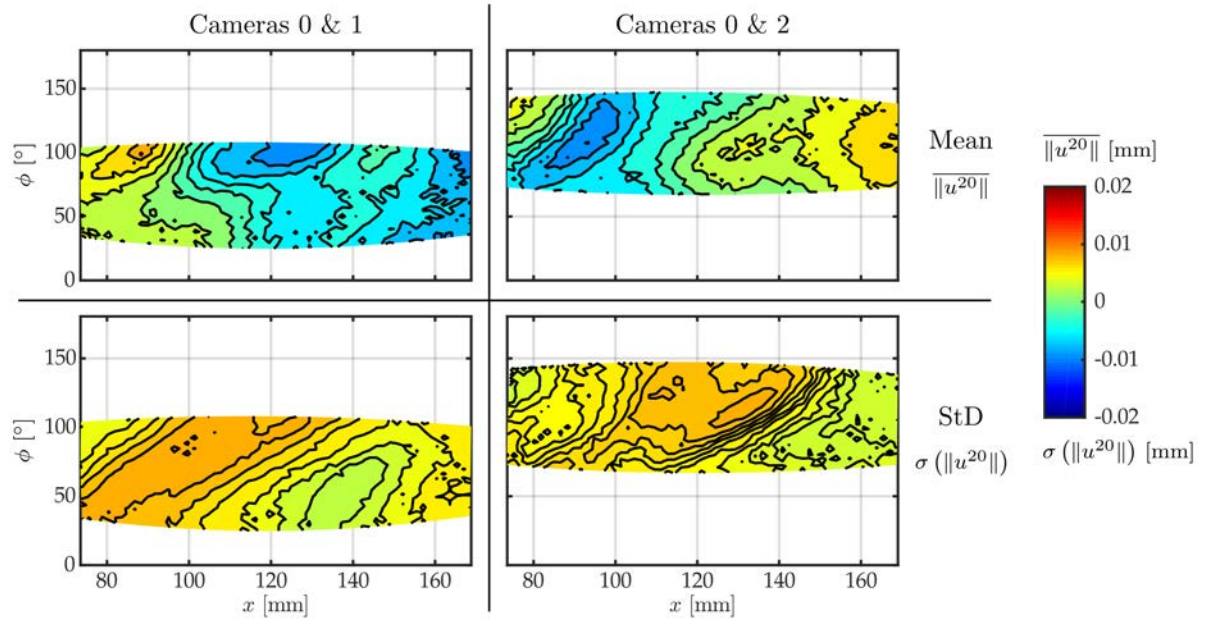
Figure 5.18: Statistical illustration of the DIC accuracy on the displacement magnitude for each couple of cameras (Egg O/003)

are summarized in Table 5.6 for all specimens. As shown in Table 5.6, the error on the displacement field is reasonable for all specimens. According to the mean and standard deviation values, the DIC accuracy on the displacement field can be estimated to +/- 20 μm. This amplitude of error is quite good considering the high curvature of the specimen.

O/00#	Cameras 0 and 1		Cameras 0 and 2	
	Mean	StD	Mean	StD
	μm	μm	μm	μm
2	-5	17	2	12
3	-2	8	1	7
4	3	8	4	13
5	-8	8	3	8
6	-2	10	-1	12

Table 5.6: Statistical parameters of the accuracy of the DIC displacement fields

5.3.2   Experimental results

Five specimens were tested. In this subsection the results of these experiments
and their analysis are presented. Several points need to be assessed in order to
compare the experimental analysis with the numerical ones. First as for the plates,
the measured displacement field can give a lot of information on the buckling ini-
tiation point as well as the buckling mode itself. This subsection will first present
the evolution of the deformation during the buckling tests performed on hemi-egg
shells. Then, interesting features of the experiments will be presented, they intend
to bound the experimental bifurcation point.

For the rest of this analysis, a normalized pressure/time space is used. The
critical values presented are defined as follows.

$$P_c^\star = P_c/P_{inf} \text{ and } t_c^\star = (t_c - t_0)/t_{ref}, \tag{5.9}$$

with P_c the critical pressure, P_{inf} the saturation pressure of the pressure profile, $P_c^\star$
the normalized critical pressure, t_c the critical time, t_{ref} the reference time of the
pressure profile, t_0 the start time of the experiment and $t_c^\star$ the normalized critical
time.

The pressure histories measured are depicted for all experiments in Figure 5.19.
In the normalized space, a good repeatability is observed especially in the pre-
buckling phase. It shows that we achieved a good repeatability in the manufacturing
process.
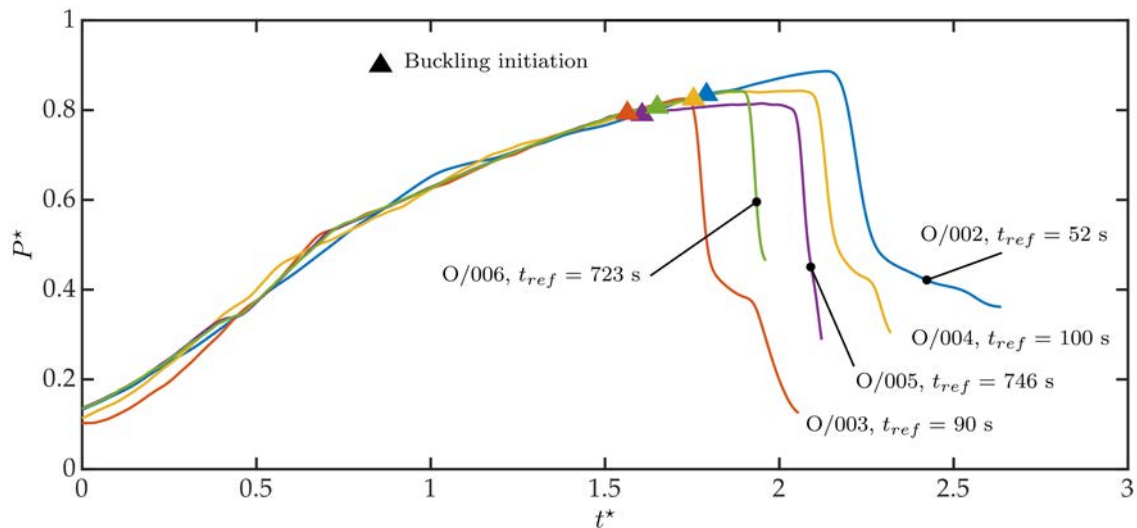
Figure 5.19: Normalized pressure histories for all specimens

In Figure 5.20, the evolution of the experimental displacement magnitude is
depicted with respect to the normalized time and pressure. Only the pre-buckling
and buckling phases were considered for DIC analysis. In the post buckling phase

the deformation is too fast to be well captured. The deformed specimen is rapidly out of the depth of field of the cameras. One can see that two lobes are growing continuously during the experiments until buckling.
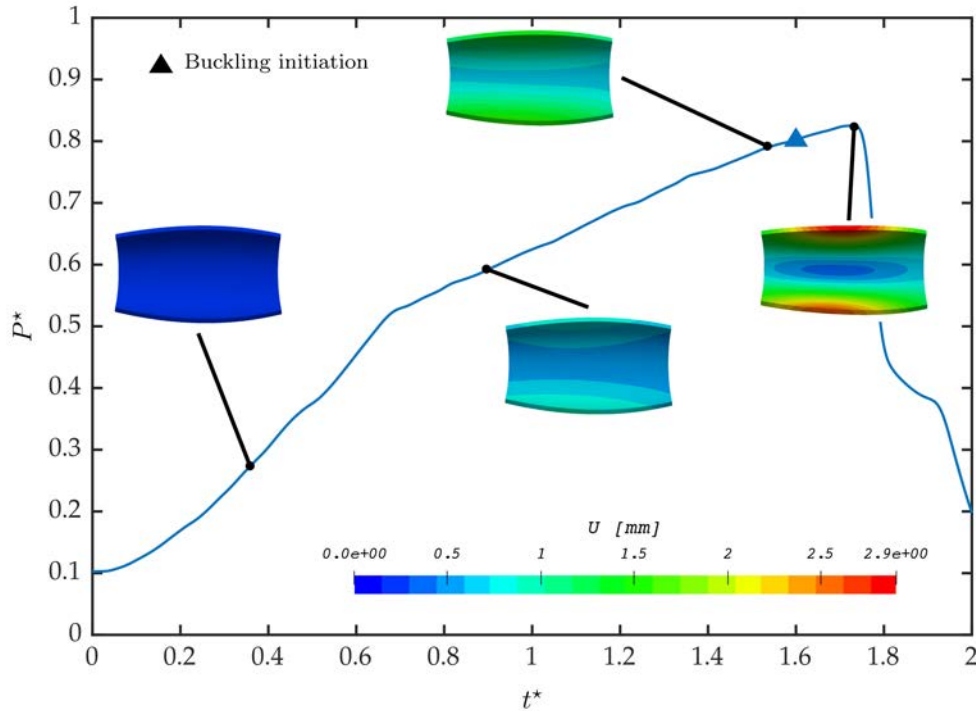
Figure 5.20: Deformed shape with respect to the normalized time and pressure (O/003)

For four out of five experiments, one lobe is preferred to the other and an asymmetrical post-buckling deformed shape is obtained, as in Figure 5.21 for specimens O/002, O/003, O004 and O/006 . For the other specimen (O/005) a symmetrical post buckling deformed shape is obtained, as shown in Figure 5.21.

Experimental buckling detection criteria

In Figure 5.20, one can see that the displacement magnitude on the top of the egg is back to zero or near zero at the maximum pressure. This particular phenomenon is also described in Figure 5.22(a), where the displacement component U_z at the top of the egg (cross surrounded) is plotted with respect to the normalized time. For a particular pressure, a min value is observed for the displacement on the top of the egg, followed by a rapid increase. This point is marked by a black triangle in Figure 5.22(a). This phenomenon is assumed to be the buckling initiation. Indeed, as shown in Table 5.3, the first and the second bifurcations almost happen simultaneously, moreover the second buckling mode presents an elevation of the summit of the egg, as observed here.

Figure 5.21: Deformed specimens after buckling; from left to right: specimen O/006, O/005, O/004, O/003 and O/002

In addition the same analysis was performed on a FE simulation of an imperfect egg shell. As shown in Figure 5.22(b) the predicted bifurcation happens just before the vertical inversion of the displacement. As for every structure, the amplitude of the imperfection can affect the order (prediction / displacement inversion). Nevertheless this phenomenon is close to the predicted bifurcation and it is associated to the initiation of the buckling.

One cannot be certain that this point completely defines the bifurcation initiation point. Therefore a critical range is defined for each specimen. It is assumed that this range starts from the buckling initiation point previously defined, and ranges to the maximum pressure point. The maximum pressure point is associated to the collapse of the shell structure, it is therefore an upper bound of the bifurcation. This range is then used to be compared to the numerical critical values predicted.

The buckling initiation point and the maximum pressure point properties are summarized in Table 5.7. Their corresponding normalized values can be defined according to the different pressure profile scenario presented in Table 5.4.

Experimental buckling modes

Finally the buckling modes can be extracted at the initiation point and at the maximum pressure point for each specimen. The same method as in the previous section is used. A Fast Fourier Transformation is performed on the experimental displacement field at the section of biggest radius. The harmonics corresponding to the elastic and plastic trivial displacements are removed from the solution in order to visualize an approximation of the buckling mode. The normalized buckling modes are presented in Figure 5.23 at the initiation point and at the maximum pressure point. They are plotted in a cylindrical reference frame as in Figure 5.1(b). The
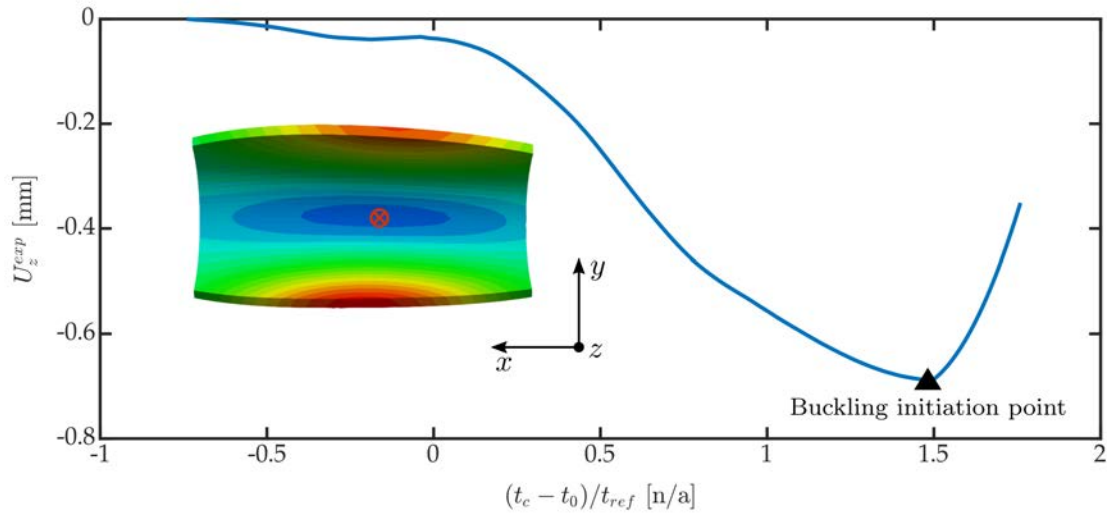
(a)
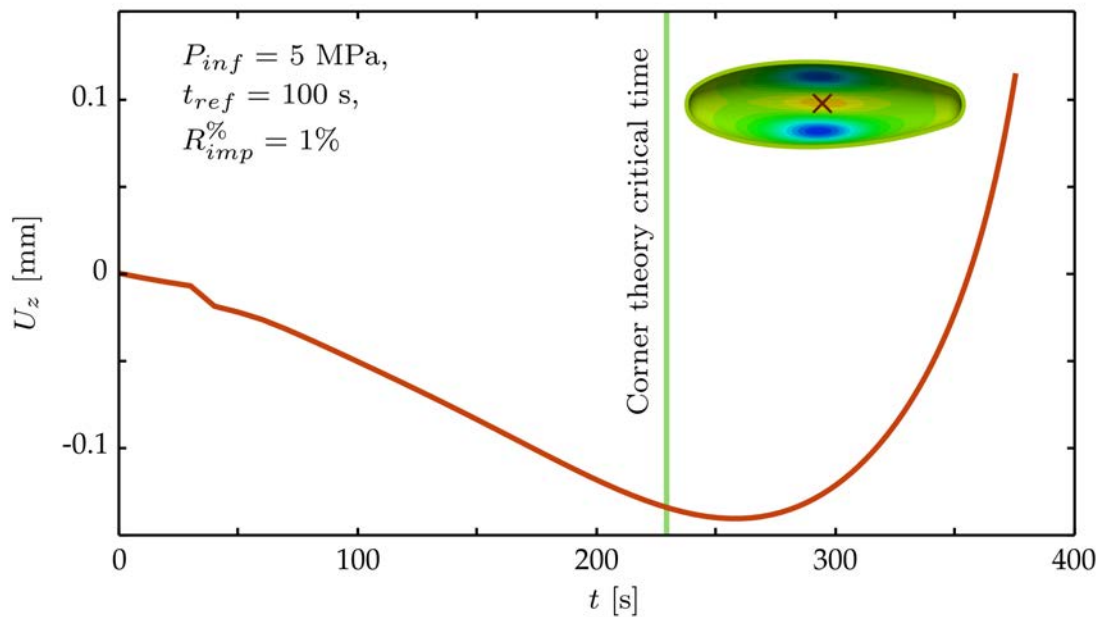
(b)

Figure 5.22: (a) U_z experimental displacement at the top of egg O/003 with respect to the normalized time; (b) U_z displacement at the top of egg from FEA with P_{inf} = 5 MPa, t_{ref} = 100 s and an initial imperfection of 1% of the shell thickness.

FFT analysis was performed on a sub-domain of the total egg, corresponding to the DIC ROI (Region of Interest). Therefore, only a reduced part of the buckling mode is visible, mostly contained between 60° and 120°.

O/00#	Buckling init.		Max. pressure		Testing temp.
	P_c	$t_c - t_0^{mean}$	P_{max}	$t_{max} - t_0^{mean}$	
	MPa	s	MPa	s	°C
2	3.85	90.2	4.17	112.0	27
3	3.90	135.1	4.14	155.8	28
4	3.72	169.4	3.96	206.9	26
5	3.52	1146	3.65	1454	24
6	3.52	1142	3.71	1348	23

Table 5.7: Properties of the buckling initiation point and the maximum pressure point
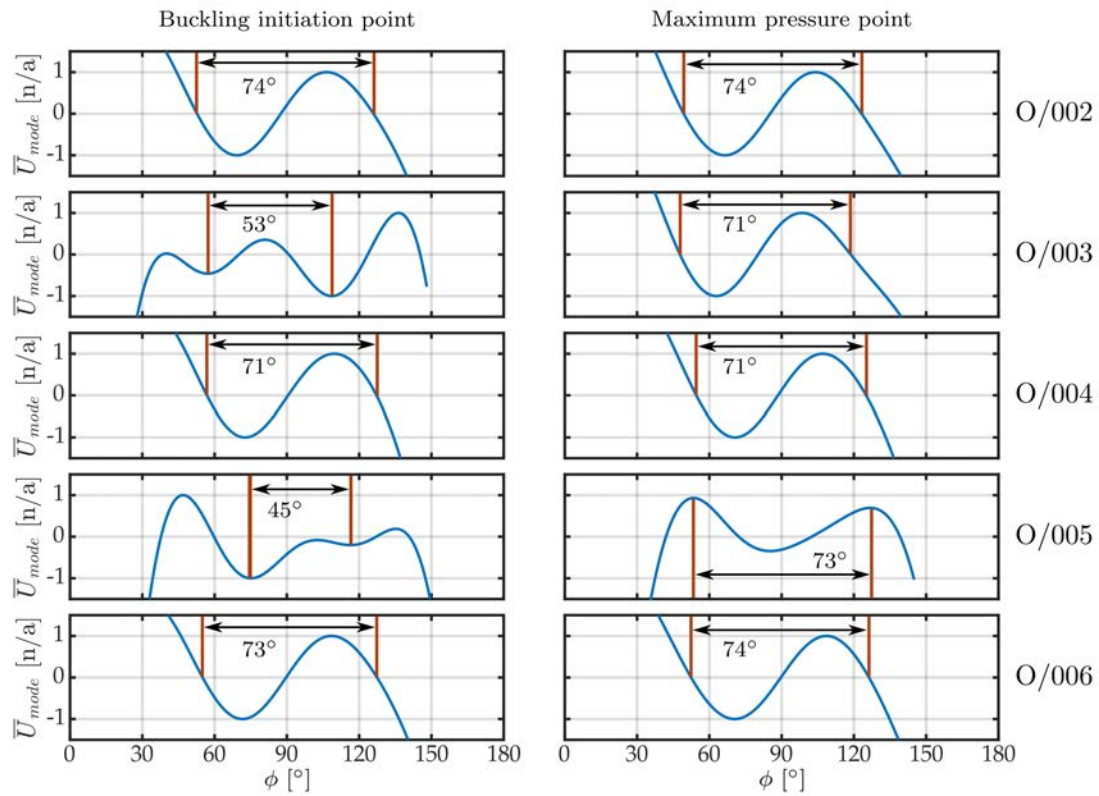
Figure 5.23: Normalized buckling modes on the section of biggest radius for all specimens at the buckling initiation point and at the maximum pressure point

For most of the specimens, the buckling mode is asymmetrical at the maximum pressure point, except for specimen O/005 as already identified earlier. At the buckling initiation point, one can observe quasi-symmetrical buckling modes for specimens O/003 and O/005 and asymmetrical ones for specimens O/002, O/004 and

O/006. Symmetrical modes have a wave length around 73° while the asymmetrical ones have a wave length around 71 °, as shown in Figure 5.23 (right).

The mix of quasi symmetrical (i.e. O/003 and O/005) and asymmetrical buckling modes at the buckling initiation point shows the proximity of the first two buckling modes. Moreover, as discussed in [Gerard and Gilbert 1958], for specimen O/005 the shell seems to hesitate on which mode to buckle. The pressure is constant before the collapse of the shell (cf. 5.13). This special case is discussed in the next section.

5.3.3 FEA of the buckling experiments: Discussion on the material constitutive law and test imperfections

The last step of the analysis of the experiments consists in running FEA of the experiments. The FE modelling of the experiments has several objectives.

First, the FEA is used to define the yield stress decrease (ΔR_0). The FEA is also used to assess the validity of the material constitutive model with respect to this type of loading.

Finally the FEA is used to assess the potential loading imperfections and their effects on the buckling behaviour. This is done by comparing several models with the experiments.

In all cases SHB8PS element are used to model the egg shells with an updated Lagrangian scheme. Cast3M is used as the FE solver. The reference constitutive law (cf. Chapter 3) is also used here with a possible decrease on the yield stress R_0.

5.3.3.1 Identification of the yield stress decrease ΔR_0

As mentioned many times in this work, the mechanical properties of the material depend on the cooling rate during the solidification of the alloy.

As already introduced in Chapter 3, the yield stress decrease was identified for each specimen using a light FEMU approach. The FE model used for this identification process was detailed in Section 2.5 of Chapter 2. This approach is detailed in Appendix G. The identified yield stress decreases are given for each specimen in Table 5.8.

The identified yield stress decreases are comparable to the ones already identified in this work (cf. Table 3.6). These data are used in the next sections in order to compare the experiments with the buckling predictions.

5.3.3.2 Correlation of the FEA with the experiments

Following the identification of the yield stress decrease, the FEA of each experiment is performed. As an example, Figure 5.24 presents the evolution of the relative and absolute errors between the experimental and the FE displacement field for specimen O/003 and for a selection of time steps.

O/00#	ΔR_0	R_0
	MPa	MPa
2	-5.3	10.1
3	-4.5	10.7
4	-6.1	9.4
5	-4.6	10.9
6	-5.2	10.3

Table 5.8: Yield stress decrease identified in the pre-buckling phase

As shown in Figure 5.24 the absolute error is around 0.02 mm in average and the relative one is lower than 10% on the entire lower skin of the egg portion. As a reminder, the DIC precision is also around 0.02mm. The observed errors are within the DIC process precision tolerance. Moreover, the location of the main error spot is close to the edge of a buckling lobe. In this region the displacement gradient is high, a small error in the location of this edge can increase locally the error.

For all specimens a chronograph presenting the evolution of the error between experimental and numerical out of plane displacements at the section of biggest radius is plotted with respect to time in Figure 5.25. The error is stable until the buckling of the FE model. The FE displacement field diverge from the experimental one. The bifurcation of the FE model seems to happen earlier than the one observed during the experiments.

Even if the numerical buckling seems to happen earlier, it shows that the FE model and the constitutive law correctly model the structural behaviour of the egg portion with the boundary conditions defined in Section 2.5 of Chapter 2. These boundary conditions can impact the buckling behaviour of the egg shell. This point is discussed in the next paragraph.

A good correlation between experiments and simulations is observed, it improves the confidence in the identified constitutive law and the yield stress decrease.

5.3.3.3 Analysis of the imperfections from the boundary conditions

Up to here, all FE simulations of the experiments were performed on the mesh defined from the DIC ROI, this model is called **Model 1**. It was described in Section 2.5 of Chapter 2.

Here, a simulation of each experiment on the equivalent perfect structure is performed. The equivalent perfect structure is defined as the hemi-egg shell perfectly clamped. The simulations on the equivalent perfect structure are run with the same material parameters as for **Model 1**. The experimental pressure history is also applied to the perfect hemi-egg shell. This model is called **Model 2**.

In addition the effect of boundary condition imperfections on the buckling of
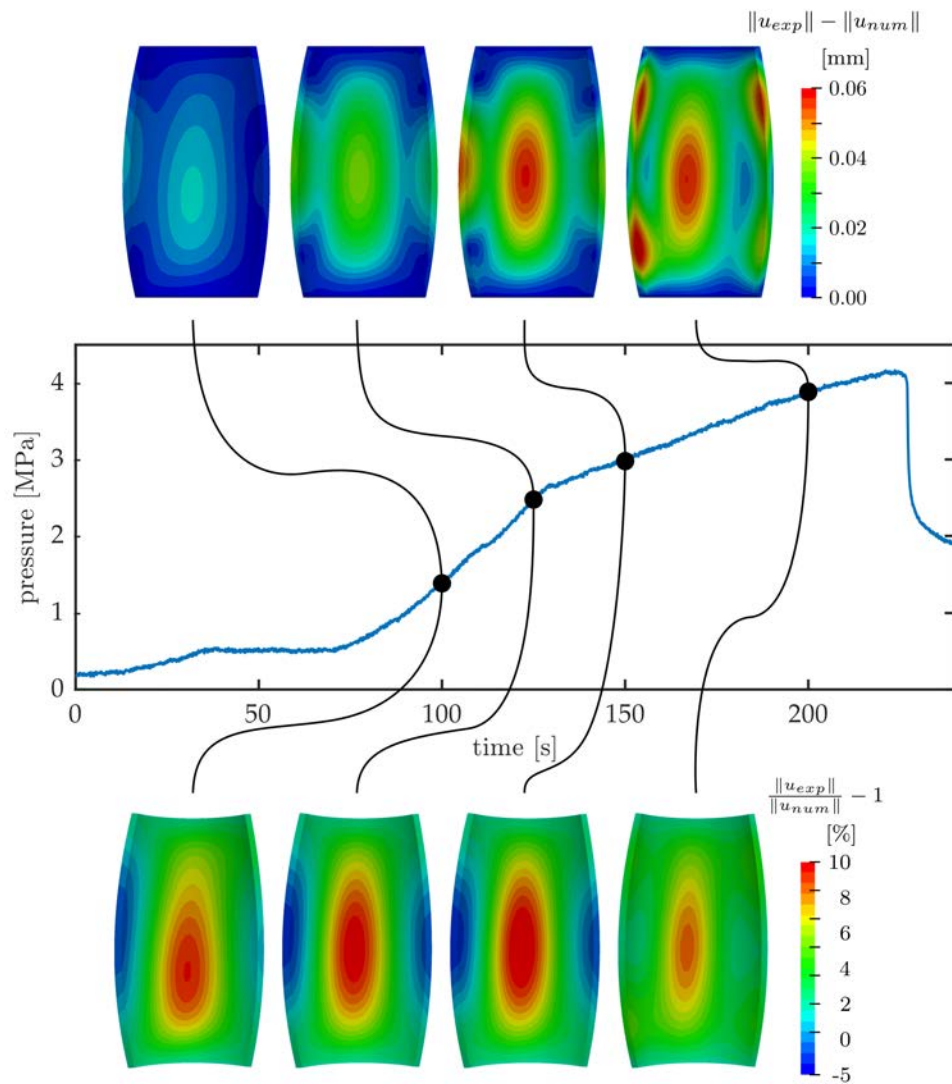
Figure 5.24: Absolute and relative errors between numerical and experimental displacements after the identification of ΔR_0 (O/003).

the hemi-egg is studied through another model called **Model 3**. In this model the boundary conditions are softened compared to the ones of **Model 2**. The details of **Model 3** are discussed in a further paragraph.

All models are described in Table 5.9.

Observation of the boundary condition imperfections

Because of the good correlation previously observed between the FEA on **Model 1** and the experiments, any difference between the results of **Model 1** and **Model 2** would show the effects of boundary condition imperfections.
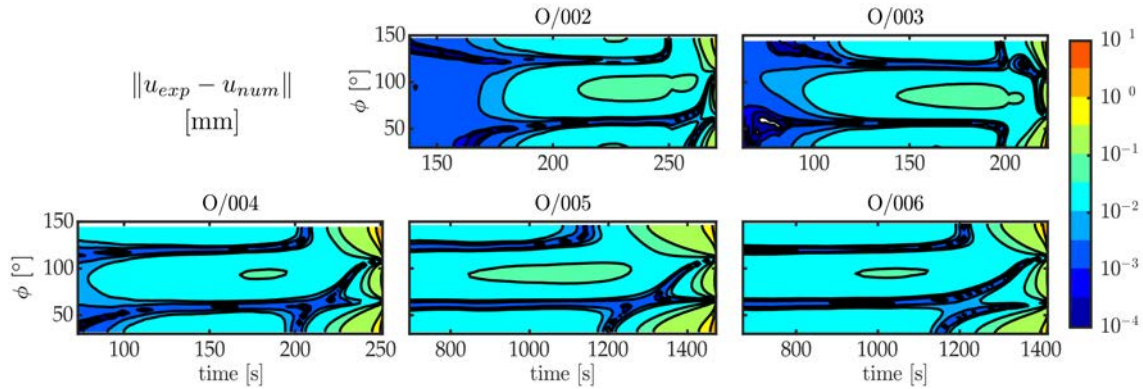
Figure 5.25: Chronograph of the error on the out of plane displacement between experiments and simulations at the section of biggest radius for all specimens

Models	Model 1	Model 2	Model 3
Mesh	DIC ROI (in blue)	Hemi-egg	Hemi-egg
FE elements	SHB8PS		
B.C.	DIC disp. (cf. Section 2.5)	Perfectly clamped	Softened (cf. Figure 5.28)
Load	Mean experimental pressure		
Material	Mean reference law and yield stress decrease (cf. Tables 3.5 and 5.8)		

Table 5.9: Summary of FEA models

To illustrate this point, the evolution of the out of plane displacement of a point on the top of the egg is plotted with respect to time for both models (i.e. **Model 1** and **Model 2**) in Figure 5.26(a).

As shown in Figure 5.26(a), the displacements extracted from the results of **Model 1** and **Model 2** diverge from the beginning of the experiment. This divergence is due to the bending of the specimen holder as well as the specimen flange. The bending is due to the applied pressure. Indeed, in **Model 2** the hemi-egg is perfectly clamped, the point on the top of the egg only experiences the displacement due to the deflection of the egg. In Figure 5.26(b) the vertical displacement (i.e.

172
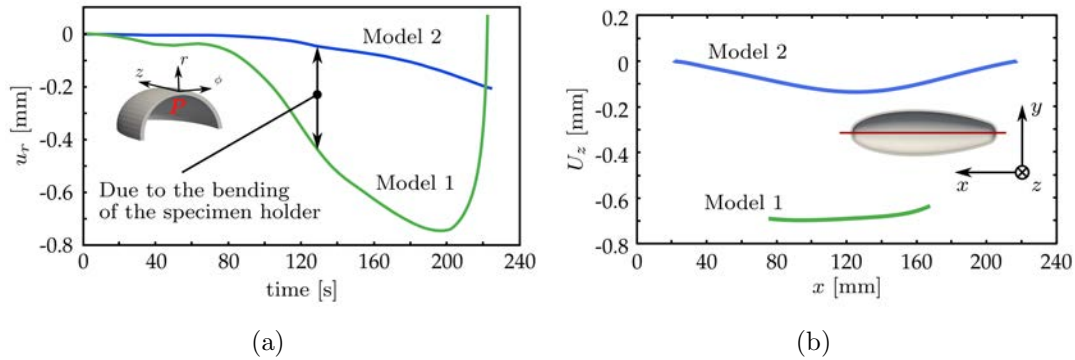
Figure 5.26: (a) Effect of the loading imperfection on the radial deflection u_r of a point (P) on the top on the egg (O/003), green **Model 1**, blue **Model 2**; (b) Effect of the loading imperfection on the vertical deflection U_z of an axial section of the lower skin (red line) of egg O/003), green **Model 1**, blue **Model 2**

U_z) of the axial section of the lower skin (red line in Figure 5.26(b)) is depicted for **Model 1** and **Model 2** at $t = 200$ s. The displacement fields have different shapes. On **Model 2**, the deflection in the center due to the pressure is well visible. On **Model 1**, the same deflection is embedded in the bending displacement field of the specimen holder. Therefore the deformation is less localized in the center of the egg.

The bending moment applied to the egg during the experiment affects the axial (σ_z) and the circumferential (σ_ϕ) stress amplitudes as shown in Figure 5.27 for a point on the top of the egg.
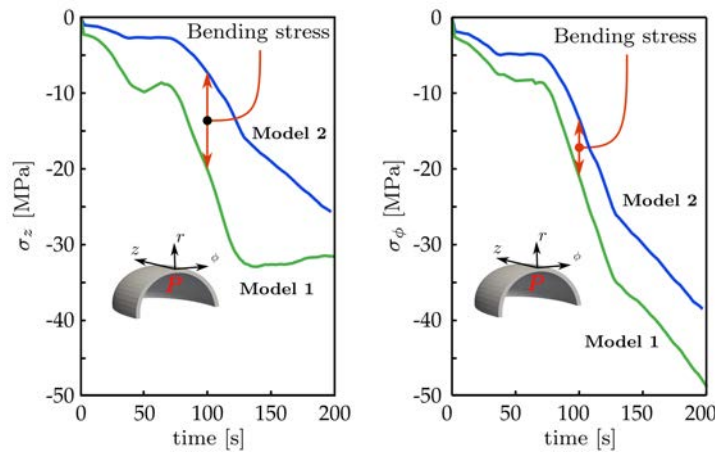
Figure 5.27: Effect of the loading imperfection on the stress state for a point (P) at the top of the egg (O/003), σ_z the axial stress and σ_ϕ the circumferential stress

The axial stress is more affected than the circumferential one as seen in Figure 5.27. As the egg buckles on a circumferential mode, this axial bending of the egg

should not affect the buckling behaviour of the shell. The effects of such loading imperfections are discussed in the next paragraph.

Effect of boundary condition imperfections on buckling

In this paragraph we intend to evaluate the effect of the boundary imperfections on the buckling behaviour of the hemi-egg shell.

In the previous paragraph a first source of imperfection was identified, i.e. the bending of the specimen holder on the egg flange. It is also very likely that the joint between the egg flange and the hemi-egg shell is not perfectly rigid.

In order to study the effect of both sources of imperfections two additional models included in **Model 3** were defined. They are named **Model 3'** and **Model 3''**, and are defined as follows:

- **Model 3'**: A displacement field is applied to the edge of hemi-egg shell. This field is derived from the elastic bending of a clamped circular plate: $w = A \left(r^2 - R^2 \right)^2 / R^4$, where R is the plate radius, r is the radial coordinate of the current point and A is the maximum deflection at the center of the plate. In addition A is a proportional function of the applied pressure. $A = A_p \times P$. As the FE elements are volume shell elements (SHB8PS), the rotations are also constrained.

- **Model 3''**: The edge of the external skin of the hemi-egg shell is perfectly clamped ($U_x = U_y = U_z = 0$). Vertical elastic springs are used on the edge of the inner skin in order to model a rotational elastic stiffness. This allows to model a flexible joint between the hemi-egg shell and its flange.

Figure 5.28 presents both sets of boundary conditions.

The critical time ratios were predicted for both perturbed boundary conditions as well as for the perfect ones. The predicted critical time ratios are summarized in Figure 5.29. Blue bars are associated to **Model 2**, the red ones to **Model 3'** and the yellow ones to **Model 3''**. The buckling modes are not affected by perturbed boundary conditions.

As we can notice the predicted critical time ratios evaluated with **Model 3'** (red bars) are generally slightly higher than the ones predicted with **Model 2** (blue bars). Moreover the critical time ratios evaluated with **Model 3''** (yellow bars) are generally lower than the ones predicted with **Model 2**. The hemi-egg shell seems more sensitive to a small flexibility at the flange/egg joint than to the bending of the specimen holder.

In **Model 3''** the flange/egg joint flexibility was magnified. A ΔU_z^{flex} at buckling of 0.18 mm was numerically observed between the lower and upper skin edges, as shown in Figure 5.30. This would correspond to a very flexible material. In reality the joint is stiffer.

It seems that the bending introduced in **Model 3'** stiffens the structure and therefore delays the bifurcation. This is probably due to the compressive axial
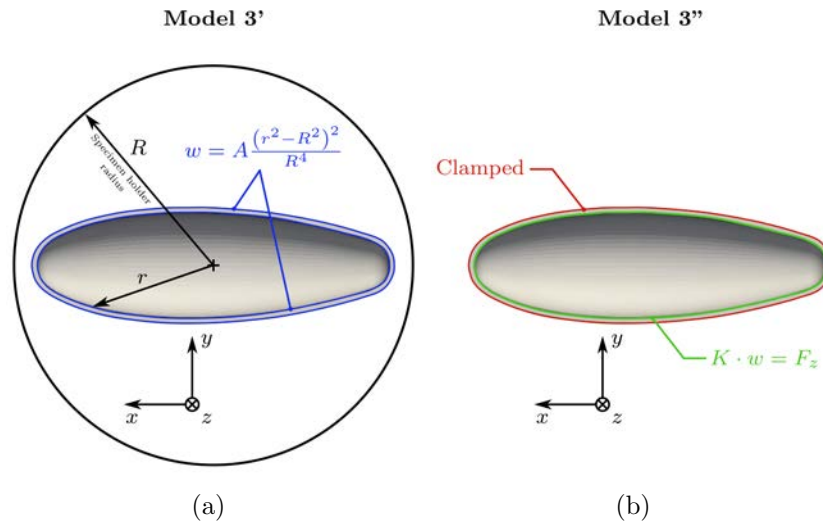
Figure 5.28: (a) Boundary conditions on **Model 3'**; (b) Boundary conditions on **Model 3"**.
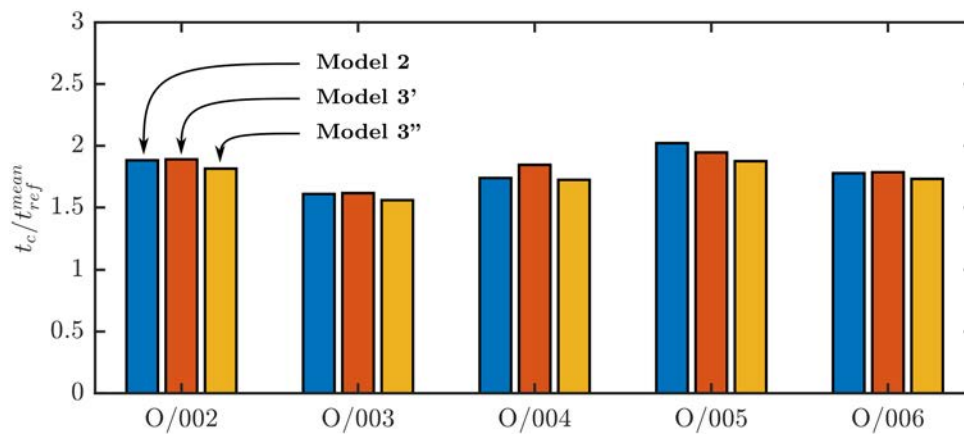
Figure 5.29: Effect of the imperfections on the boundary conditions on the predicted critical time ratio for all specimens; for **Model 3'** $A_p = 0.275$ mm.MPa^{-1}; for **Model 3"** $K = 2000$ N.mm^{-1}

stress introduced by the bending load. On the other hand, the flexibility introduced in **Model 3"** reduces the critical time ratio as its boundary conditions are more flexible.

In Figure 5.29 all critical time ratio are very close. Therefore the predictions from **Model 2** are kept as reference predictions.
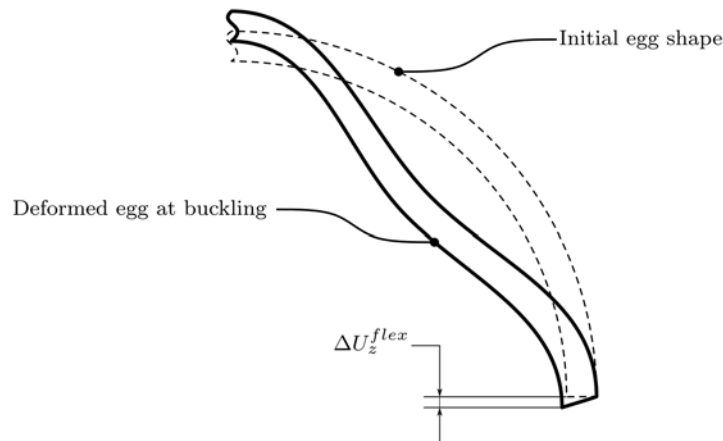
Figure 5.30: Displacement of the edge of the lower skin of **Model 3"** due to the introduced flexibility

5.4   Validation of the buckling prediction method

In the previous sections the numerical and experimental sets of data to be compared have been generated. In this section the comparison of both sets of results is performed and discussed in order to validate the bifurcation prediction method.

5.4.1   Comparison of the experimental data with the numerical predictions

In the previous section, the yield stress decrease was defined for each specimen. Moreover different pressure profiles were defined for each experiment according to the uncertainty on the pressure measures. Finally, the boundary condition imperfections were neglected. In this section the numerical predictions of the buckling of each specimen are computed according to the yield stress decrease identified, the different pressure profiles defined and the perfect boundary conditions. The calibrated corner theory is used to predict the buckling of the perfect hemi-egg shell (i.e. **Model 2** previously defined).

Comparison of the critical values

In Figure 5.31, the predictions are compared to the experimental critical values defined with respect to both criteria, the buckling initiation point (in blue) and the maximum pressure point (in red). Therefore the blue points correspond to the critical values predicted with respect to the experimental critical values defined on the buckling initiation point. The red points correspond the predicted critical values with respect to the experimental critical values defined on the maximum pressure point. Each symbol is associated to a specimen.

Each set includes all experiments and the different pressure profile scenario (mean, min and max, cf. Table 5.4. Ideally, at least one set of crosses should be superimposed with the black curve (defining the ideal prediction).

(a)   (b)
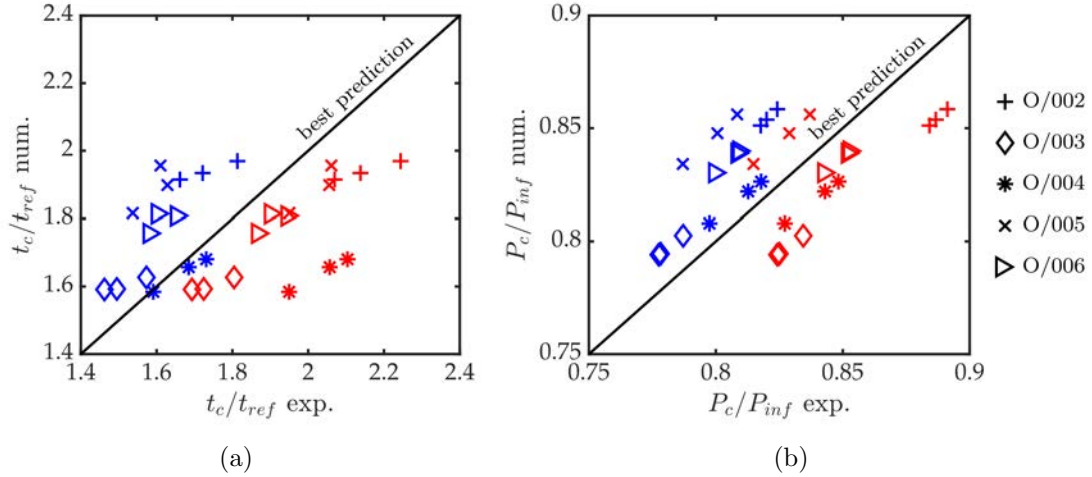
Figure 5.31: (a) Comparison of the experimental normalized critical times with the predicted ones; (b) Comparison of the experimental normalized critical pressures with the predicted ones; both experimental detection methods are evaluated (buckling initiation points in blue and maximum pressure point in red).

As shown in Figure 5.31 both sets of coloured symbols are close to the black curve. This observation is true for the critical pressure (Figure 5.31(b)) as well as for the critical time (Figure 5.31(a)). Each set of coloured symbols is positioned on one side of the black curve. It shows that the prediction method predicts a first bifurcation just after the assumed buckling initiation point, and just before the maximum pressure point. It is likely that the buckling initiates in this range for all experiments, but we cannot be sure where within this range.

Comparison of the buckling modes

In order to completely validate the prediction method, the buckling modes extracted from the experiments need to be compared to the predicted ones. As discussed in Appendix G, the buckling mode is not affected by neither the saturation pressure P_{inf} nor by the reference time t_{ref}. An extraction of the first predicted buckling mode on the section of biggest radius is presented in Figure 5.32.

In Figure 5.32, we can visualize the wave length of the buckling mode as well as its asymmetric shape. The wave length is equal to 87° as shown in Figure 5.32. This value is close to the one found experimentally for specimens O/002, O/003, O/004 and O/006 at the maximum pressure time (cf. Figure 5.23).

The 15° difference can be explained by the FFT process applied to the egg portion. As the FFT was performed on a 120° angular sector, some wave lengths
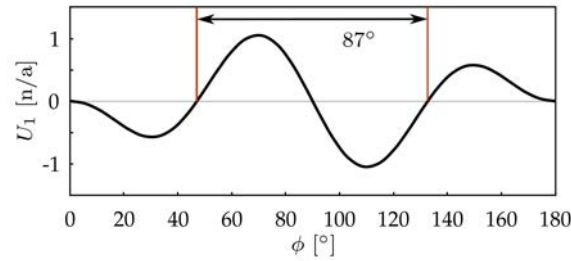
Figure 5.32: Shape of the normalized first buckling mode predicted. Shape extracted on the lower skin and on the section of biggest radius

can be missing in the FFT analysis. Moreover, it was assumed that the harmonics corresponding to the trivial elasto-plastic deformation did not contribute to the buckling mode. This is globally true, but a small amount of these harmonics can probably contribute to the buckling mode. Therefore it would not be relevant to compare more accurately the predicted mode with the experimental ones, as this last ones are only an approximation of the real buckling modes. Nevertheless, more than the wave length value, the global shape and the asymmetrical character of the experimental buckling modes (cf. Figure 5.23) are very similar to the one found with the prediction method.

The case study of specimen O/005 is interesting since the experimental buckling mode is symmetric. It corresponds to the second buckling mode (as shown in Table 2.5). The wave length of the second mode is equal to the wave length of the first one, only the phase is different. The experimental buckling mode for specimen O/005 and the second predicted buckling mode share similar wave lengths and the symmetrical property.

All other specimens buckle on an asymmetrical mode. As the first two modes almost coincide for this structure (cf. Table 5.3), in some specific cases the second mode can appear. The asymmetrical mode is often preferred, as an asymmetrical source of imperfection always exists. The O/005 specimen allows to observe this phenomenon and also to confirm that the two first modes coexist at buckling initiation.

All the buckling characteristics (critical values and buckling modes) identified from the experiments agree well with the numerical predictions.

5.4.2 Discussion on the relevance of the corner theory

As seen in the first section of this chapter, the buckling prediction method is based on the corner theory of Christoffersen and Hutchinson. Two parameters θ_c and θ_0 define the corned yield surface and the transfer function from the deformation theory to the elastic unloading.

Here the effect of these two parameters on the critical values is discussed as well

as the relevance of using such approach. Using a set of reduction factor, defined numerically, the experimental results are projected on an axis parallel to the t_{ref} axis in the space defined by $(P_{inf}, t_{ref}, \Delta R_0)$. This axis is defined by $P_{inf} = 4.5$ MPa and $\Delta R_0 = $ -5 MPa. These parameters were selected according to the experimental pressure profiles and the identified yield stress decreases. The reduction factors are defined for each critical value (P_c, t_c) as follows:

$$
\begin{aligned}
r_{P_c} &= P_c^{num}(P_{inf}, t_{ref}, \Delta R_0)/P_c^{num}(4.5, t_{ref}, -5), \\
r_{t_c} &= t_c^{num}(P_{inf}, t_{ref}, \Delta R_0)/t_c^{num}(4.5, t_{ref}, -5).
\end{aligned}
\tag{5.10}
$$

The projected experimental critical values $P_c'^{\,exp}$ and $t_c'^{\,exp}$ are defined as follows:

$$
\begin{aligned}
P_c'^{\,exp} &= P_c^{exp}/r_{P_c}, \\
t_c'^{\,exp} &= t_c^{exp}/r_{t_c}.
\end{aligned}
\tag{5.11}
$$

The experimental critical values corresponding to the buckling initiation point and the maximum pressure point are projected using this last set of equations. They are plotted with respect to t_{ref} in Figure 5.33. The critical values corresponding to the buckling initiation point criterion are depicted by blue box plots while the red box plots correspond to the maximum pressure point criterion. Each experiment has two box plots, a red one and a blue one. The box plots include the experimental sources of discrepancy, as the different pressure profile scenario (cf. Table 5.4) and the yield stress decrease discrepancy (cf. Table G.1 in Appendix F).

In addition, the prediction curves corresponding to the corner theory with $\theta_c = $ 105, 112.5 and 120°, and $\theta_0 = 0.45(\theta_c - pi/2)$ with $P_{inf} = 4.5$ MPa and $\Delta R_0 = $ -5 MPa are also plotted in Figure 5.33. The three curves, green, black and magenta correspond respectively to $\theta_c = $ 105, 112.5 and 115°. These values of θ_c are within the parameters tolerance region defined in Figure 5.10, with $\theta_c = 112.5°$ the optimal and reference value. First, the three curves are almost identical and difficult to distinguish. Moreover both set of box plots still envelop the prediction curves. It means that in the tolerance area defined, the value of θ_c does not affect significantly the predictions.

In order to evaluate the effect of θ_0, the same method was used, with $\theta_c = 112.5°$ and $\theta_0 = 0.45(\theta_c - pi/2)$ as reference and $\theta_c = 117.5°$ and 125° and respectively $\theta_0 = 0.25(\theta_c - pi/2)$ and 0 as second and third point. This new set of data is also in the tolerance area of parameters defined in Figure 5.10. The third value of θ_0 was chosen in order to observe the effect of a fully non-linear tangential moduli and therefore a tangential bifurcation. The predictions using these three couples of parameters and $P_{inf} = 4.5$ MPa and $\Delta R_0 = $ -5 MPa are plotted in Figure 5.34 with the projected experimental critical values. Same conclusions as for θ_c can be made. The effect of θ_0 on the prediction is also negligible here as long as the corner theory parameters stay in the tolerance area defined.
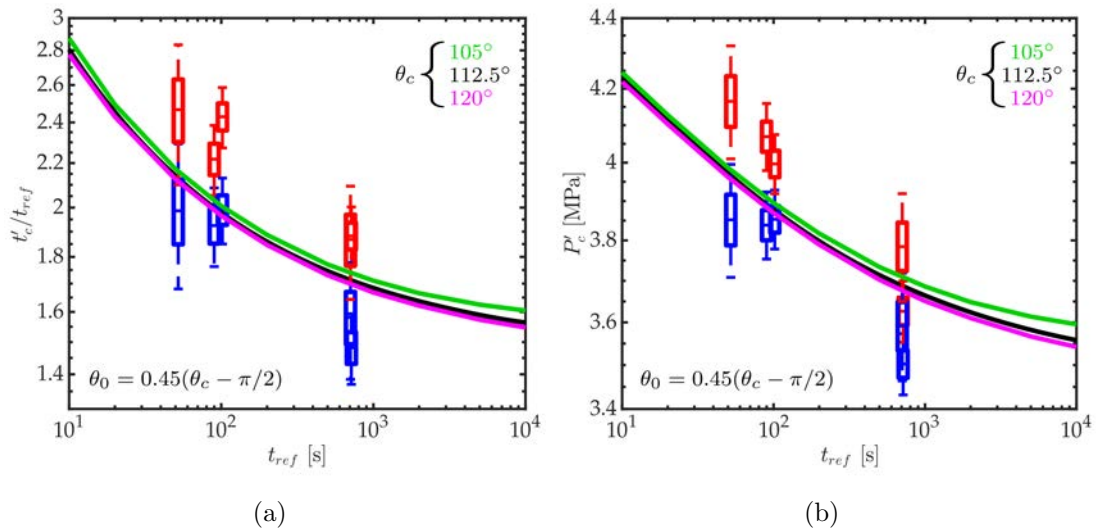
Figure 5.33: (a) Comparison of the projected experimental critical time ratio with the numerical predictions for three values of θ_c; (b) Comparison of the projected experimental critical pressures with the numerical predictions for three values of θ_c.

When θ_0 is 0, the prediction increases as the tangential moduli is stiffer due to the non-linearity. The predictions obtained with $\theta_0 = 0$ (magenta curve) are closer to the maximum pressure point critical values. Nevertheless this set of predictions is still within the buckling range defined experimentally. The particular value of θ_0 is very specific of the corner theory. In this manner, the predictions are necessarily different to the predictions obtained with *Hencky*'s deformation theory or the *Mises* flow theory. This particular point allows to validate the relevance of using the corner theory for structures subjected to non-proportional loadings.

For any parameters within the tolerance area defined in Section 5.1, the buckling predictions given with the corner theory agree well with the experimental critical values.

Finally the predictions using the corner theory with $\theta_c = 112.5°$ and $\theta_0 = 0.45(\theta_c - pi/2)$ are compared to the predictions obtained with the *Mises* flow theory and *Hencky*'s deformation theory in Figure 5.35. The three curves, green, black and magenta correspond respectively to the predictions using the *Mises* flow theory, the corner theory and *Hencky*'s deformation theory.

The different predictions are also compared to the experimental critical values with the same conventions as in Figure 5.33. One can see that the *Mises* flow theory overestimates the critical values. The predicted values are even higher than the critical values associated to the maximum pressure point criterion. Concerning the deformation theory, as the average value of θ is reasonable, the corner theory is very close to the deformation theory. Nevertheless some differences can be observed when t_{ref} is low and especially when t_{ref} is high, as shown in Figure 5.35.

180
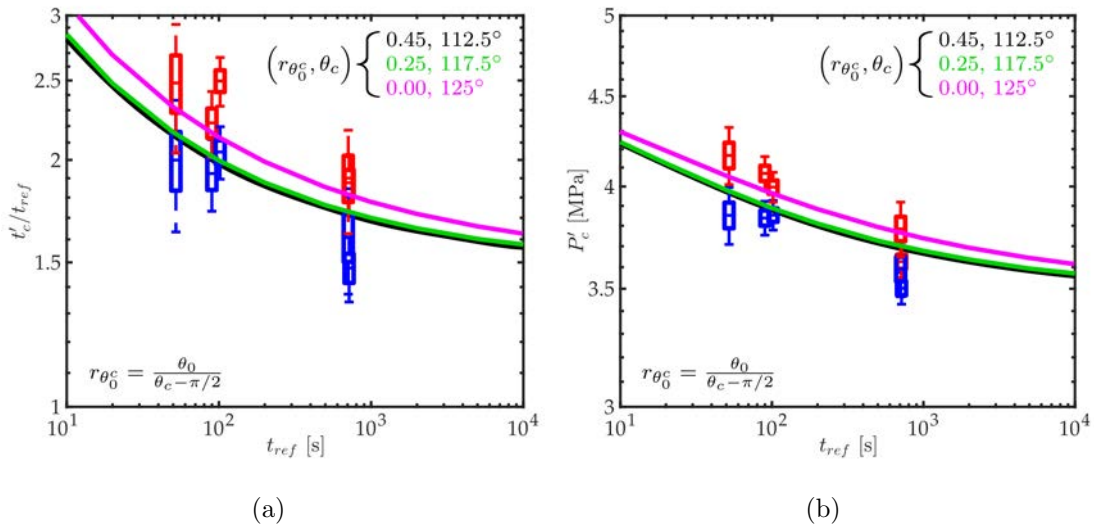
Figure 5.34: (a) Comparison of the projected experimental critical time ratio with the numerical predictions for three values of θ_0; (b) Comparison of the projected experimental critical pressures with the numerical predictions for three values of θ_0.
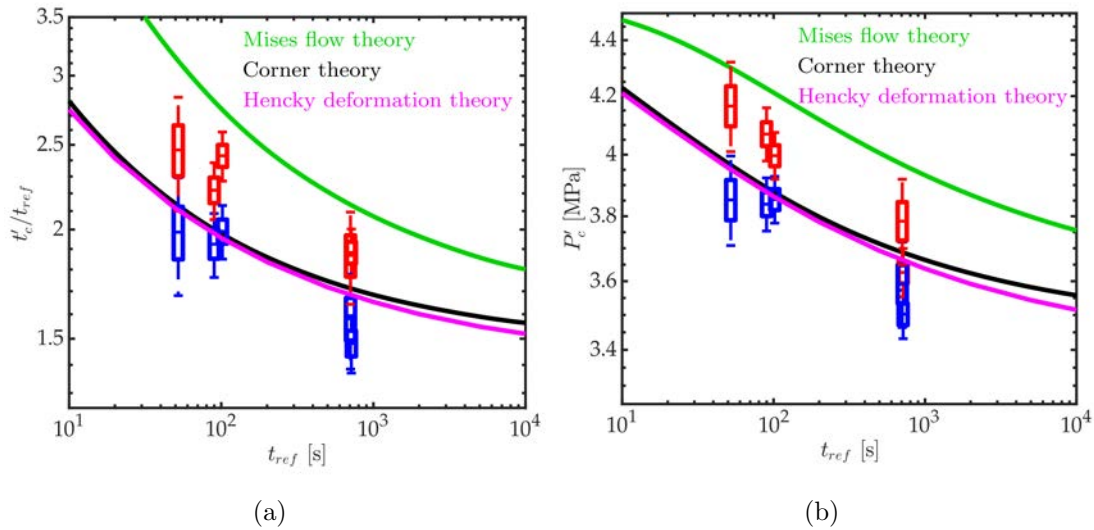
Figure 5.35: (a) Comparison of the three prediction methods with the projected experimental critical time ratio; (b) Comparison of the three prediction methods with the projected experimental critical pressures.

The corner theory well predicts the buckling of moderately thick hemi-egg shells subjected to external pressure. It shows better agreement with the experiments than the *Mises* flow theory especially. In addition, it allows to consider within the same model, the buckling paradox extensively discussed in the literature for elasto-plastic

181

materials, and non-proportional loadings.

It is also possible to see that the predictions from the corner theory are very close to the ones from the deformation theory. Budiansky demonstrated in [Budiansky 1958] that the predictions from the slip theory for quasi-proportional loadings were similar to the ones from the deformation theory. Therefore, the deformation theory can be used to predict the buckling of shells subjected to quasi-proportional loadings, such as the hemi-egg shells tested in this work. This work allows to extend the result from [Budiansky 1958] for elasto-plastic materials to elasto-visco-plastic ones.

5.5   Conclusion

Following the proposed identification of the corner theory parameters, θ_c and θ_0, and a parametric analysis on the buckling of the hemi-egg shell, the experimental results of the buckling of hemi egg shells were presented.

A good estimation of the buckling behaviour of the hemi-egg shell was given with the buckling prediction method. The predicted critical values are within the experimental buckling range defined. The predicted buckling modes present similar shapes with the observed ones.

We also successfully observed a symmetrical buckling mode with specimen O/005. It experimentally demonstrated the mode proximity identified numerically.

The experiments were performed for different pressure rates. The predictions show good agreement with experiments for all pressure rates experimented. It validates the relevancy of *Bodner*'s hypothesis for this shell geometry and this loading case.

The coupling of the corner theory with *Bodner*'s hypothesis predicts well the buckling of hemi-egg shells subjected to external pressure.

Predictions with other corner theory parameters were also compared to experimental data. Within the tolerance area defined, the corner theory parameters have a limited impact on the buckling predictions. The correlation with the experiment is still good.

The corner theory parameters have to be considered as material parameters, as they define the shape of the corner on the yield surface, the loading/unloading criterion and the tangential constitutive law. Their identification and the definition of the tolerance region allow to set a frame around the usage of the corner theory. Ideally these parameters would need to be identified on specific tests with non-proportional loadings.

Finally, the corner theory was compared to the classic *Mises* flow theory and *Hencky*'s deformation theory. As expected the *Mises* flow theory overestimates the critical values. *Hencky*'s deformation theory gives critical values close to the ones predicted with the corner theory for perfect structures. This can be explained by the limited non-proportionality of the loading observed on the hemi-egg shell.

The extension of the deformation theory to quasi-proportional loadings (cf. [Bu-

diansky 1958]) for elasto-plastic materials was also observed for elasto-visco-plastic materials. It means that the deformation theory can be used efficiently to predict the buckling of thick elasto-visco-plastic shells subjected to quasi-proportional loadings. In the case of a very non-proportional loading, the corner theory of *Christoffersen* coupled with *Bodner*'s hypothesis can be used.

The chapter demonstrates the efficiency of the corner theory and the deformation theory coupled with *Bodner*'s hypothesis to predict the buckling of moderately thick shells. The corner theory requires the identification of θ_c and θ_0. The buckling prediction method was also validated experimentally. The results presented here could be easily extended to thick and very thick shells, as long as they experience buckling. This method allows us to give a good estimate of the buckling load and bucking modes for thick elasto-visco-plastic shells subjected to quasi-proportional and non-proportional loadings.

Conclusions and perspectives

Conclusions

In this work the numerical and experimental aspects of the buckling behaviour of elasto-visco-plastic thick shells were studied. A first part was dedicated to the development of a numerical method predicting the buckling of thick elasto-visco-plastic shells. The other was oriented on the experimental validation of the developed buckling prediction method.

The numerical method was built on two main concepts. The first one allows to have an estimation of the bifurcation point for elasto-visco-plastic materials. This estimation was first introduced by Bodner, Naveh, and Merzer for thin shells. To define this estimation, it is assumed that the strain rate is constant at buckling for elasto-visco-plastic materials. The second one is based on the corner theory. Following several discussions in the literature on the buckling paradox, Christoffersen and Hutchinson proposed an incremental approach to rationalize the buckling paradox to structure subjected to non-proportional loadings. This approach was presented in Chapter 1 and extended to elasto-visco-plastic materials in Chapter 2. Both elements were assembled into a single method to predict the buckling of thick elasto-visco-plastic shells subjected to non-proportional loadings.

In order to validate this buckling prediction method, an experimental strategy was developed. It includes a fine characterisation of the material behaviour and the development of two different types of buckling experiment. These two different types of experiment also had different objectives.

A first set of buckling experiments was focused on the buckling behaviour of thick elasto-visco-plastic plates subjected to in-plane compressive load. This particular case presented an interesting buckling behaviour. First it follows the buckling paradox. Then its shape is so simple that many post-processing of the displacement fields can be performed in order to characterise the buckling initiation. This particular point allowed us to investigate the limitations of *Bodner*'s hypothesis. The methods developed showed good correlation with the experiments. Nevertheless, we found that it should be limited to small strain rates, lower than 0.01 s^{-1}. This first observation is important, as for higher strain rates more sophisticated methods should be used to predict the buckling of elasto-visco-plastic structures. A possible candidate could be the method developed in [Triantafyllidis, Massin, and Leroy

185

1997].

The second set of buckling experiments investigated the buckling behaviour of thick elasto-visco-plastic hemi-egg shells subjected to external pressure. Because of the loading and the boundary conditions, this type of structure experiences non-proportional loadings as the sodium manifold. These experiments allow us to evaluate the accuracy of the corner theory to predict the buckling of thick structures subjected to non-proportional loadings. A good agreement of the predictions with the experiments was also observed. This set of experiments also shows that the deformation theory can be used to predict the buckling of thick elasto-visco-plastic shells subjected to quasi-proportional loadings. While the deformation theory allows to safely size to buckling a thick shell subjected to a quasi-proportional loading, the corner theory allows a better prediction thanks to its two additional parameters θ_c and θ_0. Nevertheless, these two parameters needs to be identified carefully in order to be considered as material parameters and to not be structure dependent.

For all types of experiment, DIC methods to measure the displacement fields on the surface of the different specimens was extensively used. This particular tool allows us to identify the buckling modes for the different experiments. For both types of experiment, mode proximity and simultaneous bifurcations or successive bifurcations were observed. These experimental observations were also observed with the prediction methods. This specific point is a valuable experimental result, as it improves the confidence in the prediction of the bifurcations and the buckling modes. The mode proximity could not have been observed without the use of DIC methods. Coupled to the DIC methods, the implementation of the SHB8PS in Cast3M allows to improve the link between the experiments and the FE models.

The present work presented a unified method to predict the buckling of thick elasto-visco-plastic shells subjected to quasi-proportional and non-proportional loading. The method was validated against experiments on several shell structures subjected to different types of loading. The method developed here can be used on other structures with a rate-dependency. Nevertheless, the method requires a fine characterisation of the mechanical behaviour of the material as well as the corner theory yield surface. Moreover the present method is limited to small strain rates, lower than 0.01 s^{-1}.

The method presented and validated in this document gives good results within the limitations defined previously. As it uses existing bricks of any FE software, the prediction method could be implemented to any FE software. At the moment, it is implemented in Cast3M through a new procedure and for any elasto-visco-plastic user materials.

Perspectives

Industrial perspectives

The prediction method derived in this work could be easily used for the sizing of thick industrial components presenting an elasto-visco-plastic behaviour, such as the sodium manifold or pipes subjected to complex loading.

Moreover the 316L(N) stainless steel alloy is often modelled by a Chaboche constitutive model, as used in this work. This would facilitate the application of the present method to the sizing of the sodium manifold. As shown in this work a statistical description of the material behaviour should be used in order to safely size the component.

Other variables would also need to be considered, as the thermal gradient, the manufacturing tolerance, the different load cases, the loading history, and so on. As discussed in the last chapter, the boundary conditions and more importantly the perfectness of the boundary conditions can affect the buckling behaviour. The joint between the sodium manifold and the heat exchanger module would need to be well characterized and modelled. One solution to solve this issue could be the modelling of the boundary condition with a super-element. This last one would model the stiffness of the joint. Its contribution to the global stiffness matrix would need to be considered as well.

Finally structural experiments would still be necessary to validate the sizing of such components, as the buckling is a complex problem and no model can include all physical phenomena.

Scientific perspective

In this work the prediction method was compared to two different experiments and one material. In order to increase the confidence in the actual method, additional experiments could be performed on more academic structures, such as plates or pipes. Different loadings and boundary conditions could be experimented. Moreover a more non-proportional load case would need to be performed. This could be investigated through the combination of different simple load cases, as the combined torsion and external pressure on a pipe or the torsion and compression of a pipe.

Moreover the model material used in this work presented some manufacturing issues, as the cooling rate dependency. Similar experiments, as presented in this work, could be performed with a more compliant material.

In this work the buckling experiments were performed in the elasto-visco-plastic regime. In order to complete the experimental data base, buckling experiments in the creep regime would be valuable. The experiments presented by Gerard and Gilbert in [Gerard and Gilbert 1958] could be compared to the predictions of the present methods. Nevertheless only proportional loadings were tested in [Gerard and Gilbert 1958]. Creep buckling experiments on the hemi-egg shell geometry presented would

be more valuable. Moreover in the creep regime the egg-shell showed interesting numerical results, as shown in 2.9. This point would need more attention.

As already discussed in this document, a more rigorous method could be applied to predict the buckling of thick elasto-visco-plastic shells. This method would be based on the sufficient condition defined by Triantafyllidis, Massin, and Leroy in [Triantafyllidis, Massin, and Leroy 1997]. It could be coupled to a complex yield surface including corners. This method could cover more load cases, especially with high strain rates. It would also give a rigorous prediction of the buckling. In order to use this type of approach the fine definition of the complex yield surface would be required. This could be done with the adequate experiments and instrumentation. The definition of such yield stress is a complex task indeed. Moreover the implementation of the sufficient condition defined by Triantafyllidis, Massin, and Leroy into a FE software would not be straightforward. This method would be interesting to study as it removes the main hypothesis of this work, *Bodner*'s hypothesis. Experiments at high strain rate would also be required in order to validate this method.

Appendix A

Mathematical notations and algebraic operators

We describe in this appendix the main notations used in the manuscript as well as the algebraic operators.

Contents

A.1   General notations and operators

The following conventions are generally respected for notations and algebraic operators:

- The scalar values are written with normal typology or in capital letters. (a, b, A, B,).

- Vectors are written in bold for normal typology and capital letters. ($\mathbf{a}$, $\mathbf{b}$, $\mathcal{A}$, $\mathcal{B}$).

- Matrices are written in bold and capital letters. ($\mathbf{A}$, $\mathbf{B}$).

- Second order tensors for mechanical purposes are written in bold Greek symbols. ($\boldsymbol{\sigma}$, $\boldsymbol{\varepsilon}$).

- Fourth order tensors for mechanical purposes are written in bold capital or calligraphic letters. ($\boldsymbol{C}$, $\boldsymbol{\mathcal{L}}$).

- Matrix product between two second order tensors is denoted without any operator: $\mathbf{A} = \mathbf{BC}$.

- Tensorial product is classically denoted: $\cdot$.

- Scalar product is classically denoted with a point: $.$, it is also denominated dot product.

- Cross product is classically denoted: $\times$.

Global symbol	General description	Example	Description
a	Scalar	p	equivalent plastic strain
A	Scalar	F	Load
$\mathbf{a}$	Vector	$\mathbf{u}$	displacement vector
$\mathcal{A}$	Vector	$\mathcal{U}$	nodal displacement vector
$\mathbf{A}$	Matrix	$\mathbf{K}_t$	tangential stiffness matrix
$\mathbf{A}$	Second order tensor	$\boldsymbol{\sigma}$	Cauchy stress tensor
$\mathbf{A}$	Forth order tensor	$\boldsymbol{C}_t$	Moduli of the tangential constitutive law

Table A.1: Main used notations.

Appendix B

Analysis of the water quenched casting process

This appendix presents the analysis carried out in order to define the parameters of the water quench process.

The key element of the casting process is the water quench as it defines the cooling rate experienced by the alloy. The water quench cooling allows to to obtain a high cooling rate. The value of the cooling rate is completely defined by the mould design, the water temperature and the volume of water used.

The water quench process is finally defined by 5 parameters:

- The thermal conductivity of the mould material;

- The thickness of the mould;

- The effective thickness of the ingot;

- The water temperature;

- The volume of water.

It is very difficult to measure precisely the cooling rate, therefore the optimal cooling rate was defined through numerical simulations and material observations. Most of the material observations are visual. They are completed with the mechanical properties obtained through tests.

Numerically, the cooling rate is easy to obtain. This cooling rate is evaluated at 220°C, defining the cooling rate at solidification. The density of porosity can be linked to the cooling rate gradient within the thickness.

A parametric study was performed with Cast3M to study the effect of the water temperature, the mould material and the mould thickness. Semi-infinite plates model the mould and the ingots, as depicted in Figure B.1(a) .

The water is considered as a perfect heat source. The thermal fluxes between the water and the mould, and the liquid alloy and the mould are modelled by convective flux. The exchange coefficient between water and the mould is plotted with respect of the hot surface temperature and the water temperature in Figure B.1(b), the law is extracted from ["Simulation of Heat Treatment Distortion"]. The exchange coefficient between the liquid alloy and the mould is set to 10 mW.mm^{-2}.K^{-1} (cf. [Bricard and Gobin 2001]). Table B.2 summarises the numerical conditions tested. The ingot thickness is fixed to 13 mm. The thermal conduction coefficient used are summarized in Table B.1

Material	Thermal conductivity	Units
Steel	40	W.m^{-1}.s^{-1}
Aluminium	150	W.m^{-1}.s^{-1}
SAC 305	60	W.m^{-1}.s^{-1}

Table B.1: Thermal conductivities of the mould materials and the SAC 305

The results of this parametric study are presented in Figure B.2. As expected the thinner the mould is the higher the cooling rate is. Moreover an aluminium
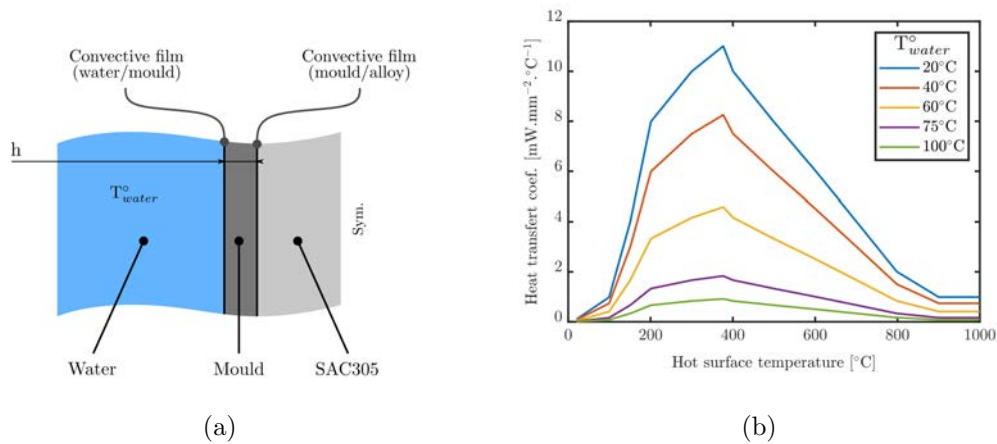
Figure B.1: (a) Semi-infinite plate modelling to simulate quenching; (b) Heat transfer coefficient law between water and mould with respect of the mould temperature and the water temperature

mould offers better cooling rates than a steel one. With a thin aluminium mould the cooling rate gradient within the alloy thickness is higher than the one with a thick mould or a steel mould. In addition a higher quench temperature allows to decrease the cooling rate gradient. Experimentally we observed large porosity with a 5 mm thick aluminium mould quenched at 20°C, when none were observed for a 5 mm thick steel mould quenched at 20°C.

Combining experimental observations with numerical analysis it seems reasonable to choose cooling rate below $20°C.s^{-1}$ to guaranty acceptable micro-structure and material properties. In addition the mould thickness is set to 5 mm because of machining constraints and to minimize the weight of the different moulds. Two ideal quench conditions can be defined with respect to the mould material, they are summarized in Table B.3.

These ideal quench conditions could not be reach for the aluminium mould because of heating issues. The quench temperature was reduced to 40°C.

Mould material n/a	Mould thickness [mm]	Quench temperature [°C]	Mould material n/a	Mould thickness [mm]	Quench temperature [°C]
Steel	5	20	Aluminium	5	20
Steel	6	20	Aluminium	6	20
Steel	7	20	Aluminium	7	20
Steel	8	20	Aluminium	8	20
Steel	9	20	Aluminium	9	20
Steel	10	20	Aluminium	10	20
Steel	5	30	Aluminium	5	30
Steel	5	40	Aluminium	5	40
Steel	5	50	Aluminium	5	50
Steel	5	60	Aluminium	5	60
Steel	5	70	Aluminium	5	70
Steel	5	80	Aluminium	5	80

Table B.2: Mould parameter and quench temperature tested for the parametric study

Mould material n/a	Mould thickness [mm]	Target quench temperature [°C]
Steel	5	20
Aluminium	5	60

Table B.3: Quench temperatures and mould design parameters selected

194
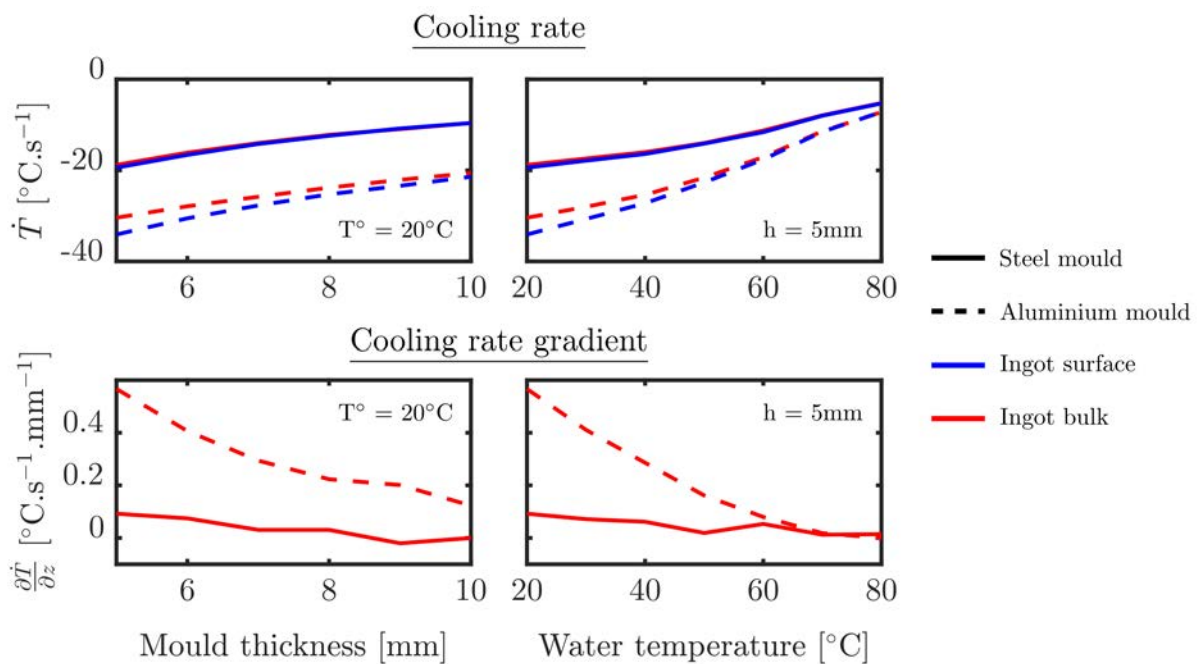
Figure B.2: Results of the quench parametric study; top graphs correspond to cooling rate at the surface of the ingot (in blue) and in the bulk (in red) with respect of the mould thickness and water temperature; bottom graphs correspond to the cooling rate gradient between the surface an the bulk of the ingot. Results are presented for Aluminium mould (dashed line) and steel mould (plain line)

<div align="right">

Appendix C

Thick shell modelling

</div>

This appendix introduces the theoretical framework of the shell theory. The presentation of the formulation of a volume shell called SHB8PS follows. Finally the developments performed to use the SHB8PS with elasto-visco-plastic materials are presented.

Contents

In this work we are interested in the buckling of a structure defined as shells. In this section the assumptions and the formulation used to define a shell problem are presented. The plates and shells theories are presented first. The plate theory is used to introduce the shell one. The basic formulation of a 3D volume shell element is presented then. This element called SHB8PS is implemented in many FE softwares, it is a good candidate to link experiments and FE simulations. Finally the developments performed in this work in order to use the SHB8PS with elasto-visco-plastic materials are presented.

C.1 Shell theories

The modelling of a 3D structure as a shell or a plate is often used, as it reduces the complexity and the time to solve the mechanical problem. In this section the hypothesis defining the different plate and shell theories as well as their formulations are presented.

First, it is needed to define the vocabulary used.

Plate: A plate is an element of volume delimited by two parallel planes spaced of the thickness h. The thickness h is small compared to the other dimensions of the plate. The 3D volume is reduced to a 2D plane called the mean plane.

Shell: By analogy to the plate, a shell is an element of volume delimited by two parallel surfaces spaced of the thickness h. The 3D volume is reduced to a 3D surface called the mean surface.

Thin/thick: The shells and plates can be considered as thin or thick. It is commonly assumed that a shell is thin if the thickness is at least 10 times smaller than the second smallest dimension of the plate or shell. Two examples can illustrate this definition. For a plate defined by its length a, its width b and its thickness h, the plate is considered as thin if $b/h >> 10$, it will be thick if $b/h \leq 10$ and moderately thick if $10 \leq b/h \leq 20$. Equally for a cylinder defined by its length L, its radius R and its thickness h, the cylinder is thin if $R/h >> 10$, it will be thick if $R/h \leq 10$ and moderately thick if $10 \leq R/h \leq 20$.

C.1.1 Thin and thick plate theory

Two main theories were developed to model a mechanical plate problem, the Kirchhoff-Love one and the Reissner-Midlin theory. The Kirchhoff-Love theory is limited to thin plates, while the Reissner-Midlin one also considers thick plates and shells. Only the Reissner-Midlin theory is presented in this work, as the Kirchhoff-Love theory is a specialisation of the Reissner-Midlin theory.

The Reissner-Midlin theory is based on the following assumptions:

- any point from the mean plane can only move in the normal direction with respect to the mean plane,

- the thickness does not vary through the plate,

- the normal stress is negligible,

- a line initially normal to the mean plane stays straight but not necessary normal to the mean plane.

Moreover at least one of the following statements needs to be verified:

- The plate is assumed as infinitely long,

- the boundary conditions can be reduced in order to obtain bending loadings only.
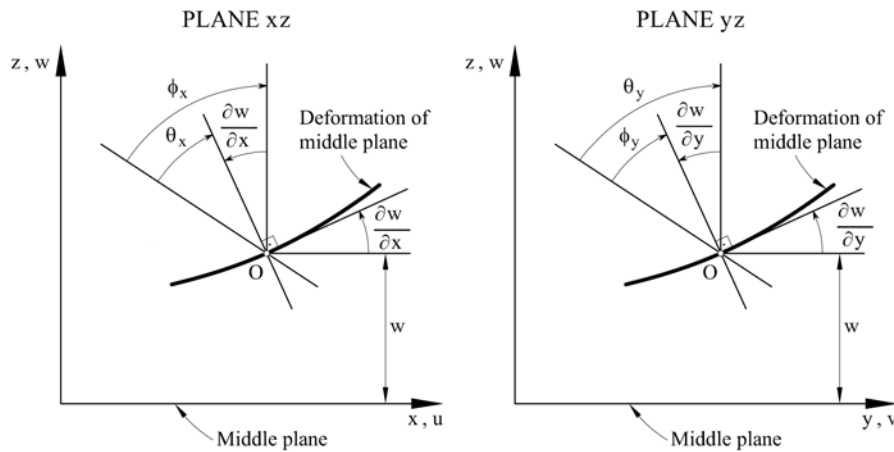
Figure C.1: Local coordinate system of a plate [Oñate 2013b]

Based on this set of assumptions, the displacement fields can be defined at a point defined by its coordinates (x, y, z) as follows:

$$
\begin{aligned}
u(x, y, z) &= z\,\phi_x(x, y), \\
v(x, y, z) &= z\,\phi_y(x, y), \\
w(x, y, z) &= w(x, y),
\end{aligned}
\tag{C.1}
$$

with u and v the in-plane displacement fields, w the out of plane displacement field, and ϕ_x and ϕ_y the rotations of a normal of the undeformed mean plane around y and x axis respectively as shown in Figure C.1. The x and y coordinates positioned the

considered point in the mean plane of the plate, while the z coordinate positioned the considered point normally to the mean plane as shown on Figure C.1.

The displacement vector is defined as follows:

$$\boldsymbol{u} = \begin{bmatrix} w \\ \phi_x \\ \phi_y \end{bmatrix} = \begin{bmatrix} w \\ -\frac{\partial w}{\partial x} + \theta_x \\ -\frac{\partial w}{\partial y} + \theta_y \end{bmatrix}, \tag{C.2}$$

with θ_x and θ_y the angle between a normal of the undeformed mean plane and a normal of the deformed mean plane around y and x respectively, as shown in Figure C.1. In the Kirchhoff-Love theory $\theta_x = \theta_y = 0$.

The strain tensor can be defined as follows:

$$\boldsymbol{\varepsilon} = \frac{1}{2}\left(\nabla u + \nabla^t u\right). \tag{C.3}$$

Therefore one can write:

$$\boldsymbol{\varepsilon} = \begin{Bmatrix} \varepsilon_{xx} \\ \varepsilon_{yy} \\ \varepsilon_{xy} \\ \varepsilon_{yz} \\ \varepsilon_{xz} \end{Bmatrix} = \begin{bmatrix} z & 0 & 0 & 0 & 0 \\ 0 & z & 0 & 0 & 0 \\ 0 & 0 & z & 0 & 0 \\ 0 & 0 & 0 & 1 & 0 \\ 0 & 0 & 0 & 0 & 1 \end{bmatrix} \cdot \begin{bmatrix} \frac{\partial \phi_x}{\partial x} \\ \frac{\partial \phi_y}{\partial y} \\ \frac{1}{2}\left(\frac{\partial \phi_x}{\partial y} + \frac{\partial \phi_y}{\partial x}\right) \\ \frac{1}{2}\phi_x + \frac{\partial w}{\partial x} \\ \frac{1}{2}\phi_y + \frac{\partial w}{\partial y} \end{bmatrix} = \boldsymbol{S} \cdot \hat{\boldsymbol{\varepsilon}}, \tag{C.4}$$

with $\varepsilon_{zz} = 0$ and $\hat{\boldsymbol{\varepsilon}}$ the generalized strain tensor.

This formulation allows to separate the components of the strain tensor. One part corresponds to the plate bending while the other to the plate shearing. This approach can also be adopted for the stress tensor, which leads to:

$$\boldsymbol{\varepsilon} = \left\{ \frac{\boldsymbol{\varepsilon}_b}{\boldsymbol{\varepsilon}_s} \right\} \text{ and } \boldsymbol{\sigma} = \left\{ \frac{\boldsymbol{\sigma}_b}{\boldsymbol{\sigma}_s} \right\}, \tag{C.5}$$

and

$$d\boldsymbol{\sigma} = \boldsymbol{\mathcal{C}} : d\boldsymbol{\varepsilon},$$
$$\left\{ \frac{d\boldsymbol{\sigma}_b}{d\boldsymbol{\sigma}_s} \right\} = \begin{bmatrix} \boldsymbol{\mathcal{C}}_b & \boldsymbol{0} \\ \boldsymbol{0} & \boldsymbol{\mathcal{C}}_s \end{bmatrix} \left\{ \frac{d\boldsymbol{\varepsilon}_b}{d\boldsymbol{\varepsilon}_s} \right\}, \tag{C.6}$$

where $\boldsymbol{\mathcal{C}}$ is the tangential constitutive law, the subscript $_b$ defines the bending part of the tensor while the subscript $_s$ defines the shear one.

It is sometime convenient to describe the plate problem with its resultant load tensor $\hat{\boldsymbol{\sigma}}$. This is done by integrating the stress tensor on the thickness of the plate, as follows:

$$\hat{\boldsymbol{\sigma}} = \left\{ \begin{array}{c} \hat{\boldsymbol{\sigma}}_b \\ \hline \hat{\boldsymbol{\sigma}}_s \end{array} \right\} = \left\{ \begin{array}{c} M_x \\ M_y \\ M_{xy} \\ \hline T_x \\ T_y \end{array} \right\} = \int_{-\frac{t}{2}}^{\frac{t}{2}} \boldsymbol{S} \cdot \boldsymbol{\sigma} dz. \tag{C.7}$$

$\hat{\boldsymbol{\sigma}}$ can be linked to the generalized strain tensor thanks to a generalized constitutive law, as follows:

$$\begin{aligned} d\hat{\boldsymbol{\sigma}} &= \int_{-\frac{t}{2}}^{\frac{t}{2}} \{\boldsymbol{S} d\boldsymbol{\sigma}\} dz \\ &= \left[\int_{-\frac{t}{2}}^{\frac{t}{2}} \{\boldsymbol{S}\boldsymbol{\mathcal{C}}\boldsymbol{S}\} dz \right] d\hat{\boldsymbol{\varepsilon}} \\ &= \hat{\boldsymbol{\mathcal{C}}} d\hat{\boldsymbol{\varepsilon}}. \end{aligned} \tag{C.8}$$

As $\boldsymbol{\mathcal{C}}$ and $\boldsymbol{S}$ are symmetrical on can write:

$$\begin{aligned} \hat{\boldsymbol{\mathcal{C}}} &= \hat{\boldsymbol{S}} \cdot \boldsymbol{\mathcal{C}} \\ \hat{\boldsymbol{S}} &= \int_{-\frac{t}{2}}^{\frac{t}{2}} \boldsymbol{S}^2 dz \\ &= \begin{bmatrix} \frac{t^3}{12} & 0 & 0 & 0 & 0 \\ 0 & \frac{t^3}{12} & 0 & 0 & 0 \\ 0 & 0 & \frac{t^3}{12} & 0 & 0 \\ 0 & 0 & 0 & t & 0 \\ 0 & 0 & 0 & 0 & t \end{bmatrix}, \end{aligned} \tag{C.9}$$

$\hat{\boldsymbol{\mathcal{C}}}$ is the generalized tangential constitutive law.

C.1.2 Shell theory

The elements just presented on plates can be extended to shells. The structures modelled are not plane anymore, and the shell can experienced in-plane strain and stress. Two strategies can be adopted.

C.1.2.1 Plane shells

The first one models the shell with several plate elements. This is the easiest one as all the previous theoretical elements can be used in a local coordinate system (x', y', z') attached to the plate, where the plane (x', y') coincides with the mean

plane of the plate. The in-plane strains and stresses are introduced through the local displacement fields:

$$u'(x', y', z') = u'_m(x', y') + z'\phi'_x(x', y'),$$
$$v'(x', y', z') = v'_m(x', y') + z'\phi'_y(x, y),$$
$$w'(x', y', z') = w'_m(x', y').$$

(C.10)

u'_m is the displacement along x' in the mean plane. It only depends on x' and y' coordinates.

v'_m is the displacement along y' in the mean plane. It only depends on x' and y' coordinates.

This leads to dissociate the local strain tensor into a membrane part ε'_m, a bending part ε'_m and a transverse shear part ε'_m as follows:

$$\varepsilon' = \left\{ \begin{array}{c} \varepsilon'_m \\ \hline \varepsilon'_b \\ \hline \varepsilon'_c \end{array} \right\}$$

$$= S' \cdot \left\{ \begin{array}{c} \hat{\varepsilon}'_m \\ \hline \hat{\varepsilon}'_b \\ \hline \hat{\varepsilon}'_c \end{array} \right\}$$

$$= \begin{bmatrix} 1 & 0 & 0 & z' & 0 & 0 & 0 & 0 \\ 0 & 1 & 0 & 0 & z' & 0 & 0 & 0 \\ 0 & 0 & 1 & 0 & 0 & z' & 0 & 0 \\ 0 & 0 & 0 & 0 & 0 & 0 & 1 & 0 \\ 0 & 0 & 0 & 0 & 0 & 0 & 0 & 1 \end{bmatrix} \cdot \begin{bmatrix} \frac{\partial u'_m}{\partial x} \\ \frac{\partial v'_m}{\partial y} \\ \frac{1}{2}\left(\frac{\partial u'_m}{\partial y} + \frac{\partial u'_m}{\partial y}\right) \\ \frac{\partial \phi_x}{\partial x} \\ \frac{\partial \phi_y}{\partial y} \\ \frac{1}{2}\left(\frac{\partial \phi_x}{\partial y} + \frac{\partial \phi_y}{\partial x}\right) \\ \frac{1}{2}\phi_x + \frac{\partial w}{\partial x} \\ \frac{1}{2}\phi_y + \frac{\partial w}{\partial y} \end{bmatrix}$$

(C.11)

$$= S' \cdot \hat{\varepsilon}',$$

with $\varepsilon'_{zz} = 0$.

As previously mentioned, the local stress increment can be related to the local strain increment through the tangential constitutive law $\boldsymbol{C}$:

$$d\boldsymbol{\sigma}' = \boldsymbol{C}\,\boldsymbol{\varepsilon}' = \begin{bmatrix} \boldsymbol{C}_{ps} & \mathbf{0} \\ \mathbf{0} & \boldsymbol{C}_s \end{bmatrix} \cdot \left\{ \begin{array}{c} \boldsymbol{\varepsilon}_{ps} \\ \hline \boldsymbol{\varepsilon}_s \end{array} \right\} \text{ with: } \boldsymbol{\varepsilon}_{ps} = \left\{ \begin{array}{c} \varepsilon_{xx} \\ \varepsilon_{yy} \\ \varepsilon_{xy} \end{array} \right\} \text{ and } \boldsymbol{\varepsilon}_s = \left\{ \begin{array}{c} \varepsilon_{yz} \\ \varepsilon_{xz} \end{array} \right\}$$

(C.12)

The strain and stress tensors are therefore defined in the local coordinate system and the constitutive law is integrated in the local coordinate system to solve the

mechanical problem. The constitutive law is divided into a plane stress constitutive law $\mathcal{C}_{ps}$ and a transverse shear one $\mathcal{C}_s$.

C.1.2.2 Curved shells

Finally, to be as close as possible to the real geometry, curved shell elements can be used. The previous theoretical elements can be re-used as long as a local coordinate system can be defined. This is possible through the definition of an additional coordinate system attached to the curved shell and deforming with it. Three coordinate systems are therefore defined:

- the global coordinate system (x, y, z), it corresponds to the frame where the structure is placed,

- the curvilinear parametric coordinate system (ξ, η, ζ), it deforms with the shell element,

- the local coordinate system (x', y', z') is tangent to the surface defined by $\zeta = Cst.$.

Figure C.2 presents the three different coordinate systems.
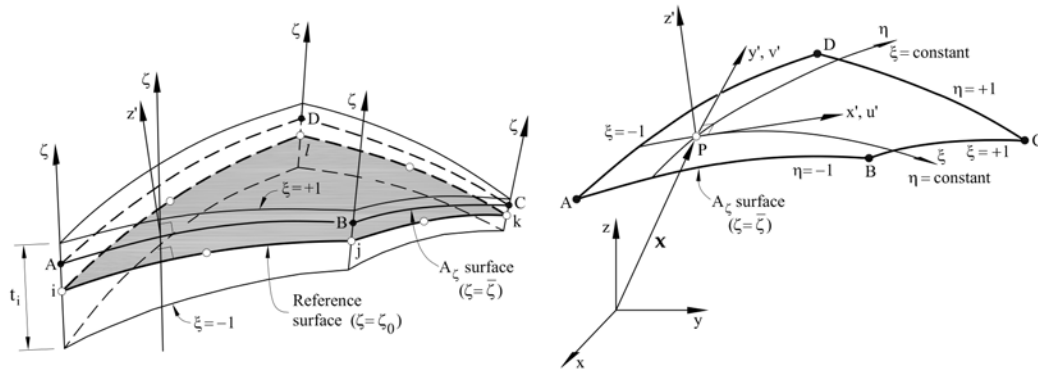
Figure C.2: Coordinate systems of a curved shell [Oñate 2013a]

The curvilinear parametric coordinate system (ξ, η, ζ) is defined as its third direction ζ is linear in the thickness direction. Other directions depend on the numbering of the element nodes (cf. [Oñate 2013a]). The curvilinear coordinate system deforms with the shell.

The local coordinate system is different in every point of the shell. It is defined such as the third direction z' is normal to a plane formed by two vectors respectively tangent to curves defined by ξ constant and $\zeta = \bar{\zeta}$, and η constant and $\zeta = \bar{\zeta}$. $\bar{\zeta}$ corresponds to the actual point *zeta* coordinate:

$$\boldsymbol{z'}_{\bar{\zeta}} = \left(\frac{\partial \boldsymbol{x}}{\partial \xi}\right)_{\eta=Cst.,\bar{\zeta}} \wedge \left(\frac{\partial \boldsymbol{x}}{\partial \eta}\right)_{\xi=Cst.,\bar{\zeta}}. \tag{C.13}$$

The first direction $\boldsymbol{x'}$ is chosen as tangent to the curve defined by η constant in the plane defined by $\bar{\zeta}$:

$$\boldsymbol{x'}_{\bar{\zeta}} = \left(\frac{\partial \boldsymbol{x}}{\partial \xi}\right)_{\eta=Cst.,\bar{\zeta}}. \tag{C.14}$$

The last direction is parallel to the cross product of $\boldsymbol{z'}$ with $\boldsymbol{x'}$.

Therefore the stress and strain tensors can be defined in the local coordinate as well as the constitutive law integration.

This subsection gives the theoretical elements to formulate shell elements in FE softwares. Most of them are formulated with 3D surface elements, which is not well adapted for experimental/numerical comparison. In the next subsection a 3D volume shell element is presented. Its geometrical representation eases the direct comparison between numerical simulations and experiments.

C.2 The SHB8PS element

Many elements exist to model shell structures, most of them reduce the 3D volume of the structure to a 3D surface. Abed-Meraim and Combescure developed in [Abed-Meraim and Combescure 2002] a 3D shell element which allows to model completely the shell with its volume. It is named SHB8PS. The main benefit of this 3D formulation is the absence of rotational degrees of freedom, because of its fully 3D displacement fields. Many works describe its formulation for elastic and elasto-plastic material. Its basic formulation is presented here as a baseline. The specific developments, especially concerning the material behaviour, are detailed in Section C.2.2.

C.2.1 The SHB8PS elastic formulation

Its parametric mesh shape is a cube. The physical coordinates of any point $\boldsymbol{x}$ in this cube are linked to their parametric coordinates (ξ, η, ζ) by the following equation:

$$\boldsymbol{x} = \sum_{i=1}^{8} \boldsymbol{x}_i N_i(\xi, \eta, \zeta), \tag{C.15}$$

where the N_i are the shape functions of the element and $\boldsymbol{x} = [x\,y\,z]^t$. The parametric coordinates system is defined in [Abed-Meraim and Combescure 2002]. The N_i functions are defined as follows:

$$N_i(\xi, \eta, \zeta) = \frac{1}{8}(1 + \xi_i\xi)(1 + \eta_i\eta)(1 + \zeta_i\zeta) \text{ with: } (\xi, \eta, \zeta) \in [-1, 1]^3, \qquad \text{(C.16)}$$

subscript i corresponds to quantities linked to node i of the parametric mesh.

Using the same formalism as above the displacement fields inside a mesh is defined by:

$$\boldsymbol{u}(\boldsymbol{x}) = \sum_{i=1}^{8} \boldsymbol{u}_i(\boldsymbol{x}) N_i(\xi, \eta, \zeta), \qquad \text{(C.17)}$$

with $\boldsymbol{u} = [u_x\, u_y\, u_z]^t$.

Finally the displacement gradient can be expressed as follows:

$$\nabla \boldsymbol{u} = \boldsymbol{B} \cdot \boldsymbol{d}$$

$$\boldsymbol{B} = \begin{bmatrix} \boldsymbol{b}_x^t + \sum_{\alpha=1}^{4} h_{\alpha,x} \boldsymbol{\gamma}_\alpha^t & 0 & 0 \\[2ex] 0 & \boldsymbol{b}_y^t + \sum_{\alpha=1}^{4} h_{\alpha,y} \boldsymbol{\gamma}_\alpha^t & 0 \\[2ex] 0 & 0 & \boldsymbol{b}_z^t + \sum_{\alpha=0}^{4} h_{\alpha,z} \boldsymbol{\gamma}_\alpha^t \\[2ex] \boldsymbol{b}_y^t + \sum_{\alpha=1}^{4} h_{\alpha,y} \boldsymbol{\gamma}_\alpha^t & \boldsymbol{b}_x^t + \sum_{\alpha=1}^{4} h_{\alpha,x} \boldsymbol{\gamma}_\alpha^t & 0 \\[2ex] 0 & \boldsymbol{b}_z^t + \sum_{\alpha=1}^{4} h_{\alpha,z} \boldsymbol{\gamma}_\alpha^t & \boldsymbol{b}_y^t + \sum_{\alpha=1}^{4} h_{\alpha,y} \boldsymbol{\gamma}_\alpha^t \\[2ex] \boldsymbol{b}_z^t + \sum_{\alpha=1}^{4} h_{\alpha,z} \boldsymbol{\gamma}_\alpha^t & 0 & \boldsymbol{b}_x^t + \sum_{\alpha=1}^{4} h_{\alpha,x} \boldsymbol{\gamma}_\alpha^t \end{bmatrix}, \qquad \text{(C.18)}$$

with:

$$\begin{aligned}
\boldsymbol{b}_X &= \frac{\partial \boldsymbol{N}}{\partial X}(\boldsymbol{0}) \\
h_{1,X} &= \frac{\partial}{\partial X}(\eta\zeta), \\
h_{2,X} &= \frac{\partial}{\partial X}(\xi\zeta), \\
h_{3,X} &= \frac{\partial}{\partial X}(\xi\eta), \\
h_{4,X} &= \frac{\partial}{\partial X}(\xi\eta\zeta), \text{ with: } X = x,\, y \, or \, z, \\
\boldsymbol{h}_\alpha &= [h_{\alpha,x}, h_{\alpha,y}, h_{\alpha,z}]^t, \\
\boldsymbol{\gamma}_\alpha &= \frac{1}{8}\left[\boldsymbol{h}_\alpha - \left((\boldsymbol{h}_\alpha^t \cdot \boldsymbol{x})\boldsymbol{b}_x + (\boldsymbol{h}_\alpha^t \cdot \boldsymbol{y})\boldsymbol{b}_y + (\boldsymbol{h}_\alpha^t \cdot \boldsymbol{z})\boldsymbol{b}_z\right)\right],
\end{aligned} \tag{C.19}$$

with $\boldsymbol{x} = [x_1 \dots x_8]^t$, $\boldsymbol{y} = [y_1 \dots y_8]^t$, $\boldsymbol{z} = [z_1 \dots z_8]^t$ and $\boldsymbol{N} = [N_1 \dots N_8]^t$ corresponding to the eight nodes coordinates and shape functions and $\boldsymbol{d} = [\boldsymbol{d}_x \, \boldsymbol{d}_y \, \boldsymbol{d}_z]^t$ the nodal displacement vector.

The stiffness matrix is computed using a reduced integration scheme with five integration points (as detailed in [Abed-Meraim and Combescure 2009]). The properties of the five integration points are described in Table C.1.

Integration point	ξ	η	ζ	ω
1	0	0	-0.906179845938664	0.236926885056189
2	0	0	-0.538469310105683	0.479628670499366
3	0	0	0	0.568888888888889
4	0	0	0.538469310105683	0.479628670499366
5	0	0	0.906179845938664	0.236926885056189

Table C.1: Integration point properties, parametric coordinates and weight

The elementary stiffness matrix can be expressed as:

$$\boldsymbol{K} = \int_{\Omega_e} \boldsymbol{B}^t \cdot \boldsymbol{C} \cdot \boldsymbol{B} d\Omega = \sum_{i=1}^{5} \omega(\zeta_i) J(\zeta_i) \boldsymbol{B}^t(\zeta_i) \cdot \boldsymbol{C} \cdot \boldsymbol{B}(\zeta_i), \tag{C.20}$$

with Ω_e the elementary domain, J the jacobian of the transformation from the parametric to the physical space and $\omega(\zeta_i)$ the integration point weight.

With this method, $\boldsymbol{h}_3 = \boldsymbol{h}_4 = \boldsymbol{0}$ at the integration points and $\boldsymbol{B}$ is reduced to $\boldsymbol{B}_{12}$. $\boldsymbol{B}_{12}$ is defined by:

$$\boldsymbol{B}_{12} = \begin{bmatrix} \boldsymbol{b}_x^t + \sum_{\alpha=1}^{2} h_{\alpha,x}\boldsymbol{\gamma}_\alpha^t & 0 & 0 \\ 0 & \boldsymbol{b}_y^t + \sum_{\alpha=1}^{2} h_{\alpha,y}\boldsymbol{\gamma}_\alpha^t & 0 \\ 0 & 0 & \boldsymbol{b}_z^t + \sum_{\alpha=1}^{2} h_{\alpha,z}\boldsymbol{\gamma}_\alpha^t \\ \boldsymbol{b}_y^t + \sum_{\alpha=1}^{2} h_{\alpha,y}\boldsymbol{\gamma}_\alpha^t & \boldsymbol{b}_x^t + \sum_{\alpha=1}^{2} h_{\alpha,x}\boldsymbol{\gamma}_\alpha^t & 0 \\ 0 & \boldsymbol{b}_z^t + \sum_{\alpha=1}^{2} h_{\alpha,z}\boldsymbol{\gamma}_\alpha^t & \boldsymbol{b}_y^t + \sum_{\alpha=1}^{2} h_{\alpha,y}\boldsymbol{\gamma}_\alpha^t \\ \boldsymbol{b}_z^t + \sum_{\alpha=1}^{2} h_{\alpha,z}\boldsymbol{\gamma}_\alpha^t & 0 & \boldsymbol{b}_x^t + \sum_{\alpha=1}^{2} h_{\alpha,x}\boldsymbol{\gamma}_\alpha^t \end{bmatrix}, \tag{C.21}$$

Because of its basic formulation, the SHB8 element presents some Hourglass modes (due to the reduced integration) and is subjected to locking issues (as most of shell elements). To overcome this issue Abed-Meraim and Combescure proposed a new formulation to stabilize the element and to treat the locking phenomenon. Details of the formulation can be found in [Abed-Meraim and Combescure 2009]. The key elements of the formulation are presented thereafter.

First the Hallquist vectors $\boldsymbol{b}_X$ are replaced by Flanagan-Belytschko ones. They are defined by:

$$\hat{\boldsymbol{b}}_X = \frac{1}{\omega_e} \int_{\Omega_e} \boldsymbol{N}_{,X}(\xi, \eta\zeta)d\Omega \text{ with: } X = x, y \, or \, z. \tag{C.22}$$

Then the discrete gradient operator $\boldsymbol{B}$ becomes $\hat{\boldsymbol{B}}$. One can observe that $\hat{\boldsymbol{B}}$ is a sum of a constant term $\hat{\boldsymbol{B}}_c$ and a variable one $\hat{\boldsymbol{B}}_n$ such as:

$$\hat{\boldsymbol{B}} = \hat{\boldsymbol{B}}_c + \hat{\boldsymbol{B}}_n, \tag{C.23}$$

with,

$$\hat{\boldsymbol{B}}_c = \begin{bmatrix} \hat{\boldsymbol{b}}_x^t & 0 & 0 \\ 0 & \hat{\boldsymbol{b}}_y^t & 0 \\ 0 & 0 & \hat{\boldsymbol{b}}_z^t \\ \hat{\boldsymbol{b}}_y^t & \hat{\boldsymbol{b}}_x^t & 0 \\ 0 & \hat{\boldsymbol{b}}_z^t & \hat{\boldsymbol{b}}_y^t \\ \hat{\boldsymbol{b}}_z^t & 0 & \hat{\boldsymbol{b}}_x^t \end{bmatrix}, \hat{\boldsymbol{B}}_n = \begin{bmatrix} \hat{X}_{1234}^t & 0 & 0 \\ 0 & \hat{Y}_{1234}^t & 0 \\ 0 & 0 & \hat{Z}_{1234}^t \\ \hat{Y}_{1234}^t & \hat{X}_{1234}^t & 0 \\ 0 & \hat{Z}_{1234}^t & \hat{Y}_{1234}^t \\ \hat{Z}_{1234}^t & 0 & \hat{X}_{1234}^t \end{bmatrix}, \tag{C.24}$$

and,

$$\hat{X}_{1234}^t = \sum_{\alpha=1}^{4} h_{\alpha,x} \hat{\boldsymbol{\gamma}}_\alpha^t,$$

$$\hat{Y}_{1234}^t = \sum_{\alpha=1}^{4} h_{\alpha,y} \hat{\boldsymbol{\gamma}}_\alpha^t, \tag{C.25}$$

$$\hat{Z}_{1234}^t = \sum_{\alpha=1}^{4} h_{\alpha,z} \hat{\boldsymbol{\gamma}}_\alpha^t.$$

Then the stiffness matrix and the internal forces are computed in the corotational frame defined at mid-step. The corotational frame is oriented by:

$$\boldsymbol{a}_1 = \boldsymbol{a}_1^0,$$
$$\boldsymbol{a}_2 = \boldsymbol{a}_2^0 + \boldsymbol{a}_c, \tag{C.26}$$
$$\boldsymbol{a}_3 = \boldsymbol{a}_1 \wedge \boldsymbol{a}_2,$$

with,

$$\boldsymbol{a}_1^0 = [\boldsymbol{\Lambda}_1^t \cdot \boldsymbol{x}, \boldsymbol{\Lambda}_1^t \cdot \boldsymbol{y}, \boldsymbol{\Lambda}_1^t \cdot \boldsymbol{z}]^t,$$
$$\boldsymbol{a}_2^0 = [\boldsymbol{\Lambda}_2^t \cdot \boldsymbol{x}, \boldsymbol{\Lambda}_2^t \cdot \boldsymbol{y}, \boldsymbol{\Lambda}_2^t \cdot \boldsymbol{z}]^t, \tag{C.27}$$

$$\boldsymbol{a}_c = -\frac{\boldsymbol{a}_1^{0t} \cdot \boldsymbol{a}_2^0}{\boldsymbol{a}_1^{0t} \cdot \boldsymbol{a}_1^0} \boldsymbol{a}_1^0, \tag{C.28}$$

and,

$$\boldsymbol{\Lambda}_1 = [-1, 1, 1, -1, -1, 1, 1, -1]^t,$$
$$\boldsymbol{\Lambda}_2 = [-1, -1, 1, 1, -1, -1, 1, 1]^t, \tag{C.29}$$
$$\boldsymbol{\Lambda}_3 = [-1, -1, -1, -1, 1, 1, 1, 1]^t.$$

The stiffness matrix and the internal forces are finally defined by:

$$\boldsymbol{K}_e = \int_{\Omega_e} \hat{\boldsymbol{B}}_{12}^t \boldsymbol{C} \hat{\boldsymbol{B}}_{12} dV + \boldsymbol{K}_{STAB},$$

$$\boldsymbol{f}_{int} = \int_{\Omega_e} \hat{\boldsymbol{B}}_{12}^t \cdot \boldsymbol{\sigma} dV + \boldsymbol{f}_{STAB}. \tag{C.30}$$

For linear problems an improved plane-stress constitutive law is chosen which inhibit locking phenomena. The constitutive law is defined by:

$$\boldsymbol{C} = \begin{bmatrix} \lambda + 2\mu & \lambda & 0 & 0 & 0 & 0 \\ \lambda & \lambda + 2\mu & 0 & 0 & 0 & 0 \\ 0 & 0 & E & 0 & 0 & 0 \\ 0 & 0 & 0 & \mu & 0 & 0 \\ 0 & 0 & 0 & 0 & \mu & 0 \\ 0 & 0 & 0 & 0 & 0 & \mu \end{bmatrix}, \tag{C.31}$$

$$\mu = \frac{E}{2(1+\nu)}, \ \lambda = \frac{E\nu}{1-\nu^2}, \tag{C.32}$$

with E the Young modulus and ν the Poisson ratio.

$\boldsymbol{K}_{STAB}$ is defined in elasticity by:

$$\boldsymbol{K}_{STAB} = \begin{bmatrix} \boldsymbol{k}_{11} & \boldsymbol{k}_{12} & \boldsymbol{k}_{13} \\ \boldsymbol{k}_{21} & \boldsymbol{k}_{22} & \boldsymbol{k}_{23} \\ \boldsymbol{k}_{31} & \boldsymbol{k}_{32} & \boldsymbol{k}_{33} \end{bmatrix}, \tag{C.33}$$

with:

$$\begin{aligned}
\boldsymbol{k}_{11} &= (\lambda + 2\mu)H_{11}\left[\hat{\boldsymbol{\gamma}}_3 \cdot \hat{\boldsymbol{\gamma}}_3^t + \frac{1}{3}\,\hat{\boldsymbol{\gamma}}_4 \cdot \hat{\boldsymbol{\gamma}}_4^t\right], \\
\boldsymbol{k}_{22} &= (\lambda + 2\mu)H_{22}\left[\hat{\boldsymbol{\gamma}}_3 \cdot \hat{\boldsymbol{\gamma}}_3^t + \frac{1}{3}\,\hat{\boldsymbol{\gamma}}_4 \cdot \hat{\boldsymbol{\gamma}}_4^t\right], \\
\boldsymbol{k}_{33} &= \frac{\mu}{3}H_{11}\left[\hat{\boldsymbol{\gamma}}_4 \cdot \hat{\boldsymbol{\gamma}}_4^t\right], \\
\boldsymbol{k}_{ij} &= \boldsymbol{0}, \ i \neq j,
\end{aligned} \tag{C.34}$$

and:

$$\begin{aligned}
H_{11} &= \tfrac{1}{3}\frac{(\boldsymbol{\Lambda}_2^t \boldsymbol{y})(\boldsymbol{\Lambda}_3^t \boldsymbol{z})}{(\boldsymbol{\Lambda}_1^t \boldsymbol{x})}, & H_{12} = H_{21} = \tfrac{1}{3}\boldsymbol{\Lambda}_3^t \boldsymbol{z}, \\
H_{22} &= \tfrac{1}{3}\frac{(\boldsymbol{\Lambda}_1^t \boldsymbol{x})(\boldsymbol{\Lambda}_3^t \boldsymbol{z})}{(\boldsymbol{\Lambda}_2^t \boldsymbol{y})}, & H_{13} = H_{31} = \tfrac{1}{3}\boldsymbol{\Lambda}_2^t \boldsymbol{y}, \\
H_{33} &= \tfrac{1}{3}\frac{(\boldsymbol{\Lambda}_1^t \boldsymbol{x})(\boldsymbol{\Lambda}_2^t \boldsymbol{y})}{(\boldsymbol{\Lambda}_3^t \boldsymbol{z})}, & H_{23} = H_{32} = \tfrac{1}{3}\boldsymbol{\Lambda}_1^t \boldsymbol{x},
\end{aligned} \tag{C.35}$$

f_{STAB} is defined by:

$$\boldsymbol{f}_{STAB} = \begin{pmatrix} f_x^{STAB} = \sum_{\alpha=3}^{4} = \mathcal{Q}_{x\alpha}\hat{\boldsymbol{\gamma}}_\alpha \\ f_y^{STAB} = \sum_{\alpha=3}^{4} = \mathcal{Q}_{y\alpha}\hat{\boldsymbol{\gamma}}_\alpha \\ f_z^{STAB} = \sum_{\alpha=3}^{4} = \mathcal{Q}_{z\alpha}\hat{\boldsymbol{\gamma}}_\alpha \end{pmatrix}. \tag{C.36}$$

$\mathcal{Q}$ is called the generalized stress tensor, which is related to $\boldsymbol{q}$ (called generalized strain tensor) by the following set of equations in elasticity:

$$\dot{\mathcal{Q}}_{x3} = (\lambda + 2\mu)H_{11}\dot{q}_{x3},$$

$$\dot{\mathcal{Q}}_{x4} = \frac{1}{3}(\lambda + 2\mu)H_{11}\dot{q}_{x4},$$

$$\dot{\mathcal{Q}}_{y3} = (\lambda + 2\mu)H_{22}\dot{q}_{y3},$$

$$\dot{\mathcal{Q}}_{y4} = \frac{1}{3}(\lambda + 2\mu)H_{22}\dot{q}_{y4}, \tag{C.37}$$

$$\dot{\mathcal{Q}}_{z3} = 0,$$

$$\dot{\mathcal{Q}}_{z4} = \frac{1}{3}\mu H_{11}\dot{q}_{z4},$$

with,

$$\dot{q}_{x\alpha} = \hat{\boldsymbol{\gamma}}^t \boldsymbol{d}_x,$$

$$\dot{q}_{y\alpha} = \hat{\boldsymbol{\gamma}}^t \boldsymbol{d}_y, \tag{C.38}$$

$$\dot{q}_{z\alpha} = \hat{\boldsymbol{\gamma}}^t \boldsymbol{d}_z.$$

The generalized stress is computed in the half-step configuration, leading to the following expression:

$$\boldsymbol{\mathcal{Q}}^{n+1} = \boldsymbol{\mathcal{Q}}^n + \Delta t\dot{\boldsymbol{\mathcal{Q}}}|_{n+1/2}. \tag{C.39}$$

This brief description of the SHB8PS formulation in elasticity intends to set a framework in order to present the numerical development done in Cast3M. More details on the formulation can be found in [Abed-Meraim and Combescure 2009] and [Abed-Meraim and Combescure 2002], including the expression of the geometrically nonlinear operator $\boldsymbol{K}_\sigma$ or the following pressure operator $\boldsymbol{K}_p$. The extension of the existing formulation (in elasticity and elasto-plasticity) to anisotropic inelastic rate dependent behaviours is presented in the next section. It is then implemented in Cast3M and used for numerical simulations.

C.2.2   SHB8PS for anisotropic visco-plasticity

As mentioned in the previous section, the SHB8PS element is particularly efficient to model thick shell structures. In this section its implementation to Cast3M FE software for a generic anisotropic inelastic behaviour will be detailed.

SHB8PS in Cast3M and Mfront
The SHB8PS element was already present in Cast3M, but its usage was limited to linear elastic analysis. This paragraph intends to present the developments performed in Cast3M to use the SHB8PS element in non-linear analysis, including nonlinear constitutive laws and anisotropic behaviours. We constrained ourselves to use only existing Cast3M operators. In order to ease to implementation of the

SHB8PS element to Cast3M. The Mfront software was used for the constitutive law integration. The numerical developments were focused on three topics:

- Geometrical non-linearity,

- Material non-linearity,

- Inelastic anisotropic behaviour.

In next paragraphs the numerical developments concerning each topic are presented.

Geometrical non-linearity

The first task was focused on geometrical non-linearity. Because of the deformation of the structure some operators as, the stiffness matrix or the internal forces are impacted. The geometrical integration domain is modified for both operators. Moreover the stabilization of the internal forces presents a time dependency as mentioned in Equation C.39.

The time dependency of the stabilisation forces is solved by introducing an internal variable to store the five non-zero components of the general stress tensor $\mathcal{Q}$ (defined in Equation C.37). This internal variable is computed in the Cast3M operator 'BSIGMA' from the previous general stress tensor $\mathcal{Q}$ and the displacement increment $\Delta \boldsymbol{u}$. This additional internal variable field is called 'VSHB'.

The implementation of the SHB8PS element is limited to an updated Lagrangian formulation in this work. Therefore, it is needed to update the geometry of the shell at each increment. The kinematics of the SHB8PS element does not include thickness change due to the plane-stress formulation. Indeed the shell thickness changes during loading. The thickness strain can be defined as follows in the co-rotational frame:

$$\varepsilon_{33}^{tot} = \varepsilon_{33}^{PS} + \varepsilon_{33} \tag{C.40}$$

with ε_{33} computed from the displacement field, while ε_{33}^{PS} is defined during the constitutive law integration. ε_{33}^{PS} is the thickness strain due to the in-plane plane-stress formulation.

The out of plane displacement field is then updated as follows:

$$\hat{\boldsymbol{B}}^t \hat{\boldsymbol{B}} \Delta \boldsymbol{U}_3^{PS} = \hat{\boldsymbol{B}}^t \begin{bmatrix} 0 \\ 0 \\ \Delta \varepsilon_{33}^{PS} \\ 0 \\ 0 \\ 0 \end{bmatrix}, \tag{C.41}$$

with ε_{33}^{PS} declared as an internal variable. This linear system can be solved in a weak formulation defined by:

$$\int_\Omega \hat{\boldsymbol{B}}^t \hat{\boldsymbol{B}} \Delta \boldsymbol{U}_3^{PS} d\Omega = \int_\Omega \hat{\boldsymbol{B}}^t \begin{bmatrix} 0 \\ 0 \\ \Delta\varepsilon_{33}^{PS} \\ 0 \\ 0 \\ 0 \end{bmatrix} d\Omega,$$
(C.42)

which can be expressed as:

$$\boldsymbol{K}_{rig}^{33} \Delta \boldsymbol{U}^{33} = \boldsymbol{f}_\varepsilon^{33}.$$
(C.43)

The internal forces are defined on the new configuration, including the thickness change. At convergence of the Newton iterations of the global resolution algorithm, the configuration is updated to the new configuration including the thickness change.

Material non-linearity

This first development allows to perform simulations in updated Lagrangian formulation. For non-linear constitutive material law more developments are needed. These developments concern the material law integration and the stabilisation strategy.

In order to be able to use as many constitutive laws as possible it was chosen to follow a generic approach already mentioned in literature (cf. [Trinh 2009]). This approach consists in dividing the constitutive law into a plane-stress law and a 3D law. The plane-stress components (red in Equation C.44) of the constitutive law are integrated inelastically while the other components stay fully elastic (green in Equation C.44). The inelastic constitutive law can be written in the co-rotational frame as follows:

$$\dot{\boldsymbol{\sigma}} = \boldsymbol{C}_t \dot{\boldsymbol{\varepsilon}} = \begin{bmatrix} \boldsymbol{Ps_{1111}} & \boldsymbol{Ps_{1122}} & 0 & \boldsymbol{Ps_{1112}} & 0 & 0 \\ \boldsymbol{Ps_{2211}} & \boldsymbol{Ps_{2222}} & 0 & \boldsymbol{Ps_{2212}} & 0 & 0 \\ 0 & 0 & \boldsymbol{E} & 0 & 0 & 0 \\ \boldsymbol{Ps_{1211}} & \boldsymbol{Ps_{1222}} & 0 & \boldsymbol{Ps_{1212}} & 0 & 0 \\ 0 & 0 & 0 & 0 & \boldsymbol{\mu} & 0 \\ 0 & 0 & 0 & 0 & 0 & \boldsymbol{\mu} \end{bmatrix} \dot{\boldsymbol{\varepsilon}}.$$
(C.44)

This strategy allows to use any existing integration algorithm to integrate the constitutive law. Every inelastic constitutive law can be integrated that way, it can be elasto-plastic or elasto-visco-plastic as wished. Nevertheless we have to be careful in defining the tangent stiffness matrix and the internal forces as the stabilisation can be impacted. Inelastic behaviour was implemented through a user subroutine created with Mfront (cf. [Helfer et al. 2013]). Mfront is a software used to develop material constitutive laws. This approach reduced the development work in Cast3M to two main topics:

212

- the sub-division of the 3D problem into a plane-stress one and a 3D elastic one,

- the stabilisation of the stiffness matrix and the internal forces.

The first one is relatively easy to perform in small strain formulation as the strain and stress are computed in the co-rotational frame. The strain tensor $\boldsymbol{\varepsilon}$ derived from the displacement field is divided into a plane stress part ($\boldsymbol{\varepsilon}_{PS}$) and a 3D one ($\boldsymbol{\varepsilon}_{3D}$) as follows:

$$\boldsymbol{\varepsilon} = \boldsymbol{\varepsilon}_{PS} + \boldsymbol{\varepsilon}_{3D} = \begin{bmatrix} \varepsilon_{11} \\ \varepsilon_{22} \\ 0 \\ 2\varepsilon_{12} \\ 0 \\ 0 \end{bmatrix} + \begin{bmatrix} 0 \\ 0 \\ \varepsilon_{33} \\ 0 \\ 2\varepsilon_{23} \\ 2\varepsilon_{13} \end{bmatrix}. \tag{C.45}$$

Same approach is followed for the stress tensor:

$$\boldsymbol{\sigma} = \boldsymbol{\sigma}_{PS} + \boldsymbol{\sigma}_{3D} = \begin{bmatrix} \sigma_{11} \\ \sigma_{22} \\ 0 \\ \sigma_{12} \\ 0 \\ 0 \end{bmatrix} + \begin{bmatrix} 0 \\ 0 \\ \sigma_{33} \\ 0 \\ \sigma_{23} \\ \sigma_{13} \end{bmatrix}. \tag{C.46}$$

The stress increment is then computed through Mfront thanks to an implicit integration algorithm. The plane stress components are integrated inelastically while the 3D components are integrated elastically.

The final stress tensor is re-combined into a three dimensional one to be used in the global resolution algorithm. From the integration algorithm the consistent tangent operator is also computed.

These two last sets of data are important for the global resolution algorithm. The stress tensor is used to compute the internal forces and the tangent operator the tangent stiffness matrix. As mentioned before, in order to consider as many constitutive laws as possible, the stabilisation forces and the stabilisation stiffness matrix are modified compared to the formulation detailed in [Abed-Meraim and Combescure 2009].

As a reminder, the stabilisation terms of the stiffness matrix are derived in the co-rotational frame as follows:

$$\boldsymbol{K}_{STAB} = \int_{\Omega_e} \hat{\boldsymbol{B}}_{34}^t \boldsymbol{C}_t \hat{\boldsymbol{B}}_{34} dV, \tag{C.47}$$

with $\boldsymbol{K}_{STAB}$ also defined by:

$$\boldsymbol{K}_{STAB} = \begin{bmatrix} \boldsymbol{k}_{11} & \boldsymbol{k}_{12} & \boldsymbol{k}_{13} \\ \boldsymbol{k}_{21} & \boldsymbol{k}_{22} & \boldsymbol{k}_{23} \\ \boldsymbol{k}_{31} & \boldsymbol{k}_{32} & \boldsymbol{k}_{33} \end{bmatrix} . \tag{C.48}$$

One can show that only the diagonal terms are needed for the stabilization of the element in elasticity. The hypothesis is conserved in inelasticity as mentioned in [Abed-Meraim and Combescure 2009]. Instead of applying an inelasticity factor to the stabilisation terms as performed in [Abed-Meraim and Combescure 2002; Abed-Meraim and Combescure 2009], the stabilisation stiffness matrix is computed using the tangential constitutive law. Only the relevant terms are conserved (cf. [Abed-Meraim and Combescure 2009]).

Finally the stabilization stiffness matrix can be defined by:

$$\begin{aligned}
\boldsymbol{k}_{11} &= P s_{1111} H_{11} \left[\hat{\boldsymbol{\gamma}}_3 \cdot \hat{\boldsymbol{\gamma}}_3^t + \frac{1}{3} \hat{\boldsymbol{\gamma}}_4 \cdot \hat{\boldsymbol{\gamma}}_4^t \right], \\
\boldsymbol{k}_{22} &= P s_{2222} H_{22} \left[\hat{\boldsymbol{\gamma}}_3 \cdot \hat{\boldsymbol{\gamma}}_3^t + \frac{1}{3} \hat{\boldsymbol{\gamma}}_4 \cdot \hat{\boldsymbol{\gamma}}_4^t \right], \\
\boldsymbol{k}_{33} &= \frac{\mu}{3} H_{11} \left[\hat{\boldsymbol{\gamma}}_4 \cdot \hat{\boldsymbol{\gamma}}_4^t \right], \\
\boldsymbol{k}_{ij} &= \boldsymbol{0}, \ i \neq j.
\end{aligned} \tag{C.49}$$

Equally the stabilisation forces are still defined by Equation C.36, with:

$$\begin{aligned}
\dot{\mathcal{Q}}_{x3} &= P s_{1111} H_{11} \dot{q}_{x3}, \\
\dot{\mathcal{Q}}_{x4} &= \frac{1}{3} P s_{1111} H_{11} \dot{q}_{x4}, \\
\dot{\mathcal{Q}}_{y3} &= P s_{2222} H_{22} \dot{q}_{y3}, \\
\dot{\mathcal{Q}}_{y4} &= \frac{1}{3} P s_{2222} H_{22} \dot{q}_{y4}, \\
\dot{\mathcal{Q}}_{z3} &= 0, \\
\dot{\mathcal{Q}}_{z4} &= \frac{\mu}{3} H_{11} \dot{q}_{z4},
\end{aligned} \tag{C.50}$$

Anisotropy

The strategy followed to implement anisotropic behaviour is detailed in this paragraph. First only inelastic anisotropy has been considered in the work. The strategy developed here consists in defining the anisotropy axis in the co-rotational frame. The anisotropic behaviour is only applied to the plane stress components of the strain and stress tensors. As a baseline the strain and stress tensors are defined in the co-rotational frame. Before the integration of the constitutive law, the strain and strain components are transported in the anisotropic frame. The constitutive law is integrated, therefore the stress increment and stress tensor are defined as

well as the linear tangent operator and finally transported back to the co-rotational frame.

It is important to notice that the present method is managed by Mfront (cf. [Helfer et al. 2013]). The problem is therefore concentrated on the element orientation and the definition of the axis of anisotropy.

This formulation is then used for all finite element analysis with the exception of the FEMU process. The developments performed on the SHB8PS in Cast3M were validated against test cases from the literature.

Appendix D

Development of the FEMU process

This appendix presents the details of the FEMU process developed.

Contents
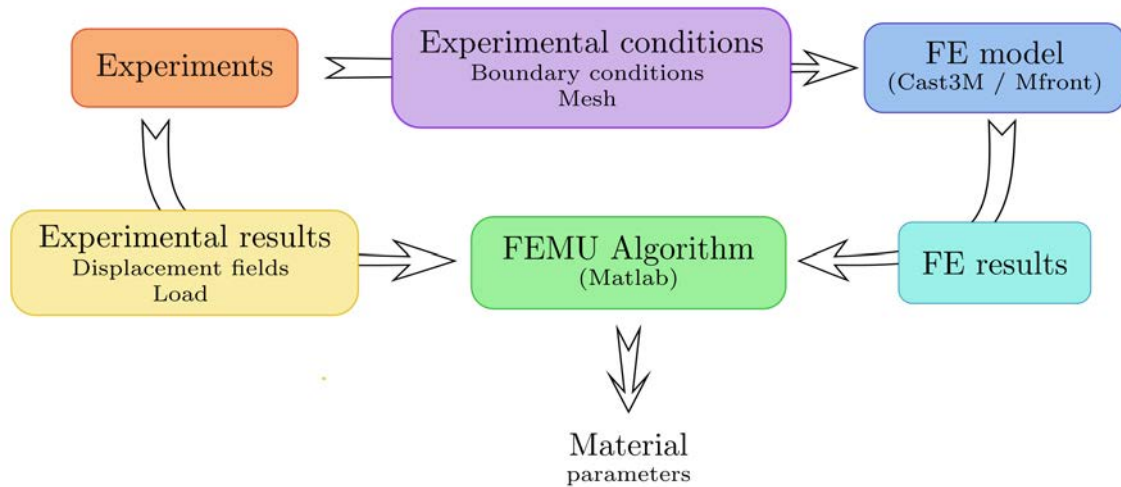
Figure D.1: FEMU method data flow

The buckling behaviour of any structure is highly dependent of the constitutive law of its material. An inverse method was implemented to identify the constitutive law selected for the SAC305 alloy and presented thereafter. This method is named FEMU for Finite Flement Model Updating. This method is based on the update of the material parameters of a finite element model until convergence of the model with experimental data, as described in [Avril et al. 2008]. This identification is therefore based on experimental data, a finite element model, the constitutive law chosen and an optimisation algorithm. The different elements are presented in Figure D.1

D.1 2D-DIC

As already mentioned, the FEMU approach is based on experimental data, as the displacement fields on the surface of the specimens. They are defined through a 2D-DIC method.

The pictures taken by the cameras are post processed following a global 2D-DIC method as described in [Besnard, Hild, and Roux 2006]. 2D-DIC is performed with Ufreckles, a FE-DIC global approach software developed by [Réthoré 2018]. The global approach is based on a FE kinematic formulation to identify the displacements fields on the specimen observed. Because of the speckle pattern properties, a Q4 element mesh with a mean cell size of 41 px was created. This numerical link between experiments and FE simulations reduces numerical errors due to data exchange. The DIC mesh is directly built on the reference images. Points on the specimen edges are selected and a parametric mesh is fitted to the specimen shape. The parametric mesh is controlled by a set of control points. In Figure D.2 the process followed to create the DIC mesh is presented. Figure D.2(a) depicts the points selected on

the specimen edges. An optimisation algorithm is used to fit the parametric shape and its control points to the selected points (see Figure D.2(b)). Finally the control points are transferred to Cast3M to build the FE and DIC mesh, as shown in Figure D.2(c).
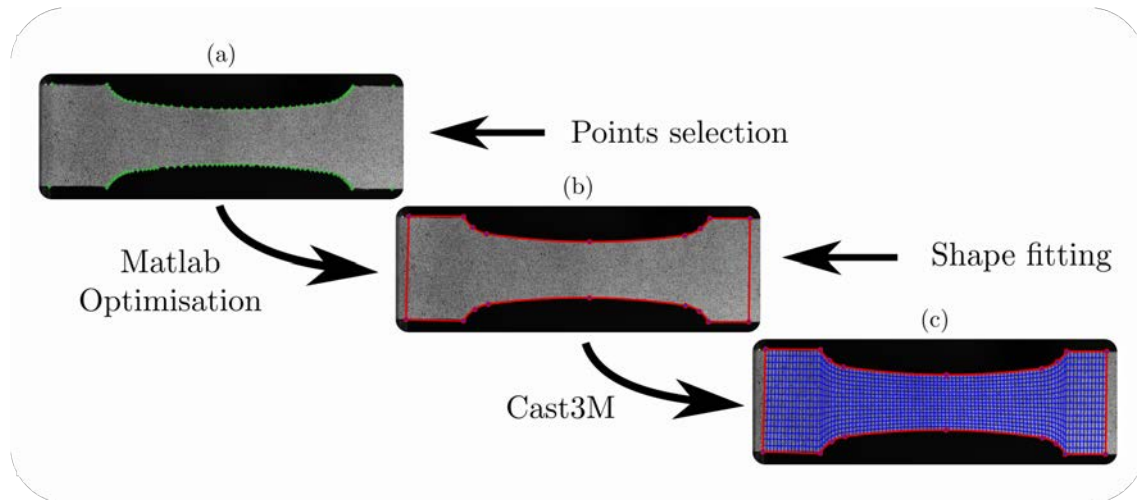
Figure D.2: DIC mesh fitting for FEMU method

This method presents different advantages:

- The numerical mesh models accurately the specimen geometry,

- Pre-test measurements of the specimen define the metric definition of the DIC and FE meshes,

- Data transfer between experiments and FE model is direct.

The mesh definition is particularly important in this case as it defines the quality of the DIC results as well as the FE results. Ideally the FE mesh would be as fine as possible. Nevertheless, a single mesh of the DIC mesh needs to include at least 10 different gray levels. Because of the speckle pattern dimensions a compromise needs to be found to respect DIC constraints and FE convergence quality constraints.

D.2   Tensile tests modelling

The purpose of the FEMU method is to compare data with finite element results in order to identify the material parameters, in this subsection the different bricks of the finite element model will be detailed.

D.2.1   FE model

The finite element model intends to simulate the experiments with high fidelity. Cast3M, a FE software, is used to model the tensile experiment. The material constitutive law is integrated with an implicit scheme through Mfront (see [Helfer et al. 2015]).

Because of the specimen geometry and the loading conditions, Q4 elements with reduced integration are used under plane stress condition. The plane stress condition allows to reduce computation time and therefore to increase the robustness of the FEMU algorithm (discussed in the next subsection). As the strain level stays low (under 10 %), localisation issues and high triaxiality levels should be low, which motivate the use of plane stress assumption. This model was compared favourably with a full 3D FE model, the results are presented in Chapter 3. The experiment is divided into several time steps. Each time increment corresponds to a picture. The time discretization is compliant with the small strain assumption during an increment. An update lagrangian formulation is used with an implicit time scheme to solve the mechanical problem. The thickness of every element is also updated during the simulation.

The loading of the specimen is performed by applying the DIC displacement fields to each end of the specimen. To reduce inherent DIC errors on the boundaries of the mesh, two rows of elements were removed at each end of the specimen, as shown in Figure D.3. Because of the noisy displacement fields, in time and space, the DIC displacement fields are smoothed to reduce numerical integration issues during FE simulations.
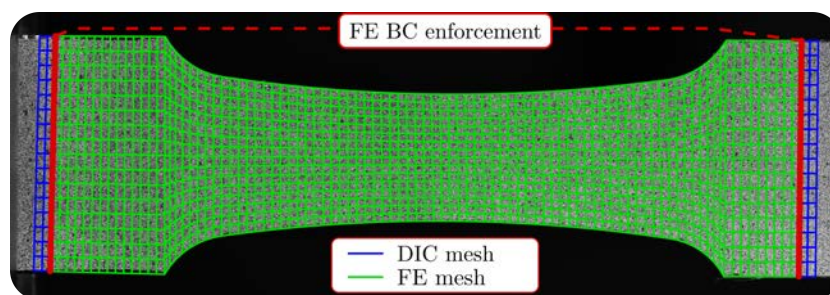
Figure D.3: FE mesh and boundary condition enforcement

D.2.2   Material constitutive law

The constitutive law of SAC305 alloy is modelled with a unified elasto-visco-plastic model. Creep behaviour is model with a Norton law and the hardening with three Voce equations. Because of the orthotropic properties of Tin crystal, SAC305 presents an isotropic transverse behaviour. This anisotropic behaviour is modelled with the Hill yield criterion. It was chosen to keep elasticity isotropic. The constitutive law is defined by the following set of equations:

$$\boldsymbol{\sigma} = \boldsymbol{\mathcal{C}}\,\boldsymbol{\varepsilon}_e,$$
$$\boldsymbol{\varepsilon} = \boldsymbol{\varepsilon}_e + \boldsymbol{\varepsilon}_p,$$
$$\dot{p} = \left(\frac{F}{K}\right)^n,$$
$$F = \sigma_{eq} - R(p), \tag{D.1}$$
$$R(p) = R_0 + \sum_{i=1}^{3} R_i\left(1 - e^{-b_i p}\right),$$
$$\sigma_{eq} = \sqrt{\boldsymbol{\sigma} : \boldsymbol{H} : \boldsymbol{\sigma}},$$

with, $\boldsymbol{\sigma}$ the Cauchy stress tensor, $\boldsymbol{\varepsilon}$ the Biot strain tensor, $\boldsymbol{\varepsilon}_e$ the elastic strain tensor and $\boldsymbol{\varepsilon}_p$ the plastic strain tensor, $\boldsymbol{\mathcal{C}}$ the isotropic elastic linear operator, σ_{eq} the Hill equivalent stress defining the yield surface, $\boldsymbol{H}$ the Hill tensor (used here for transverse anisotropy), p the equivalent plastic strain, R the hardening variable and $\dot{p}$ the equivalent strain rate.

In the general case the Hill tensor is defined by:

$$\boldsymbol{H} = \begin{bmatrix} F+H & -F & -H & 0 & 0 & 0 \\ -F & G+F & -G & 0 & 0 & 0 \\ -H & -G & H+G & 0 & 0 & 0 \\ 0 & 0 & 0 & L & 0 & 0 \\ 0 & 0 & 0 & 0 & M & 0 \\ 0 & 0 & 0 & 0 & 0 & N \end{bmatrix}, \tag{D.2}$$

with:

$$F = 0.5\left(\frac{1}{R_{11}^2} + \frac{1}{R_{22}^2} - \frac{1}{R_{33}^2}\right)$$
$$G = 0.5\left(\frac{1}{R_{11}^2} + \frac{1}{R_{33}^2} - \frac{1}{R_{22}^2}\right)$$
$$H = 0.5\left(\frac{1}{R_{22}^2} + \frac{1}{R_{33}^2} - \frac{1}{R_{11}^2}\right)$$
$$L = \frac{3}{2}\left(\frac{1}{R_{12}^2}\right) \tag{D.3}$$
$$M = \frac{3}{2}\left(\frac{1}{R_{23}^2}\right)$$
$$N = \frac{3}{2}\left(\frac{1}{R_{13}^2}\right)$$

In case of transverse isotropy the Hill tensor is completely defined by the Lankford coefficient R_{lank}:

$$\begin{array}{ll} R_{11} = 1 & R_{12} = 1 \\ R_{22} = 1 & R_{13} = 1 \\ R_{33} = \sqrt{\frac{R_{lank}+1}{2}} & R_{23} = 1 \end{array} \tag{D.4}$$

and:

$$R_{Lank} = \varepsilon_{yy}/\varepsilon_{zz}, \tag{D.5}$$

with $\boldsymbol{y}$ the width direction of the specimen, $\boldsymbol{z}$ its thickness direction.

The material parameters to be identified are R_0, R_1, b_1, R_2, b_2, R_3, b_3, K, n, R_{lank} and $\boldsymbol{\mathcal{C}}$ defined by the Young's modulus and Poisson ratio. Many parameters needs to be defined, the associated identification process is therefore complex. Nevertheless, the complexity of the constitutive law allows to better model the SAC 305 behaviour and especially its tangential behaviour. This is particularly important for inelastic buckling analysis.

D.3   FEMU algorithm

The algorithm used to identify the material parameters is the main component of the FEMU method. This algorithm compares experimental data with data from the FE model. The different data are compiled into an objective function. By minimizing the objective function, a set of material parameters can be identified. In the next paragraphs the objective function and the minimization strategy will be discussed.

D.3.1   Objective function

The objective function can be defined as the difference between experimental and numerical observable variables. Those variables can be the displacement fields, the strain fields, the load or other relevant variables.

The displacement fields and the reaction load are often chosen as components of the objective function. Due to the coarse microstructure of SAC305, a noisy displacement field is observed on the specimen surfaces. Using a noisy measurement in the function to minimize would imply a large number of local minimums. Therefore, a regularized strain field was introduced in the objective function instead of the displacement field. The regularized strain field is defined as the average of the strain field within a 2 mm radius circle surrounding the current integration point.

The objective function is defined as follow:

$$f = \boldsymbol{R}^t \cdot \boldsymbol{R}$$

$$\boldsymbol{R} = \begin{bmatrix} \left(\dfrac{\boldsymbol{F}^n - \boldsymbol{F}^e}{\eta_F} \right) \\[2em] \left(\dfrac{\boldsymbol{\varepsilon}_{xx}^n - \boldsymbol{\varepsilon}_{xx}^e}{\eta_{\varepsilon_{xx}}} \right) \\[2em] \left(\dfrac{\boldsymbol{\varepsilon}_{yy}^n - \boldsymbol{\varepsilon}_{yy}^e}{\eta_{\varepsilon_{yy}}} \right) \\[2em] \left(\dfrac{\boldsymbol{\lambda}^{(i)} - \boldsymbol{\lambda}_0^{(i)}}{C_\lambda^{(i)}} \right) \end{bmatrix} \tag{D.6}$$

with subscript ^{n} and ^{e} respectively stand for numerical and experimental data. $\boldsymbol{F}$ contains the value of the reaction load for each increment. $\boldsymbol{\varepsilon}_{xx}$ and $\boldsymbol{\varepsilon}_{yy}$ are vectors containing respectively the strain value at every integration point and for every time increment in $\boldsymbol{x}$ and $\boldsymbol{y}$ directions. $\boldsymbol{\lambda}$ and $\boldsymbol{\lambda}_0$ are the vectors containing the material parameters for the current increment and their initial value. Each type of value is normalised by its acceptable error value, η_F, $\eta_{\varepsilon_{xx}}$ and $\eta_{\varepsilon_{yy}}$, as proposed in [Neggers et al. 2017]. Each component of the material difference vector $(\boldsymbol{\lambda} - \boldsymbol{\lambda}_0)$ is also normalized with respect to an acceptable change of the corresponding parameter during the optimisation process.

D.3.2 Minimization algorithm

The identification of the best material parameters $\boldsymbol{\lambda}^*$ is conditioned by the following optimisation problem:

$$\boldsymbol{\lambda}^* = \underset{\boldsymbol{\lambda}}{\arg\min}(f(\boldsymbol{\lambda})) \tag{D.7}$$

This optimisation problem is solved with a Matlab$^{\circledR}$ function *lsqnonlin*. A Newton type approach is used to minimize f. At each optimisation increment the next material parameters are defined by solving the following equation:

$$f(\boldsymbol{\lambda} + d\boldsymbol{\lambda}) = f(\boldsymbol{\lambda}) + \nabla f^t d\boldsymbol{\lambda} + \frac{1}{2} d\boldsymbol{\lambda}^t \boldsymbol{H} d\boldsymbol{\lambda} \text{ with: } \boldsymbol{H} = \frac{\partial^2 f}{\partial \boldsymbol{\lambda}^2} \tag{D.8}$$

$\boldsymbol{H}$ is the Hessian of f, $\boldsymbol{\lambda}$ is the current material vector and $d\boldsymbol{\lambda}$ is the material vector increment to find. As $\boldsymbol{R}$ is explicitly known, $\boldsymbol{H}$ can be approximated by:

$$\boldsymbol{H} = 2 \boldsymbol{J}^t \cdot \boldsymbol{J}, \text{ with: } \boldsymbol{J} = \frac{\partial \boldsymbol{R}}{\partial \boldsymbol{\lambda}}, \tag{D.9}$$

$\boldsymbol{J}$ is the Jacobian matrix of $\boldsymbol{R}$.

To solve Equation D.8, a "Trust-Region" method is implemented (see [Moré and Sorensen 1983]). First, the material vector increment, $d\boldsymbol{\lambda}$, is constrained by the following equation:

$$||\boldsymbol{D} \cdot d\boldsymbol{\lambda}|| \leq \Delta, \tag{D.10}$$

with $\boldsymbol{D}$ a scaling matrix and Δ a scalar parameter defining the size of the confidence area of Equation D.8.

Then the Equation D.8 is solved on a sub-space $\mathcal{S}$ of two dimensions (cf. [Branch, Coleman, and Li 1999]). Because of its size, this sub-problem is easy to solve.

The difficulty is in the definition of the sub-space $\mathcal{S}$. $\mathcal{S}$ is defined by two vectors $\boldsymbol{s}_1$ and $\boldsymbol{s}_2$ as follow:

$$\boldsymbol{s}_1 \times \nabla f = \boldsymbol{0},$$
$$\boldsymbol{H} \cdot \boldsymbol{s}_2 = -\nabla f,$$
$$\text{or:} \tag{D.11}$$
$$\boldsymbol{s}_2^t \cdot \boldsymbol{H} \cdot \boldsymbol{s}_2, < 0$$

To summarise, the following steps are followed:

1. Definition of the sub-space $\mathcal{S}$,

2. Resolution of Equation D.8 on $\mathcal{S}$,

3. If $f(\boldsymbol{\lambda} + d\boldsymbol{\lambda}) < f(\boldsymbol{\lambda})$, then $\boldsymbol{\lambda} = \boldsymbol{\lambda} + d\boldsymbol{\lambda}$,

4. Update of the size of confidence area, Δ.

This solving method is particularly efficient for large optimisation problem. The quadratic approach combined with the definition of the objective function accelerates the convergence. Only the Jacobian $\boldsymbol{J}$ of $\boldsymbol{R}$ is needed to compute the gradient and the Hessian of f. Thanks to the sub-problem approach the solver time is reduced. Its confidence area keeps the solver stable and maximizes the convergence probability. Nevertheless as the Jabocian $\boldsymbol{J}$ is computed numerically, a large number of FE simulations is needed. Most of the computation time is dedicated to the Jacobian computation.

In addition to the solving method of the minimisation algorithm, a random multi-start strategy has been implemented. The minimisation problem is solved several times with a randomly chosen initial material vector. Thanks to the simple modelling method adopted combined with a parallel approach, several local minimums can be found in an acceptable computation time. The Pareto frontier or a global minimum of the problem can be found. This last issue was discussed in Chapter 3. This minimisation method gives us confidence in the set of material parameters selected at the end.

Appendix E

FEMU detailed results

The detailed results of the FEMU process are presented in the appendix

Contents

This appendix presents the detailed results of the FEMU process. First the a brief introduction of the uncertainty associated to the optical measure system is presented. Then, the results of a sensitivity study on the material parameters is introduced. Finally the FEMU results are compared to the tensile test results.

E.1   Uncertainty assessment

The uncertainties associated to the optical set-up and the DIC processing were evaluated through the mean and standard deviation of the displacement fields identified from a set of still images.

For each specimen the error on the displacement is defined by a Gaussian distribution, characterized by its mean value and its standard deviation respectively $\overline{U}^{err}_{x/y}$ and $StD\left(U^{err}_{x/y}\right)$. Table E.1 summarises these parameters for all specimens. The calibration factor is also given for all specimens in Table E.1.

Specimen ID	Calibration factor [mm.px^{-1}]	$\overline{U}^{err}_x$ [μPx]/[μm]	$StD\left(U^{err}_x\right)$ [μPx]/[μm]	$\overline{U}^{err}_y$ [μPx]/[μm]	$StD\left(U^{err}_y\right)$ [μPx]/[μm]
TT/11	0.024	27/0.64	21/0.49	-41/-0.98	26/0.63
TT/12	0.025	0/-0.01	19/0.47	-20/-0.50	19/0.48
TT/21	0.0225	19/0.42	10/0.23	3/0.08	29/0.65
TT/22	0.0225	-14/-0.32	22/0.48	-51/-1.15	15/0.35
TT/31	0.0225	-15/-0.34	15/0.33	50/1.13	31/0.70
TT/32	0.0225	-30/-0.68	28/0.64	107/2.41	49/1.11
TT/41	0.021	11/0.22	19/0.41	-13/-0.28	22/0.47
TT/42	0.021	-37/-0.77	36/0.76	26/0.55	17/0.35

Table E.1: Summary of displacement errors due to calibration, camera set-up and DIC process

The measurement error is very small, mostly lower than 1 μm. The low error amplitude shows the quality of the experimental optical set-up as well as its calibration.

E.2   Sensitivity study

First the sensitivity of each parameter is defined in order to select the best set of material parameters and to understand how they interact with each other.

This can be easily done by analysing the Hessian matrix with respect to the residual load or/and the residual strain as described in [Neggers et al. 2017]. As presented in the previous chapter the Hessian matrix is defined thanks to the Ja-

cobian matrix of the objective function. The Jacobian matrix can also be defined with respect to the different components of the objective function as follows:

$$\boldsymbol{J} = \left[\begin{array}{c} \boldsymbol{J}_F \\ \boldsymbol{J}_{\varepsilon_{xx}} \\ \boldsymbol{J}_{\varepsilon_{yy}} \end{array} \right] = \left[\begin{array}{c} \frac{\partial \boldsymbol{R}_F}{\partial \boldsymbol{\lambda}} \\ \frac{\partial \boldsymbol{R}_{\varepsilon_{xx}}}{\partial \boldsymbol{\lambda}} \\ \frac{\partial \boldsymbol{R}_{\varepsilon_{xx}}}{\partial \boldsymbol{\lambda}} \end{array} \right], \tag{E.1}$$

with:

$$\boldsymbol{R} = \left[\begin{array}{c} \boldsymbol{R}_F \\ \boldsymbol{R}_{\varepsilon_{xx}} \\ \boldsymbol{R}_{\varepsilon_{yy}} \end{array} \right]. \tag{E.2}$$

Finally the Hessian matrix can be defined as:

$$\begin{aligned} \boldsymbol{H} &= \boldsymbol{J}^t \cdot \boldsymbol{J}, \\ &= \boldsymbol{J}_F^t \cdot \boldsymbol{J}_F + \boldsymbol{J}_{\varepsilon_{xx}}^t \cdot \boldsymbol{J}_{\varepsilon_{xx}} + \boldsymbol{J}_{\varepsilon_{yy}}^t \cdot \boldsymbol{J}_{\varepsilon_{yy}}, \\ &= \boldsymbol{H}_F + \boldsymbol{H}_{\varepsilon_{xx}} + \boldsymbol{H}_{\varepsilon_{yy}}. \end{aligned} \tag{E.3}$$

Each Hessian matrix, $\boldsymbol{H}_F$, $\boldsymbol{H}_{\varepsilon_{xx}}$, $\boldsymbol{H}_{\varepsilon_{yy}}$ can be used to study the sensitivity of the algorithm with respect to each material parameter and to each component of the objective function. The diagonal terms of the Hessian give information about the sensitivity of each parameter independently. The other terms of the Hessian matrix give information about the sensitivity of the coupling of material parameters with each other. As an example the value of H_{11} shows the impact of R_0 on the global solution. Equally H_{19} shows how R_0 and n interact with each other and their coupled impact on the global solution. The coupled sensitivity can also be analysed using the covariance matrix $\boldsymbol{C}$ defined by:

$$C_{ij} = \frac{H_{ij}^{-1}}{\sqrt{H_{ii}^{-1} H^{-1} jj}}. \tag{E.4}$$

While the Hessian matrix gives the amplitude of the coupling effect, the covariance matrix shows how the parameters interact with each other.

The Hessian and Jacobian matrices can be extracted at each increment of the resolution. We chose to study the sensitivity of the algorithm around a minimum of the objective function. Therefore only the final Hessian matrix is analysed.

In Figure E.1 the Hessian and covariance matrices are plotted with respect of each component of the objective function, i.e. F, ε_{xx} and ε_{yy}.

In addition the diagonal terms of the Hessian matrix are plotted in Figure E.2.

Figure E.2 depicts the influence of each material parameter on each component of the objective function and their cumulated effects. First, Figure E.2 shows that the material parameters have a strong impact on the load components of the objective function. Only few parameters have a non-negligible effect on the strain components, b_i, R_{lank} and ν. The most influential parameter is n, this results is also discussed later. The hardening coefficients R_i and the yield stress come next.
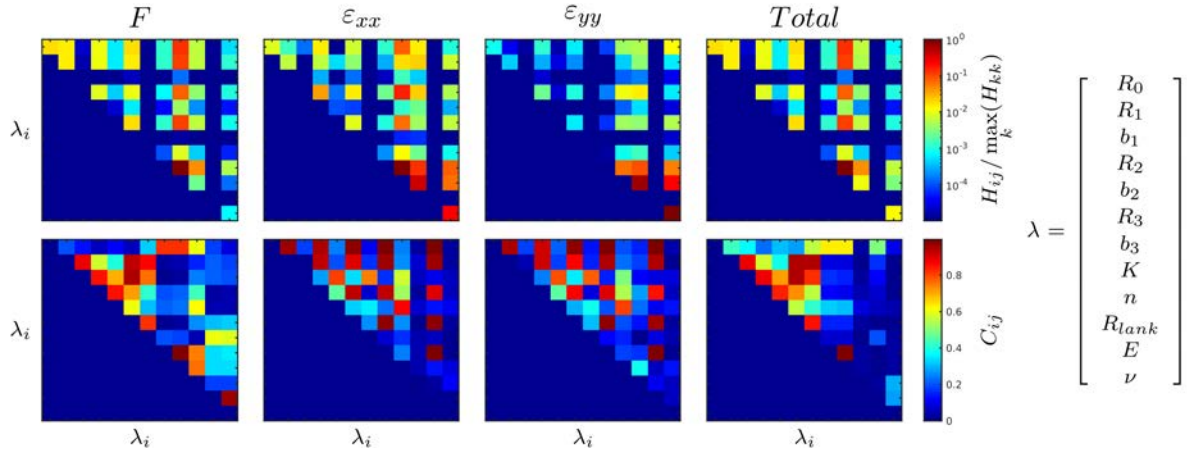
Figure E.1: Hessian and covariance matrices of the minimisation problem
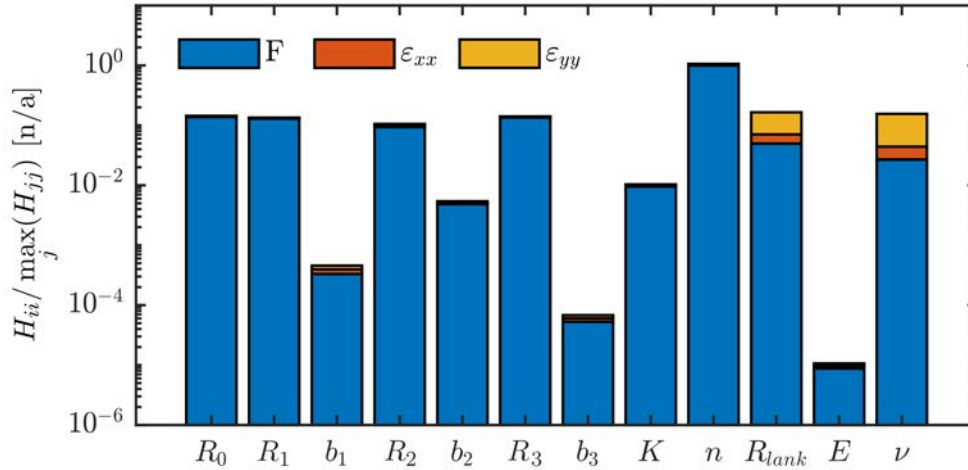
Figure E.2: Normalized diagonal terms of the Hessian matrix

The following observation can be made by analysing the non-diagonal terms of the Hessian and the covariance matrices:

- The yield stress R_0 interacts with the creep parameters K and n, their coupling have a strong impact on the load response,

- The yield stress R_0 coupled with the hardening coefficients R_i has a strong impact on the strain components of the objective function,

- The hardening coefficients and exponents (R_i and b_i) interact with each other and impact especially the load response,

- The hardening coefficients coupled with each other have an important effect on the strain components of the objective function,

228

- The young modulus interacts with the hardening coefficient and the creep coefficient K without affecting the solution,

- The couple Lankford's ratio / Poisson's ratio affects especially the strain components of the objective function.

This sensitivity analysis helped to understand the different links between all material parameters and their impacts on the correlation of the numerical model with the experiments. This sensitivity analysis should also indicate if the solution is unique. Ideally all parameters should be independent to obtain a unique solution. From this analysis four groups of parameters can be defined, the hardening group containing the R_i coefficients, the b_i exponents and R_0, the creep group containing R_0, K and n, the geometrical group with R_{lank} and ν, and finally the elastic group with E and ν. These groups have different impacts on the quality of the identification process, with a special interest for the creep group discussed in the next section. This sensitivity analysis has also allowed to define the C_λ coefficients and the η_i coefficients of the objective function in Equation D.6.

As strain localisation on grain boundaries was observed (cf. 3.2), large coefficients for $\eta_{\varepsilon_{xx}}$ and $\eta_{\varepsilon_{xx}}$ were chosen. As the hardening group of parameters affect mainly the load, their C_λ coefficients are large in order to unconstrained their evolution. On the opposite, the C_λ parameters for the creep group are small, except for R_0, as it is also included in the hardening group. Same strategy is applied to the geometrical group. Finally as the young modulus sensitivity is almost negligible, its C_λ value is also small in order to keep E close to its initial value (defined from the literature). This low sensitivity of E can be explained by a smaller amount of data collected in the elastic range rather than in the inelastic one. Tables E.2 and E.3 summarize the sensitivity parameters defined.

η	F [N]	ε_{xx} [%]	ε_{yy} [%]
/	1.0	5.0	5.0

Table E.2: Summary of η sensitivity parameters

C_λ	R_0	R_1	b_1	R_2	b_2	R_3	b_3	K	n	R_{lank}	E	ν
$\times \lambda_i^{ini}$	10^6	10^6	10^6	10^6	10^6	10^6	10^6	10^{-2}	10^{-3}	10^{-3}	10^{-2}	10^{-3}

Table E.3: Summary of C_λ sensitivity parameters

E.3 FE results vs. Experimental results

The validation of the constitutive laws identified for each material batch is performed through the FE analysis of each tensile experiment. For each material batch,

both experiments are simulated with the material parameters identified. The generated numerical data are then compared to the experimental data. Scalar data are compared through time, while the strain field data are compared in two different ways. The global spatial distribution of the field data is compared first. Then the spatial distribution of the strain fields are analysed statistically over time and compared to experiments.
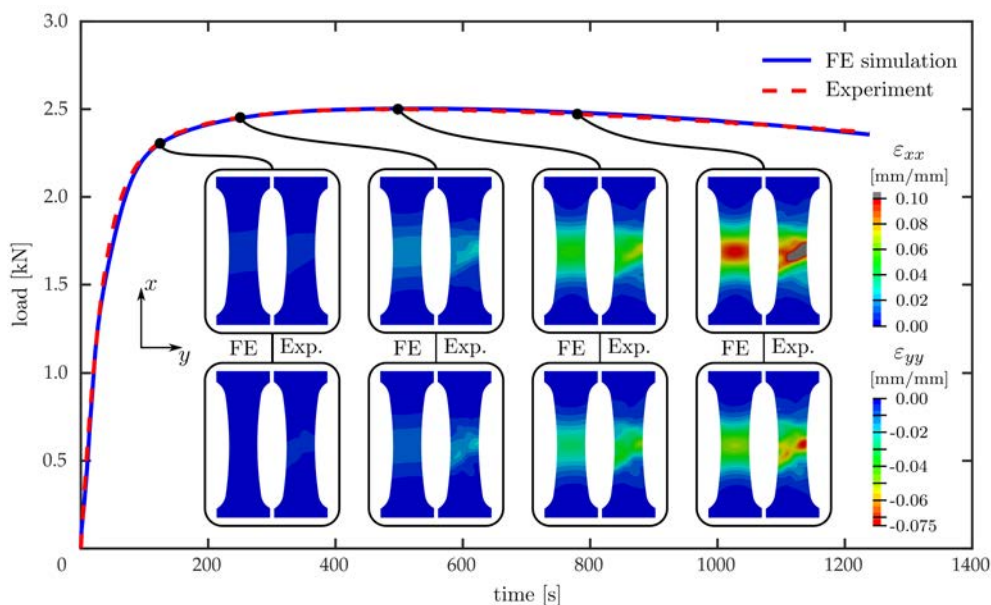
Figure E.3: FE simulation vs. experiment TT/31

Figures E.3 and E.4 illustrates these two approaches for specimen TT/31. First, the load history from the post identification FE analysis (in blue in Figure E.3) fits well to the experimental load history (in red in Figure E.3). The global shape, and especially in the plastic region, corresponds well to the experimental measurement. The strain fields obtained from the FE analysis are compared at four time steps in Figure E.3. For all four time steps, both numerical strain fields (ε_{xx} and ε_{yy}) are compared to experimental ones. In Figure E.3 the upper cases depict the numerical and experimental ε_{xx} strain fields and lower ones the ε_{yy} strain fields. The spatial distribution of the FE strain fields corresponds well to the experimental strain fields as shown in Figure E.3. The plastic region as well as the strain amplitude on both components (ε_{xx} and ε_{yy}) extracted from the FE analysis are comparable with the experimental ones. The difference observed is due to the localisation of the experimental strain on material defects or grain boundaries. This can be observed in Figure E.3 where strain hotspots can be observed on the edges of the specimen. This effect is even more visible by analysing the strain field statistically over time as illustrated in Figure E.4. While the average, the second and third quartiles of the strain fields extracted from the FE simulation fit well to the experiment, the FE maximum and minimum strain on both components diverge from the experimental

ones. This phenomenon corresponds well to the localisation issue on a material defect described before. Outside of the range defined by $[1^{st}$ quartile, 3rd quartile], the strain difference between numerical simulations and experiments is not relevant to analyse as both strain fields do not describe the same physical problem locally. Nevertheless a good correlation within the second and third quartiles is observed.
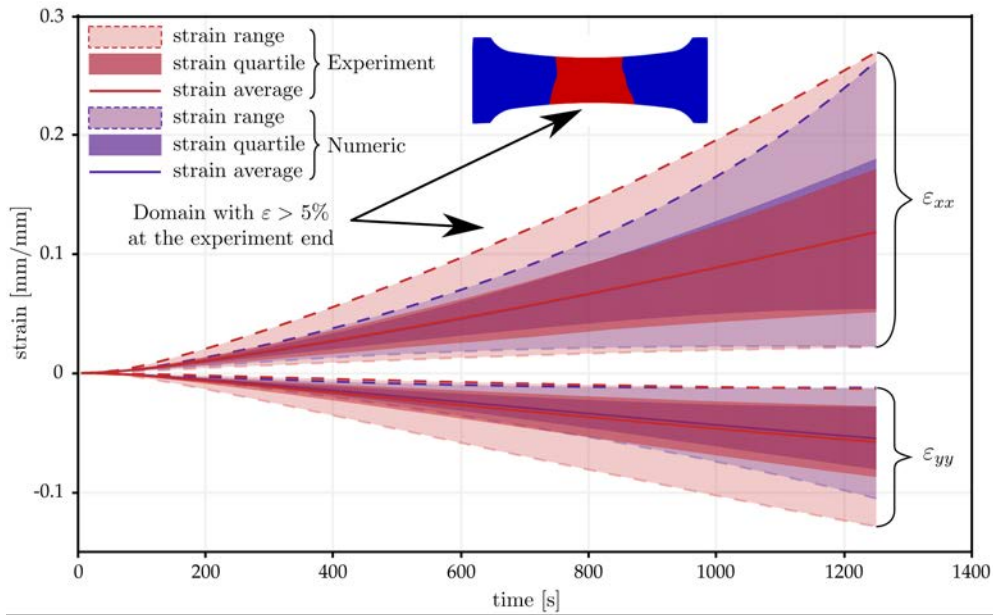
Figure E.4: FE vs. experiment, statistical analysis of the strain fields (TT/31)

This last observation leads to the conclusion that the material laws identified are sufficient at the structure scale. Nevertheless localisation issues and microscopic issues cannot be analysed with the identified laws. This limitation is not an issue for buckling analysis as the localisation is more related to the post-buckling behaviour of the structure. In the pre-buckling phase and at buckling, localisation phenomenon is often in-existent.

The same analysis can be done for all experiments. Instead of analysing both strain fields (experimental and numerical), the difference between experimental and numerical strain fields is statistically analysed with respect to the average experimental strain in Figure E.5. Only the results on ε_{xx} are presented in Figure E.5. Equivalent results on ε_{yy} were also observed. The numerical load is also compared to the experimental one in Figure E.5. It can be observed that the strain difference ranging from the first quartile to the third one is relatively small (lower than 0.005 in absolute value) as shown in Figure E.5. The relative error is therefore lower than 10% within this range.

As shown in Figure E.5, the average strain error is almost zero and the difference between experimental load and numerical one is also very small. Good correlation is observed between all experiments and simulations.
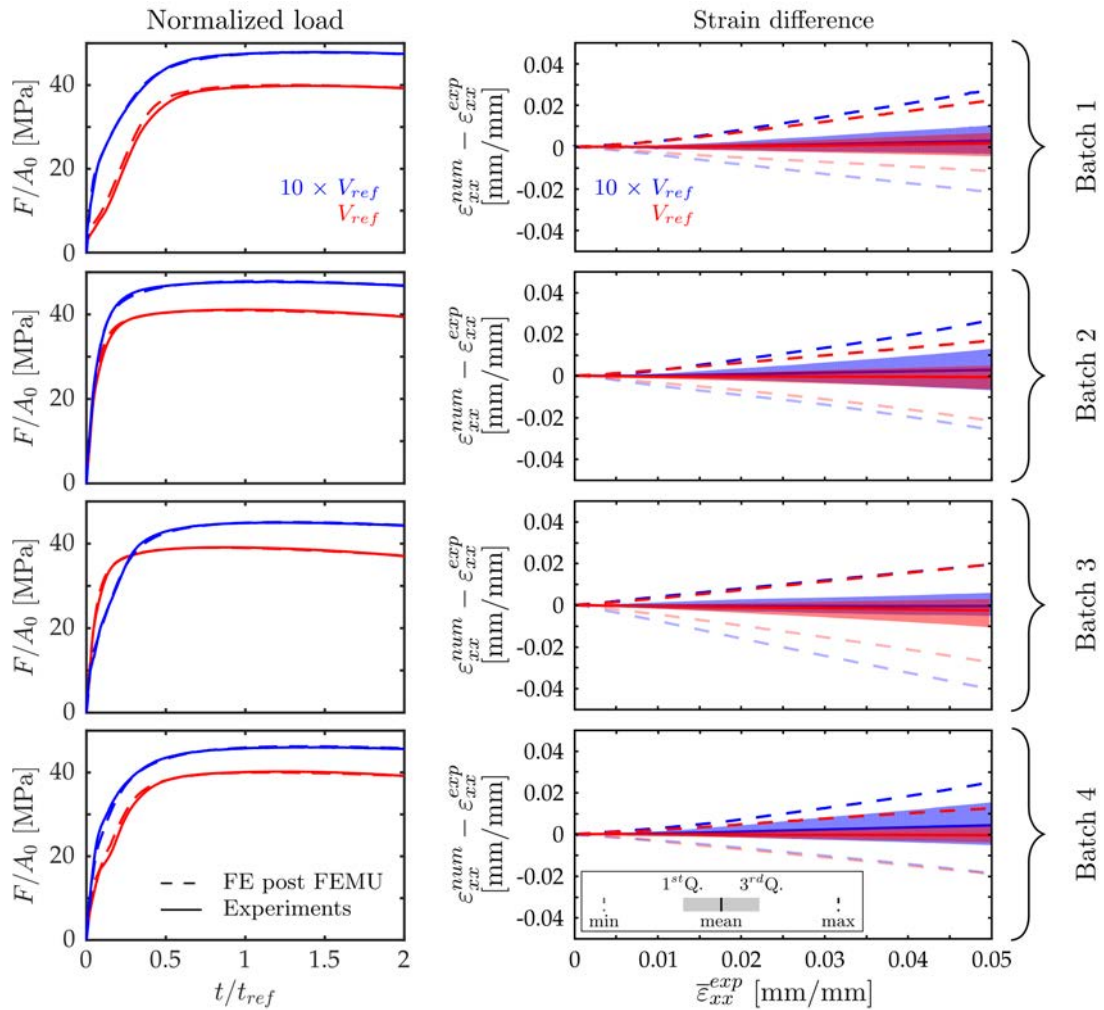
Figure E.5: FE post FEMU vs. experiments for all tensile experiments, (left) Normalized load with respect to the normalized time, (right) statistical description of the strain difference between FE post FEMU and experimental strain ε_{xx} with respect to the mean experimental axial strain $\overline{\varepsilon}_{xx}^{exp}$.

Appendix F

Parametric analysis of the buckling of a hemi-egg shell

The results of the parametric analysis carried out in order to study the buckling of thick hemi-egg shells is presented in this appendix.

Contents

In this appendix the results of the parametric analysis on the buckling of hemi egg shell is presented. In a first section, the effect of P_{inf} and t_{ref} on the buckling of the hemi-egg shell is analysed in the nominal conditions (no imperfection, neither on the geometry nor on the material). The effect of imperfections (material or geometrical imperfections) on the critical values is presented in Sections F.2 and F.3. The material imperfections are defined through the parameter ΔR_0 and the geometrical ones by $R_\%^{imp}$.

A a reminder the different parameters can take the values presented in Table F.1. Every combination is simulated. The outputs of the analysis are, the critical pressure P_c and the critical time t_c.

P_{inf}	t_{ref}	$R_\%^{imp}$	ΔR_0
[MPa]	[s]	[%]	[MPa]
4.00	10	0	-7.5
4.25	20	0.1	-5.5
4.50	50	0.2	-2.5
4.75	100	0.5	0
5.00	200	1.0	2.5
5.25	500	2.0	5.0
5.50	1000	5.0	
5.75	2000	10	
6.00	5000	20	
	10000		

Table F.1: Summary of input parameter values

The reference time, t_{ref}, is taken as a major parameter, as it mainly defines the loading rate and therefore the strain rate within the shell structure. Both outputs are presented with respect to t_{ref} and another parameters (P_{inf}, $R_\%^{imp}$ or ΔR_0).

F.1 Effect of the pressure history in the nominal conditions

A first post processing of the results of the parametric analysis was performed in order to study the effect of the pressure profile parameters (P_{inf} and t_{ref}) on the first bifurcation point. Only the simulations without any imperfection, either geometric or material imperfections are considered in this section. A first illustration of the effect of P_{inf} and t_{ref} is presented in Figure F.1. One can see on the left plot the evolution of the predicted eigen pressure (blue curves) with respect to the time ratio t/t_{ref} for different pressure rates (defined by t_{ref}) and with $P_{inf} = 5$ MPa. The bifurcation point is reached when the eigen pressure curve crosses the pressure profile one (plain black curve). In addition the buckling mode is plotted for each
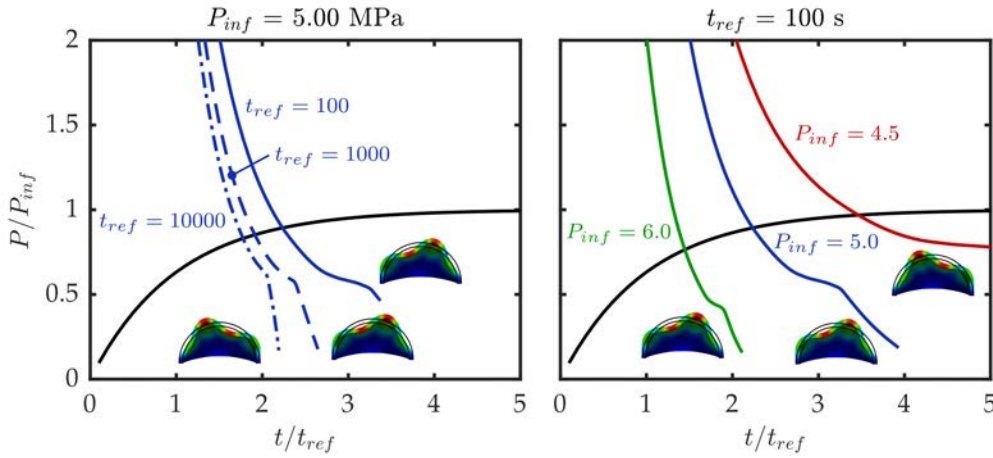
Figure F.1: (left) Eigen pressure ratio with respect to time ratio t/t_{ref} for different pressure rates; (right) Eigen pressure ratio with respect to time ratio t/t_{ref} for different saturating pressures (P_{inf} in MPa)

pressure rate. Same approach is followed on the right plot of Figure F.1, where the eigen pressure curves are drawn with respect to t/t_{ref}. Each colour corresponds to a different value of P_{inf}. As shown in Figure F.1, for a fixed value of P_{inf}, the critical pressure ratio and the critical time ratio decrease when t_{ref} increases. Equally, when P_{inf} increases, the critical pressure ratio and the critical time ratio decrease for a fixed value of t_{ref}. This normalized illustration is very convenient to present several results in different time and pressure scales. It is also convenient to visualize the effect of the pressure profile parameters. Nevertheless, we are mostly interested in visualizing the absolute critical values.

Abacuses presented in Figure F.2 were generated with the idea of visualizing the effect of the pressure profile on the critical values. The critical pressure P_c is depicted, with respect to P_{inf} and t_{ref}, by an iso-value plot in Figure F.2-(left). Same drawing process was followed in Figure F.2-(right) to present the evolution of the critical time with respect to P_{inf} and t_{ref}.

As preliminary observed in Figure F.1, the critical pressure increases with P_{inf}, and decreases with t_{ref}. Therefore, the critical pressure P_c increases with the pressure rate P_{inf}/t_{ref}. Moreover, the critical pressure P_c is contained in a pressure range from 4.1 MPa to 4.5 MPa. This observation leads to a first experimental constraint, the pressure profile used for the experiments must have a P_{inf} parameter higher than 4.5 MPa. This constraint guaranties to observe buckling of the hemi-egg shell. Regarding the critical time ratio t_c/t_{ref}, its value follows an asymptotic trend when t_{ref} increases. However, it decreases when P_{inf} increases and it follows an exponential increase when P_{inf} tends to P_c. Indeed, if P_{inf} is lower than P_c, the shell changes buckling regime to creep buckling, therefore $t_c \rightarrow t_c^{creep}$. t_c^{creep} is the creep buckling critical time for P_{inf} and t_{ref}. If P_{inf} is too small the shell can
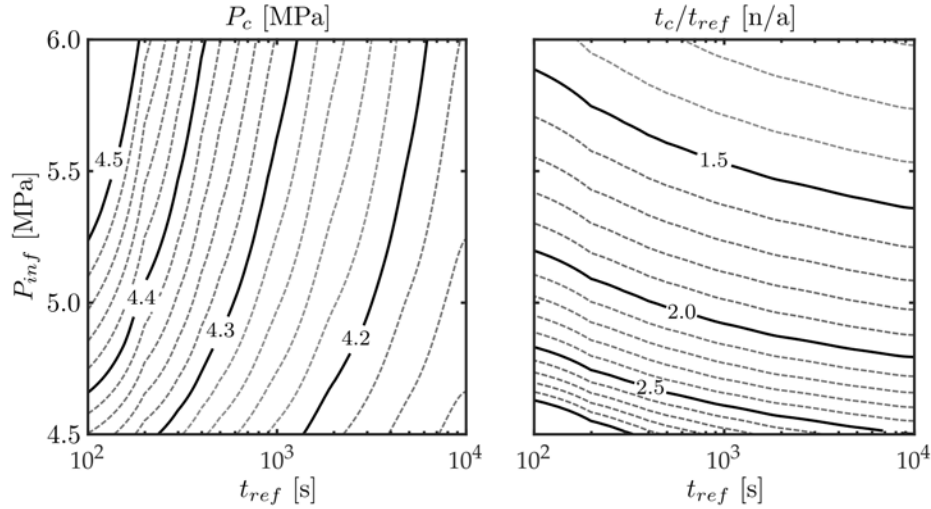
Figure F.2: Predicted critical pressure (left) and time (right) with respect to P_{inf} and t_{ref} in nominal conditions.

even not buckle at all. Another observation can be made on the buckling regime, when t_c/t_{ref} is high we are in the creep regime, while when it is small we are in the elasto-visco-plastic regime. Finally, as shown on Figure F.1 the buckling mode does not seem to be affected by P_{inf} or t_{ref}. Therefore the first three modes still correspond to the one presented in Figure 5.8.

From this first post processing, we can assume that P_{inf} must be as small as possible, but higher than 4.5 MPa, in order to be close to the creep buckling regime. Several values of t_{ref} can be chosen to define the experimental pressure rates without any additional constraint other than the experimental ones.

In the two next sections, the effect of imperfections on the buckling of the hemi-egg shell will be investigated. First the impact of an initial geometric imperfection will be analysed. Then the effect of a material imperfection will be analysed. Both analyses tend to finalize the selection of the experimental conditions. It will also allow to generate reference data in order to validate the buckling prediction method with the experiments.

F.2   Effect of geometrical imperfections

Shell structures can be more or less dependent on geometric imperfections. It is almost impossible to avoid geometric imperfections on such structures. Geometric imperfections can be due to the machining of the component, its set-up in the test rig or some environmental conditions as the temperature. In this particular case the geometric imperfection introduced to the structure can be evaluated to 0.05 mm (or 1.5% of the shell thickness) on the mean shape. This is defined according to the

(a)

(b)

Figure F.3: (a) Critical pressure (left) and time ratio (right) iso-values with respect to P_{inf} and $R_{\%}^{imp}$ with $t_{ref} = 100$ s; (b) Critical pressure (left) and time ratio (right) iso-values with respect to t_{ref} and $R_{\%}^{imp}$ with $P_{inf} = 5$ MPa

milling machine used and the manufacturing process followed. Imperfections introduced by the test rig are difficult to measure or even to evaluate in this particular case. In this matter, we studied the impact of the initial geometrical imperfection on the critical values with respect to P_{inf} and t_{ref}.

As in Section 5.1.2, the initial geometric imperfection is defined as a linear combination of the first fifteen elastic buckling modes, with their eigenvalues as weight. The overall is normalized to obtain a maximum displacement equal to $R_{\%}^{imp} \times h$,

237

with h the shell thickness. h is not modified here.

The same drawing procedure as in Figure F.3 was adopted to present the results of this imperfection analysis. Figure F.3(a) presents the critical pressure (left) and critical time ratio (right) iso-values with respect to P_{inf} and $R_\%^{imp}$ with $t_{ref} = 100$ s. Figure F.3(b) also presents the critical pressure (left) and time ratio (right) iso-values, but with respect to t_{ref} and $R_\%^{imp}$, and with $P_{inf} = 5$ MPa. As observed in Figures F.3(a) and F.3(b), the critical pressure P_c and the critical time ratio t_c/t_{ref} are almost unchanged for imperfection amplitudes $R_\%^{imp}$ lower than 5% of the shell thickness. 5% of the shell thickness corresponds to 0.15 mm, much higher than 0.05 mm imperfection estimated for the machining imperfections. Therefore we can assume that the shell structure selected is not very dependent on initial geometrical imperfections. Other types of imperfections will have to be considered in order to post process the experimental results. Nevertheless the initial geometric imperfections can be neglected based on this analysis.

F.3 Effect of material imperfections

Finally the potential material imperfections are analysed. In this section an imperfection on the initial yield stress is considered. Indeed, as mentioned and observed in the previous chapters, the yield stress can be affected by the cooling rate (cf. [Kim, Huh, and Suganuma 2002]). This last one can vary according to the water temperature, the environmental temperature, the size of the mould, the volume of alloy cast, etc... Therefore, all specimens can have a different yield stress.

This section has two objectives. First, it analyses the effect of a yield stress offset ΔR_0 on the critical values and the buckling behaviour. Secondly, it presents abacuses allowing to normalize the imperfect experimental critical values. This is used later in order to compare the test data to the numerical analysis with the same reference data.

As in the previous section the critical pressure P_c and the critical time t_c were studied according to the pressure P_{inf}, the pressure rate defined through t_{ref} and the yield stress offset ΔR_0. To present the results of the analysis, the same approach as in the previous section was followed. In Figure F.4(a), the iso-values of the critical values are drawn with respect to P_{inf} and ΔR_0, equally in Figure F.4(b) the critical values are drawn with respect to t_{ref} and ΔR_0. As expected the lower the yield stress is, the earlier the bifurcation happens. On the opposite, when the yield stress is too high, we change regime from elasto-visco-plastic buckling to pure creep buckling. This limit is defined by a thick red line and the labels "Creep buckling" or "C.B." in Figure F.4.
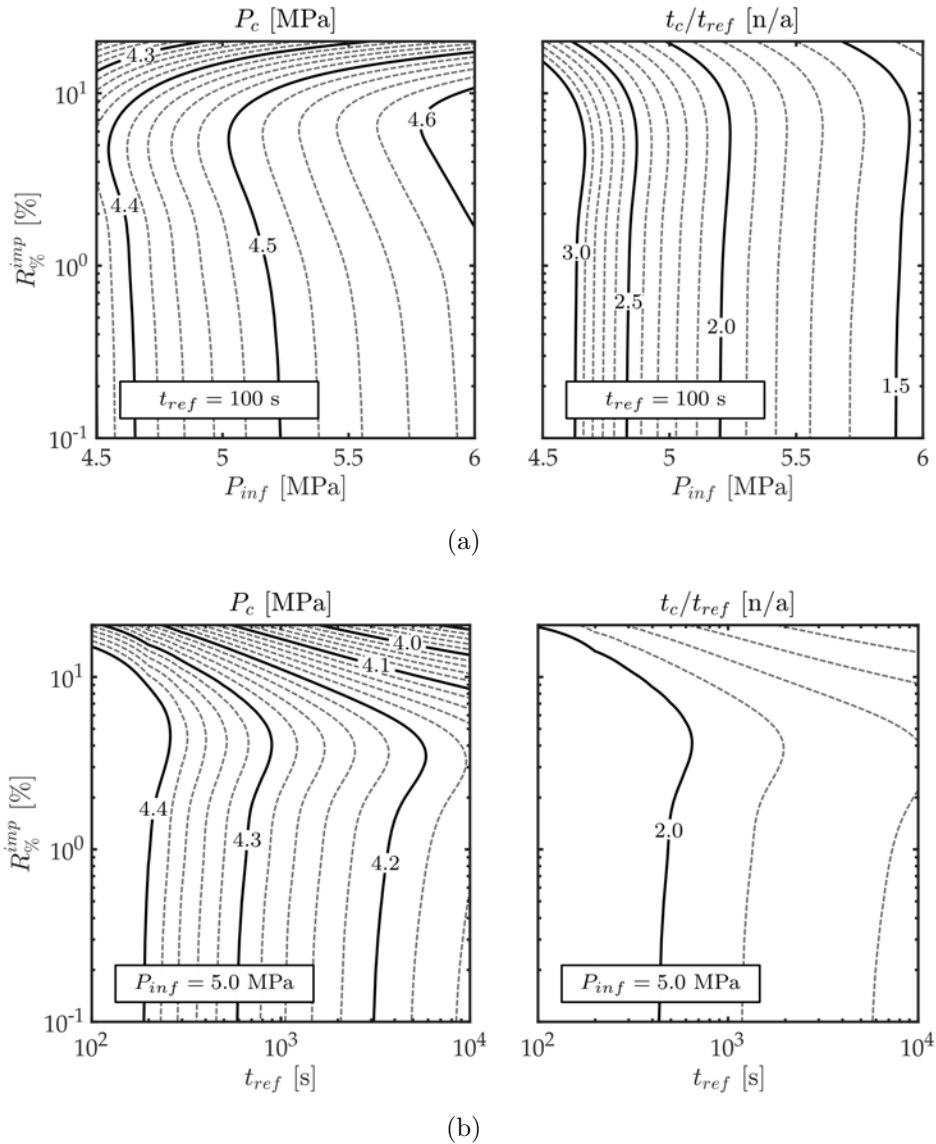
(a)

(b)
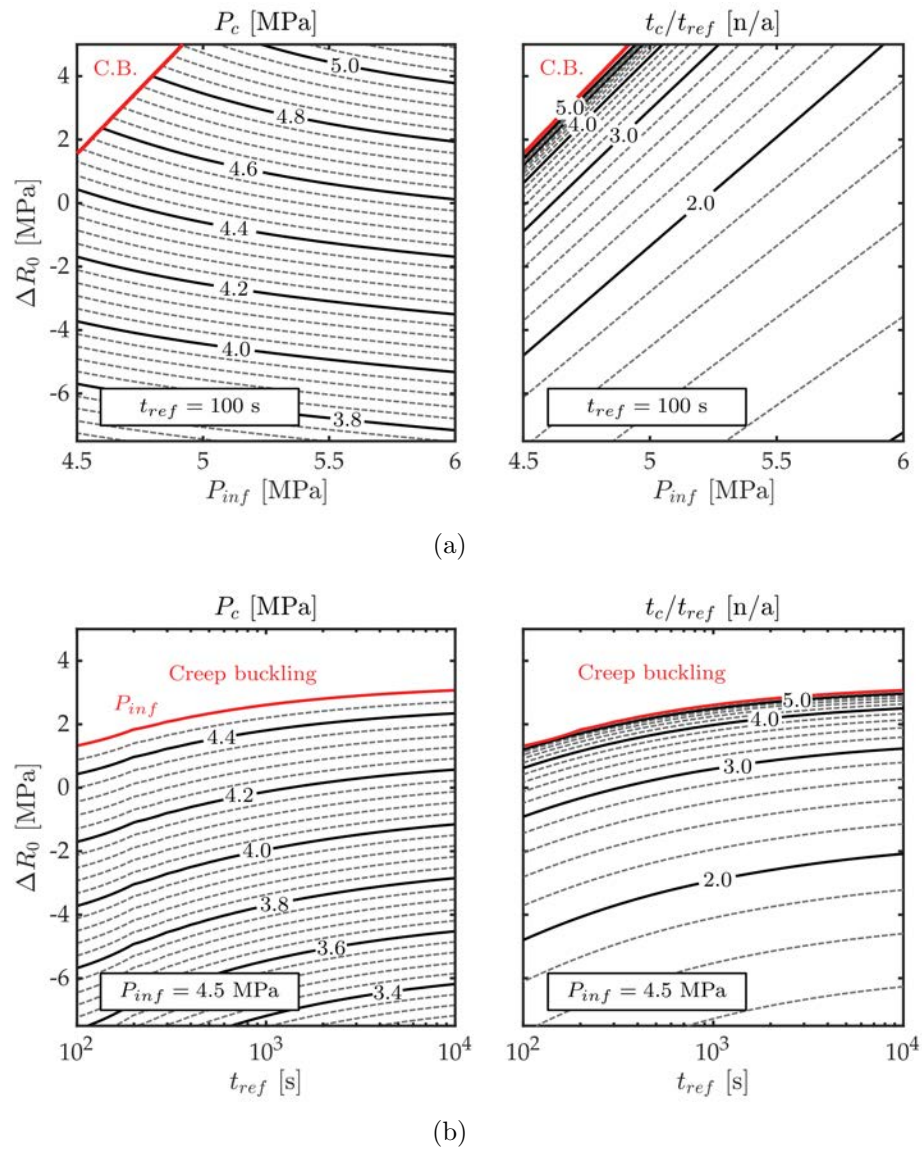
Figure F.4: (a) Critical pressure (left) and time ratio (right) iso-values with respect to P_{inf} and ΔR_0 with $t_{ref} = 100$ s; (b) Critical pressure (left) and time ratio (right) iso-values with respect to t_{ref} and ΔR_0 with $P_{inf} = 4.5$ MPa

Appendix G

Identification of the yield stress on the hemi-egg specimens

This appendix details the approach used to identify the yield stress on the hemi-egg specimens

Because of the complexity of the component as well as the casting process, it is very difficult to characterise with simple tensile tests the yield stress abatement. Indeed, the only solution would be to extract tensile specimens from the buckling specimen flange. Nevertheless this area of the specimen is thicker than the other ones, therefore the cooling rate could have been lower as well as the mechanical properties. These tests would not be representative of the material properties in the egg region.

A numerical approach was followed in order to identify the yield stress abatement of each specimen. A light FEMU process with the FE model **Model 1** was used. **Model 1** is presented in Section 2.5 of Chapter 2. The objective function is defined as follows:

$$f = \boldsymbol{R}^t \cdot \boldsymbol{R} \text{ with } : R_i = \frac{\|\boldsymbol{U}_{exp}(t_i) - \boldsymbol{U}_{num}(t_i)\|}{0.01}, \qquad (G.1)$$

where $\boldsymbol{R}$ is the residual vector, $\boldsymbol{U}_{exp}$ the experimental displacement fields, $\boldsymbol{U}_{num}$ the FE displacement fields, and the t_i correspond to the time steps where the measured pressure is within the pressure range [25%, 95%] of the maximum pressure. This allows to be in a phase where the egg shell has not buckled yet. The normalization by 0.01 mm corresponds to the order of magnitude of the measured displacement error discussed earlier.

Following this approach the yield stress abatement is defined in order to minimise the error between the experimental displacements and the numerical ones.

The identified yield stress abatements are presented for each specimen in Table G.1. In addition the effect of the upper bound of the pressure range used for the identification was also considered. The yield stress abatement range (presented in Table 5.8) is defined for an upper bound of the pressure range going from 92.5% to 97.5%.

O/00#	ΔR_0 (95% P_{max})	ΔR_0 (92.5% P_{max})	ΔR_0 (97.5% P_{max})
	MPa	MPa	MPa
2	-5.36	-5.70	-4.87
3	-4.78	-5.26	-4.35
4	-6.15	-6.55	-5.55
5	-4.59	-4.97	-3.75
6	-5.21	-5.85	-4.26

Table G.1: Yield stress abatement identified in the pre-buckling phase

Bibliography

Abed-Meraim, F. and A. Combescure (2002). "SHB8PS—a new adaptative, assumed-strain continuum mechanics shell element for impact analysis". *Computers & Structures* 80.9, pp. 791–803.

Abed-Meraim, Farid and Alain Combescure (2009). "An improved assumed strain solid–shell element formulation with physical stabilization for geometric nonlinear applications and elastic–plastic stability analysis". en. *International Journal for Numerical Methods in Engineering* 80.13, pp. 1640–1686.

Avril, Stéphane et al. (2008). "Overview of Identification Methods of Mechanical Parameters Based on Full-field Measurements". en. *Experimental Mechanics* 48.4, pp. 381–402.

Bai, Ning, Xu Chen, and Hong Gao (2009). "Simulation of uniaxial tensile properties for lead-free solders with modified Anand model". *Materials & Design* 30.1, pp. 122–128.

Bardi, F. C. and S. Kyriakides (2006). "Plastic buckling of circular tubes under axial compression—part I: Experiments". en. *International Journal of Mechanical Sciences* 48.8, pp. 830–841.

Batdorf, S. B. and Bernard Budiansky (1949). *A Mathematical Theory of Plasticity Based on the Concept of Slip*. English. Report. Number: NACA-TN-1871.

Bath, Jasbir, ed. (2007). *Lead-Free Soldering*. en. Springer US.

Benbagdad, Kaddour (1992). "Critères de flambage plastique avec lois de comportement complexes sur l'exemple de l'éprouvette cruciforme". fr. PhD thesis. Université Paul Verlaine - Metz.

Besnard, G., F. Hild, and S. Roux (2006). ""Finite-Element" Displacement Fields Analysis from Digital Images: Application to Portevin–Le Châtelier Bands". en. *Experimental Mechanics* 46.6, pp. 789–803.

Bodner, S. R. and M. Naveh (1988). "Viscoplastic Shell Buckling". *Studies in Applied Mechanics*. Ed. by I. Elishakoff et al. Vol. 19. Buckling of Structures. Elsevier, pp. 47–60.

Bodner, S. R., M. Naveh, and A. M. Merzer (1991). "Deformation and buckling of axisymmetric viscoplastic shells under thermomechanical loading". *International Journal of Solids and Structures* 27.15, pp. 1915–1924.

Branch, Mary Ann, Thomas F. Coleman, and Yuying Li (1999). "A subspace, interior and conjugate gradient method for large-scale bound-constrained minimization problems". *SIAM Journal on Scientific Computing*.

Bricard, Alain and Dominique Gobin (2001). "Transferts de chaleur avec changement d'état solide-liquide". fr, p. 17.

Budiansky, Bernard (1958). *A reassessment of deformation theories of plasticity.* Tech. rep. HARVARD UNIV CAMBRIDGE MA.

Chakrabarty, J. (2000). "Plastic Buckling". en. *Applied Plasticity.* Mechanical Engineering Series. Springer, New York, NY, pp. 459–537.

Che, F. X. et al. (2010). "The study of mechanical properties of Sn–Ag–Cu lead-free solders with different Ag contents and Ni doping under different strain rates and temperatures". *Journal of Alloys and Compounds* 507.1, pp. 215–224.

Christoffersen, J. and J. W. Hutchinson (1979). "A class of phenomenological corner theories of plasticity". en. *Journal of the Mechanics and Physics of Solids* 27.5, pp. 465–487.

Combescure, Alain and Jean-Francois Jullien (2017). "Creep buckling of cylinders under uniform external pressure: Finite element simulation of buckling tests". *International Journal of Solids and Structures* 124, pp. 14–25.

Cuddalorepatta, Gayatri and Abhijit Dasgupta (2007). "Viscoplastic Behavior of Hypo-Eutectic Sn3.0Ag0.5Cu Pb-Free Alloy Under Creep Loading Conditions", pp. 159–167.

Dompierre, Benoît (2011). "Fiabilité mécanique des assemblages électroniques utilisant des alliages du type SnAgCu". fr. PhD thesis. Ecole Centrale de Lille.

Eslami, M. R. and M. Shariyat (1997). "Elastic, Plastic, and Creep Buckling of Imperfect Cylinders Under Mechanical and Thermal Loading". en. *Journal of Pressure Vessel Technology* 119.1. Publisher: American Society of Mechanical Engineers Digital Collection, pp. 27–36.

Galletly, G. D. et al. (1987). "Buckling of shallow torispherical domes subjected to external pressure — a comparison of experiment, theory, and design codes". en. *The Journal of Strain Analysis for Engineering Design* 22.3, pp. 163–175.

Gerard, George and Arthur C. Gilbert (1958). "A Critical Strain Approach to Creep Buckling of Plates and Shells". en. *Journal of the Aerospace Sciences* 25.7, pp. 429–434.

Gusic, G, A Combescure, and J. F Jullien (2000). "The influence of circumferential thickness variations on the buckling of cylindrical shells under external pressure". *Computers & Structures* 74.4, pp. 461–477.

Hardin, R A. "Simulation of Heat Treatment Distortion". en, p. 32.

Helfer, T et al. (2013). "Le générateur de code mfront : écriture de lois de comportement mécanique". fr, p. 88.

Helfer, Thomas et al. (2015). "Introducing the open-source mfront code generator: Application to mechanical behaviours and material knowledge management within the PLEIADES fuel element modelling platform". en. *Computers & Mathematics with Applications* 70.5, pp. 994–1023.

Hill, R. (1958). "A general theory of uniqueness and stability in elastic-plastic solids". *Journal of the Mechanics and Physics of Solids* 6.3, pp. 236–249.

— (1998). *The Mathematical Theory of Plasticity*. Oxford Classic Texts in the Physical Sciences. Oxford, New York: Oxford University Press.

Hoff, N. J. (1976). "Theory and Experiment in the Creep Buckling of Plates and Shells". en. *Buckling of Structures*. International Union of Theoretical and Applied Mechanics. Springer, Berlin, Heidelberg, pp. 67–77.

Huh, Seok-Hwan, Keun-Soo Kim, and Katsuaki Suganuma (2001). "Effect of Ag Addition on the Microstructural and Mechanical Properties of Sn-Cu Eutectic Solder". en. *MATERIALS TRANSACTIONS* 42.5, pp. 739–744.

Hutchinson, J. W. and B. Budiansky (1976). "Analytical and Numerical Study of the Effects of Initial Imperfections on the Inelastic Buckling of a Cruciform Column". en. *Buckling of Structures*. International Union of Theoretical and Applied Mechanics. Springer, Berlin, Heidelberg, pp. 98–105.

Hutchinson, John W. (1974). "Plastic Buckling". *Advances in Applied Mechanics*. Ed. by Chia-Shun Yih. Vol. 14. Elsevier, pp. 67–144.

Kim, K. S, S. H Huh, and K Suganuma (2002). "Effects of cooling speed on microstructure and tensile properties of Sn–Ag–Cu alloys". *Materials Science and Engineering* 333.1, pp. 106–114.

Kim, Sok Won et al. (2009). "Thermophysical Properties of Sn–Ag–Cu Based Pb-Free Solders". en. *International Journal of Thermophysics* 30.4, pp. 1234–1241.

Kyriakides, S., F. C. Bardi, and J. A. Paquette (2005). "Wrinkling of Circular Tubes Under Axial Compression: Effect of Anisotropy". *Journal of Applied Mechanics* 72.2, pp. 301–305.

Kyriakides, S. and P. K. Shaw (1982). "Response and stability of elastoplastic circular pipes under combined bending and external pressure". *International Journal of Solids and Structures* 18.11, pp. 957–973.

Kyriakides, Stelios and Edmundo Corona (2007). *Mechanics of Offshore Pipelines*. en. Elsevier.

Lemaitre, Jean et al. (2009). *Mécanique des matériaux solides - 3ème édition*. fr. Dunod.

Massin, P., N. Triantafyllidis, and Y. M. Leroy (1999). "On the stability of strain-rate dependent solids.: I—Structural examples". *Journal of the Mechanics and Physics of Solids* 47.8, pp. 1737–1779.

Mikkelsen, L. P. (2001). "A Numerical Elastic-Viscoplastic Collapse Analysis of Circular Cylindrical Shells under Axial Compression". en. *IUTAM Symposium on Creep in Structures*. Solid Mechanics and its Applications. Springer, Dordrecht, pp. 499–508.

Mikkelsen, Lars Pilgaard (1993). "On the analysis of viscoplastic buckling". *International Journal of Solids and Structures* 30.11, pp. 1461–1472.

Molnar, Aliz et al. (2014). "Effect of silver content on the properties of lead-free solders". *Materials Science and Engineering* 39.2, pp. 51–58.

Montague, P. (1969). "Experimental Behaviour of Thin-Walled Cylindrical Shells Subjected to External Pressure". en. *Journal of Mechanical Engineering Science* 11.1, pp. 40–56.

Moré, J. and D. Sorensen (1983). "Computing a Trust Region Step". *SIAM Journal on Scientific and Statistical Computing* 4.3, pp. 553–572.

Needleman, A. and V. Tvergaard (1982). "Aspects of Plastic Postbuckling Behavior". en. *Mechanics of Solids.* Ed. by H. G. Hopkins and M. J. Sewell. Oxford: Pergamon, pp. 453–498.

Neggers, J. et al. (2017). "Improving full-field identification using progressive model enrichments". *International Journal of Solids and Structures* 118-119, pp. 213–223.

Nestorović, M. D., Y. M. Leroy, and N. Triantafyllidis (2000). "On the stability of rate-dependent solids with application to the uniaxial plane strain test". en. *Journal of the Mechanics and Physics of Solids* 48.6, pp. 1467–1491.

Onat, E. T. and D. C. Drucker (1953). "Inelastic Instability and Incremental Theories of Plasticity". *Journal of the Aeronautical Sciences* 20.3. Publisher: American Institute of Aeronautics and Astronautics _eprint: https://doi.org/10.2514/8.2585, pp. 181–186.

Oñate, Eugenio (2013a). "Curved 3D Shell Elements and Shell Stiffners". en. *Structural Analysis with the Finite Element Method Linear Statics.* Lecture Notes on Numerical Methods in Engineering and Sciences. Springer, Dordrecht, pp. 605–674.

— (2013b). "Thick/Thin Plates. Reissner-Mindlin Theory". en. *Structural Analysis with the Finite Element Method Linear Statics.* Lecture Notes on Numerical Methods in Engineering and Sciences. Springer, Dordrecht, pp. 291–381.

Paley, Moshe and Jacob Aboudi (1991). "Viscoplastic bifurcation buckling of plates". en. *AIAA Journal* 29.4, pp. 627–632.

Réthoré, Julien (2018). *Ufreckles.*

Sammari, A. and J. F. Jullien (1995). "Creep buckling of cylindrical shells under external lateral pressure". en. *Thin-Walled Structures.* Buckling Strength of Imperfection-sensitive Shells 23.1, pp. 255–269.

Sawamura, Tadashi and Takeo Igarashi (2005). "Difference between various Sn/Ag/Cu solder compositions". *Almit Ltd Technical Paper.*

Simo, J. C. and T. J. R. Hughes (1998). *Computational Inelasticity.* en. Interdisciplinary Applied Mathematics. New York: Springer-Verlag.

Triantafyllidis, Nicolas, Patrick Massin, and Yves M. Leroy (1997). "A sufficient condition for the linear instability of strain-rate-dependent solids". en. *Comptes Rendus de l'Académie des Sciences - Series IIB - Mechanics-Physics-Chemistry-Astronomy* 324.3, pp. 151–157.

Trinh, Vuong-Dieu (2009). "Development and validation of finite elements of type solid-shells reduced integration stablizied usable for non linears cinematic and behavior problems". Theses. Arts et Métiers ParisTech.

Tvergaard, Viggo (1983). "Plastic buckling of axially compressed circular cylindrical shells". en. *Thin-Walled Structures* 1.2, pp. 139–163.

Tvergaard, Viggo and Alan Needleman (2000). "Buckling localization in a cylindrical panel under axial compression". en. *International Journal of Solids and Structures* 37.46, pp. 6825–6842.

Wang, C. M. and Tun Myint Aung (2007). "Plastic buckling analysis of thick plates using p-Ritz method". *International Journal of Solids and Structures* 44.18, pp. 6239–6255.

Wang, C. M., Y. Xiang, and J. Chakrabarty (2001). "Elastic/plastic buckling of thick plates". *International Journal of Solids and Structures* 38.48, pp. 8617–8640.

Wei, Guoqiang and Lei Wang (2012). "Effects of cooling rate on microstructure and microhardness of lead-free Sn-3.0Ag-0.5Cu solder". en. IEEE, pp. 453–456.

Yeh, M. K. and S. Kyriakides (1986). "On the Collapse of Inelastic Thick-Walled Tubes Under External Pressure". en. *Journal of Energy Resources Technology* 108.1, pp. 35–47.

Zhang, Jian et al. (2017). "Buckling of egg-shaped shells subjected to external pressure". *Thin-Walled Structures* 113, pp. 122–128.

Département FEDORA – INSA Lyon - Ecoles Doctorales – Quinquennal 2016-2020

SIGLE	ECOLE DOCTORALE	NOM ET COORDONNEES DU RESPONSABLE
CHIMIE	**CHIMIE DE LYON** http://www.edchimie-lyon.fr Sec. : Renée EL MELHEM Bât. Blaise PASCAL, 3e étage secretariat@edchimie-lyon.fr INSA : R. GOURDON	M. Stéphane DANIELE Institut de recherches sur la catalyse et l'environnement de Lyon IRCELYON-UMR 5256 Équipe CDFA 2 Avenue Albert EINSTEIN 69 626 Villeurbanne CEDEX directeur@edchimie-lyon.fr
E.E.A.	**ÉLECTRONIQUE, ÉLECTROTECHNIQUE, AUTOMATIQUE** http://edeea.ec-lyon.fr Sec. : M.C. HAVGOUDOUKIAN ecole-doctorale.eea@ec-lyon.fr	M. Gérard SCORLETTI École Centrale de Lyon 36 Avenue Guy DE COLLONGUE 69 134 Écully Tél : 04.72.18.60.97 Fax 04.78.43.37.17 gerard.scorletti@ec-lyon.fr
E2M2	**ÉVOLUTION, ÉCOSYSTÈME, MICROBIOLOGIE, MODÉLISATION** http://e2m2.universite-lyon.fr Sec. : Sylvie ROBERJOT Bât. Atrium, UCB Lyon 1 Tél : 04.72.44.83.62 INSA : H. CHARLES secretariat.e2m2@univ-lyon1.fr	M. Philippe NORMAND UMR 5557 Lab. d'Ecologie Microbienne Université Claude Bernard Lyon 1 Bâtiment Mendel 43, boulevard du 11 Novembre 1918 69 622 Villeurbanne CEDEX philippe.normand@univ-lyon1.fr
EDISS	**INTERDISCIPLINAIRE SCIENCES-SANTÉ** http://www.ediss-lyon.fr Sec. : Sylvie ROBERJOT Bât. Atrium, UCB Lyon 1 Tél : 04.72.44.83.62 INSA : M. LAGARDE secretariat.ediss@univ-lyon1.fr	Mme Emmanuelle CANET-SOULAS INSERM U1060, CarMeN lab, Univ. Lyon 1 Bâtiment IMBL 11 Avenue Jean CAPELLE INSA de Lyon 69 621 Villeurbanne Tél : 04.72.68.49.09 Fax : 04.72.68.49.16 emmanuelle.canet@univ-lyon1.fr
INFOMATHS	**INFORMATIQUE ET MATHÉMATIQUES** http://edinfomaths.universite-lyon.fr Sec. : Renée EL MELHEM Bât. Blaise PASCAL, 3e étage Tél : 04.72.43.80.46 infomaths@univ-lyon1.fr	M. Luca ZAMBONI Bât. Braconnier 43 Boulevard du 11 novembre 1918 69 622 Villeurbanne CEDEX Tél : 04.26.23.45.52 zamboni@maths.univ-lyon1.fr
Matériaux	**MATÉRIAUX DE LYON** http://ed34.universite-lyon.fr Sec. : Stéphanie CAUVIN Tél : 04.72.43.71.70 Bât. Direction ed.materiaux@insa-lyon.fr	M. Jean-Yves BUFFIÈRE INSA de Lyon MATEIS - Bât. Saint-Exupéry 7 Avenue Jean CAPELLE 69 621 Villeurbanne CEDEX Tél : 04.72.43.71.70 Fax : 04.72.43.85.28 jean-yves.buffiere@insa-lyon.fr
MEGA	**MÉCANIQUE, ÉNERGÉTIQUE, GÉNIE CIVIL, ACOUSTIQUE** http://edmega.universite-lyon.fr Sec. : Stéphanie CAUVIN Tél : 04.72.43.71.70 Bât. Direction mega@insa-lyon.fr	M. Jocelyn BONJOUR INSA de Lyon Laboratoire CETHIL Bâtiment Sadi-Carnot 9, rue de la Physique 69 621 Villeurbanne CEDEX jocelyn.bonjour@insa-lyon.fr
ScSo	**ScSo*** http://ed483.univ-lyon2.fr Sec. : Véronique GUICHARD INSA : J.Y. TOUSSAINT Tél : 04.78.69.72.76 veronique.cervantes@univ-lyon2.fr	M. Christian MONTES Université Lyon 2 86 Rue Pasteur 69 365 Lyon CEDEX 07 christian.montes@univ-lyon2.fr

FOLIO ADMINISTRATIF

THESE DE L'UNIVERSITE DE LYON OPEREE AU SEIN DE L'INSA LYON

NOM : JACQUET
(avec précision du nom de jeune fille, le cas échéant)

DATE de SOUTENANCE : 19/01/2021

Prénoms : Nicolas Hugues Roger

TITRE : ELASTO-VISCO-PLASTIC BUCKLING OF THICK SHELLS

NATURE : Doctorat

Numéro d'ordre : 2021LYSEI005

Ecole doctorale : MEGA ED162

Spécialité :Génie Mécanique

RESUME :
Le sujet de thèse traite du flambage de structure épaisses dont le comportement est élasto-visco-plastique. Un modèle prédictif a été développé. Ce dernier a été confronté à des résultats expérimentaux.
Deux campagnes d'essais ont été menées afin de générer un jeu de données expérimentales suffisant. Lors de ces campagnes, le flambage de deux structures a été évalué. L'une portait sur le flambage de plaques en compression, l'autre sur le flambage de demi-oeufs soumis à une pression externe.
Les essais ont été instrumentés par des moyens optiques afin de mesure la déformation de certaines zones des éprouvette. Ce type d'instrumentation a permis d'améliorer le poste traitement et la validation du modèle prédictif.
Une bonne corrélation entre le modèle prédictif et les essais a été observée. Ce niveau de corrélation porte aussi bien sur les efforts et temps critiques de flambage que sur les modes de flambage observés.
Le modèle développé permet alors de prédire le flambage de structures épaisses dont le comportement est élasto-visco-plastique. De plus il est applique à des chargements non proportionnels. Ce modèle donne de très bon résultats moyennant le respect de certaines hypothèses discutées dans le mémoire de thèse.

MOTS-CLÉS : Flambage, fluage, DIC, FEMU, elasto-visco-plastique, bifurcation, instablilité, stéréo-corrélation d'image.

Laboratoire (s) de recherche : Laboratoire de Mécanique des Contacts et des Structures
Université de Lyon, CNRS, INSA-Lyon UMR5259
27 bis avenue Jean Capelle - F69621 Villeurbanne Cedex France

Directeur de thèse: Thomas ELGUEDJ
Co-encadrant de thèse: Nicolas TARDIF
Co-encadrant de thèse: Christophe GARNIER

Président de jury :

Composition du jury :

THUILLIER, Sandrine	Professeur, Université Bretagne Sud	Rapporteuse
ZAHROUNI, Hamid	Professeur, Université de Lorraine	Rapporteur
KYRIAKIDES, Stelios	Professeur, Université du Texas	Examinateur
CORET, Michel	Professeur, École Centrale de Nantes	Examinateur
BOUCLIER, Robin	Maître de conférences, INSA de Toulouse	Examinateur
ELGUEDJ, Thomas	Professeur, INSA de Lyon	Directeur de thèse
TARDIF, Nicolas	Maître de conférences, INSA de Lyon	Invité et co-encadrant de thèse
GARNIER, Christophe	Ingénieur, CEA Cadarache	Invité et co-encadrant de thèse